Physically-Based Compact Modelling of Organic Electronic Devices

Sungyeop Jung

NNT : 2016SACLX115

THESE DE DOCTORAT
DE
L'UNIVERSITE PARIS-SACLAY
PREPAREE A
L'ÉCOLE POLYTECHNIQUE

ÉCOLE DOCTORALE N°573
Interfaces : approches interdisciplinaires, fondements, applications et innovation

Spécialité de doctorat : Physique

Par

M. Sungyeop Jung

MODÈLISATION COMPACTE À BASE PHYSIQUE DES COMPOSANTS ÉLECTRONIQUES ORGANIQUES

Thèse présentée et soutenue à Palaiseau, le 21 décembre 2016 :

Composition du Jury :

M. Benjamin Iñiguez	Professeur, Universitat Rovira i Virgili	Rapporteur
M. Paul Heremans	Professeur/Fellow, Katholieke Universiteit Leuven/IMEC	Rapporteur
M. Louis Giraudet	Professeur, Université de Reims	Président du jury/ Examinateur
Mme. Natalie Stingelin-Stutzmann	Professeure, Imperial College London	Examinatrice
M. Yvan Bonnassieux	Professeur, École polytechnique	Examinateur
M. Ahmed Nejim	R&D Projects Manager, Silvaco Europe Ltd.	Invitée
M. Gilles Horowitz	Professeur/Directeur de Recherche Émérite, École polytechnique/CNRS	Directeur de thèse

PHYSICALLY-BASED COMPACT MODELLING OF ORGANIC ELECTRONIC DEVICES

Sungyeop Jung
sungyeop.jung@polytechnique.edu

Thesis Advisor:
Professor / Emeritus Research Director Gilles Horowitz

A thesis for the degree of
Ph.D. in Physics

2016

Abstract

In spite of a remarkable improvement in the performance of organic electronic devices, there is still a lack of rigorous theoretical understanding on the device operation. This thesis is dedicated to establishing practical models of organic electronic devices with a full physical basis. A physically-based compact model of a circuit element is a mathematical equation that enables an accurate, simple and rigorous description of the device operation. In this context, distinctive features of charge carrier injection and transport in organic semiconductors are incorporated in the models that improve the accuracy without compromising the mathematical simplicity. The concomitant effect on the current-voltage characteristics of prototypical organic diodes and transistors are studied. Parameter extraction methods consistent to the models are presented which enable unambiguous determination of device parameters used to predict device operation and evaluate device performance and properties of organic thin-films and interfaces. The approaches encompass analytical development of physical equations, two-dimensional numerical simulation based on finite-element method and experimental validation. The original and fully analytical compact models and parameter extraction methods provide fundamental understanding on how energetic disorder in an organic semiconductor thin-film, described by the Gaussian density of states, affects the observable current-voltage characteristics of the devices.

Keywords : Organic electronics, device physics, analytical modeling, diodes, field-effect transistors, Gaussian density-of-states

Résumé

En dépit d'une amélioration remarquable de la performance des composants électroniques organiques, il y a encore un manque de compréhension théorique rigoureuse sur le fonctionnement du composant. Cette thèse est consacrée à la création de modèles pratiques pour composants électroniques organiques à base physique complète. Un modèle compact à base physique d'un élément de circuit est une équation mathématique qui permet une dèscription précise, simple et rigoreuse du fonctionnement du dispositif. Dans ce contexte, les caractéristiques distinctives de l'injection et du transport des porteurs de charge dans les semi-conducteurs organiques sont incorporées dans les modèles qui améliorent la précision sans compromettre la simplicité mathématique. L'effet concomitant sur les caractéristiques courant-tension des diodes et des transistors organiques prototypiques sont étudiés. Les méthodes d'extraction des paramètres cohérents aux modèles sont présentées qui permettent la détermination univoque des paramètres du composant utilisés pour prévoir le fonctionnement du composant et évaluer la performance du composant et les propriétés des couches minces et interfaces organiques. Les approches englobent le dévelopement analytique des équations physiques, la simulation numérique à deux dimensions basé sur la méthode des éléments finis et la validation expérimentale. Les modèles compacts originaux et entièrement analytiques et des méthodes d'extraction de paramètres fournissent une compréhension fondamentale sur la façon dont le désordre énergétique dans une couche mince de semi-conducteur organique, décrit par la densité d'états Gaussienne, affecte les caractéristiques courant-tension observables des composants.

Mots-clés : Électronique organique, physique des composants électroniques, modélisation analytique, diodes, transistors à effet de champ, densité d'états Gaussienne

Acknowledgments

First and foremost, I would like to appreciate my advisor Prof. Gilles Horowitz for his continuous guidance and support in my journey to become an independent researcher. I am grateful to Prof. Yvan Bonnassieux, the group leader at OLAE in LPICM, for his responsibility for the KHU-EP dual master degree program through which I could come to study in France, and his kind support during the thesis. I also wish to thank Prof. Bernard Drévillon and Prof. Pere Roca i Cabarrocas, former and present director of LPICM, for their leadership and encouragement. I would like to mention OLAE members; Abderrahim Yassar, Gaël Zucchi, Bernard Geffroy, Jean-Charles Vanel, Denis Tondelier, Bérengère Lebental, Subimal Majee, Edoardo Milana, Mallesh Goudumala, Xiaoguang Huang, Jong Woo Jin, Chang-Hyun Kim, Taewoo Jeon, Tiphane Bourgeteau, Jinwoo Choi, Warda Hadouchi, Khaoula Jemli, Heejae Lee, Fulvio Michelis, Anna Shirinskaya and Miguel Torres Miranda. It was a joyful experience to work with them. I appreciate kindness and professional work of all LPICM members who have administratively, technically or personally supported me.

I am truly thankful to Dr. Ahmed Nejim and Dr. Andrew Plews at Silvaco Europe Ltd., Prof. Arokia Nathan at Cambridge University and Prof. Ioannis Kymissis at Columbia University for inviting me to conduct research visits that broadened my personal and academic spectrum. The doctoral mobility grants from Horizon 2020 Marie Skłlodowska-Curie Fellowship Research and Innovation Staff Exchange (RISE) Programme, École Doctorale Interfaces at Univerdsité Paris-Saclay, and Paris-Columbia Alliance Program are kindly acknowledged. I would like to thank Dr. Guillaume Gruntz, Prof. Yohann Nicolas and Prof. Thierry Toupance at Université de Bordeaux and Dr. Vincent Mosser at Itron Inc. for the fruitful collaborations. I am grateful for the Ph.D. fellowships from Centre National de la Recherche Scientifique (CNRS) and Direction des Relations Internationales (DRI) in École polytechnique. I appreciate Prof. François Hache, the director of École Doctorale Interfaces, and Audrey Lemarechal, Ph.D. administrative officer.

I wish to extend my gratitude to my friends I met from Catholic Community in Paris, STX Scholarship Foundation, and schools. Finally, I would like to express my deepest gratitude to my family for their love and support.

Contents

List of Figures

List of Tables

Chapter 1

Introduction

1.1 Organic electronics

Organic electronics, which is also called plastic electronics or polymer electronics, is a branch of electronics making use of electrically conducting and semiconducting polymers and small molecules [1]. The term 'organic' is given because the polymers and small molecules mostly consist of carbon atoms with some extent of hydrogen, oxygen, nitrogen, sulfur, phosphor or heavy metal atoms incorporated to endow functionalised characteristics to polymers and molecules. This is the most significant difference compare to conventional electronics, in which inorganic semiconductors, such as silicon (Si), gallium arsenide (GaAs), etc. are used. In 1862, H. Letheby obtained a weakly conducting polymer though anodic oxidation of aniline in sulfuric acid, which was thought to be polyaniline [2]. After the report in 1977 [3], which stated that polyacetylene can be oxidized with halogens to produce materials with a wide range of conductivity from an insulator to a conductor, research on conducting polymers gained much more attention. On the other hand, researchers discovered conducting organic molecules in the 1950s. For example, a semiconducting charge-transfer complex, perylene-iodine which is a kind of salts consists of polycyclic aromatic molecules and halogens, with high conductivity of 0.12 S/cm was reported in 1954 [4]. These demonstrate that electrical current can pass through organic polymers and molecules.

Since the discovery of conducting and semiconducting properties, organic semiconductors have been used actively in various electronic and optoelectronic devices. First, organic polymers and molecules were adopted in solar cells, and the earlier and recent progress in organic solar cells (OSCs) are well summarized in the articles [5–7], which have been made since the first observation of photoconductivity in organic semiconductors reported in 1950s [8,9]. Second, there have been a large

number of reports demonstrating the use of organic materials for organic light-emitting diodes (OLEDs) since the pioneering work by C. W. Tang [7]. Third, polythiophene which is a class of organic conjugated polymers discovered in the late 1970s was successfully introduced in organic field-effect transistors (OFETs) by Koezuka and coworkers in 1986 [10, 11].

One of the most distinctive features of organic materials is given by their molecular nature. In contrast to inorganic crystals that consist of atoms held in place by covalent bonds, organic solids are formed by molecules or polymers bound by van der Waals force. Thanks to this weak van der Waals force [1], organic solids possess mechanical flexibility (Young's modulus lower than a few tens of GPa) and solids can be assembled more easily. The latter means that organic layer can be formed from solution containing an organic semiconductor and proper solvent (called organic ink) or evaporated at a moderate temperature (below a few hundreds of °C). In particular, printed organic electronics, which combines organic ink and conventional ink jet printing technique, holds a clear advantage of being able to control the deposition of functional layers only at desired points on the substrate and to reduce of material waste and process time compared to conventional shadow masking and lithographic patterning techniques [12, 13]. On this account, the subsequent progress has been made towards realization of 'large-area', 'flexible' and 'low-cost' electronic systems.

We have seen impressive progress in organic electronics over recent years. Amongst them, OLEDs are remarkable for diverse products already available or in the prototype phase. OLED's display application showed particularly significant success. Owing to their inherently wider color gamut, moving-picture response, and low power-consumption, OLEDs are replacing conventional liquid-crystal displays (LCDs) not only in mobile devices but also in consumer electronic devices. Figure 1-1(a)-(b) shows a curved OLED display mounted on a commercial mobile phone produced by Samsung Electronics (2015) [14] and a television produced by LG electronics (2016) [15]. Another key application of OLEDs in the future might be solid-state lighting by white (or coloured) OLEDs with a particular articulation on the uniform light emission from a large surface area [16–18]. OPVs for generating electrical power from sunlight are a particularly important application due to increasing demand for environmentally benign energy production. Infinitypv [19] has demonstrated various types of printed OPV modules with excellent flexibility, scalability ($1 \sim 4$ W/m) and light weight ($220 \sim 450$ g/m^2) Figure 1-1(c). Organic diodes and OFETs can be used for various circuit applications. PolyIC [20] demonstrated a polymer based RFID tag Figure 1-1(d). OFETs are adopted in

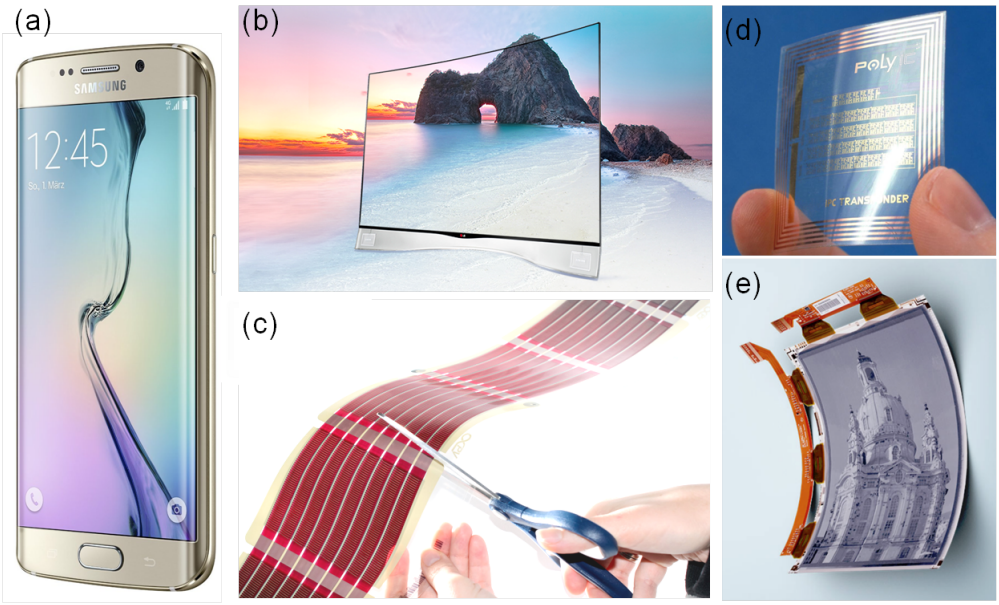

Figure 1-1: State-of-of-the-art organic electronic devices, systems, and circuits: a curved OLED display employed in (a) a mobile phone and (b) a television, (c) a flexible and thin OPV module scalable by cutting with a pair of scissors, (d) polymer-based RFID tag, and (e) a flexible and lightweight OFET display driving circuit.

active-matrix pixel drivers in LCDs or OLEDs, and OFET-based display backplanes are under consistent development [21, 22]. Plastic Logic's ultra-flexible paper-like display in Figure 1-1(e) has developed a backplane circuitry composed of OFET arrays [23]. OFET-based large-area sensors for optical and mechanical read-out are also significant for advanced applications such as conformable image scanners, electronic skins [24–27].

Today, organic electronics is still actively evolving. Researchers have overcome many critical challenges encountered at its infancy, such as performance and stability issues. However, the industrial acceptance seems not prompt probably due to pre-existing or other emerging technologies, especially where the unique advantages of organic semiconductors are diluted (i.e. market takeover). More recently, the concepts of creating new-market or targeting niche-market are also emphasized, and novel applications are continuously being envisaged. Encouraged by multidisciplinary character of organic electronics, physicists, chemists and engineers are exploring a wide range of new materials and device functionalities, which led to the conceptualisation of various new of organic devices. Amongst them, biomedical application is regarded as one of the most attractive orientations that organic electronics community can proceed toward [28, 29]. A variety of initiative works on chemical and biological sensors are being reported [30]. We anticipate a

further advancement that will promote organic electronics to a more competitive position, where attractive features of organic semiconducting materials will be in full bloom.

1.2 Motivation

The foremost motivation of this thesis is the lack of mature theoretical understanding on organic semiconductors and devices. Because it provides a reliable, comprehensive, and well-documented knowledge base, conventional microelectronics still represents the main source for modelling, interpreting, and conceiving organic electronic devices. However, a considerable amount of theoretical and experimental effort has been carried out during the recent decades to develop more adequate models to account for the specificities of organic semiconductors. In pursuit of physical modelling, the material aspect has been the principal concern, such as the effect of aforementioned molecular nature of organic solids on the electronic structure, and concomitant charge carrier transport and injection processes. Unique features of these processes in organic disordered semiconductors (ODSs) are being continuously discovered by physical modelling (such as *ab-initio* approach based on Monte-Carlo simulation method or a direct numerical solution of physical equations) of a simple organic semiconductor medium and/or metal/organic semiconductor junction. For example, the concept of describing the density-of-states as a random distribution of localised states was introduced [31]. In addition, the dependence of mobility, a transport parameter, on surrounding conditions such as lattice temperature, charge carrier concentration and electric field has been highlighted [32, 33]. Nonetheless, these recent findings have not been fully addressed to the device-level physical modelling mainly due to its mathematical complexity and two- or three-dimensional structures of actual devices. As a consequence, correlation between the result of physical device modelling and the experimental data is still lacking. The former is indeed highly recommended in that it enables validation or refinement (that may need) of the model, facilitates interpretation or even predictions of experimental results, and provides feedback for an improved device design and fabrication process control.

The second motivation is to develop a physically-based compact model that is sufficiently simple for it to be adopted in circuit simulators and sufficiently accurate for the result of modelling to be useful for circuit designers [34]. During past decades, there has been a growing interests in integrating organic electronic devices (i.e. single diodes or transistors) into a circuit or system (single diodes or

transistors. display driving circuit, PV modules, RFID system and matrix-based sensors). In this context, the necessity of a physically-based compact model is getting more recognised. In circuit simulators such as SPICE (Simulation Program with Integrated Circuit Emphasis) [35], device characteristics are represented by an equation (or a set of equations). In this case, directly adopting the genuine physical modelling that often requires iterative numerical calculation might not be a suitable choice. Therefore,it is necessary to examine and employ an analytical or empirical approach, such as through physical approximations or parametrisations, in order to achieve the required level of simplicity of the compact model for a device. A related work for optimising the trade-off between the simplicity and physical rigorousness is also required. In summary, a reliable compact model will serve as an intermediary between the device-level and the circuit level modelling practices.

1.3 Thesis overview

This thesis is titled 'physically-based compact modelling of organic electronics devices'. Mathematical device modelling is developing a numerical or analytical model that describes the behaviour of the electrical devices. As the title implies, our principal goal is to develop specific models for organic devices that possess both physical basis and practical applicability. These two aspects are in line with the two major motivations described above. In this context, we paid a balanced effort in reviewing a wide range of charge carrier transport and injection physics as well as theoretical and experimental methods (**Chapter 2 and 3**), and adopting them into the compact models of typical devices (**Chapter 4 and 5**). Here, a short description of each chapter is given for overview.

Chapter 1 Introduction outlines a field of organic electronics, explains the motivations for the thesis and related aim and scope of the thesis.

Chapter 2 Fundamentals provides short summaries on the most basic physical backgrounds required for understanding organic semiconductors and electronic devices. The origin of the semiconducting properties in organic materials is explained briefly. Square-root, exponential and Gaussian DOS models are presented for describing how energy states are distributed in organic solids with different degrees of crystallinity. Related charge carrier transport physics are delineated, defining a clear boundary of its pertinence. The effect of disorder on charge carrier injection at metal/organic semiconductor interface is demonstrated.

Chapter 3 Methods explains a variety of experimental and theoretical meth-

ods used for the analysing and modelling organic electronics devices. A basic information on impedance spectroscopy, analytical modelling, numerical modelling, and experimental validation is given, focusing on the complementary functions between each methods. Special considerations for practice are presented which has been key factors for obtaining a reliable result.

Chapter 4 Organic diodes is the first chapter devoted to the scientific results. Organic rectifying diodes are studied by means of theoretical and experimental techniques. The concept of full-depletion in unintentionally-doped organic semiconductors is presented, and its limit in relation to the charge injection is described. The theoretical development for the electrostatic distribution and current-voltage characteristics are elaborated in the weak and strong injection conditions.

Chapter 5 Organic field-effect transistors (OFET) is the second chapter devoted to the scientific results. OFETs having staggered geometry are investigated. Numerical modelling results are presented for understanding the current path in the transistor, identifying the origin of the contact voltage drop and power-law gate voltage dependence of contact resistivity. A modified equivalent circuit based on current crowding model is presented that leads to power-law mobiltiy. Theoretical and experimental evidences are provided to support the existent of power-law dependent mobility and contact resistance in the OFETs with Gaussian DOS and hopping transport. Such phenomena is newly introduced into the drain current model and related parameter extraction method, maintaining the physically-based compact modelling philosophy.

Chapter 6 Conclusion and perspectives summarise major results found and analysed in the thesis with concluding remarks. Limitations of the presented work and suggestions for the further investigation is also specified.

Chapter 2

Fundamentals

In this chapter, fundamental physics of organic semiconductors and charge transport and injection processes is summarized. We focused on emphasizing distinct features of organic materials and devices, providing concise comparison with the inorganic counterparts. For basic knowledge on solid-state physics and semiconductor device physics, we recommend referring to typical textbooks [36–38]. First, we discuss the semiconducting property and electronic structure of organic materials. Then, the charge carrier transport is elaborated illuminating how different density of states (DOS) models and/or transport mechanisms of organic materials could explain experimentally observed mobility behaviours. Finally, energetic alignment and formation of the carrier injection barrier upon forming a metal/organic semiconductor junction is described.

2.1 Organic semiconductor

2.1.1 π-conjugated molecules and polymers

Organic semiconductors are a class of organic compounds that possesses a semiconducting property, i.e. organic small molecules or polymers, made up by carbon and hydrogen atoms and at times heteroatoms such nitrogen, sulfur and oxygen.

Carbon is a group four element in the periodic table with four valence electrons accommodated individually in 2s, $2p_x$, $2p_y$ and $2p_z$ atomic orbitals. A special property of carbon is the ability to hybridise its atomic orbitals upon bonding with other atoms. Three different ways are possible according to the number of directional p atomic orbitals engaged in the hybridisations: sp_1, sp_2 and sp_3, which leads to a wide variety of bonding configurations [1]. In particular, sp_2-hybridisations are interesting where the sp_2-orbitals form a triangle within a plane and the p_z-

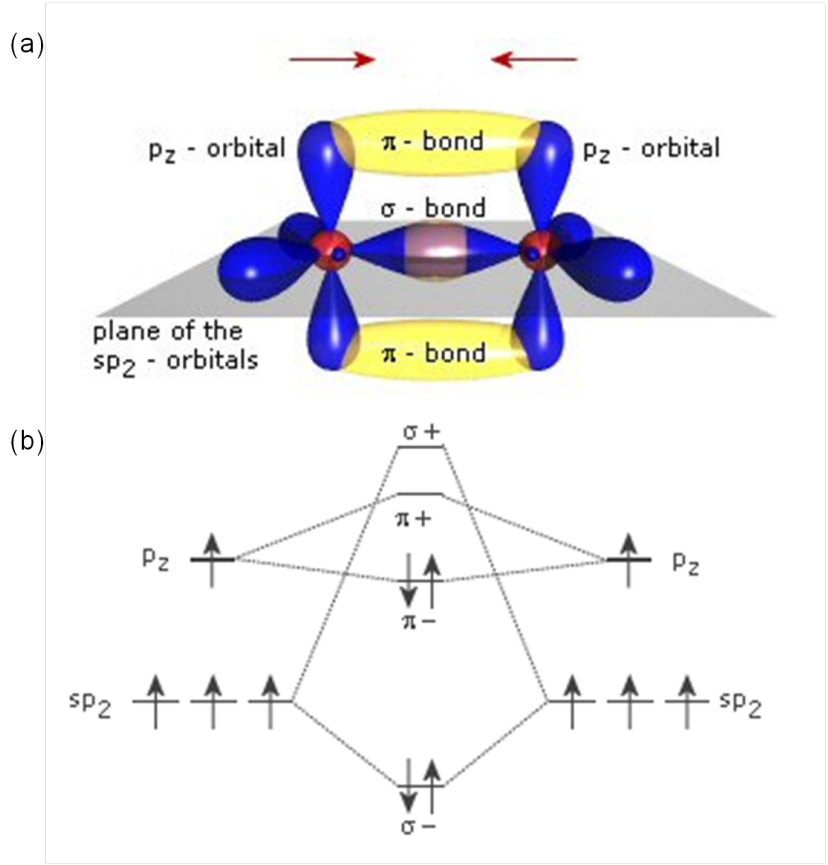

Figure 2-1: (a) Hybridised atomic orbitals and chemical bonding in an ethylene C_2H_2 molecule. (b) Energy diagram of the carbon-carbon bonding with the sp_2 hybridisation.

orbitals are in the plane perpendicular to it. The simplest example of this kind is ethylene C_2H_2 Figure 2-1(a). When two carbon atoms with sp_2-hybridisations approach, a large orbital overlap of two sp_2-orbitals forms a strong σ-bond. The energy difference between the occupied binding orbitals ($\sigma+$) and the unoccupied anti-binding orbitals (σ-) is quite large and well beyond the visible spectral range. Correspondingly, longer chains of bound carbon atoms would have a large gap between the highest occupied molecular orbital (HOMO) and the lowest unoccupied molecular orbital (LUMO), leading to insulating properties Figure 2-1(b). On the other hand, in the sp_2-hybridisations, two p_z-orbitals form additionally π-bonds. These bonds have much smaller energetic difference between the HOMO and LUMO, leading to strong absorption in or near the visible spectral range and to semiconducting properties. Therefore, in principal, organic compounds that have frontier orbitals (HOMO and LUMO) formed by π-bonded electrons are considered as semiconductors.

This argument pertains in larger molecules. Figure 2-2 illustrates the orbital

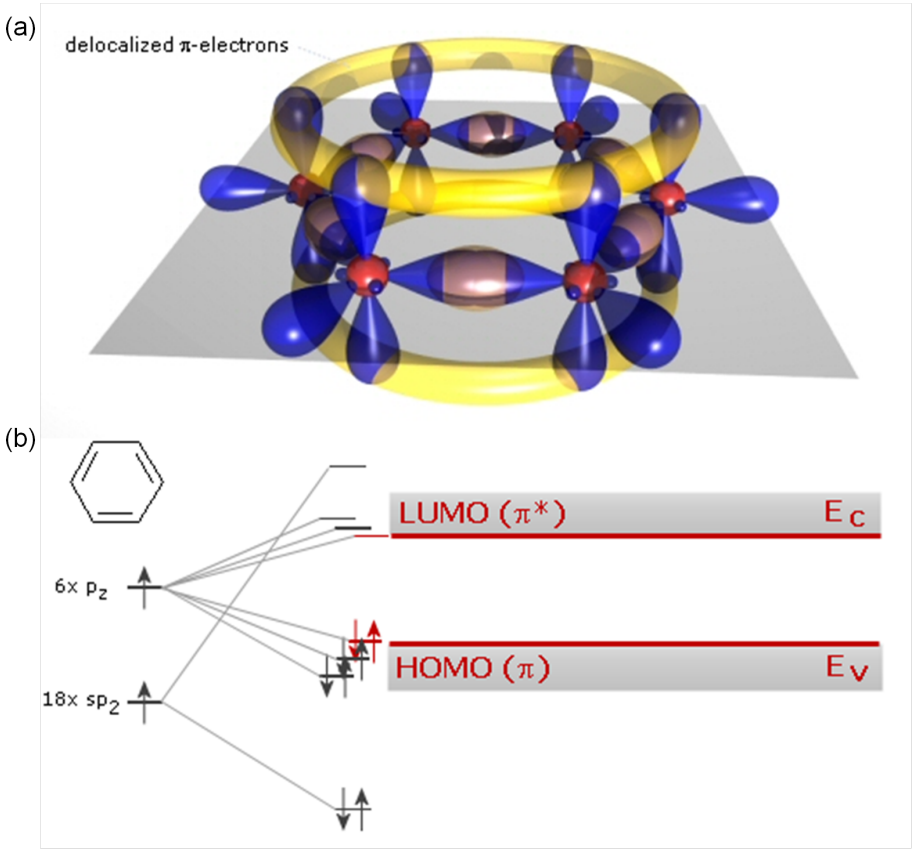

Figure 2-2: (a) Hybridised atomic orbitals of benzene (C_6H_6) molecule. (b) Chemical structure and energy diagram of benzene.

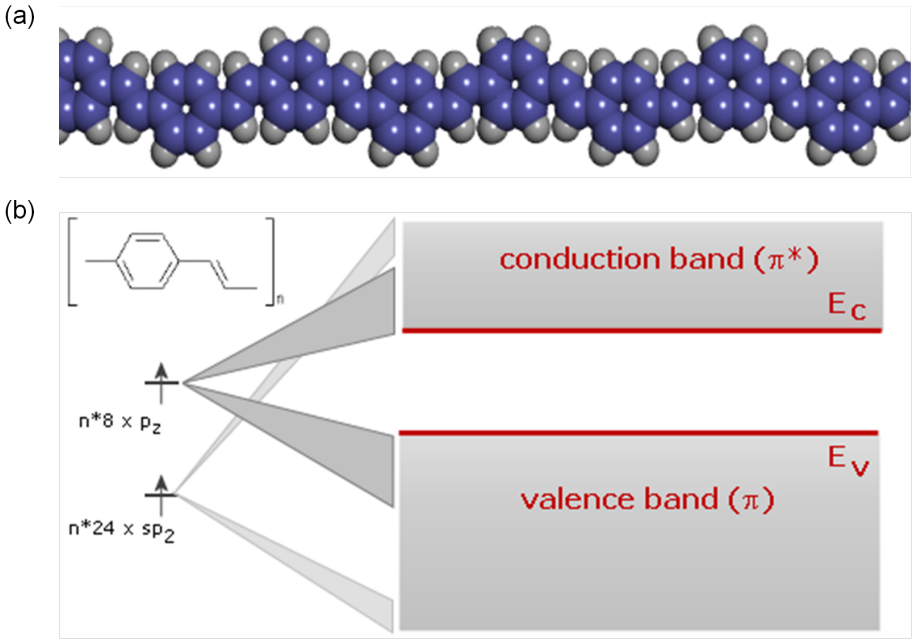

Figure 2-3: (a) Chemical structure and (b) energy diagram of poly-para-phenylene-vinylene (PPV).

picture of benzene (C_6H_6). Because there exist 3 pairs of p_z-orbitals to form π-bonds compared to 6 pairs of sp_2-orbitals in the ring, it was represented by an alternating single and double bonds in the conventional chemical structure. However, all the six electrons coming from the six carbon p_z orbitals are so weakly bound to the neighbouring atoms that they are in effect delocalised through the whole cyclic chain of the molecule, giving rise to geometrical symmetry. Another important aspect demonstrated by the benzene molecule is the split of the binding and anti-binding orbitals into close but different energy levels shown in Figure 2-1(b). This is analogous to the formation of energy bands of inorganic semiconductors when the number of atoms increases to make a crystal network. Thus, it can be said that the HOMO and LUMO 'levels' widen into the HOMO and LUMO 'bands', which are often interchangeably used with the valence band and the conduction band, respectively. The gap between occupied and empty states in these π-systems becomes smaller with increasing delocalisation, leading to absorption and fluorescence in the visible. Also, thanks to higher molar mass, these substances can be prepared as solid.

If a long chain of carbon atoms is formed, the π-bonds become delocalised along the chain and form a one-dimensional electronic system. This type of chemical system where the π-electrons are delocalised through alternating single and double bonds is often called a π-conjugated system. Figure 2.3 shows an example of the π-conjugated polymer, poly-para-phenylene-vinylene (PPV). In general, as the conjugation length increases, the bandwidth increases and the band-gap decreases as a result of the splitting of the frontier molecular orbitals. Polymer organic semiconductors are usually deposited in wet processes, like spin-coating or printing.

2.1.2 Material classification

Organic semiconductors are most frequently categorized as small molecules or polymers based on the size and molecular weight. In contrast to a defined chemical structure of an organic small molecule an organic polymer has dispersion in size and molecular weights according to the number of repeating units. Despite the differences in the size-originating properties, they share a common feature of alternating single and double bond, π-conjugations, for a semiconducting property.

The second criteria for classifying organic semiconductor is solubility which determines the type or easiness of deposition process. Although polymers has been regarded as a soluble material and preferably used for solution process [39, 40], the solubility of small molecules has been improved by strategic synthesis including the attachment of substitution groups that enhance solubility [41, 42]. Now, selective

solubility to a specific solvent, namely orthogonality, is regarded as a key factor for achieving successive deposition of organic layer on top of pre-existing organic layers without damaging the latter [43, 44].

The third criteria is the conduction type of the organic semiconductor either *p*-type (hole-transporting) or *n*-type (electron-transporting). This should not be confused with the same denomination used for inorganic semiconductors. Since inorganic semiconductors are generally used in a doped form, the appellation of *p*- or *n*-type is based on the type of doping impurities: *p*-type inorganic semiconductors are doped by acceptor impurities, and *n*-type by donors. In contrast, organic semiconductors are used mostly without intentional doping. In effect, it is not the type of dopant but the type of 'injected' charge that determines the type of conduction in organic semiconductor. This was evidenced in OFETs by the minimum difference between the electron affinity of organic semiconductor and work function of source and drain contact metal to achieve *n*-type conduction [45].

Since the first discovery of *p*-type organic semiconductor, the vast majority of demonstration have been concerned with is *p*-type organic semiconductor and devices. The *n*-type OFETs are especially useful for organic complementary circuits (OCCs). Indeed, compared to the unipolar circuits based only on *p*-type OFETs, the use of both *n*- and *p*-type OFETs enables larger noise margin and lower power consumption [46, 47]. At its infancy, *n*-type organic semiconductors, such as lutetium diphthalocyanine [48], C_{60} [49, 50] or those bearing electron withdrawing groups such as cyanide [51] or imide [52, 53], suffered from highly sensitive to ambient air, humidity and light. Over the past two decades, developing a *n*-type organic semiconductor with good stability and electron-transporting behaviour has been one of the first priorities for the improvement of the material property [54–59]. Among them, the perylene and naphthalene carboxydiimide derivatives are two famous families of *n*-type organic semiconductors [60–64]. Also, electron-transporting triphenodioxazine (TPDO) derivatives, which can be produced at the industrial scale, have gain significant attention [65, 66].

2.1.3 Organic solids

At variance with inorganic semiconductors, where covalent bonds between atoms are the only contribution to the formation of macroscopic crystal of solid, organic molecules are bounded by weak van der Waals force [1], which means that semiconducting properties at the macroscopic level is possible only if the inter-molecular interaction is significant for the π-conjugated electrons can be delocalised and moved from one molecule to another. This brings both unique opportunities and

ultimate limitations to device applications.

The process temperature of an electronic device can be significantly lowered through simple evaporation or printing techniques. Even, deposition of functional organic materials on a plastic or rubber-like substrate for flexible and even stretchable electronics [67–70]. On the other hand, due to the weak electronic coupling between molecules, there is a significant limitation to the charge-carrier transport, as discussed in more detail in Section 2.3.

For illustrative purposes, organic semiconductors exist in form of molecular crystals, polycrystals or amorphous thin films with different long-range of disorder. Organic single crystals can be obtained either from small-molecules through physical vapour transport method under controlled pressure and temperature gradient [71–73] or through solution growth [74] as a free-standing single crystal piece or as a thin-film deposited and fixed on a substrate. Organic polycrystals and amorphous can be obtained vacuum evaporation or solution-based techniques mostly as a thin-film [75]. This implies that inter-molecular interaction of organic solid and concomitant physical processes varies significantly according to the macroscopic morphology of the solid.

Considering that a majority of organic electronic devices is composed of organic solids, despite existence of a single molecule or polymer-based electronic devices [76–78], understanding the effect of macroscopic morphology on various semiconductor properties (structure-property relationship) constitutes the core of organic semiconductor material and device physics.

2.2 Density-of-states models

In order to understand charge carrier transport and injection in organic solids, we need to elaborate on the electronic structure of organic solids. The density-of-states (DOS) model describes the shape and characteristics of the electronic structure. We will present representative DOS models for different degree of solid phases: square-root extended band with and without localised exponential trap-states (namely, square-root and exponential DOS models) and Gaussian DOS model, respectively for crystalline, polycrystalline and amorphous phases (Figure 2-4). We note that the first two models were conceived from inorganic crystals and polycrystals and have been frequently adopted for organic semiconductors, which would be legitimate for highly crystalline organic solids. At present, there is increasing consensus on Gaussian DOS as a more pertinent description for energy structure of organic disordered semiconductors (ODS). This section is dedicated

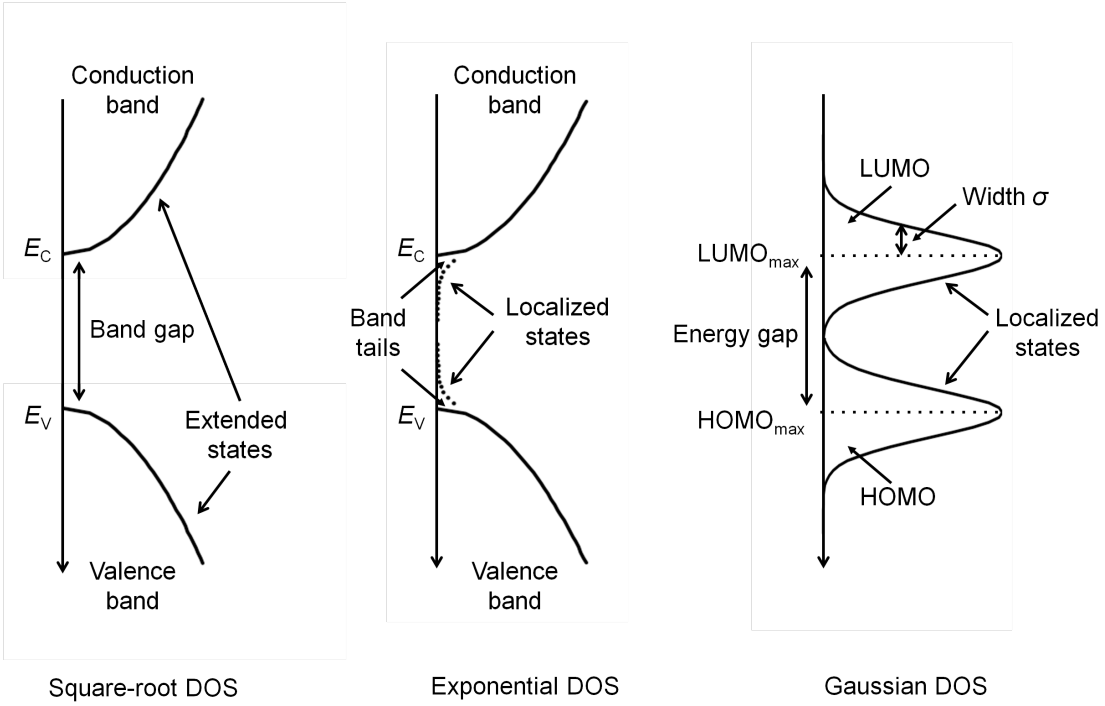

Figure 2-4: Density of states (DOS) models: square-root, exponential and Gaussian.

to illustrate the fundamental differences between each model and underlying assumptions of each model, reserving a more conclusive remark for Section 2.3.

2.2.1 Square-root density-of-states

A complete description on energy bands in solids is found in several text books [36, 37]. Here, we will limit our scope to the energy band of the representative inorganic semiconductor, single crystal silicon (c-Si).

Free-electrons in a Fermi gas of 3-D system results in density of states following parabolic shape. For electrons and holes

$$D_C(E) \propto \sqrt{E - E_C}, \tag{2.1}$$

$$D_V(E) \propto \sqrt{E_V - E}, \tag{2.2}$$

where E_C and E_V are the conduction band and valence band edges, respectively. The 'sharp edge' signifies that the DOS does strictly fall to zero at $E = E_C$ and $E = E_V$ and takes zero value in the energy gap ($E_V < E < E_C$).

Then, the charge carrier concentration is determined by integrating the product of the DOS function and the Fermi-Dirac distribution function for electrons $f_{F-D}(E,$

$E_{\mathrm{F}}) = 1/[1 + \exp((E - E_{\mathrm{F}})/kT)]$ or for holes $[1 - f_{\mathrm{F-D}}(E, E_{\mathrm{F}})]$:

$$n = \int_{-\infty}^{\infty} D(E) f_{\mathrm{F-D}}(E, E_{\mathrm{F}}) \mathrm{d}E, \tag{2.3}$$

$$p = \int_{-\infty}^{\infty} D(E) \left[1 - f_{\mathrm{F-D}}(E, E_{\mathrm{F}})\right] \mathrm{d}E, \tag{2.4}$$

where E_{F} is the Fermi energy, k Boltzmann constant and T the temperature. Although the integration does not lead to an analytical result in the general case, the following very simple approximate solution emerges at low charge carrier density, when the Fermi level is sufficiently far from the band edges:

$$n = N_{\mathrm{C}} \exp\left(-\frac{E_{\mathrm{C}} - E_{\mathrm{F}}}{kT}\right), \tag{2.5}$$

$$p = N_{\mathrm{V}} \exp\left(-\frac{E_{\mathrm{F}} - E_{\mathrm{V}}}{kT}\right), \tag{2.6}$$

where N_{C} and N_{V} are the effective density of states at conduction and valence band edge, respectively. For silicon at room temperature, $N_{\mathrm{C}} = 2.9 \times 10^{19}\mathrm{cm}^{-3}$ and $N_{\mathrm{V}} = 1.04 \times 10^{19}\mathrm{cm}^{-3}$. Under such circumstances, the semiconductor is said to be in the non-degenerate regime.

Ultraviolet photo-emission spectroscopy (UPS) and inverse photo-emission spectroscopy (IPES) are the methods of choice to determine the energy structure of semiconductors. Inspired by the first work on the external photoelectric effect of metals by Einstein [79] and the same of semiconductors by Condon *et al.* [80], Apker *et al.* not only determined the position of the valence band edge but also demonstrated that the density-of-states in the valence band can be experimentally deduced from the energy of photoelectrons [81]. These initial works on photoelectrons support the band theory for crystalline semiconductors providing a link between the existence of the band edge with the sharp cut-off of stopping potential from photo-emission measurement.

2.2.2 Exponential density-of-states

Disorder in amorphous silicon gives rise to the localisation of the states. Anderson described in [82] that when disorder is introduced in a regular crystal structure extended states gradually change to localised states. The lack of long-range order results in the loss of sharp band edges so that the density of states shows a tail of localised states extending into the energy gap [83, 84]. The degree of localisation can be quantified by comparing the amount of disorder to the width of the energy

band.

In silicon, the conduction and valence bands have a width around 5 eV, so the degree of disorder in amorphous silicon is weak [85]. As a consequence, there still exist extended states; as shown in Figure 2-4, localised states appear as band tails inside the energy gap. These tails are usually described as an exponential density of states referring to the energy of photoelectrons from amorphous silicon proposed by Peterson *et al.* [86]. It is experimentally determined from the onset of the UPS or IPES signals and considered to indicate the same position as the band edge of the same semiconductor in its crystalline phase [87, 88]. Mathematically, thus, the total DOS is represented as the sum of band and exponential tail DOSs, $D(E) = D_{\mathrm{C}}(E) + D_{\mathrm{TC}}(E) + D_{\mathrm{V}}(E) + D_{\mathrm{TV}}(E)$, with

$$D_{\mathrm{TC}}(E) = \frac{N_{\mathrm{TC}}}{kT_{\mathrm{CC}}} \exp\left(\frac{E - E_{\mathrm{C}}}{kT_{\mathrm{CC}}}\right) \qquad E < E_{\mathrm{C}}, \tag{2.7}$$

$$D_{\mathrm{TV}}(E) = \frac{N_{\mathrm{TV}}}{kT_{\mathrm{CV}}} \exp\left(\frac{E_{\mathrm{V}} - E}{kT_{\mathrm{CV}}}\right) \qquad E_{\mathrm{V}} < E, \tag{2.8}$$

where T_{CC} and T_{CV} are characteristic decay temperature describing the distribution of trap states, N_{TC} and N_{TV} are conduction and valence band edge intercept densities.

2.2.3 Gaussian density-of-states

The foremost difference between typical inorganic and organic semiconductors is the binding energy between the elemental constituent of the solid: weak van der Waals interaction in organic solids versus strong covalent binding in silicon. As a direct consequence, the width of the valence (HOMO) and conduction (LUMO) bands is two orders of magnitude lower in organic semiconductors typically of order 0.1 eV [89]. This is about one order of magnitude larger than the corresponding transfer integrals [89], meaning that all the states are now localised with the localization centres being molecules or molecular subunits, called herein sites [89–92].

Because the site energies, which are to a great extent determined by electronic polarization, are mainly controlled by disorder, the density of states in organic disordered semiconductors (ODS) (i.e. non-crystalline that is most of them to the exception of single crystals) can now be safely approximated to a Gaussian distribution function. For simplicity, we will develop equations only for holes in

the HOMO. The Gaussian DOS of the HOMO is written as

$$g(E) = \frac{N_0}{\sqrt{2\pi}\sigma}\exp\left\{-\frac{(E - \mathrm{HOMO_{max}})^2}{2\sigma^2}\right\}, \tag{2.9}$$

where σ is the width of the distribution, N_0 is the total density-of-states per unit volume and $\mathrm{HOMO_{max}}$ is the energy level in the HOMO at which the DOS is the greatest. In general, we take the density of molecule for N_0 [93].

The hole concentration is estimated in a similar manner to (2.4):

$$p = \int_{-\infty}^{\infty} g(E) f_{\mathrm{F-D}}(E, E_{\mathrm{F}}) \mathrm{d}E. \tag{2.10}$$

Under Boltzmann's approximation, the hole concentration has analytical form:

$$p_{\mathrm{ndeg}} = N_0 \exp\left[-\frac{1}{k_{\mathrm{B}}T}\left\{E_{\mathrm{F}} - \left(\mathrm{HOMO_{max}} + \frac{\sigma^2}{2k_{\mathrm{B}}T}\right)\right\}\right]. \tag{2.11}$$

At this point, it is worth pointing out a specificity of the Gaussian DOS, first analysed in details by Tessler and Roichman [94]. A remarkable outcome of this investigation was that the Gaussian DOS only leads to the simple non-degenerate equations (2.11) at very low charge carrier density, when the Fermi level is far from the maximum of the DOS. For higher concentrations, as those seen in the accumulation layer of field-effect transistors or in doped organic semiconductors, the dependence of p with E_{F} is no longer analytical; this is more pronounced as the width of the Gaussian distribution is large. Nonetheless, approximation of the Fermi-Dirac distribution function to a Heaviside step function, for holes $f_{\mathrm{H}}(E, E_{\mathrm{F}}) = 1$ for $E < E_{\mathrm{F}}$ and 0 for $E_{\mathrm{F}} < E$, we have a semi-analytical expression:

$$p_{\mathrm{deg}} = \frac{N_0}{2}\mathrm{erfc}\left[\frac{E_{\mathrm{F}} - \mathrm{HOMO_{max}}}{\sqrt{2}\sigma}\right], \tag{2.12}$$

where $\mathrm{erfc}(x)$ is the complementary error function.

Recently, Paasch [95] established semi-analytical approximations for the charge carrier concentration dependent to the Fermi level by merging (2.11) and (2.12) with transition functions $H(\hat{\sigma})$ and $K(\hat{\sigma})$ given by

$$H(\hat{\sigma}) = \frac{\sqrt{2}}{\hat{\sigma}}\mathrm{efrc}^{-1}\left[\exp\left(-\frac{\hat{\sigma}^2}{2}\right)\right], \tag{2.13}$$

$$K(\hat{\sigma}) = 2\left\{1 - \frac{H(\hat{\sigma})}{\hat{\sigma}}\sqrt{\frac{2}{\pi}}\exp\left[\frac{1}{2}\hat{\sigma}(1 - H(\hat{\sigma})^2)\right]\right\}, \tag{2.14}$$

where $\mathrm{erfc}^{-1}(x)$ is an inverse complementary function and $\hat{\sigma} = \sigma/kT$ is the reduced dimensionless width of Gaussian DOS. We have, for holes,

$$p_{\mathrm{Paasch}} = \begin{cases} \dfrac{N_0 \exp\left[-\left(E_{Fr} - \dfrac{\hat{\sigma}^2}{2}\right)\right]}{1 + \exp\left[-K(\hat{\sigma})(E_{Fr} - \hat{\sigma}^2)\right]} & E_{Fr} > \hat{\sigma}^2 \quad (2.15) \\ \dfrac{N_0}{2} \exp\left(-\dfrac{\hat{\sigma}^2}{2}\right) & E_{Fr} = \hat{\sigma}^2 \quad (2.16) \\ \dfrac{N_0}{2} \mathrm{erfc}\left[\dfrac{E_{Fr}}{\sqrt{2}\hat{\sigma}} H(\hat{\sigma})\right] & E_{Fr} < \hat{\sigma}^2 \quad (2.17) \end{cases}$$

where E_{Fr} is the reduced dimensionless Fermi level and width of Gaussian DOS defined by $E_{Fr} = (E_F - \mathrm{HOMO}_{\max})/kT$.

2.3 Charge carrier transport

Charge carrier transport is a movement of charge carrier in space with electric potential gradient. Distinctive characteristics of charge carrier transport in organic solids are closely related with their electronic structure. Thus, it requires a unique model that could take into account the molecular nature of organic solids. Moreover, a real challenge exists in understanding and developing charge carrier transport models covering a large number of material classes that have different energetic configurations related to the molecular structure itself and also the process-dependent film microstructure.

The temperature dependence of mobility has been regarded as indicative for the DOS model as well as the transport model. Figure 2-5 shows a simplified categorization of the observed temperature dependence of mobility according to the density of state and charge transport model as well as organic solid phase. A detailed description will be given in the following.

2.3.1 Band transport model

The band conduction of delocalised electrons is described by Drude's free electron model [36,96]. The model describes the drift of charge carriers placed in an applied electric field as a repeated process of acceleration and collision with the lattice through which they lose completely their energy. This process results in an average drift velocity proportional to the electric field strength, from which the constant

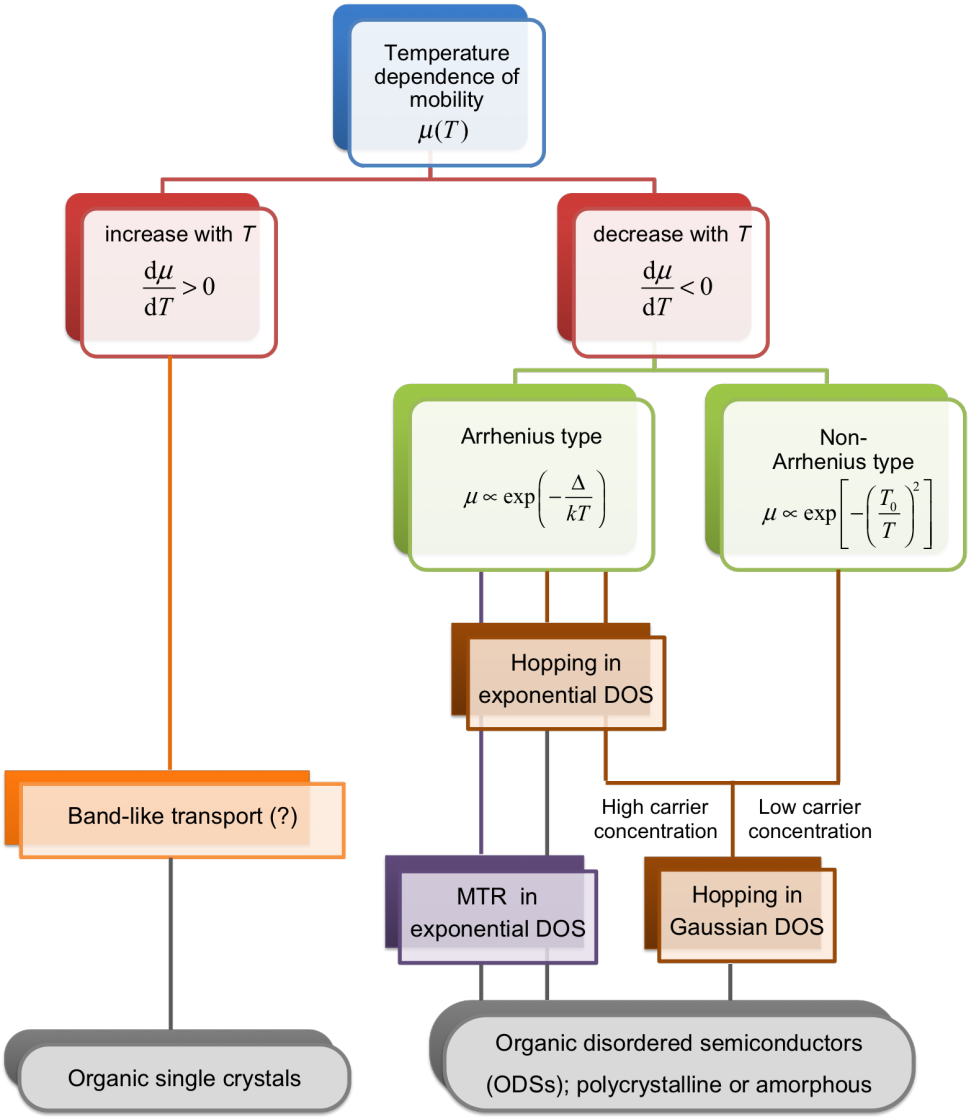

Figure 2-5: Categorisation of the density of state and charge transport models based on the experimental observations on temperature dependent mobility. Correlation between models and organic solid phases is shown.

of proportionality is defined as mobility μ by

$$\mu = \frac{F}{v_{\text{th}}} = \frac{q\tau}{m} = \frac{q\lambda_{\text{m}}}{mv_{\text{th}}} \tag{2.18}$$

Here, q is the elementary charge, m is the effective mass, τ is the mean time between lattice collisions, λ_{m} the mean free path, and v_{th} the thermal velocity. As illustrated in Figure 2-6(a), band transport is not thermally activated because increasing temperature reduces λ_{m} and μ. This behaviour is usually modelled by $\mu \propto T^{-n}$ with $n > 0$ [36], where T is the absolute temperature.

However, for most organic semiconductors, band transport is unlikely because

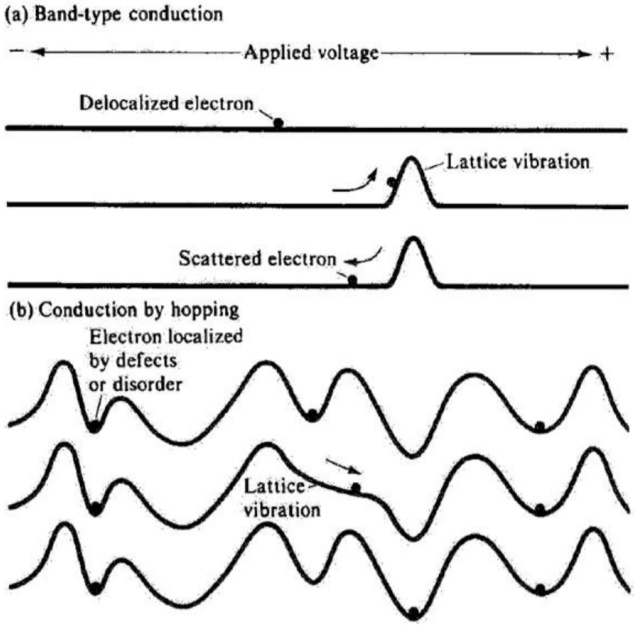

Figure 2-6: Illustration of the transport mechanisms in solids with applied electric field. (a) Band-like conduction; electrons are scattered by lattice vibration so that the mobility decreases with increasing temperature. (b) Hopping between localised states; lattice vibration can give electrons chance to overcome the potential barriers (thermally-activated transport

general parameters put into 2.18 give μ of the order 100 $\mathrm{cm^2V^{-1}s^{-1}}$ or higher [36]. In other words, the primary assumption of Drude's model fails for organics because $\mu < 1$ $\mathrm{cm^2V^{-1}s^{-1}}$ corresponds to a value λ_m smaller than the lattice spacing (intermolecular distance). Therefore, we consider that genuine band transport is not relevant to organic semiconductors, and it might be restricted to highly-pure and defect-free single crystals at extremely low-temperature [73, 97, 98]. As temperature increases, intra- and intermolecular vibrations destroy the coherence between adjacent sites, which makes a charge carrier scattered with a mean free path that approaches the distance between adjacent sites. As a result, band transport is no longer possible and a charge moves through a different transport mechanism, i.e. thermally assisted hopping to be discussed.

It is for this reason that occasional experimental observation of a negative temperature coefficient ($\mathrm{d}\mu/\mathrm{d}T < 0$) in low-mobility organic crystals is generally described by the band-'like' transport. The exact origin of this mechanism has not been fully understood yet [99–102].

2.3.2 Polaronic transport model

When the charge localization effect is pronounced, the transport is described by the hopping between localised states. In this case, because the lattice vibration helps localised charges to escape the potential well, transport is assisted by thermal energy ($\mathrm{d}\mu/\mathrm{d}T > 0$) as shown in Figure 2-6. In general, two origins of localisation are considered; polarization and disorder.

Electronic polarization indicates local deformation of the charge density due to the additional charge staying at this location [75]. This leads to an immediate relaxation of that particular state by the induced potential. As a consequence, the further motion of the staying charge is hindered, thus called the self-trapping effect. Once this charge moves to another molecule (or a segment of molecule), this effect takes place again. Therefore, this type of charge transport is visualised by a collective movement of a charge and its accompanying polarization (of the opposite sign) which are called a 'polaron'.

Polaronic transport is a distinctive feature of all organic semiconductors. Because of small transport bandwidth, residence time becomes longer than polarization time. Also, because of small dielectric constant of organic materials, the localizing potential gets intensified.

2.3.3 Multiple-trapping and release (MTR) model

The second mechanism of localisation is induced by energetic and geometrical disorder. We will first discuss the case when the degree of disorder is not significant (compared to the transport bandwidth), namely 'weak localisation'. In this case, the energy structure is best represented by the DOS model of the extended band with localised exponential trap states (2.8). This picture is widely-used in conventional model for amorphous silicon (a-Si) [103, 104]. For organic semiconductors, organic solids with poly-crystalline phase can be generally well described by this model. They can form relatively well-ordered small domains with different orientation between domains. The main origin of localised tail states in a-Si are dangling bonds, and that in polycrystalline organic semiconductors can generally be attributed to the grain boundaries [105].

In this energetic situation, the charge-transport is based on the multiple trapping and release (MTR) process illustrated in Figure 2-7. In this model, it is assumed that most of the charge carriers are trapped in localized states, and the charge carrier transport is manifested only by the temporarily released charge carriers to an extended-state transport level (above the valence band edge for classical

p-type semiconductors, i.e. mobility edge), the amount of which depends on the electronic structure of the localized states, temperature and injection. Therefore, the MTR model adopts the DOS model of the extended band with localised exponential trap states in (2.8).

A detailed analytical formulation for obtaining trapped and free charge carrier density will be given in [105]. Here, for discussion purpose, we simply present the expression of the effective mobility μ_{MTR} determined by the trapped-to-total carrier density,

$$\mu_{\mathrm{MTR}} = \mu_0 \frac{p_{\mathrm{f}}}{p_{\mathrm{f}} + p_{\mathrm{t}}} \simeq \mu_0 \frac{N_{\mathrm{C}}}{N_{\mathrm{T}}} \exp\left(-\frac{E_{\mathrm{F}} - E_{\mathrm{V}}}{kT}\right) \tag{2.19}$$

where μ_0 is the band mobility, p_{f} the free hole density, p_{t} the trapped electron density, N_{C} the effective DOS at the conduction band edge, E_{F} the Fermi level, and k the Boltzmann constant. We assume $E_C \gg kT$ and $p_{\mathrm{t}} \gg p_{\mathrm{f}}$ for (2.19). The key feature of (2.19) is Arrhenius temperature dependence for thermally activated charge transport:

$$\mu(T) \simeq \mu^{'} \exp\left[-\frac{\Delta}{kT}\right], \tag{2.20}$$

2.3.4 Variable-range hopping model

Now, we will discuss the case when the degree of disorder is significant. The basic ideas of variable-range hopping can be briefly formulated as follows: charge transport in organic disordered semiconductors is manifested by incoherent hopping of charge carriers in randomly distributed localised states i.e. the Gaussian DOS.

The hopping rate (or the jump rate) is a key element of this model. It considers the high localization of charge carriers in disordered organic materials (sites) and its effect on charge transport. The jump rate of a carrier between two localised sites i and j is assumed to be of the Miller-Abraham type [31,89], [90–92,106,107], i.e., it is the product of a prefactor ν_0, a carrier wave-function overlap factor, and a Boltzmann factor for jumps upward in energy.

$$\nu_{ij} = \begin{cases} \nu_0 \exp\left(-2\alpha r_{ij} - \dfrac{E_j - E_i}{kT}\right) & E_j > E_i, \quad (2.21) \\ \nu_0 \exp\left(-2\alpha r_{ij}\right) & E_j \leq E_i, \quad (2.22) \end{cases}$$

Here ν_{ij} is the rate for the hop between an occupied site, i, and an empty site, j, separated by distance r_{ij}; α is the inverse decay length of the carrier wave function in the localised states; ν_0 is the attempt-to-escape frequency (also, the maximum

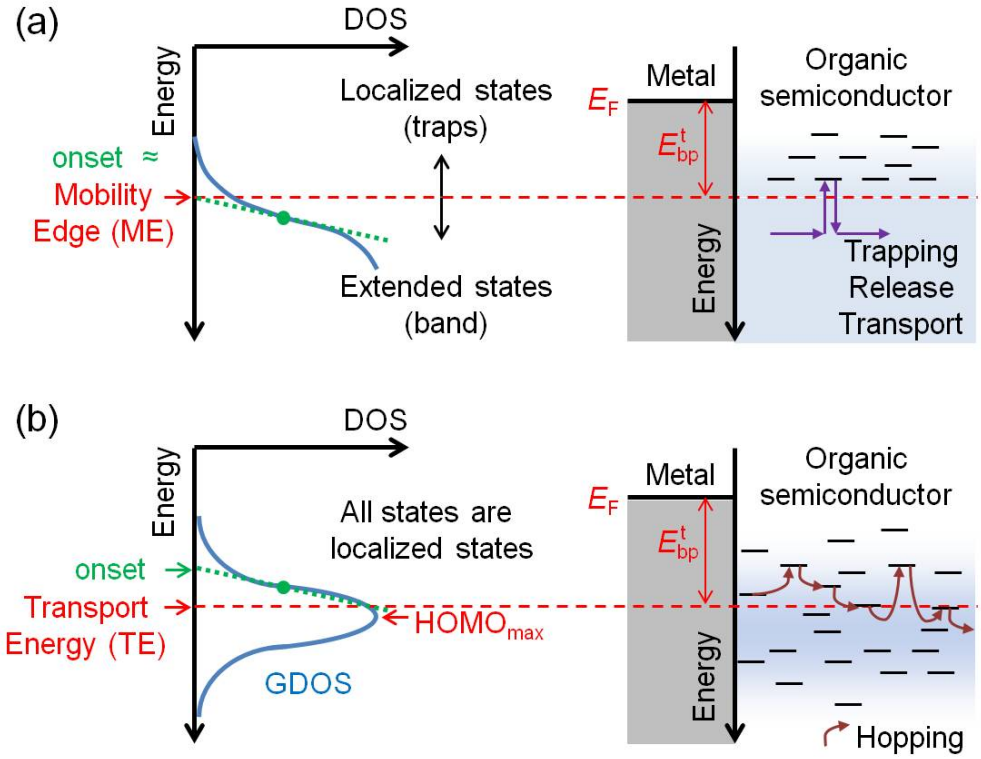

Figure 2-7: Schematic diagrams for the density-of-states and hole transport mechanism based on the (a) multiple trapping-and-releasing model and (b) Gaussian disorder model. The symbol $E_{\mathrm{bp}}^{\mathrm{t}}$ denotes the transport based definition of the IB.

hopping rate); k is the Boltzmann constant.

In essence, describing the distributions of sites in space r_i and energy E_i is a central quest for the description of charge transport under the hopping model. If spatial positions and energies of localised states can be considered independent from each other, this model is traditionally called the Gaussian Disorder Model (GDM) [31]. Until recently, the effect of the distribution of sites in energy has been actively investigated, upon assuming the uniform distribution of sites in space, $r_{ij} \approx r$. In particular, the structure of the DOS in ODSs is probably the most controversial issue in research on these materials. The discussion is mostly focused on whether the DOS is Gaussian as described by 2.8or exponential in the form given by 2.9 [33]. In order to evaluate the pertinence of each DOS model, the mobility (an observable parameter) is determined from the hopping rate, and its dependence on environmental factors, such as the temperature T, charge carrier concentration p and electric field F, are compared to the experimental observations.

The first merit of adopting the Gaussian DOS delineated in previous reviews [31, 33] is based on the temperature dependence of the carrier zero-field mobility $\mu(T)$, measured in time-of-flight experiments at low carrier concentrations. Experi-

mental data for carrier mobility in ODSs at low carrier concentrations demonstrate a strong temperature dependence in the form [33, 92, 108–110]

$$\mu(T) \simeq \mu_0 \exp\left[-\left(\frac{T_0}{T}\right)^2\right], \tag{2.23}$$

with properly adjusted parameters T_0 and μ_0. At high carrier concentrations, particularly in OFETs, the dependence μ_T often has the Arrhenius form with a weaker temperature dependence [111] well known also for inorganic disordered semiconductors, such as chalcogenide glasses and amorphous silicon. While the hopping transport in a Gaussian DOS exhibits both non-Arrhenius and Arrhenius temperature dependence of mobility (depending on the charge carrier concentration [112, 113]), the hopping process in an exponential DOS reproduces only the Arrhenius temperature dependence [33].

Second, the asymptote behaviour of mobility with the decrease of charge carrier concentration can be explained uniquely by Gaussian DOS [33]. This provides a fundamental insight on two contrasting observations: a strong charge carrier concentration dependence of the field-effect mobility extracted from FETs and independence of the mobility from determined from diodes [114].

Here, we illustrate an empirical equation for the hopping mobility in a Gaussian DOS that reproduces the exact *ab-initio* simulation based on Monte-Carlo method [32]. In the *ab-initio* approach, the numerical solution of the master equation for hopping transport, $\sum_{ji}[\nu_{ij}p_i(1-p_j) - \nu_{ji}p_j(1-p_i)] = 0$ with p_i and $1-p_i$ being the probability of occupancy and vacancy of the site i by a charge, leads to an exact description for hopping mobility:

$$\mu = \sum_{i,j} \nu_{i,j} p_i (1-p_j) r_{ijx} / pFV, \tag{2.24}$$

where $p = \langle p_i \rangle / a^3$ and V is the system volume. The empirical equation established by following parametrisation scheme provides a good fit to numerical data over a wide range of T, p and F. For a hole mobility in a Gaussian DOS with its width σ,

$$\mu(T, p, F) = \mu_0(T) \times g_1(p, T) \times g_2(F, T) \tag{2.25}$$

with purely temperature dependent mobility at zero charge carrier concentration and electric field

$$\mu_0(T) = \mu(0) c_1 \exp(-c_2 \hat{\sigma}^2) \tag{2.26}$$

and mobility enhancement factor by charge carrier concentration

$$g_1(c,T) = \begin{cases} \exp\left[\frac{1}{2}\left(\hat{\sigma}^2 - \hat{\sigma}\right)(2c)^{\delta}\right] & \text{c} \leqq 0.1 \quad (2.27) \\ g_1(0.1,T) & \text{c} > 0.1, \quad (2.28) \end{cases}$$

and mobility enhancement factor by electric field

$$g_2(F,T)$$

$$= \begin{cases} \exp\left[0.44\left(\hat{\sigma}^{3/2} - 2.2\right)\left\{\sqrt{1 + 0.8\left(\frac{qaF}{\sigma}\right)^2} - 1\right\}\right] & F \leqq \frac{2\sigma}{qa} \quad (2.29) \\ g_2\left(\frac{2\sigma}{qa}, T\right) & F > \frac{2\sigma}{qa}, \quad (2.30) \end{cases}$$

where $c_1 = 1.8 \times 10^9$ and $c_2 = 0.42$ are parametrization constants, $\hat{\sigma} = \sigma/kT$, $c = p/a^3$, a is the lattice constant $a = N = 10/\alpha$, and g_1 and g_2 are the drift enhancement factor (i.e. mobility enhancement) by the hole concentration and the electric field, δ is a constant related with the degree of disorder

$$\delta = 2\frac{\ln(\hat{\sigma}^2 - \hat{\sigma}) - \ln(\ln 4)}{\hat{\sigma}^2}. \quad (2.31)$$

2.4 Charge carrier injection

Evidence for a Gaussian density of state comes from the dominant charge transport mechanism in organic semiconductors. As luminously pointed out by Baranovskii [33], only a Gaussian DOS, through the Gaussian disorder model (GDM) [31], is able to account for the main features of charge carrier transport in organic semiconductors; these include, in particular, the different regimes occurring at low and high charge carrier densities, and the non-dispersive regime observed at very low charge carrier density.

However, the work by Bassler, Baranovskii, and many others focuses on the problem of charge transport. Under this aspect, the most pertinent energy level is the so-called transport energy [33] located close to the maximum of the Gaussian DOS, and which can be viewed as an equivalent of the mobility edge in amorphous silicon, in that sense that charge carrier transport mainly occurs at energies close to the transport level.

Now, we are more interested in defining the energy levels involved in charge

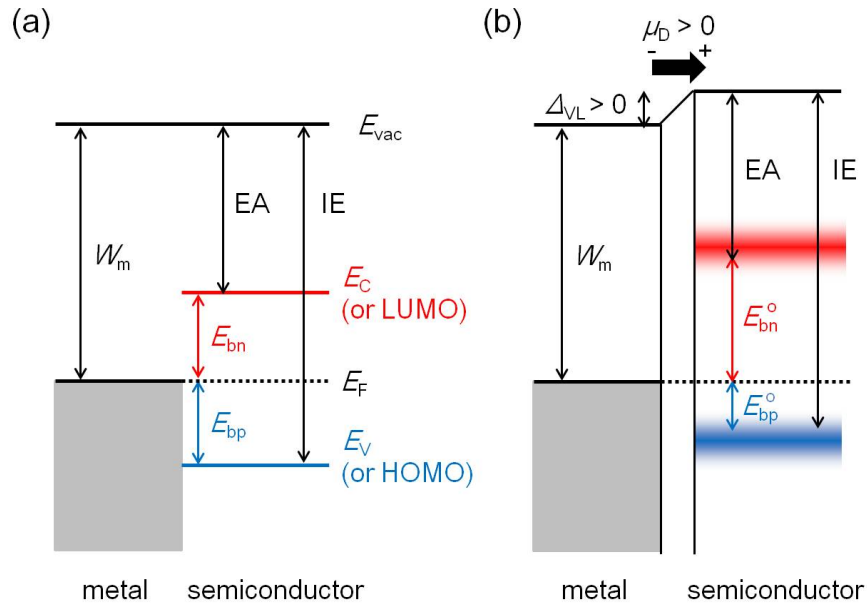

Figure 2-8: (a) Energy diagram for an ideal metal/semiconductor junction, where E_{bn} and E_{bp} denotes the injection barrier (IB) for electrons and holes, respectively. (b) The same for a realistic metal/semiconductor junction with the vacuum level mismatch Δ_{VL} and energetic disorder. Here, $E^{\mathrm{o}}_{\mathrm{b}}$ is determined in reference to the onsets of the UPS or IPES signals, which are not specific to the density-of-states model.

injection from electrodes into the organic semiconductor, which also intervene when establishing the energy diagram of organic electronic devices.

2.4.1 Ideal metal/semiconductor junction

As shown in Figure 2-8(a), the Schottky-Mott rule defines the IB for an ideal metal/in-organic semiconductor junction [115, 116] as the difference between the metal work function and the semiconductor electron affinity for electrons or the semiconductor ionization energy for holes:

$$E_{\mathrm{bn}} = W_{\mathrm{m}} - \mathrm{EA}, \tag{2.32}$$

$$E_{\mathrm{bp}} = \mathrm{IE} - W_{\mathrm{m}}. \tag{2.33}$$

This assumes that there are no gap states in semiconductor's forbidden gap and that the conduction and valence band edges are sharp. In addition, the concept of IB in the Schottky-Mott rule premises immediate band transport of charge carriers. The latter makes possible a transport-based definition of the IB, which is alternatively written as $E^{\mathrm{t}}_{\mathrm{bp}} = E_{\mathrm{F}} - E_{\mathrm{V}}$ ($E^{\mathrm{t}}_{\mathrm{bn}} = E_{\mathrm{C}} - E_{\mathrm{F}}$), as the energy required

to inject holes (electrons) from the electrode into the semiconductor at the valence (conduction) band edge.

On the other hand, the IB can also be understood in reference to the charge carrier concentration at the junction. We recall the hole concentration in crystalline semiconductor under Boltzmann approximation from (2.6):

$$p = N_{\mathrm{V}} \exp\left(-\frac{E_{\mathrm{F}} - E_{\mathrm{V}}}{k_{\mathrm{B}}T}\right), \tag{2.34}$$

Since, in equilibrium, the Fermi level of the metal and semiconductor aligns at the metal/semiconductor interface, E_{F} can be used interchangeably to indicate the Fermi level of the metal and semiconductor. Now, $E^{\mathrm{c}}_{\mathrm{bp}} = E_{\mathrm{F}} - E_{\mathrm{V}}$ represents a charge carrier based definition of the IB. Note that both approaches result in the same and consistent quantity in the case of ideal metal/semiconductor junction: $E^{\mathrm{t}}_{\mathrm{bp}} = E^{\mathrm{c}}_{\mathrm{bp}} = E_{\mathrm{bp}}$. This can be readily extended for electrons.

Upon the same assumptions, the ideal M/O junctions have been frequently described by the Schottky-Mott rule. In this case, the IB for holes is defined by replacing the valence band edge with the highest-occupied molecular orbitals (HOMO) as $E_{\mathrm{bp}} = E_{\mathrm{F}} - \mathrm{HOMO}$. Similarly, for the IB for electrons, $E_{\mathrm{bn}} = \mathrm{LUMO} - E_{\mathrm{F}}$, where LUMO stands for the lowest-unoccupied molecular orbitals.

2.4.2 Non-ideal factors

Although the intuitive picture by Schottky and Mott successfully describes an ideal junction, for a realistic junction, it was observed that the Schottky-Mott rule is not always valid [117]. The primary non-ideal factor is the existence of the vacuum level mismatch Δ_{VL}, which can significantly modify the IB [118, 119]. Figure 2-8(b) shows the formation of the vacuum level mismatch. The positive (negative) dipole moment vector μ_{D} created by the interface dipole shifts the vacuum level upward (downward), and consequently increases (decreases) the IB for electrons and decreases (increases) the IB for holes by the amount Δ_{VL}. The interface dipole is often found to be zero either by deliberate passivation with inert buffer layers [120] or by contamination through exposure to atmosphere and/or solvent. However, in general, microscopic charge carrier rearrangements manifested by a variety of chemical and physical process can lead to a non-negligible interface dipole [119, 121, 122].

Nevertheless, it is possible to extend the Schottky-Mott rule to a system with a vacuum level mismatch by defining the effective metal work function as the sum

of the metal work function and vacuum level mismatch $W_{\mathrm{m}}^{\mathrm{eff}} = W_{\mathrm{m}} + \Delta_{\mathrm{VL}}$:

$$E_{\mathrm{bn}}^{\mathrm{o}} = W_{\mathrm{m}} + \Delta_{\mathrm{VL}} - \mathrm{EA}, \tag{2.35}$$

$$E_{\mathrm{bp}}^{\mathrm{o}} = \mathrm{IE} - (W_{\mathrm{m}} + \Delta_{\mathrm{VL}}). \tag{2.36}$$

Here, the superscript in $E_{\mathrm{b}}^{\mathrm{o}}$ denotes the onset of the ultraviolet photo-emission spectroscopy (UPS) and inverse photo-emission spectroscopy (IPES) signals by which the EA and IE are usually determined for both ideal and realistic junctions without specificity to the materials.

The second non-ideal factor is the energetic disorder that are present in solid phase semiconductors to some extent except for a perfect crystal. The energetic disorder illustrated in Figure 2-8(b) originates from the absence of long-range order in the position and direction to a various degree, which requires specific models for the description of the electronic structures discussed in more detail in section 2.4.3. The presence of the energetic disorder makes difficult a unique determination of the EA and IE, which results in the divergent definition of the EA and IE, and hence the IBs. In case of organic semiconductors, the EA and IE are determined most frequently referring either to the onset [120,123] or the maximum [124] of the HOMO and LUMO. The effect of ambiguity becomes more significant as the metal Fermi level is approaching the indistinct edge and arrives at the fundamental limit called the Fermi level pinning, where the IB does not follows the change in the metal work function. Although often attributed to surface states [125] and metal-induced interface gap states [126, 127], it has been shown that the Fermi level pinning in the organic semiconductor energy gap mainly occurs from electrostatics [123, 128]. Thus, recalling the considerable effect of the electronic structure on the charge carrier concentration at the junction, a complete understanding of the effect of the energetic disorder on the injection barrier is gaining in importance. In the following, we will discuss in detail on the second non-ideal factor. While doing so, we will neglect the existence of the vacuum level mismatch for an exclusive analysis of the effect of energetic disorder.

2.4.3 Disordered metal/organic semiconductor junction

For exponential DOS under MTR model

The UPS and IPES had been actively utilised for organic semiconductors as well [129], recently paying special attention to their vulnerability to high energy photons and electrons [130]. Surprisingly, in spite of the importance of the parameter,

very little is found in the literature regarding the experimental estimation of the injection barrier in view of hopping transport model in Gaussian DOS. Instead, most of reports are based on MTR model. We have seen that the transport of charge carriers takes place around the ME. This means, more precisely, the band edge in the Schottky-Mott model for an ideal junction is replaced with the ME to define the injection barrier.

When the MTR model is applied to disordered organic semiconductors as shown in Figure 2-7(a), the transport based definition of the IB becomes $E_{\mathrm{bp}}^{\mathrm{t}} = E_{\mathrm{F}} - \mathrm{ME}$, which is close to the IB determined from the onset of the UPS $E_{\mathrm{bp}}^{\mathrm{t}} \approx E_{\mathrm{bp}}^{\mathrm{o}}$. The role of disorder has note been of interest, since under MTR model, charge carriers in the exponential trap states are considered immobile.

However, the presence of extended states is unlikely in disordered organic semiconductors. In addition, non-Arrhenius temperature-dependency of mobility is considered as evidence for a Gaussian rather than an exponential density-of-states [33, 113]. In this respect, currently, there is an increasing consensus on interpreting the UPS or IPES signals with a Gaussian function based on an alternative theoretical framework.

For Gaussian DOS under GDM model

In order to describe the characteristic transport of charge carriers in disordered organic semiconductors, the Gaussian Disorder Model (GDM) was proposed, which establishes that all states are randomly distributed and localised where thermally-assisted tunnelling and trapping occurs simultaneously (see figure 2-7(b)). The energy structure of organic disordered semiconductor is represented by a Gaussian DOS $g(E)$.

In GDM, the hopping transport takes place at a particular energy level called the transport energy (TE), which is indicated in figure 2-7(b). The essence is that the TE in the GDM is in full analogy with the ME in the MTR model so that the TE can replace the ME [131]. This gives theoretical basis in defining the IB as the energetic difference between the metal Fermi level E_F and the TE of semiconductor, $E_{\mathrm{bp}}^{\mathrm{t}} = E_{\mathrm{F}} - \mathrm{TE}$. Numerical analyses predict the position of the TE to be closer to $\mathrm{HOMO}_{\mathrm{max}}$ than to the onset of the HOMO [132]. Thus, the transport based IB can be roughly written as $E_{\mathrm{bp}}^{\mathrm{t}} \approx E_{\mathrm{F}} - \mathrm{HOMO}_{\mathrm{max}}$. Such a definition was used earlier without clear explanation [124]. Note, however, that unlike in the MTR model the onset does not coincide with the TE considering a GDOS so that $E_{\mathrm{bp}}^{\mathrm{t}}$ is different from $E_{\mathrm{bp}}^{\mathrm{o}}$.

This transport based definition of the IB as $E_{\mathrm{bp}}^{\mathrm{t}} = E_{\mathrm{F}} - \mathrm{TE}$ can provide a way

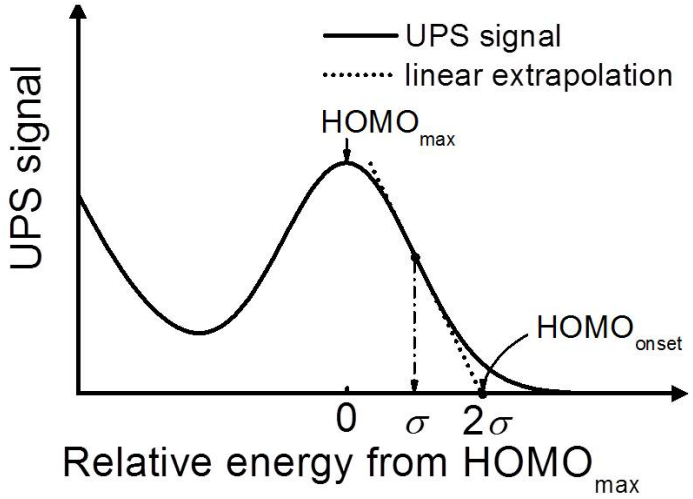

Figure 2-9: Schematic diagram of the linear extrapolation method used to determine the onset of the highest-occupied molecular orbitals. The linear extrapolation line is drawn at the inflection point at $E = \sigma$ from the $\mathrm{HOMO_{max}}$. Then, the extrapolation line crosses the base line exactly at $E = 2\sigma$ from the $\mathrm{HOMO_{max}}$ which is denoted as the $\mathrm{HOMO_{onset}}$.

of evaluating the injection property. However, it significantly underestimates the effect of gap states in facilitating charge carrier injection. Thus, for a practical reason, the onset of the HOMO ($\mathrm{HOMO_{onest}}$) is often used in determining the IB in disordered metal/organic semiconductor junction. Figure 2-9 illustrates the linear extrapolation method (LEM) used to determine $\mathrm{HOMO_{onset}}$ from the UPS (or IPES) signal assuming a GODS with a width σ [133]. In this method, the linear extrapolation line is drawn at the inflection point of which the energetic distance from $\mathrm{HOMO_{max}}$ is σ. Then, the extrapolation line crosses the base line exactly at 2σ from $\mathrm{HOMO_{max}}$ which is denoted as the $\mathrm{HOMO_{onset}}$. However, it has been little examined whether the onset can substitute the band edge of an ideal semiconductor (see section 2.4.1).

From now on, as in section 2.4.1, we discuss on the charge carrier based IB and the correct determination of $\mathrm{HOMO_{edge}}$ which is equivalent to the band edge of an ideal semiconductor. We recall the analytical expression for the hole concentration in non-degenerate organic disordered semiconductor from (2.11):

$$p = N_0 \exp\left[-\frac{1}{k_\mathrm{B}T}\left\{E_\mathrm{F} - \left(\mathrm{HOMO_{max}} + \frac{\sigma^2}{2k_\mathrm{B}T}\right)\right\}\right]. \tag{2.37}$$

In equilibrium, the Fermi level aligns at metal/organic semiconductor junction. Thus, E_{F} indicates the Fermi level of both metal and semiconductor. Then, if the numerator on the exponent is considered as the effective charge carrier based IB

$$E_{\mathrm{bp}}^{\mathrm{eff}} = E_{\mathrm{F}} - \left(\mathrm{HOMO}_{\mathrm{max}} + \frac{\sigma^2}{2k_B T} \right), \tag{2.38}$$

it is possible to define the edge of the HOMO from the second and third terms of equation (5.19) to $\mathrm{HOMO}_{\mathrm{edge}} = \mathrm{HOMO}_{\mathrm{max}} + \sigma^2/2k_{\mathrm{B}}T$, keeping the Schottky-Mott rule consistent for disordered metal/organic semiconductor. This demonstrates that the $\mathrm{HOMO}_{\mathrm{onset}}$ obtained by the LEM can not be used to define a charge carrier based IB. Instead, the $\mathrm{HOMO}_{\mathrm{edge}}$ must be used. In addition, it is now recommended to provide a full set of parameters, the $\mathrm{HOMO}_{\mathrm{max}}$ and the width of a GDOS σ, from the UPS (or IPES) signal for the analysis of injection characteristics.

Chapter 3

Methods

In order to ensure consistency, we have employed multiple theoretical and experimental approaches for modelling and analysing various organic electronic devices. The purpose of this Chapter is to elaborate on the major techniques or methods used in this thesis; impedance spectroscopy, analytical modelling, numerical modelling, and experimental validation. Background and purpose of each method as well as special considerations for practice are presented to help in understanding the results in Chapter 4 and 5.

3.1 Impedance spectroscopy

3.1.1 Basic information

Electrical impedance or impedance Z is the complex ratio of the phasor voltage to the phasor current of an alternating current (AC) circuit element or circuit, which is written as:

$$Z = |Z|\exp(j\theta) = \mathrm{Re}(Z) + j\mathrm{Im}(Z), \tag{3.1}$$

where the first equality is in the polar form and the second is in the Cartesian

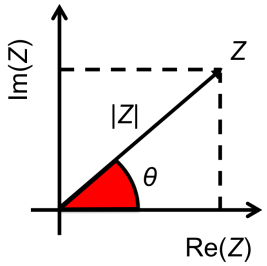

Figure 3-1: A graphical representation of the complex impedance plane.

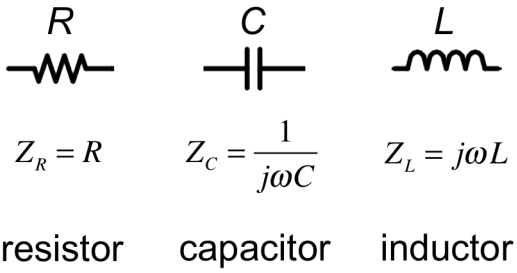

Figure 3-2: Electrical impedance of basic passive circuit elements.

form (see Figure 3-1 for a graphical representation). Here, the argument θ indicates the relative phase of the ac current I_{ac} in reference to that of the ac voltage V_{ac} applied across the system. And the impedance modulus $|Z|$ is the ratio of the voltage amplitude to the current amplitude. $\mathrm{Re}(Z)$ and $\mathrm{Im}(Z)$ denotes real and imaginary part of Z.

Impedance spectroscopy is a technique to measure the impedance modulus $|Z|$ and argument (a.k.a. phase angle) θ of an electrical or electrochemical system upon sweeping the ac small-signal frequency ($\omega = 2\pi f$) at fixed dc voltage (V_{dc}) [134]. Figure 3-2 summarizes the impedance of three basic passive circuit elements, a resistor, a capacitor and an inductor, denoted by Z_R, Z_C and Z_L in terms of its resistance R, capacitance C and inductance L and the angular ac frequency ω. The impedance of each element has a distinct ac frequency dependence. Being a pure real value, Z_R is invariant with ω, whereas Z_C and Z_L are pure imaginary values with an increasing and decreasing modulus with ω.

The equivalent impedance (also called total impedance or terminal impedance) of many simple networks of elements can be calculated by using the rules for combining impedances in series and parallel illustrated in Figure 3-3. In this case, the equivalent impedance would exhibit a more complex frequency dependence compared to a single element. When the circuit diagram is given, the prediction of the equivalent impedance and its frequency dependence is straightforward requiring complex algebra. However, a reverse process, which is usually the case in practice, would not be a simple task and requires a knowledge-based try-and-error.

3.1.2 Equivalent circuit modelling

Equivalent circuit modelling is an act of representing an electrical or electrochemical system by a combination of basic circuit elements. Its practical use is found upon analysing an impedance spectrum of a system where only the equivalent impedance and its frequency dependence are given. Because each circuit element

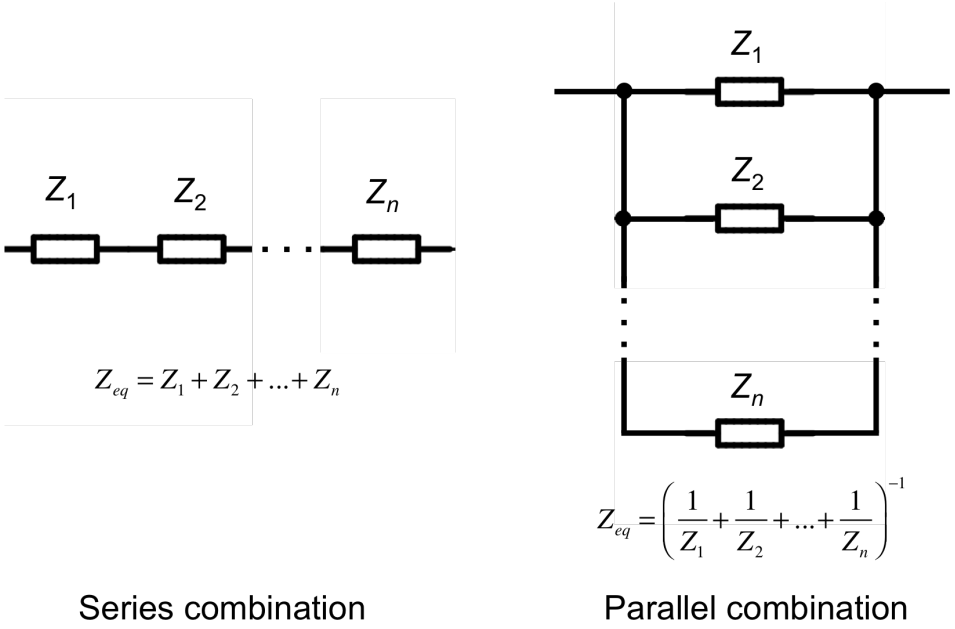

Figure 3-3: Equivalent impedance of a series connection and parallel combination of impedance elements.

responds differently to the frequency (Figrue 3-2), it is possible to identify what elements are present and how they are combined from a full impedance spectrum. For example, impedance spectroscopy and equivalent circuit modelling are used for an organic rectifying diode in this thesis (Chapter 4). In the literature, a number of reports have shown practical applications of impedance spectroscopy for the analysis of organic devices [135–139]. Nonetheless, the determination of the equivalent circuit is based on a knowledge-based guess and subsequent verification by comparing the modelled impedance spectrum to the measured one. Therefore, despite of a long list of equivalent circuits and their impedance spectra available in several impedance spectroscopy software, reviewing typical impedance spectra and understanding the effect of basic circuit elements will significantly reduce the effort and enable a quick guess.

3.1.3 Representative impedance spectra

One of the simplest circuits is a RC circuit constructed by a parallel combination of a resistor and a capacitor. The equivalent impedance of an RC circuit Z_{RC} is obtained by the combination rule presented in Figrue 3-3

$$Z_{RC} = \frac{1}{\frac{1}{Z_R} + \frac{1}{Z_C}} = \frac{R}{1 + j\omega RC}. \tag{3.2}$$

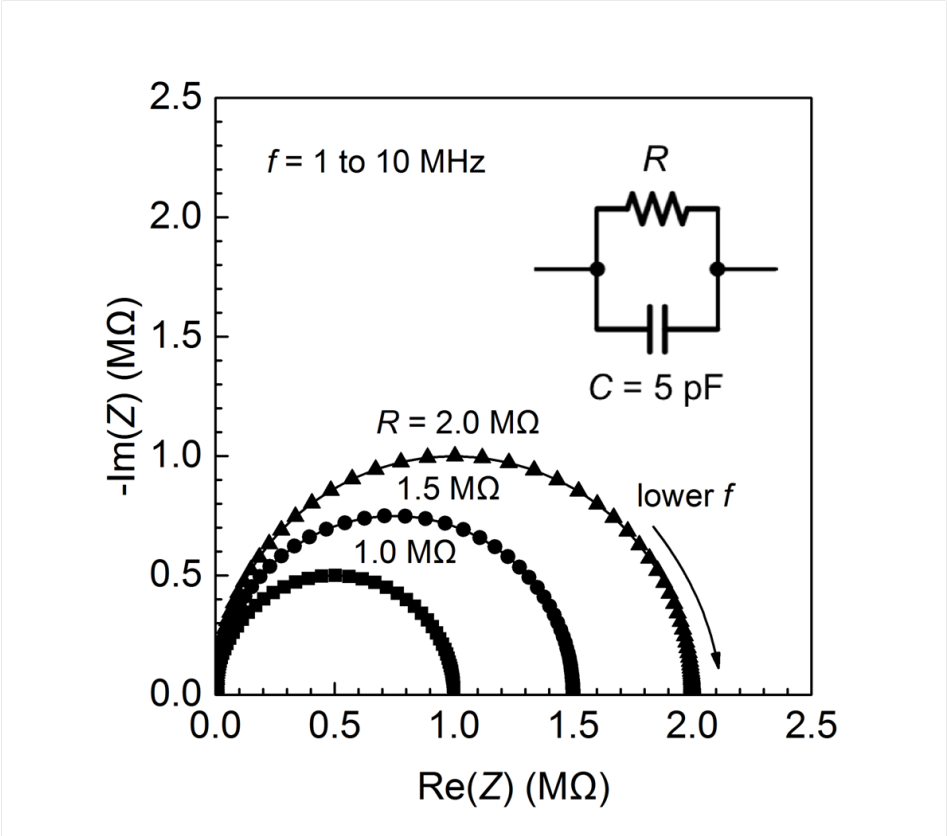

Figure 3-4: The simulated impedance spectra of RC circuits with a fixed capacitance and different resistance values plotted on the complex plane. The frequency is from 1 Hz to 10 MHz with the increment of 20 points per decade.

which can be expressed into the Cartesian coordinates:

$$\mathrm{Re}(Z_{RC}) = \frac{R}{1+\omega^2 R^2 C^2}, \tag{3.3}$$

$$\mathrm{Im}(Z_{RC}) = -\frac{\omega R^2 C}{1+\omega^2 R^2 C^2}. \tag{3.4}$$

In general, as shown by (3.3) and (3.4), the Cartesian coordinates of Z_{eq} are parametric equations of ω with constants R, C and/or L. Therefore, drawing the trajectory of Z_{eq} on the complex plane is always possible with an ordinary data analysis and graphing software once the coordinates are determined. An impedance spectroscopy software provides more adapted functionalities, such as reproducing the impedance spectrum of a user defined circuit and data fitting.

Figure 3-4 shows the impedance spectra of the RC circuits simulated by EC-Lab software [140]. The semi-circular trajectory of Z_{RC} is perfectly predictable, because merging the parametric equations (3.3) and (3.4) leads to the following

equation:

$$\mathrm{Im}(Z_{RC}) = -\sqrt{\left(\frac{R}{2}\right)^2 - \left[\mathrm{Re}(Z_{RC}) - \frac{R}{2}\right]^2}, \tag{3.5}$$

which states that the semicircle is centred at $(R/2,\, 0)$ and has radius of $R/2$. We note that $Z_{RC} \to R$ when $f \to 0$. This is because, when $f \to 0$, $Z_C \to \infty$ and the capacitor can be considered as an open circuit (a disconnection). reducing the RC circuit into a single resistor. On the other hand, when $f \to \infty$, $Z_C \to 0$ and the capacitor becomes a short circuit. Therefore, the RC circuit also becomes a short circuit resulting in $Z_{RC} \to 0$. In this case, the RC circuit becomes more like a pure capacitor upon approaching the limit, which is evidenced by the trajectory of Z_{RC} approaching the $-\mathrm{Im}(Z)$-axis ($\theta \sim -90°$).

We will emphasize two practical issues to be considered regarding the measurement limits in terms of frequency and impedance. First, the required frequency range to obtain the entire semicircle and its centre frequency have an analytical form. To begin with, the lowest point of the semicircle points the logarithmic centre of the frequency range. It corresponds to the point $\mathrm{Re}(Z_{RC}) = R/2$, and from (3.3), we can show that this condition holds at the frequency of

$$\omega_{RC} = 2\pi f_{RC} = \frac{1}{RC}, \tag{3.6}$$

which also indicates the time constant of the RC circuit. Next, it helps estimating the measurement frequency range to obtain a full impedance spectrum. When we define the full frequency range from and to the frequency which $\mathrm{Im}(Z_{RC})$ take P-% of $\frac{R}{2}$ denoted by ω^+ and ω^-, equating (3.4) to $\frac{R}{2} \cdot \frac{P}{100}$ leads to:

$$\mathrm{Im}(Z_{RC})\Big|_{\omega=\omega^\pm} = \frac{R}{2} \cdot \frac{P}{100}, \tag{3.7}$$

which have roots

$$\omega^\pm = \frac{\dfrac{100}{P} \pm \sqrt{\left(\dfrac{100}{P}\right)^2 - 1}}{RC}. \tag{3.8}$$

Taking log on both sides, we have

$$\log\left(\omega^\pm\right) = \log\left\{\frac{100}{P} \pm \sqrt{\left(\frac{100}{P}\right)^2 - 1}\right\} + \log\left(\frac{1}{RC}\right), \tag{3.9}$$

which leads to the logarithmic distance to the upper-limit and lower-limit in ref-

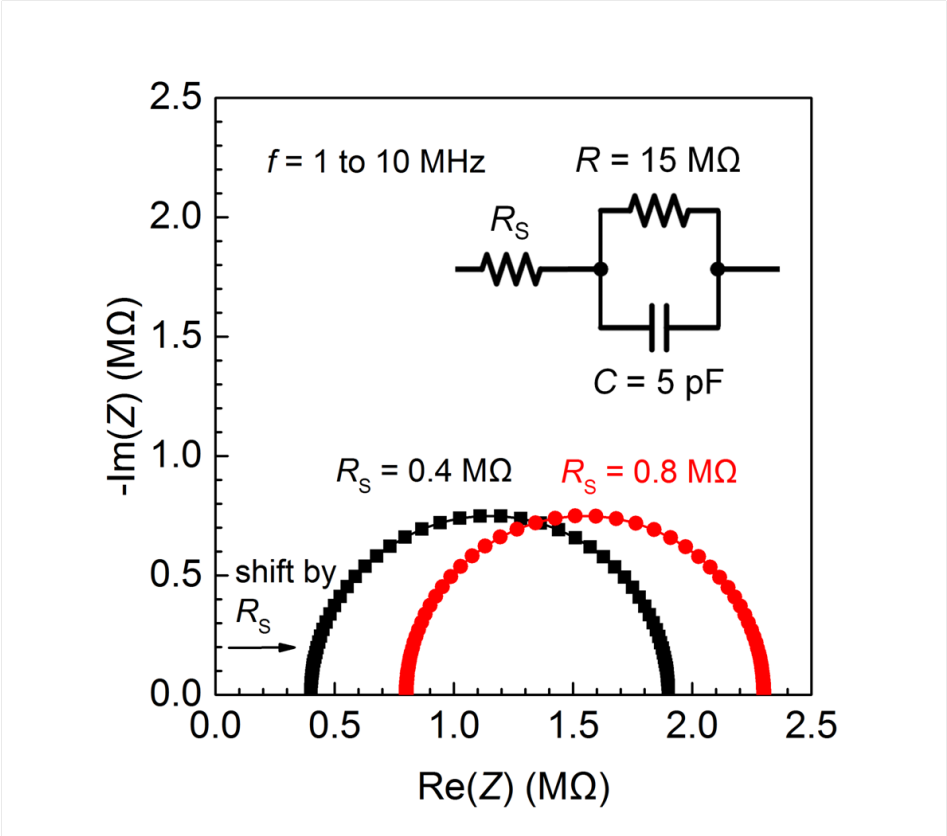

Figure 3-5: The simulated impedance spectra of the inset circuit with a fixed capacitance and parallel resistance with two different resistance values of series resistance plotted on the complex plane. The frequency is from 1 Hz to 10 MHz with the increment of 20 points per decade.

erence to ω_{RC}:

$$r^{\pm}(P) \equiv \left|\log\left(\omega^{\pm}\right) - \log(\omega_{RC})\right| = \left|\log\left\{\frac{100}{P} \pm \sqrt{\left(\frac{100}{P}\right)^2 - 1}\right\}\right|. \tag{3.10}$$

When we look for $P = 1$, the above turns to $r^{\pm}(1) = \pm 2.3$. In short, we need a frequency range of around 10^5 rad/s centred at ω_{RC}. It can be inferred that electrical noise can be more likely to be an issue for an equivalent circuit with a large impedance, because the center shifts to a lower frequency when RC gets larger.

Second, the impedance upper limit of the impedance spectrometer must be larger than the diameter of the semicircle: $R < Z_{\text{upper.limit}}$. Before an actual ac measurement, we can estimate whether the impedance upper limit can be a problem or not. Recalling that $f = 0$ is a DC bias condition, the resistance calculated by from the static current-voltage measurement of the RC circuit ($R =$

V/I) gives a perfect guideline.

The next circuit to be considered is the $R_s + RC$ circuit. This illustrate the effect of series resistance R_s on the impedance spectrum. Although it is possible to derive the Cartesian coordinates for the $R_s + RC$ in a similar manner by applying the combination rule, here, we briefly present the result of plotting on the complex plane. It is shown the addition of R_s results in the shift of the impedance spectrum without changing the initial semicircle form of the RC circuit. This is attributed to the fact that a resistor in series combination only adds the constant modulus R_s invariant with frequency. We have $Z_{R_s+RC} \to R_s + R$ when $f \to 0$, whereas $Z_{R_s+RC} \to R_s$ when $f \to \infty$. In an actual two terminal device, the observation of a series resistance generally accounts for the existence of a contact resistance that originates from the charge-injection problem at the metal/semiconductor interface [141, 142]. Compared to the RC circuit, the same frequency limit applies, and the resistance measured in static mode should be smaller than the impedance upper limit $R_s + R < Z_{\text{upper.limit}}$.

3.2 Analytical modelling

3.2.1 Definition: general and broader definition

In general, analytical modelling is development of fundamental equations used to describe changes in a system to find a closed form solution. In this thesis, the fundamental equations are in the form of differential equation such as Poisson's equation, drift-diffusion equation, and continuity equations the solution of which requires proper definition of boundary conditions. Common boundary conditions in semiconductor and device physics are the potential boundary condition defined by the reference and applied voltages and the charge carrier concentration boundary condition defined by electro-statistics.

In a broader sense, analytical modelling comprises formulation of an analytical equation that reproduces the change in a physical parameters. The analytical (or semi-analytical) equation proposed by Paasch [95] describing the hole concentration as a function of the Fermi level in the disordered semiconductor having Gaussian DOS is a good example. Parametrisation of the charge carrier mobility for the hopping transport [32] from the Monte Carlo simulation-based physical modelling on is another example.

3.2.2 Applications, limitations and overcoming methods

Applications

In our study, this approach will be exemplified by developing the current-voltage equation of organic rectifying diodes in Chapter 4 and by defining general conductivity in the transition zone of a staggered OFETs comprising the the effect of diffusion in Chapter 5.

Limitations

An apparent limitation exists in that analytical modelling rarely leads to a 'fully' analytical equation. As described earlier, a 'fully' analytical equation is that in a closed form equation so that a straight forward calculation is possible without unsimplified integrals, differentiations and/or iterative calculation processes. Upon solving fundamental equations, often we encounter a situation where no further mathematical development is possible. In the final equation is named a 'semi-analytical' equation in the sense that it results from an analytical modelling but requires a numerical calculation for determining the final value.

The values and solutions of semi-analytical equations can be obtained by numerical calculator such as Mathcad [143] and Matlab [144]. Numerical calculation with a such program can be facilitated by following techniques. First, dimensionless reduced parameters are often required to stay within the maximum and minimum values perceivable by the numerical calculator. Second, approximation could be desirable of the final equations expressed with special functions such as Airy functions $\mathrm{Ai}(x)$ and $\mathrm{Bi}(x)$ and their first derivatives and error function $\mathrm{erfc}(x)$, etc. This will be addressed in Chapter 4 for the calculation of the charge carrier concentration and potential profiles under the full-MIM model.

This approach has a great potential for modelling one-dimensional system but becomes difficult to be adopted when a multi-dimensional device is concerned. Its application to a quasi-1-D organic diode will be presented in Chapter 4. On the other hand, we will opt for another method for 2-D OFETs.

Overcoming methods

The aforementioned limit could be overcome by discrete solution for specific operation ranges with a more drastic and adaptive approximations and mathematical simplifications and subsequent merge of solution for each regimes. This requires a rigorous analysis on the robustness of the additional transition function for combin-

ing discrete regimes of operation into a single analytical equation. Cross-checking with numerical modelling results is also mandatory.

In addition, empirical modelling and/or equivalent circuit modelling can be employed to complement the analytical modelling. Our approach to model the gate voltage dependent contact resistance illustrates a successful adoption of empirical modelling and equivalent circuit modelling in the formation of a final analytical expression delineated in Chapter 5. The numerical modelling results are analysed and the empirical power-law dependence of contact resistivity on the gate voltage is observed and modelled. This is, then, adopted in the equivalent circuit of the current crowding model to yield a final analytical model for power-law dependent contact resistance.

3.3 Numerical modelling

3.3.1 Numerical device simulator

A commercially available device simulator Atlas from Silvaco, Inc. [145] has been used for numerical simulation of organic devices. In particular, Atlas is a physically-based 2-D and 3-D device simulator widely adopted for technology computer-aided design (TCAD) in semiconductor industry. The multi-dimensional simulation capability is achieved by the finite-element method (FEM).

The merits of physically-based simulation are its capabilities to predict device behaviour, provide insight and conveniently captures and visualize theoretical knowledge. On the other hand, the drawbacks of physically-based simulation must not be neglected in that all the relevant physics must be incorporated into a simulator. In addition, numerical procedures must be implemented to solve the associated equations. The user's manual provides a list of physics available in Atlas as well as detailed explanations for each model. Also, numerical calculation procedures are taken care of for Atlas users by Silvaco and briefly presented in the user's manual.

When a new physics is added to the simulator, a continuous effort for a series of updates would be necessary. Aiming at public interests, we would like to articulate that both maintenance activities by developers and feedbacks from users are critical elements for a successful installation of a new physics. In this context, we note that there has been an intimate exchange with Silvaco Europe Ltd in the United Kingdom through a research visit under the umbrella of Horizon 2020 Marie Sklodowska-Curie Fellowship for Research and Innovation Staff Exchange

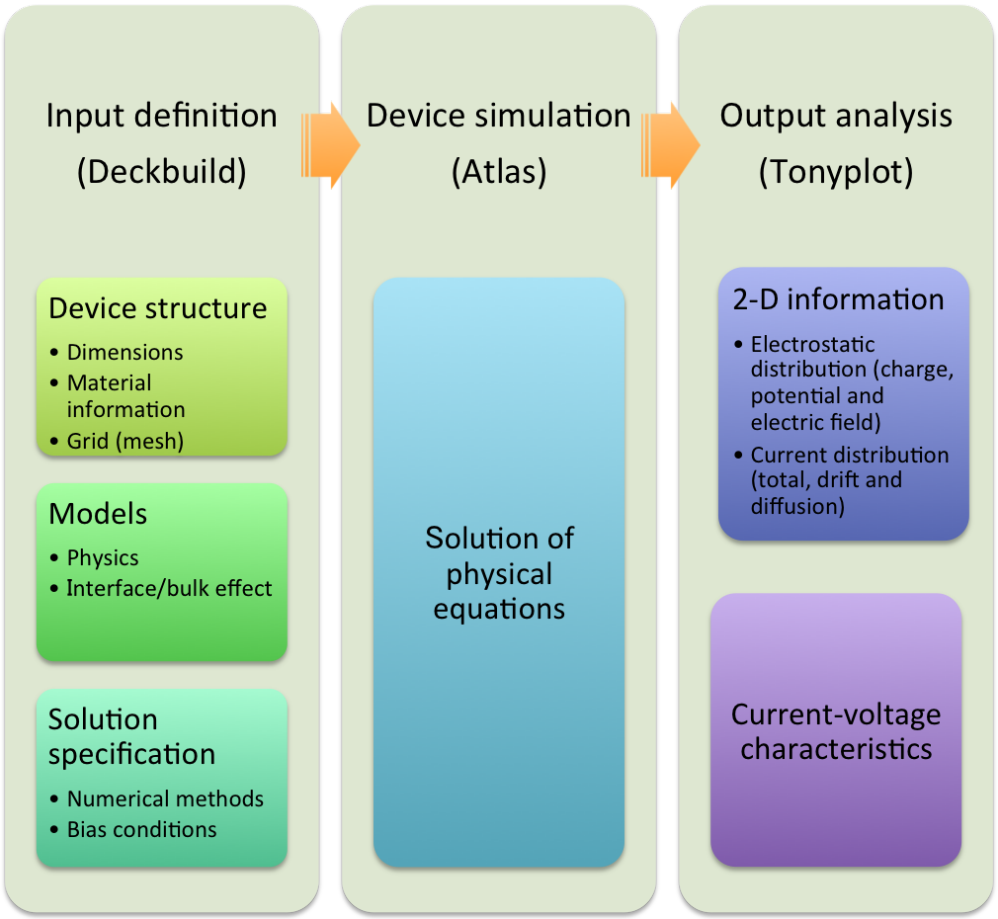

Figure 3-6: Device simulation process and tasks at each step for 2-D physically-base finite-element simulator.

(RISE) Programme entitled Design Oriented ModellINg for flexible electrOnics (DOMINO) (2015-2019) 645760 [146]. During the research visit, the convergence problem was fixed, which occurred when the Gaussian disorder is higher than 0.20 eV.

3.3.2 General simulation process

The simulation process consists of input definition, device simulation, and output analysis as shown in Figure 3-6. The device simulator, Atlas, lies at the center of numerical simulation process. The Deckbuild and Tonyplot are softwares in charge of input definition and output analysis.

At the input definition step, three tasks are executed in a script editor called Deckbuild. First, the user defines the physical structure to be simulated. In this step, geometrical dimension as well as a mesh or grid that covers the physical simulation domain. Also, material informationis clarified for each sub-domains in the

device such as types (metal, insulator or semiconductor), energy structure (band gap, DOS, etc.), transport parameters (mobility, etc.) and etc. Thus, it is at this element where Gaussian DOS and Pasveer mobility are described. Second, the user invokes the physical models to be used. In this study, Poisson's equation, carrier continuity equation, drift-diffusion equation, and Fermi-Dirac statistics are used. Third, the user declares the bias conditions for which electrical characteristics are to be simulated. The bias condition should be defined either as a fixed value or as a sweeping range and an increment at each electrode. Aforementioned elements are written with specific syntaxes perceived by Atlas.

At the device simulation step, numerical calculations are executed by Atlas. This means that all the related physical equations are solved in a self-consistent manner at each node of a mesh. The success of the device simulation could be assessed directly from the convergence of solution. If the solution does not converge, one should return to the input definition step and carefully review each elements.

At the output analysis step, the results of device simulation are visualised and analysed with Tonyplot, a data analysis and graphing software. The simulation results under a fixed bias condition (including thermal equilibrium condition) are 2-D contour plots containing information on electrostatic distribution (charge, potential and electric field) and current distribution. The simulation results under a sweeping bias condition are the current-voltage characteristics are computed without a dimensional information.

3.3.3 Practical tips

Defining a mesh

The mesh is defined by a series of horizontal and vertical lines and the spacing between them. The crossing points are called nodes where physical equations are actually solved. In the other regions, the value of physical quantities is calculated by interpolation. Figure 3-7 shows an illustration of how mesh or grid covers the 2-D physical simulation domain in this case of equal-sized mesh.

When a denser mesh is defined, results are more reliable because the nodes become a better approximation to the real continuous medium. However, the computation time and the size of the final 2-D contour data increase with the number of nodes. Therefore, a functionality to vary the size of the mesh is provided for an efficient numerical simulation without compromising the accuracy. For example, we could increase the density of the mesh in the region where parameters are expected to vary significantly. In the region where parameters do not change abruptly,

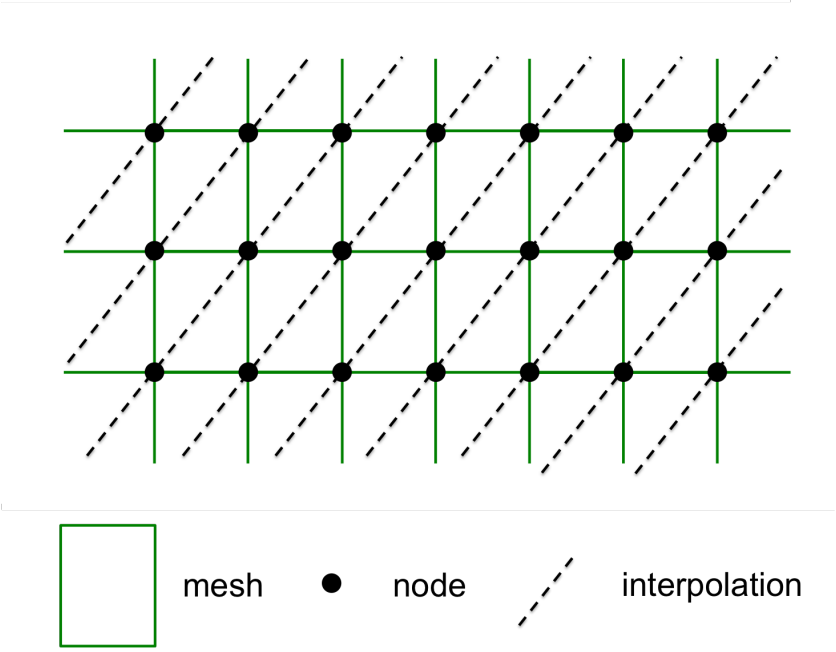

Figure 3-7: Illustration of the mesh (grid), nodes and interpolation lines in finite-element method.

approximate values calculated by interpolation could be sufficiently reasonable.

Numerical precision

The convergence and accuracy of a device simulation requires the numerical resolution of the quantities $(n-p)$ and $(n+p)$. The first appears in the charge carrier density, which is used in Poisson's equation to calculate the electrostatic potential, while the second is used implicitly in the calculation of current conservation. In order to resolve these terms, the calculations must maintain the significant bits of arithmetic precision P at least

$$P \sim \frac{|\ln(n) - \ln(p)|}{\ln(2)}. \tag{3.11}$$

When Gaussian DOS is assumed and Boltzmann statistics holds, the right hand side of the equation can be expressed in terms of the band gap E_{g} and temperature T:

$$P \sim \frac{1}{\ln(2)} \left(\frac{E_{\mathrm{g}}}{k_{\mathrm{B}} T} \right). \tag{3.12}$$

Therefore, the higher precision P is required for high-bandgap materials, and at low temperatures. Considering the badgap of organic semiconductor (typically 2.5∼4 eV) and inorganic semiconductor (1∼2 eV), it can be inferred that precision is more likely to be an issue in organic semiconductor materials. In practice, E_{g}

is often set as an arbitrary large value in order to consider single carrier type (n-type or p-type), which could gives rise to a convergence issue. In addition, as will be discussed in Chapter 4.1, we found that similar issue appears when injection becomes stronger due to an increased disorder (described by a larger width of Gaussian DOS, σ), and hence the quantity $(n - p)$ becomes large.

By default, Atlas uses a nominal arithmetic precision of 64 bits (i.e., double precision). In order to support the simulation of high-bandgap materials in particular, Atlas can now run at several levels of extended precision as well. The level of precision is selected by means of a command-line flag upto 256 bits. Note that the precision directly affects the size of the floating point numbers (that appears during the calculation and in the ouput file), an optimal precision should be used for a time-efficient calculation and data treatment.

3.4 Experimental validation

Ultimately, the validity of the model must be confirmed by experiments, as Feynman remarked on how we would look for a new law, "...Then we compute the consequences of the guess to see what would be implied if this law that we guessed is right. Then we compare the result of the computation to nature, with experiment or experience, compare it directly with observation, to see if it works. If it disagrees with experiment it is wrong. ..." [147]. In the comparison to experimental observations is a possibility to correct the model, an inspiration for further extension of the model and a practicability as the model's reason for being.

Therefore, along with our efforts to ensure physical basis in the model, we made a consistent effort to provide a comparative study between the model and experimental data throughout the thesis. While doing so, we paid a particular attention to conduct a careful interpretation of the experimental observations. It is by this philosophy that we were able to identify the loss of a capacitive behaviour of a rectifying organic diode in the forward bias regime and correlate it with a strong charge carrier injection at the anode and a subsequent bending of potential profile (Section 4.1). This formed a profound basis to consider organic semiconductor as a degenerate semiconductor which gives birth to mobility enhancement by charge carrier concentration, electric field and temperature and diffusion enhancement considered in the rest of modelling processes.

In addition, we have chosen an organic rectifying diode and a staggered organic field-effect transistor for experimental as well as theoretical study. A detailed motivation for choice is presented in the beginning of a relevant chapter. All experi-

mental conditions and methods for the device fabrication and characterisation are given in Appendix D.

Chapter 4

Organic diodes

In electronics, a diode is often defined as a two terminal electronic component that conducts current in one direction (asymmetric conductance or rectification). On the other hand, in this thesis, we employ the term 'diode' in an inclusive sense to refer a two terminal electronic component that exhibits a non-linear current-voltage characteristics. This definition does not exclude a diode that conducts current in both direction (symmetrical or non-rectifying diode), but it distinguishes a diode from other famous examples of two terminal electronic components, i.e. a resistor or a capacitor (which may be confusing when a diode is defined solely as a two-terminal electronic component).

Today, a semiconductor diode is the most common type of diode that flows current between two electrodes through a semiconductor. An organic diode is a class of semiconductor diodes that makes use of an organic semiconductor as a conducting medium. In principle, the choice of a metal and a semiconductor determines how the device operates. The major factors are the magnitude and difference of the injection barrier, the energy that a charge should overcome to be injected into transport orbitals of a given organic semiconductor, at each metal/organic semiconductor interfaces. The interface with a small injection barrier is called

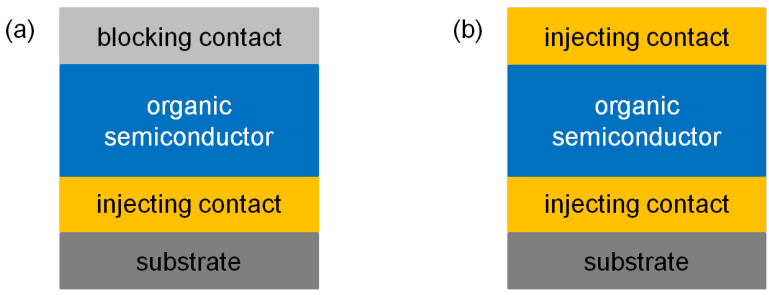

Figure 4-1: Schematic diagram of vertical (a) rectifying diode (asymmetrical) and (b) non-rectifying diode (symmetrical).

an 'injecting' contact. In contrast, the interface with a large injection barrier is called a 'blocking' contact that can only extract injected charges from the injecting contact. At least one of two electrodes must be injecting in order to achieve a substantial current flow. The conduction in a diode becomes more symmetrical when injection barrier at two electrodes decides gets more similar. According to the aforementioned classification, we illustrate two diode structures used in this thesis in Figure 4-1. The diodes have vertical configuration which reflects the direction of current in reference to the substrate.

In this chapter, we will elaborate on various theoretical and experimental methods to analyse or model the behaviours of organic diodes. We made a special effort to fully incorporate the distinctive charge injection and transport processes (presented in Chapter 2) into the model and to validate the model taking advantages of a simple structure of a diode.

4.1 Vertical rectifying diode

4.1.1 Depletion of entire organic semiconductor layer

An organic rectifying diode is not only a key and the most demanding element for a circuit application such as a radio frequency-identification (RF-ID) tag, etc but also the most convenient platform to study organic semiconductor and device physics. In the RF-ID application, the device is used to supply quasi-d.c. power to the logic circuit of the tag, in which high frequency operation enables to charge a storage capacitor in a time frame that is only a small fraction of the base-carrier period. In the literatures, the operation frequency of 50 MHz was demonstrated by Steudel *et al.* based on a Au/pentacene/Al vertical structure [148]. Recently, Kang *et al.* achieved 1-GHz-speed operation frequency by treating Au anode with a self-assembled monolayer [149]. The work by Haldi and co-workers [150] examined the feasibility of other organic semiconductors as a rectifying diodes in ITO/organic/Al structure. They used C60, pentacene, 4,4'-bis[N-(1-naphthyl)-N-phenyl-amino]biphenyl (α-NPD), and a N,N'-bis(m-tolyl)-N,N'-diphenyl-1,1'-biphenyl-4,4'-diamine (TPD) based polymer as an organic semiconductor. However, a full understanding on the device operation is still lacking.

Because of its similar rectifying behaviour, single-layer organic organic diodes have been generally described as conventional Schottky diodes [151, 152]. A characterizing feature of a Schottky diode is the existence of a partial depletion region

near the blocking contact at thermal equilibrium, the modulation of which by external bias governs the diode current [36]. In particular, the depletion region widened when the reverse bias is applied to the diode, which concomitantly decreases the measured depletion capacitance (C_d). This constitutes a foundation of so-called Mott-Schottky analysis that enables the extraction of the doping concentration and the built-in potential from the $1/{C_d}^2$-versus-V plot [153, 154].

In contrast, a constant reverse bias capacitance has been observed in rubrene organic diodes [155]. This implies that the doping concentration is so low that the entire organic layer gets depleted readily at thermal equilibrium. A similar behaviour was recently observed from the pentacene organic diode [156]. When assuming uniformly doped semiconductor layer and full depletion approximation[1], the depletion width (W_d) is inversely proportional to the square root of the doping concentration (N_A)

$$W_\mathrm{d} = \sqrt{\frac{2\epsilon_s \left(V_\mathrm{d} - V\right)}{qN_\mathrm{A}}} \tag{4.1}$$

where ϵ_s is the permittivity of the semiconductor, V_d the diffusion potential, V the applied anode voltage, and q the elementary charge [36]. V_d is also called the built-in potential, which is the difference in the work function of the metal and the semiconductor.

Figure 4-2(a) shows the 'conventional' energy diagram of a metal/semiconductor junction at thermal equilibrium (V = 0 V), in which W_d is assumed to be smaller than the semiconductor thickness. The approximate depletion width could be estimated by (5.45). The dependence of the depletion width on the doping concentration is plotted in Figure 4-2(b) for three values of diffusion potential V_d = 0.3, 0.5, and 0.7 V with fixed ϵ_s = 3.6 $\times\epsilon_0$ and V = 0 V (corresponding to the equilibrium condition).

We note that, W_d becomes larger than 100 nm when N_A is lower than $\sim$ 10^{-16} cm^{-3}. When W_d is greater than the semiconductor thickness, the depletion region reaches the opposite injecting contact, and the entire semiconductor layer is depleted. In this case, a reverse bias can no longer widen the depletion region, which results in a constant depletion capacitance.

In order to support this concept of the 'entire' depletion of organic semiconductor layer, we experimentally studied a prototypical organic rectifying diode with thick pentacene semiconductor layer. Figure 4-3 shows the measured current

[1]The 'full depletion approximation' assumes that all donor (or acceptor) dopants in the depletion region are ionized and that there is no free charge carrier. It enables analytical resolution of the Poisson's equation.

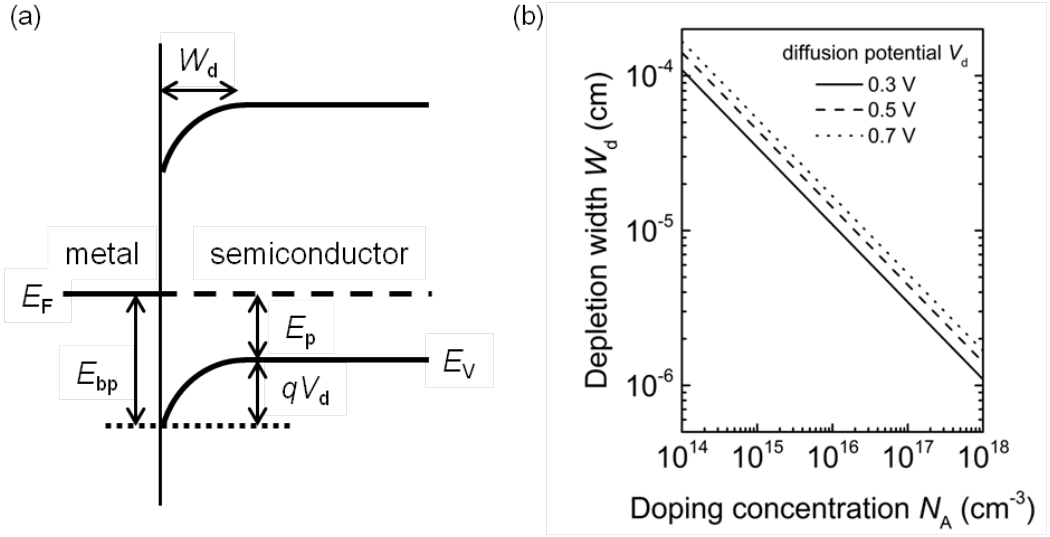

Figure 4-2: (a) Energy band diagram of a Schottky junction at thermal equilibrium: E_C conduction band edge, E_V valence band edge, and E_F Fermi level. (b) Calculated depletion width as a function of doping concentration at various diffusion potential.

density-voltage ($J - V$) characteristics of a vertical rectifying Au/pentacene/Al diode with 500-nm-thick pentacene film. The active area of the diode is 4.3×10^{-4} cm^{-2}, which is defined by the overlapping area of the Au bottom and the Al top electrodes. We note that the pentacene layer is patterned by shadow mask to achieve a minimal parasitic effect. In the given structure, the Au electrode is an injecting contact, and the Al is a blocking contact. The LUMO level of pentacene is situated sufficiently remote from the Fermi levels of both Au and Al. Therefore, the diode functions as a unipolar hole-only device. As shown in Figure 4-3(b), the diode manifested a significantly high rectification ratio.

The electrical impedance of the diode were measured at various ac voltage V_{ac} conditions, where dc bias V_{dc} is swept from - 10 to 10 V at a fixed ac bias $v_{ac} =$ 100 mV: $V_{ac} = V_{dc} + v_{ac}$. The measured impedance modulus Z_m and phase angle ϕ are shown in Figure 4-4, where a clear contrast between reverse and forward bias regime is observed. First, we observe that the impedance in the reverse bias regime exhibits the phase angle of -90° and a constant impedance modulus. This implies that the diode shows a purely capacitive behaviour and that the capacitance does not depend on the applied reverse bias. Therefore, the metal-insulator-metal (MIM) model can explain the diode behaviour. Second, as the diode is being positively biased (in forward bias regime), Z_m decreases and ϕ departs from -90° approaching zero. This means that the diode deviates from a pure capacitor, and that the resistive element of the total impedance becomes

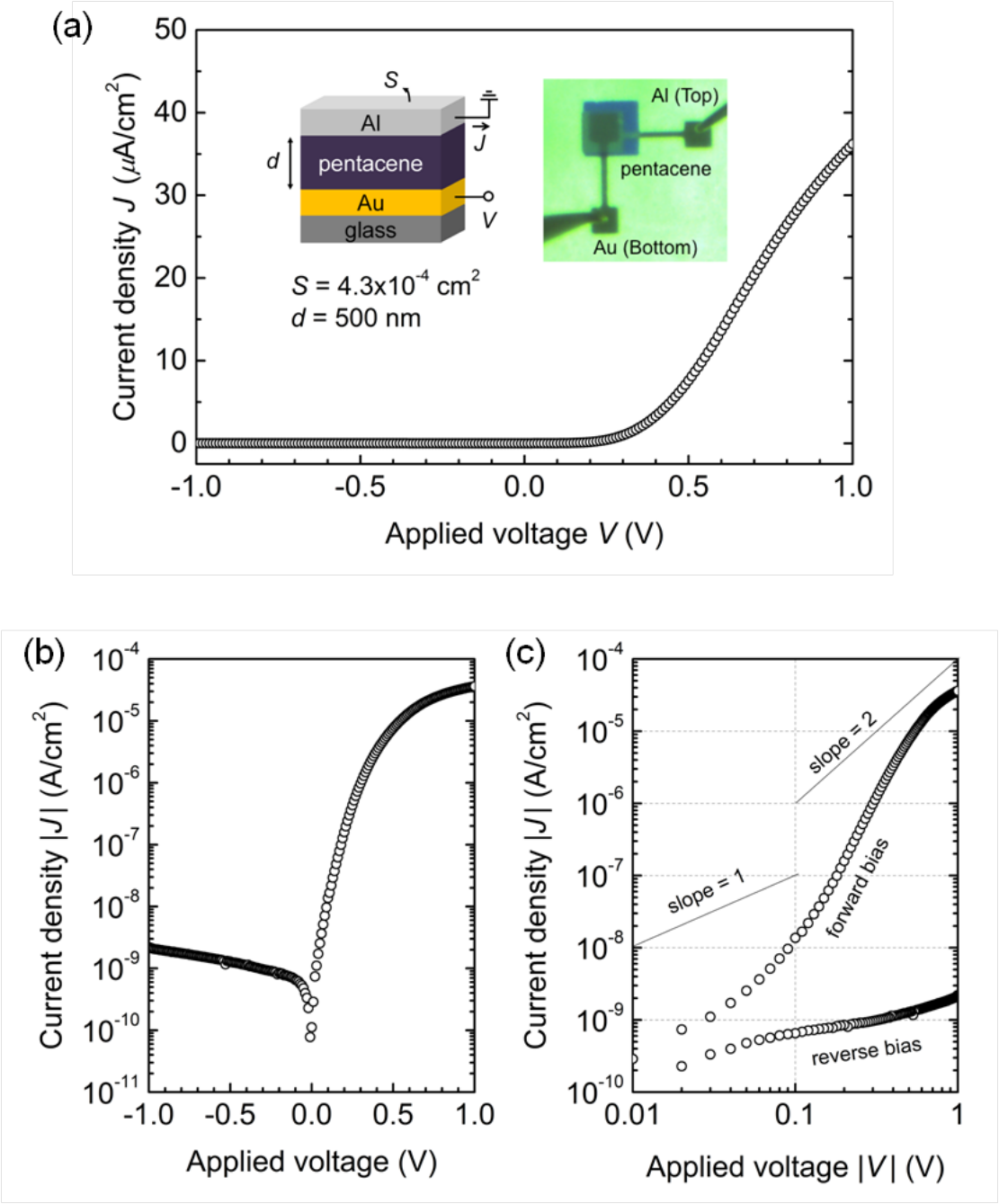

Figure 4-3: (a) Current density-voltage characteristics of a rectifying pentacene diode in a linear scale (inset: device structure). The applied voltage is define as the voltage applied to the Au bottom electrode (anode) in reference to the grounded Al top electrode (cathode). The same results in (b) a semi-logarithmic and (c) double-logarithmic scale.

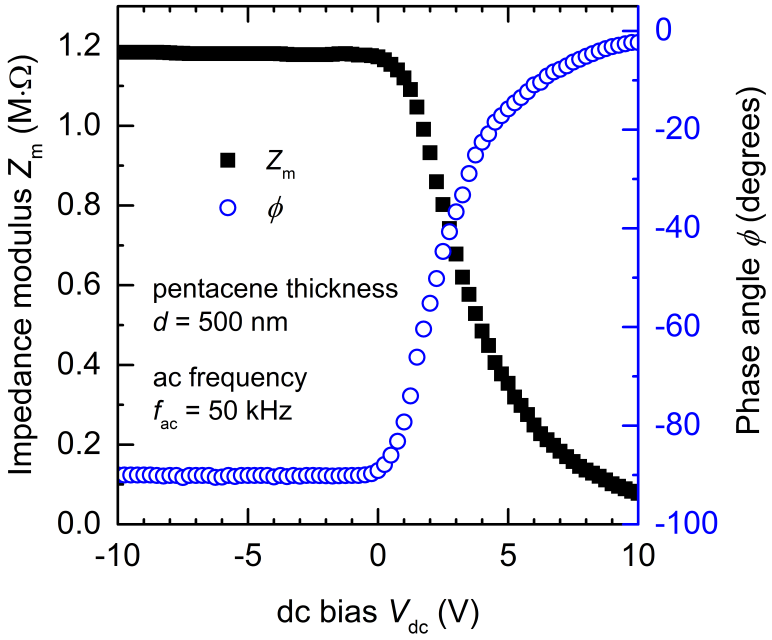

Figure 4-4: Impedance-versus-voltage characteristics of an organic rectifying diode with 500-nm-thick pentacene and Au injecting and Al blocking contacts.

dominant gradually with the increase of V_{dc}. Then, this evolution of the impedance bring information about the range of voltage, in which the MIM-model is valid.

Indeed, the depletion of entire 500-nm-thick organic semiconductor layer originates from that fact the doping concentration in pentacene is extremely low. Based on (5.45), we can estimate the doping concentration N_{A} in pentacene. Taking $V_{\mathrm{d}} = 0.6$ V and $\epsilon_s = 3.6\ \epsilon_0$, the depletion width W_{d} that extends over 500 nm would be achievable when the doping concentration is lower than 10^{15} cm^{-3}. Except for the cases where deliberate doping is desirable [157, 158], organic semiconductors are mostly used without deliberate doping. In this condition, ambient oxygen could serve as a molecular dopant in p-type molecular film [159]. Because the value is negligibly small compared to the molecular density of pentacene $\sim 3{\times}10^{21}$ cm^{-3} [93], it can be inferred that unintentional doping agent only lightly doped pentacene films.

We note that the 'entire' depletion of organic semiconductor layer has a direct impact on the description of the diode current-voltage characteristics. More precisely, it requires modifications of the fundamental assumptions made during the development of the coupled Poisson's and drift-diffusion equation into the Schottky diode equation. In contrast to the 'conventional' energy band diagram (see Figure 4-2(a)), there is no band bending due to the static charge from ionized

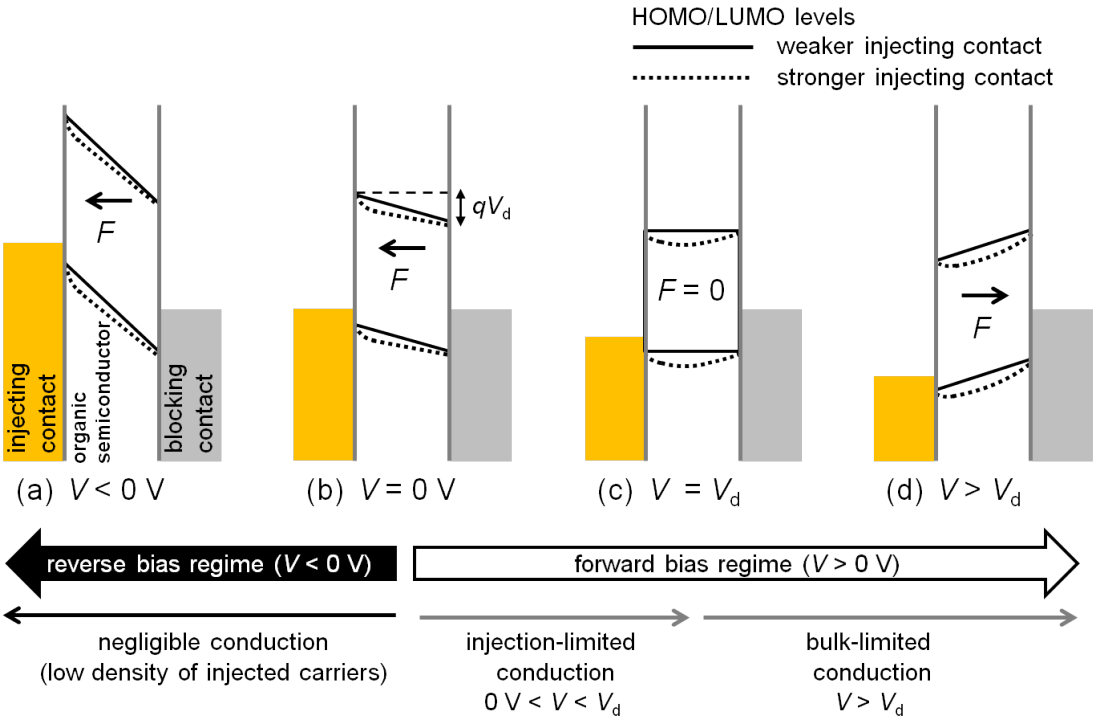

Figure 4-5: Energy diagram of an organic rectifying diode depending on the strength of injecting contact. The HOMO and LUMO levels are drawn with a solid line for a weaker injecting contact (corresponding to the MIM-model or non-degenerate), and with dotted line for a stronger injecting contact (degenerate). (a) Reverse bias regime, (b) thermal equilibrium, (c) flat-band condition, (d) bulk-limited regime. The lower side arrows indicate the dominant conduction mechanisms under each regime.

dopants in an organic diode. Instead, fully-depleted organic semiconductor layer has straight band profiles at thermal equilibrium reminding of an insulator layer. Therefore, we need a new description for the energy diagram aptly-named as the metal-insulator-metal model (see Figure 4-5).

Under the MIM model, the electrical conduction in an organic diode is manifested entirely by the 'injected' charge carriers, and the organic layer is merely regarded as a transporting medium for injection carriers. At thermal equilibrium (Figure 4-5(b)), the net current is null due to the balance between the diffusion current and the drift current. In the reverse bias regime (Figure 4-5(a)), a strong electric field in the diode (i.e. the reverse bias is enforced by the diffusion potential) prevents any transport of holes from the injecting contact to the cathode. The magnitude of the reverse current is extremely low, because the cathode cannot inject enough charge carriers. In the forward bias regime, the diffusion potential opposes the applied forward bias which cancels out at $V = V_{\mathrm{d}}$ (Figure 4-5(c)).

When a small forward bias is applied ($0 < V < V_\mathrm{d}$), though significantly reduced in magnitude, the internal electric field still hinders the drift of injected charge carriers towards the cathode. Therefore, the conduction in this regime is due mainly to the dominant diffusion of injected carriers from the anode towards the cathode, which is limited by the amount of injected charges, thus called 'injection-limited' regime. Finally, when V exceeds V_d, the internal electric field is reversed, and the current due to the drift of the anode-injected holes aligns in the same direction with the diffusion current. This regime is, thus, limited by the bulk conductivity of the organic semiconductor rather than injection-limited. In this regime, it appears the space-charge-limited current (SCLC).

Nevertheless, band bending may occur due uniquely to the regional 'accumulation' of the injected charges the degree of which would be determined by the bias condition and the strength of the injecting contact. A detailed and quantitative description will be given in Section 4.2 with the numerical simulation results. Here, we note qualitatively that, in the case of weaker injecting contact, the straight band profiles could extend into forward bias regime (injection-limited regime or even early bulk-limited regime $V \gtrsim V_\mathrm{d}$) until injected charges accumulate enough to create the upward curvature of electrical potential. On the contrary, in the case of stronger injecting contact, a certain bending that exists already at thermal equilibrium could present in all regimes, which becomes more pronounced as the increase of the forward bias. For both injecting contacts, no additional bending could occur in the reverse bias regime simply because the cathode cannot inject charges. The regional 'accumulation' leads the semiconductor function as a degenerate semiconductor. Together with the non-existence of the partial depletion layer, degenerate or non-degenerate behaviour should be taken into account for establishing a current-voltage model with a greater robustness and a wider voltage range of applicability.

4.1.2 Schottky diode model

We start by revisiting the Schottky diode model, which is an analytical form of the drift-diffusion equation coupled with Poisson's equation. The principle is that following Poisson's and drift-diffusion equations (5.46)-(5.47) are solved sequentially:

$$\frac{\mathrm{d}^2 V}{\mathrm{d}x^2} = -\frac{\mathrm{d}F}{\mathrm{d}x} = -\frac{qp(x)}{\epsilon_\mathrm{s}}, \tag{4.2}$$

$$j = qp\mu F - qD\frac{\mathrm{d}p}{\mathrm{d}x}, \tag{4.3}$$

where x is the position on one-dimensional coordinate, V the electrical potential, F the electric field, q elemental charge, $p(x)$ hole concentration, ϵ_{s} semiconductor dielectric constant, j current density, μ mobility and D diffusion constant.

In the first step, (5.46) is used to determine the shape of the potential in the diode. The result is expressed through the variation of the valence band edge E_{V} as a function of the distance x from the metal- semiconductor junction:

$$E_{\mathrm{V}} = E_{\mathrm{V}}(0) + \frac{q^2 N_{\mathrm{A}}}{\epsilon_{\mathrm{s}}} \left(W_{\mathrm{d}} x - \frac{x^2}{2} \right), \tag{4.4}$$

where W_{d} is the depletion width (5.45).

The current is now established by rewriting (5.47) as:

$$j = \mu k T \left(\frac{p}{kT} \frac{\mathrm{d}E_{\mathrm{V}}}{\mathrm{d}x} - \frac{\mathrm{d}p}{\mathrm{d}x} \right) \tag{4.5}$$

under Einstein relation $D = \mu kT/q$ that holds for non-degenerate semiconductor. Next, using $\exp(-E_{\mathrm{V}}/kT)$ as an integrating factor:

$$j \int_0^{W_{\mathrm{d}}} \exp\left(-\frac{E_{\mathrm{V}}}{kT} \right) \mathrm{d}x = -\mu k T \left[p \exp\left(-\frac{E_{\mathrm{V}}}{kT} \right) \right] \tag{4.6}$$

Taking the Fermi level of the metal (blocking electrode) as the reference energy, the boundary conditions are given by:

$$E_{\mathrm{V}}(0) = -E_{\mathrm{bp}}, \tag{4.7}$$

$$E_{\mathrm{V}}(W_{\mathrm{d}}) = -E_{\mathrm{p}} + q(V_{\mathrm{d}} - V), \tag{4.8}$$

$$p(0) = N_{\mathrm{V}} \exp\left(-\frac{E_{\mathrm{bp}}}{kT} \right), \tag{4.9}$$

$$p(W_{\mathrm{d}}) = N_{\mathrm{V}} \exp\left(-\frac{E_{\mathrm{p}}}{kT} \right), \tag{4.10}$$

where E_{bp} is the hole injection barrier at the metal-semiconductor interface, and E_{p} the energy difference between the valence band edge and the Fermi level in the bulk of the semiconductor. N_{V} is the effective density of state at valence band edge. An energy diagram of the junction and the relevant parameters are shown in Figure 4-2.

Combining all the above equations leads to:

$$j = j_{\mathrm{d}} \left(\exp \frac{qV}{kT} - 1 \right), \tag{4.11}$$

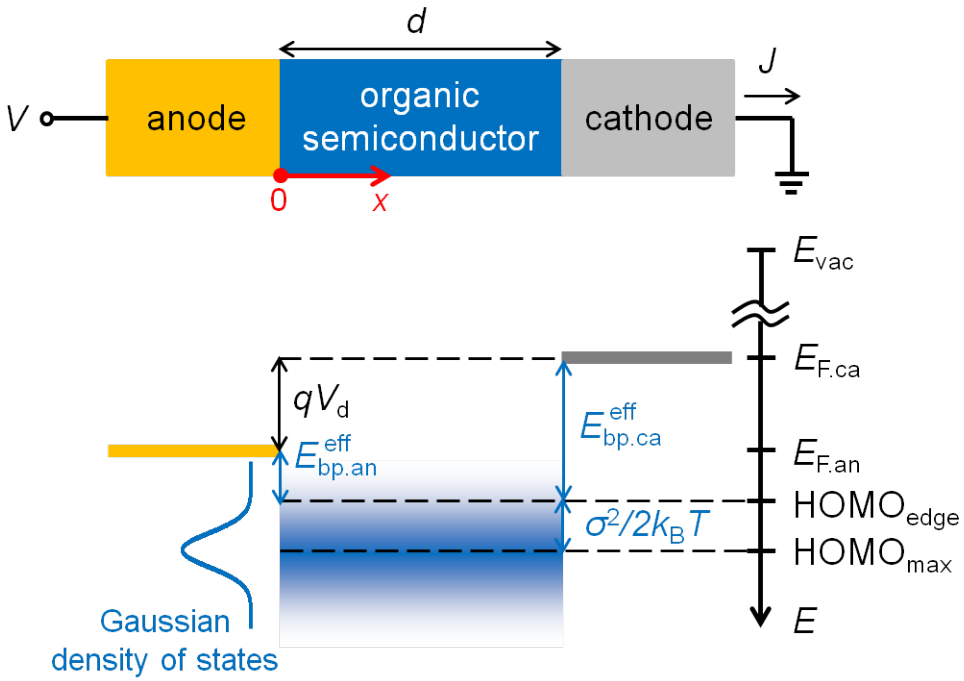

Figure 4-6: Device structure and energy diagram of an organic rectifying diode. Due to the energetic disorder described by the width of the Gaussian DOS (σ), injection barrier E_{bp} is lowered by $\sigma^2/2k_{\mathrm{B}}T$ leading to the effective injection barrier $E_{\mathrm{bp}}^{\mathrm{eff}}$. The $\mathrm{HOMO}_{\mathrm{edge}}$ which is $\sigma^2/2k_{\mathrm{B}}T$ above the $\mathrm{HOMO}_{\mathrm{max}}$ is analogous to the valence band edge E_{V} for crystalline semiconductor. The reference points for the position, potential and energy is indicated.

$$j_{\mathrm{d}} = q\mu N_{\mathrm{V}} F(0) \exp\left(-\frac{E_{\mathrm{bp}}}{kT}\right), \tag{4.12}$$

where $F(0)$ is the electric field at the metal-semiconductor interface ($x = 0$). The Schottky diode predicts an exponential increase of diode current with applied anode voltage.

4.1.3 Metal-Insulator-Metal (MIM) model

Attempts to adapt the Schottky model to the diode with entirely depleted organic semiconductor layer have been recently made [160, 161]. More recently, we presented how distinctive electronic structure of organic semiconductor could be incorporated with the MIM model [162]. In essence, the Gaussian density-of-states (DOS) is adopted to describe random distribution of fully localised states instead of the square root function of the energy $\sim \sqrt{E_{\mathrm{V}} - E}$ which is more suitable for describing free electrons in the delocalised energy band of crystalline semiconductors. Thus, we primarily use the terms HOMO (or LUMO) in the following derivation. As shown in Figure 4-6 When Gaussian DOS is invoked, the HOMO is

represented by the maximum of the HOMO ($\mathrm{HOMO_{max}}$) at which the states are the most populated.

Under the MIM model, the variation of $\mathrm{HOMO_{max}}$ is given by:

$$\mathrm{HOMO}(x) = \mathrm{HOMO_{max}}(0) + q\,(V - V_\mathrm{d})\,\frac{x}{d}, \tag{4.13}$$

where $\mathrm{HOMO_{max}}(0)$ is the HOMO level at the anode, d is the thickness of the organic semiconductor, V_d is the diffusion potential, that is, the energy difference between the work function of both electrodes. Then, (5.50) must now be integrated over the whole thickness of the semiconductor, thus leading to:

$$j = q\mu p_0 \frac{V_\mathrm{d} - V}{d} \frac{\exp\frac{qV}{kT} - 1}{\exp\frac{qV_\mathrm{d}}{kT} - \exp\frac{qV}{kT}}, \tag{4.14}$$

with following boundary conditions:

$$\mathrm{HOMO_{max}}(0) = -q(V - V_\mathrm{d}) \tag{4.15}$$

$$\mathrm{HOMO_{max}}(d) = 0 \tag{4.16}$$

$$p(0) = N_0 \exp\left(-\frac{E^{\mathrm{eff}}_{\mathrm{bp.an}}}{kT}\right) \tag{4.17}$$

$$p(d) = N_0 \exp\left(-\frac{E^{\mathrm{eff}}_{\mathrm{bp.ca}}}{kT}\right) \tag{4.18}$$

where $\mathrm{HOMO_{max}}(d)$ is the reference HOMO level, $p(0)$ and $p(d)$ are the hole concentrations at the anode ($x = 0$) and cathode ($x = d$) derived under Boltzmann approximation. Here, N_0 is the total DOS, $E^{\mathrm{eff}}_{\mathrm{bp.an}}$ and $E^{\mathrm{eff}}_{\mathrm{bp.ca}}$ are the effective injection barrier at the anode and cathode, which is the defined by the energy difference between the Fermi level and the edge of the HOMO ($\mathrm{HOMO_{edge}}$) as shown in Figure 4-6. Then, following holds

$$p(0) = p(d) \exp\left(-\frac{qV_\mathrm{d}}{k_{BT}}\right), \tag{4.19}$$

which comes from $E^{\mathrm{eff}}_{\mathrm{bp.an}} = E^{\mathrm{eff}}_{\mathrm{bp.ca}} - qV_\mathrm{d}$.

In spite of the fundamental differences in physics, the MIM and the Schottky model have some similarities. When $V < 0$ (i.e. reverse bias regime), we have

$\exp(qV/kT) \ll 1 \ll \exp(qV_\mathrm{d}/kT)$, and (4.14) is written

$$j = -q\mu p(d)\frac{V_\mathrm{d} - V}{d}, \tag{4.20}$$

which resembles the reverse bias current of the Schottky diode. Here, $p(d)$ is the hole concentration at the cathode and the term $-(V_\mathrm{d} - V)/d$ corresponds to the electric field at the cathode. Thus, in both model, the reverse bias current is basically dictated by the hole concentration and the electric field at the blocking contact. In addition, when $0 < V < V_\mathrm{d}$, we have $\exp(qV/kT) \ll \exp(qV_\mathrm{d}/kT)$. Then, (4.14) can be simplifies into

$$j = q\mu p_0 \frac{V_\mathrm{d} - V}{d}\left(\exp\frac{qV}{kT} - 1\right). \tag{4.21}$$

This means that the MIM model predicts the exponential current-voltage relation in the injection-limited conduction regime similar to the Schottky diode despite the consideration for the Gaussian DOS and the depletion of entire semiconductor layer.

One of the main assumptions that leads to (4.11) and (4.14) is that the 'shape' of the potential profile (quadratic for a Schottky diode, linear for a MIM diode) remains unchanged when a voltage is applied. This is basically true in a Schottky diode, as shown in (5.48). However, as will be shown in the following, this assumption only verified in a MIM when the injection barrier is high, which strongly restricts the applicability of the model. Therefore, further investigation is needed with a model that encompasses the case where charge injection is significant either due to a stronger injecting contact or a greater applied bias.

4.1.4 Full MIM model

We now solve the equations the with the same assumptions as the MIM model except the perfectly linear band profile, namely the 'full MIM model'[2]. We start from a combination of 5.46, 5.47 and Einstein relation:

$$j = \epsilon\mu\left(F\frac{\mathrm{d}F}{\mathrm{d}x} - \frac{kT}{q}\frac{\mathrm{d}^2F}{\mathrm{d}x^2}\right) \tag{4.22}$$

[2]The distinguishing characteristics such as low doping concentration and depletion of entire organic semiconductor layer pertain.

Then, we define the dimensionless reduced variables following Bonham and Jarvis [163]:

$$x_r = \frac{x}{d}, V_r = \frac{V}{V_T}, F_r = \frac{d}{V_T}F, p_r = \frac{qd^2}{\epsilon V_T}p, j_r = \frac{d^3}{\epsilon\mu {V_T}^2}j, \tag{4.23}$$

where$V_T = kT/q$. (4.22) now writes:

$$\frac{\mathrm{d}^2 F_r}{\mathrm{d}{x_r}^2} - F_r\frac{\mathrm{d}F_r}{\mathrm{d}x_r} + j_r = 0. \tag{4.24}$$

Note that, in the following development, potential at the anode $V(0)$ is set as a reference potential for the sake of mathematical simplicity, and then plotted in the same reference with the MIM model.

The diode without current

Integrating (4.24) with $j_r = 0$ leads to:

$$\frac{\mathrm{d}F_r}{\mathrm{d}x_r} - \frac{F_r}{2} + 2g^2 = 0, \tag{4.25}$$

where g is an integration constant. The solution of this equation for the electrical potential is given by:

$$V_r = 2\ln\left(\cosh gx_r + \sqrt{1 + \frac{p_{r0}}{2g^2}}\sinh gx_r\right) \tag{4.26}$$

where $x_{r0} = \sqrt{2/p_{r0}}$, p_{r0} being the reduced density of holes at the anode. The integration constant g can be calculated by writing the value of the reduced potential at the cathode ($x = d$ or $x_r = 1$). This replaces the perfectly straight potential profile of the MIM model at equilibrium given in (4.13).

Solution of the equation with current

Equation (4.24) has the following analytical solution:

$$F_r(x_r) = -2\alpha\frac{c_2\mathrm{A}_i'(c_1 + \alpha x_r) + \mathrm{B}_i'(c_1 + \alpha x_r)}{c_2\mathrm{A}_i(c_1 + \alpha x_r) + \mathrm{B}_i(c_1 + \alpha x_r)}, \tag{4.27}$$

where $\alpha = \sqrt[3]{j_r/2}$. A and B are the Airy functions, and A and B their first derivative; c_1 and c_2 are integration constants. Although (4.27) looks analytical, it does not allow a direct computation of the current-voltage curve of the diode, because the integration constants c_1 and c_2 must be estimated for each value of the reduced current j_r.

The following relationship between Airy's functions

$$\mathrm{A}_i^{''}(z) = z\mathrm{A}_i(z), \tag{4.28}$$

$$\mathrm{B}_i^{''}(z) = z\mathrm{B}_i(z), \tag{4.29}$$

can be used to write the reduced hole density $p_r = \mathrm{d}F_r/\mathrm{d}x_r$ as:

$$p_r = \frac{{F_r}^2}{2} - j_r x_r - 2\alpha^2 c_1. \tag{4.30}$$

Equation (4.30) can now be used to estimate the integration constants. In a first step, we write the values of the reduced hole density at the anode and cathode. Assuming a quasi-equilibrium, we postulate that these values are those at thermodynamic equilibrium (no overall current). This leads at the anode ($x_r = 0$):

$$p_{r0} = 2\alpha^2 \left\{ \left[\frac{c_2 \mathrm{A}_i^{'}(c_1) + \mathrm{B}_i^{'}(c_1)}{c_2 \mathrm{A}_i(c_1) + \mathrm{B}_i(c_1)} \right]^2 - c_1 \right\}, \tag{4.31}$$

or:

$$c_2 = -\frac{\mathrm{B}_i^{'}(c_1) - P_0 \mathrm{B}_i^{'}(c_1)}{\mathrm{A}_i(c_1) - P_0 \mathrm{A}_i(c_1)} \tag{4.32}$$

$$P_0 = \pm\sqrt{c_1 + \frac{p_{r0}}{2\alpha^2}}. \tag{4.33}$$

A similar equation is obtained at the cathode ($x_r = 1$):

$$c_2 = -\frac{\mathrm{B}_i^{'}(c_1+\alpha) - P_1 \mathrm{B}_i^{'}(c_1+\alpha)}{\mathrm{A}_i(c_1+\alpha) - P_1 \mathrm{A}_i(c_1+\alpha)} \tag{4.34}$$

$$P_1 = \pm\sqrt{c_1 + \frac{j_r + p_{r1}}{2\alpha^2}} = \pm\sqrt{c_1 + \alpha + \frac{p_{r1}}{2\alpha^2}}. \tag{4.35}$$

The sign in front of the square root in (4.33) and (4.35) depends on the orientation of the electric field at $x = 0$ and $x = d$. The constant c_1 is now obtained by eliminating c_2 between (4.32) and (4.34):

$$\begin{aligned} \Big[\mathrm{B}_i^{'}(c_1) - P_0 \mathrm{B}_i^{'}(c_1)\Big] \Big[\mathrm{A}_i(c_1+\alpha) - P_1 \mathrm{A}_i(c_1+\alpha)\Big] - \\ \Big[\mathrm{A}_i^{'}(c_1) - P_0 \mathrm{A}_i(c_1)\Big] \Big[\mathrm{B}_i^{'}(c_1+\alpha) - P_1 \mathrm{B}_i^{'}(c_1+\alpha)\Big] = 0. \end{aligned} \tag{4.36}$$

The electrical potential is obtained by integrating (4.27) between 0 and x_r:

$$V_r = -2\ln\frac{c_2 \mathrm{A}_i^{'}(c_1+\alpha x_r) + \mathrm{B}_i^{'}(c_1+\alpha x_r)}{c_2 \mathrm{A}_i(c_1) + \mathrm{B}_i(c_1)}, \tag{4.37}$$

Replacing c_2 by its value in (4.34) leads to:

$$V_r = -2\ln\pi \left[\mathrm{B}_i^{'}(c_1) - P_0\mathrm{B}_i(c_1)\right] \mathrm{A}_i(c_1+\alpha x_r) - \left[\mathrm{A}_i^{'}(c_1) - P_0\mathrm{A}_i(c_1)\right] \mathrm{B}_i(c_1+\alpha x_r), \tag{4.38}$$

where we used: $\mathrm{A}_i(z)\mathrm{B}_i^{'}(z) - \mathrm{A}_i^{'}(z)\mathrm{B}_i = 1/\pi$. The applied voltage V is connected to the reduced potential through $V_\mathrm{d} = V_T V_r(d) = V - V_\mathrm{d}$.

Approximate solution: Asymptotic form of Airy function

The use of the exact equations to calculate the electrical potential and integration constant becomes problematic at low applied voltages because the value of the constant c_1 becomes positive and large, so the second Airy function $\mathrm{B_i}$ and its first derivative diverge. To work around this issue, we develop in this appendix an analytical approximation of the equations at low current.

First, let us recall the asymptotic form of the Airy functions:

$$\mathrm{A_i}(z) \sim \frac{\exp\left(-\frac{2}{3}z^{3/2}\right)}{2\sqrt{\pi}\sqrt[4]{z}}, \tag{4.39}$$

$$\mathrm{A_i^{'}}(z) \sim \frac{\sqrt[4]{z}}{2\sqrt{\pi}}\exp\left(-\frac{2}{3}z^{3/2}\right), \tag{4.40}$$

$$\mathrm{B_i}(z) \sim \frac{\exp\left(\frac{2}{3}z^{3/2}\right)}{\sqrt{\pi}\sqrt[4]{z}}, \tag{4.41}$$

$$\mathrm{B_i^{'}}(z) \sim \frac{\sqrt[4]{z}}{\sqrt{\pi}}\exp\left(\frac{2}{3}z^{3/2}\right). \tag{4.42}$$

The asymptotic form of the ratios $\mathrm{A_i^{'}}(z)/\mathrm{A_i}(z)$ and $\mathrm{B_i^{'}}(z)/\mathrm{B_i}(z)$ write:

$$\frac{\mathrm{A_i^{'}}(z)}{\mathrm{A_i}(z)} \sim -\sqrt{z}, \tag{4.43}$$

$$\frac{\mathrm{B_i^{'}}(z)}{\mathrm{B_i}(z)} \sim \sqrt{z}, \tag{4.44}$$

We can also write the asymptotic forms of the products of Airy functions as:

$$\mathrm{A_i}(z)\mathrm{B_i}(z) \sim \frac{1}{2\pi\sqrt{z}}, \tag{4.45}$$

$$\mathrm{A_i^{'}}(z)\mathrm{B_i}(z) \sim -\frac{1}{2\pi}, \tag{4.46}$$

$$\mathrm{A_i}(z)\mathrm{B_i^{'}}(z) \sim \frac{1}{2\pi}, \tag{4.47}$$

$$\mathrm{A_i^{'}}(z)\mathrm{B_i^{'}}(z) \sim -\frac{\sqrt{z}}{2\pi}, \tag{4.48}$$

Finally, developing in first of order in α/c_1 leads to:

$$(c_1 + \alpha x_r)^{3/2} \simeq c_1^{3/2} + \frac{3}{2}\sqrt{c_1}\alpha x_r, \tag{4.49}$$

so we can write the asymptotic form of Airy function at $c_1 + \alpha$ as:

$$\mathrm{A_i}(c_1 + \alpha) \sim \mathrm{A_i}(c_1)\exp\left(-\sqrt{c_1}\alpha x_r\right), \tag{4.50}$$

$$\mathrm{A_i^{'}}(c_1 + \alpha) \sim \mathrm{A_i^{'}}(c_1)\exp\left(-\sqrt{c_1}\alpha x_r\right), \tag{4.51}$$

$$\mathrm{B_i}(c_1 + \alpha) \sim \mathrm{B_i}(c_1)\exp\left(\sqrt{c_1}\alpha x_r\right), \tag{4.52}$$

$$\mathrm{B_i^{'}}(c_1 + \alpha) \sim \mathrm{B_i^{'}}(c_1)\exp\left(\sqrt{c_1}\alpha x_r\right), \tag{4.53}$$

Approximate solution: Electrical potential

Using the asymptotic forms of Airy's functions, (4.38) writes:

$$\begin{aligned} V_r(x_r) &= 2\ln\pi\Big\{ \left[\mathrm{B_i^{'}}(c_1) - P_0\mathrm{B_i}(c_1)\right]\mathrm{A_i}(c_1 + \alpha x_r) - \\ &\qquad \left[\mathrm{A_i^{'}}(c_1) - P_0\mathrm{A_i}(c_1)\right]\mathrm{B_i}(c_1 + \alpha x_r)\Big\}, \\ &= 2\ln\pi\left[(\sqrt{c_1} - P_0)\mathrm{B_i}(c_1)\mathrm{A_i}(c_1 + \alpha x_r) - (-\sqrt{c_1} - P_0)\mathrm{A_i}(c_1)\mathrm{B_i}(c_1 + \alpha x_r)\right], \\ &= 2\ln\pi\frac{1}{2\pi}\left[\left(\frac{P_0}{\sqrt{c_1}} + 1\right)\exp\left(\sqrt{c_1}\alpha x_r\right) - \left(\frac{P_0}{\sqrt{c_1}} - 1\right)\exp\left(-\sqrt{c_1}\alpha x_r\right)\right], \\ &= 2\ln\left[\cosh\sqrt{c_1}\alpha x_r + \sqrt{1 + \frac{p_{r0}}{2c_1\alpha^2}}\sinh\sqrt{c_1}\alpha x_r\right]. \end{aligned} \tag{4.54}$$

Note that (4.54) is similar to the potential at zero current (4.28) where the integration constant g is replaced by $c_1\alpha$. Hence we deduce that as the current tends to zero, $c_1\alpha^2 \longrightarrow g^2$.

Approximate solution: Integration constant c_1

At low current, the value of c_1 becomes large and that of the current reduces; we can therefore neglect α and rewrite Equation (4.36) as follows:

$$\left[\frac{\mathrm{B_i'}(c_1)}{\mathrm{B_i}(c_1)} - P_0\right]\left[\frac{\mathrm{A_i'}(c_1)}{\mathrm{A_i}(c_1)} - P_0\right]\mathrm{B_i'}(c_1)\mathrm{A_i'}(c_1+\alpha) = \left[\frac{\mathrm{A_i'}(c_1)}{\mathrm{A_i}(c_1)} - P_0\right]\left[\frac{\mathrm{B_i'}(c_1)}{\mathrm{B_i}(c_1)} - P_0\right]\mathrm{A_i'}(c_1)\mathrm{B_i'}(c_1+\alpha). \tag{4.55}$$

Next, we approximate (4.35) as:

$$P_1 \simeq \sqrt{c_1}\sqrt{\frac{p_{r1}}{2\alpha^2}c_1 + 1} \simeq \sqrt{c_1}\left(1 + \frac{p_{r1}}{4\alpha^2 c_1}\right). \tag{4.56}$$

At this stage, we also need a further development of the asymptotic form of $\mathrm{B_i'}/\mathrm{B_i}$. A useful form was recently derived Kearney and Martin [164]:

$$\frac{\mathrm{B_i'}(z)}{\mathrm{B_i}(z)} \sim \sqrt{z} - \frac{1}{4z}, \tag{4.57}$$

which lead us to the final result:

$$(P_0 - \sqrt{c_1})\frac{\exp(-\sqrt{c_1}\alpha)}{\pi} = (P_0 - \sqrt{c_1})\left(\frac{p_{r1}}{\alpha^2} + \frac{1}{\sqrt{c_1}}\right)\frac{\exp(\sqrt{c_1}\alpha)}{8\pi c_1} \tag{4.58}$$

4.1.5 Space-charge limited current

A useful approximation of the drift-diffusion model was first introduced by Mott [165], which consists of neglecting the diffusion component of the current. The SCLC regime becomes valid at high applied voltage, and also requires strong charge carrier injection at the anode.

Neglecting the diffusion term leads to the following equation:

$$j = \epsilon\mu F\frac{\mathrm{d}F}{\mathrm{d}x}, \tag{4.59}$$

which can be integrated to:

$$F^2 = \frac{2j}{\epsilon\mu}x + C. \tag{4.60}$$

The integration constant C can be determined by establishing the hole concentration at the anode to $p(0) = p_0 = N_0/2 \cdot \mathrm{erfc}(E_{\mathrm{bp}}/\sqrt{2}\sigma)$ under degenerate condition:

$$p(x) = \frac{\epsilon}{q}\frac{\mathrm{d}F}{\mathrm{d}x} = \frac{j}{q\mu}\left(\frac{2j}{\epsilon\mu}x + C\right)^{-1/2}, \tag{4.61}$$

$$p(0) = \frac{j}{q\mu\sqrt{C}}, \tag{4.62}$$

$$C = \left(\frac{j}{q\mu p_0}\right)^2. \tag{4.63}$$

The potential a point at a distance x of the anode is obtained by integrating the electric field from the anode to this point:

$$V(x) = \int_0^x F(t)\mathrm{d}t = \frac{\epsilon\mu}{3j}\left[\left(\frac{2j}{\epsilon\mu}x + C\right)^{3/2} - C^{3/2}\right]. \tag{4.64}$$

In the Mott and Gurney model, there is no limitation to injection, so $C \to 0$ ($p_0 \to \infty$). Writing (4.64) at $x = d$ leads to the well-known equation:

$$j = \frac{9}{8}\epsilon\mu\frac{(V - V_\mathrm{d})^2}{d^3}. \tag{4.65}$$

The SCLC model describes the current as quadratic function of applied voltage.

In the opposite case, when the hole concentration at the anode becomes low, one can develop the first term in the bracket to the first power of x:

$$V(x) = \frac{\epsilon\mu}{3j}C^{3/2}\left(\frac{3}{2}\frac{2jx}{\epsilon}\right) = \sqrt{C}x, \tag{4.66}$$

and the current now writes:

$$j = -q\mu p_0\frac{V - V_\mathrm{d}}{d}, \tag{4.67}$$

which indicates the linear relationship between the current density and the applied voltage $J \sim V$. Note that both (4.65) and (4.67) are valid only when $V > V_\mathrm{d}$.

4.1.6 Validity of the MIM model

Potential profile

The first step consisted of calculating the electric field profile $F(x)$ for given values of the current, from which the potential and charge carrier density profiles were obtained through numerical integration and derivation, respectively. The parameters used for the calculations are gathered in Table 4.1.

The calculated potential profiles of the MIM diode for various values of the applied voltage are shown in Figure 4-7. It appears clearly is that the MIM approximation, that is, a linear variation of the potential with distance, is only valid in the case of a high injection barrier ($E^{\mathrm{eff}}_{\mathrm{bp.an}} = 0.46$ eV). When the injection barrier is lower ($E^{\mathrm{eff}}_{\mathrm{bp.an}} = 0.26$ eV), a slight curvature appears at the anode ($x = 0$) due to the accumulation of holes at this electrode. Also, the upward curvature of

Table 4.1: Parameters used for the calculation of the voltage profile and the current density-voltage characteristics of a MIM diode. ϵ_0 is the vacuum permittivity.

Parameters	Values	Units
Temperature, T	300	K
Permittivity, ϵ	$3.9\times\epsilon_0$	$\mathrm{F\cdot cm^{-1}}$
Mobility, μ	8.5×10^{-7}	$\mathrm{cm^2V^{-1}s^{-1}}$
Total density-of-states (DOS), N_0	3×10^{21}	$\mathrm{cm^{-3}}$
Width of a Gaussian DOS, σ	0.15	eV
Hole injection barrier, E_{bp}	0.7 or 0.9	eV
Effective hole injection barrier, $E_{\mathrm{bp}}^{\mathrm{eff}}$	0.26 or 0.46	eV
Diffusion potential, V_{d}	0.6	V
Semiconductor thickness d,	500	nm

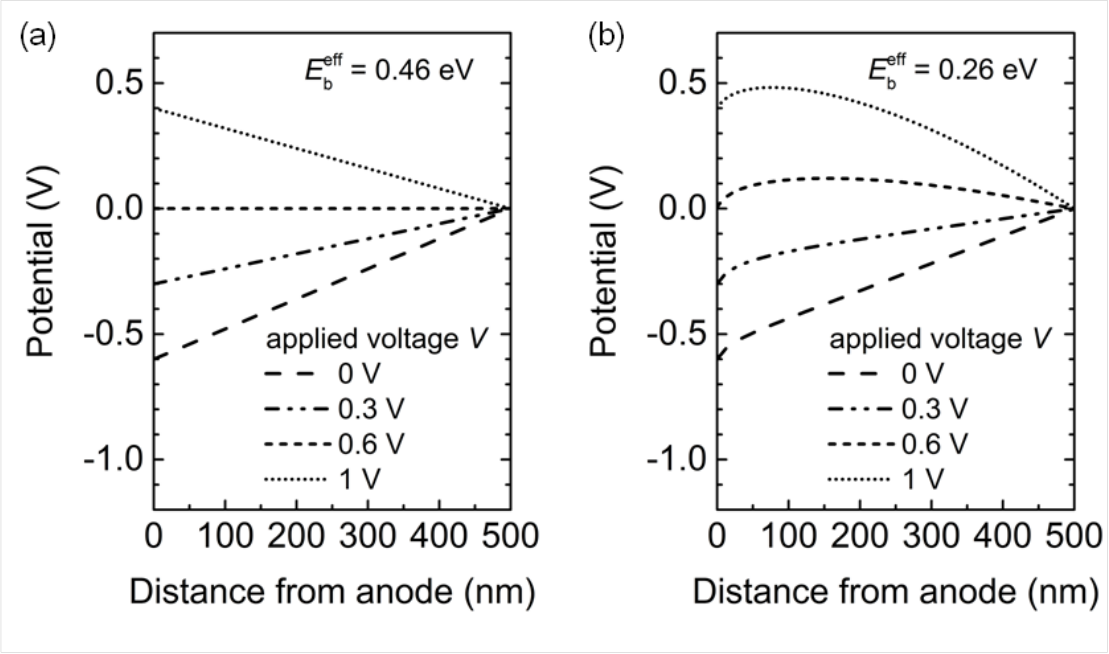

(a)

Figure 4-7: Calculated potential profile of a MIM diode with the parameters listed in Table 4.1 at various applied voltages and for an injection barrier at the anode of (a) 0.46 and (b) 0.26 eV. The applied voltage is varied from 0, 0.3, 0.6 and 1 V.

the potential profile gets more pronounced as the applied voltage increases in the forward bias regime ($V > 0$).

Current density-voltage characteristics

Calculated current-voltage curves of MIM diodes with an effective injection barrier at the anode of 0.46 and 0.26 eV are drawn in Figure 4-8 and Figure 4-9, respectively. The exact MIM model is in good agreement with the MIM model (Schottky's theory) for a hole injection barrier of 0.46 eV, that is, when injection efficiency is poor. In this case, the quadratic dependence of the current density with voltage predicted by (4.65) does not appear at high applied voltage evidenced by the slope of the double-logarithmic plot inferior to 2. On the other hand, a linear relationship $J \sim V$ in (4.67) is observed between the current density and applied voltage.

When improving charge carrier injection by lowering the injection barrier to 0.26 eV, the agreement remains good in the early injection regime ($V \ll \mathrm{V_d}$. However, the discrepancy becomes non negligible and the curve deviates from exponential function as V approaches V_d. The discrepancy becomes nearly two order of magnitude in strong injection, when the applied voltage is in excess of the diffusion potential. A double logarithmic scale plot of the strong injection regime is shown in Figure 4-9(b). Interestingly, the exact MIM curve merge with the SCLC current at high voltages, at variance with the diode having weaker injecting contact. Therefore, it can be inferred that the MIM model overestimates the diode current when injection is efficient.

It is worth mentioning that the rectification ratio decreases by ~ 10 as the injection at the anode is improved. This is because, when the diffusion potential is kept constant, the injection barrier at the cathode is lowered simultaneously by lowering that at anode, and that the increase in the reverse bias current by $\sim 10^3$ is greater than the increase in the forward bias current by $\sim 10^2$ reducing the rectification ratio by ~ 10.

Strong and weak injecting contacts

As illustrated by Figure 4-9, two distinct cases can be separated, depending on the injection barrier height: weak injection (high barrier) and strong injection (low barrier). In the former case, the organic semiconductor behaves as a perfect insulator; the voltage profile remains perfectly linear, including in the forward bias regime, when current is flowing through the diode. In this particular case,

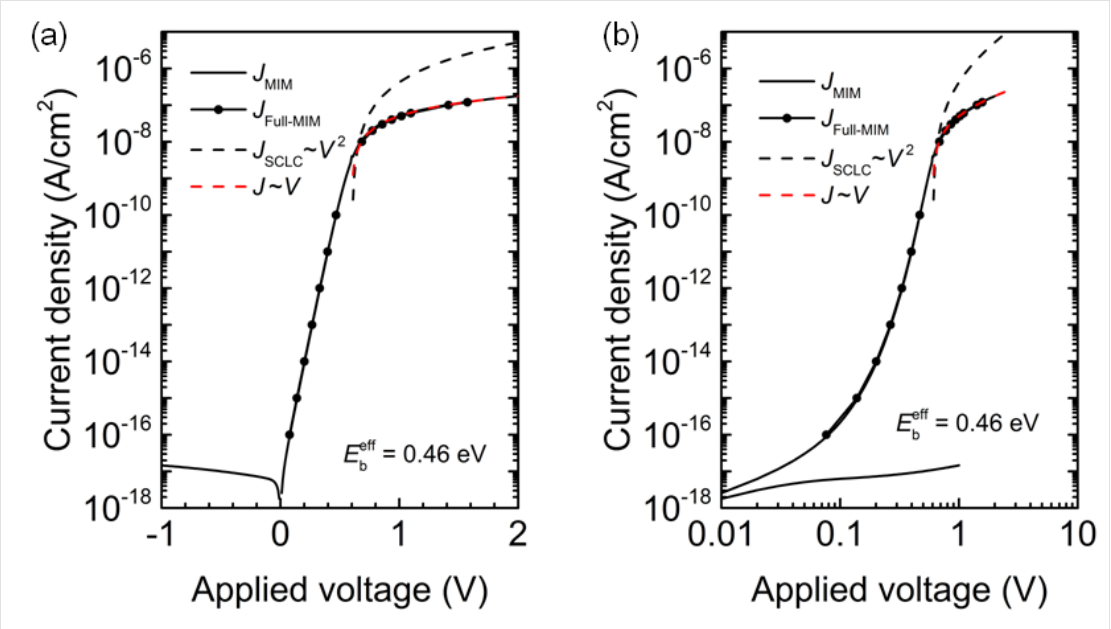

Figure 4-8: $J - V$ curve for a MIM diodes with the parameters in Table 4.1 and a effective hole injection barrier of 0.46 eV. The solid line correspond to the MIM model, filled circles to the data numerically calculated from the full MIM model, and the dashed lines to the space-charge limited current (SCLC) model (in black) and the linear model $J \sim V$ (in red).

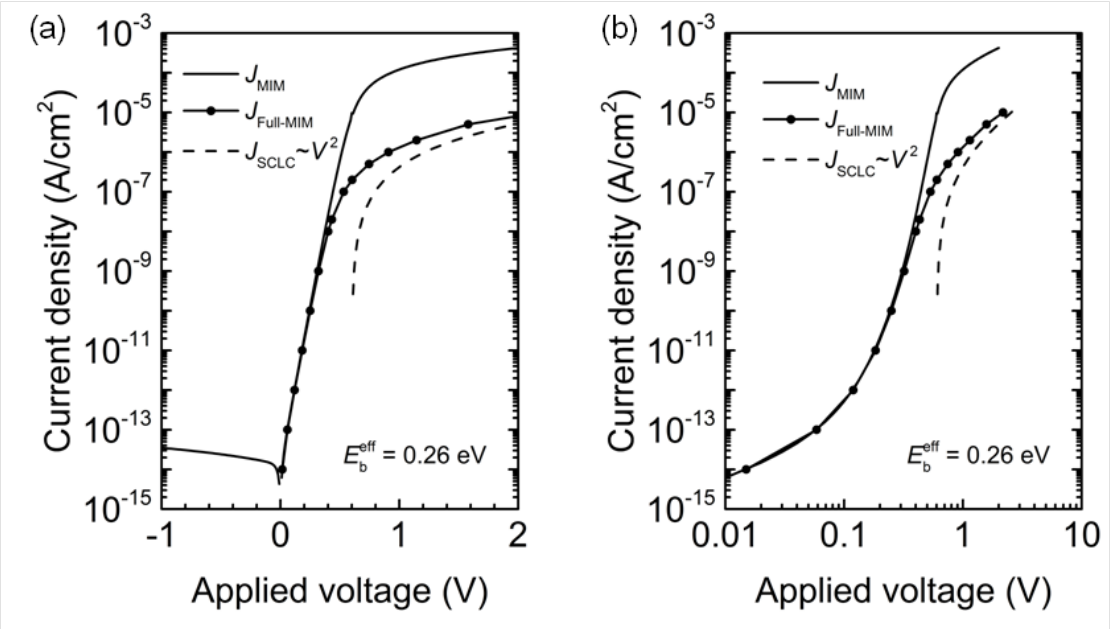

Figure 4-9: $J - V$ curve for a MIM diodes with the parameters in Table 4.1 and a effective hole injection barrier of 0.26 eV. The solid line correspond to the MIM model, filled circles to the data numerically calculated from the full MIM model, and the dashed line to the space-charge limited current (SCLC) model.

Schottky's theory leads to a current that is in perfect agreement with the full MIM calculation in all regimes. It is worth pointing out that, in agreement with our calculation, poor injection also prevents SCLC to occur at high applied voltages. Accordingly, the current at high voltage is proportional to the voltage rather than the voltage to the square.

For a diode with good hole injection, the agreement of Schottky's theory with the full MIM model restricts to weak injection, when the applied voltage is lower than the diffusion potential. At higher voltages, the current predicted by Schottky's theory in overestimated by nearly a factor of 100. This discrepancy is accompanied by two important points. First, apart from a slight curvature near the anode due to hole accumulation, the voltage profile only remains linear in the weak injection regime ($V < V_d$). In the strong inversion regime, the profile presents an upward curvature. This observation can be associated with the fact that under strong injection, the MIM current merges with the SCLC regime, with a current that is now proportional to the voltage to the square.

We remind an important message from Figure 4-6 which showed that the effective injection barrier reduces not only when the Fermi level approach the $HOMO_{max}$ but also when disorder becomes larger. In other words, injection at the contact can be facilitated by the localised states that extend into the band gap. This is an exemplary illustration on the critical role of disorder on charge injection. The result provides a strong necessity to study the effect of disorder on charge transport.

4.2 Full MIM model with enhanced drift-diffusion

In the previous section, the mobility and diffusion coefficeint were assumed constant. On the other hand, it is shown that disorder contributes to the enhancement of drift and diffusion current [32,166,167]. First, Tessler and co-workers [166] showed that disorder can give rise to an enhancement of the diffusion coefficient above the value expected from the classical Einstein relation $D/\mu = k_B T/q$, and provided an implicit relation between the diffusion coefficient and the mobility, namely the generalized Einstein relation, for the case of a Gaussian DOS. Second, the charge carrier concentration dependence of mobility were experimentally observed from both organic transistors and diodes. Vinssenberg and Matters [168] correlated the gate voltage dependence of the field-effect mobility with the gate voltage induced charge concentration, and formulated a relationship between the charge concentration on the mobility assuming an exponential DOS. Blom and co-workers explained the enhanced space-charge limited current of organic light-

emitting diodes (with the slope of the double logarithmic plot larger by the charge carrier concentration dependence of mobility [114, 169].

Roichman *et al.* were the first to incorporate both effects of disorder on the mobility and the diffusion coefficient in modelling of single-carrier sandwich-type devices [170]. However, the model used in [170] for quantifying the carrier density dependence of the mobility did not consider the percolative nature of the hopping transport that results in the strong temperature dependence of the mobility [171]. Recently, Pasveer *et al.* developed a model that correctly includes the effects of percolation on the mobility, and demonstrated that in the 'drift-dominated' high-voltage regime the temperature dependence of the current density in PPV-based hole-only devices can be described well assuming Gaussian disorder [32]. However, in their device model, the 'diffusion' contribution to the current density was neglected. More recently, the theoretical method to incorporate the contribution of the diffusion current in a sandwich-type device was presented by Mensfoort and Coehoorn [167]. Nonetheless, experimental validation of the model still rests on high voltage [172], and especially the comparison between the model and the experimental data in low applied voltage regime is still lacking.

The discussion in the rest of this chapter for extending the work of Mensfoort and Coehoorn is focused on provision of the experimental evidence for two effects of disorder on the enhancement of the diffusion coefficient and the carrier concentration and field dependence of the mobility in organic rectifying diodes. The experimental and modelled $J-V$ characteristics are compared for the reverse bias regime as well as the low voltage forward bias regime where the diffusion current is not negligible.

4.2.1 Enhancement of mobility and diffusion coefficient

The enhancement of drift in a disordered system is described by the variable mobility. In essence, the variable mobility model in (4.68) by Pasveer is an analytical equation that reproduces the temperature, charge carrier concentration and electric field dependence of mobility theoretically given by the solution of the hopping transport equation based on Monte Carlo simulation: $\sum_{ji}[\nu_{ij}p_i(1-p_j)-\nu_{ji}p_j(1-p_i)]=0$, p_i and $1-p_i$ being the probability of occupancy and vacancy of the site i by a charge and ν_{ij} being the transition rate for hopping from site i to j [106]:

$$\mu(T,p,F)=\mu_0(T)\times g_1(p,T)\times g_2(F,T). \tag{4.68}$$

Here, $\mu_0(T)$ describes the pure temperature dependence of mobility which is

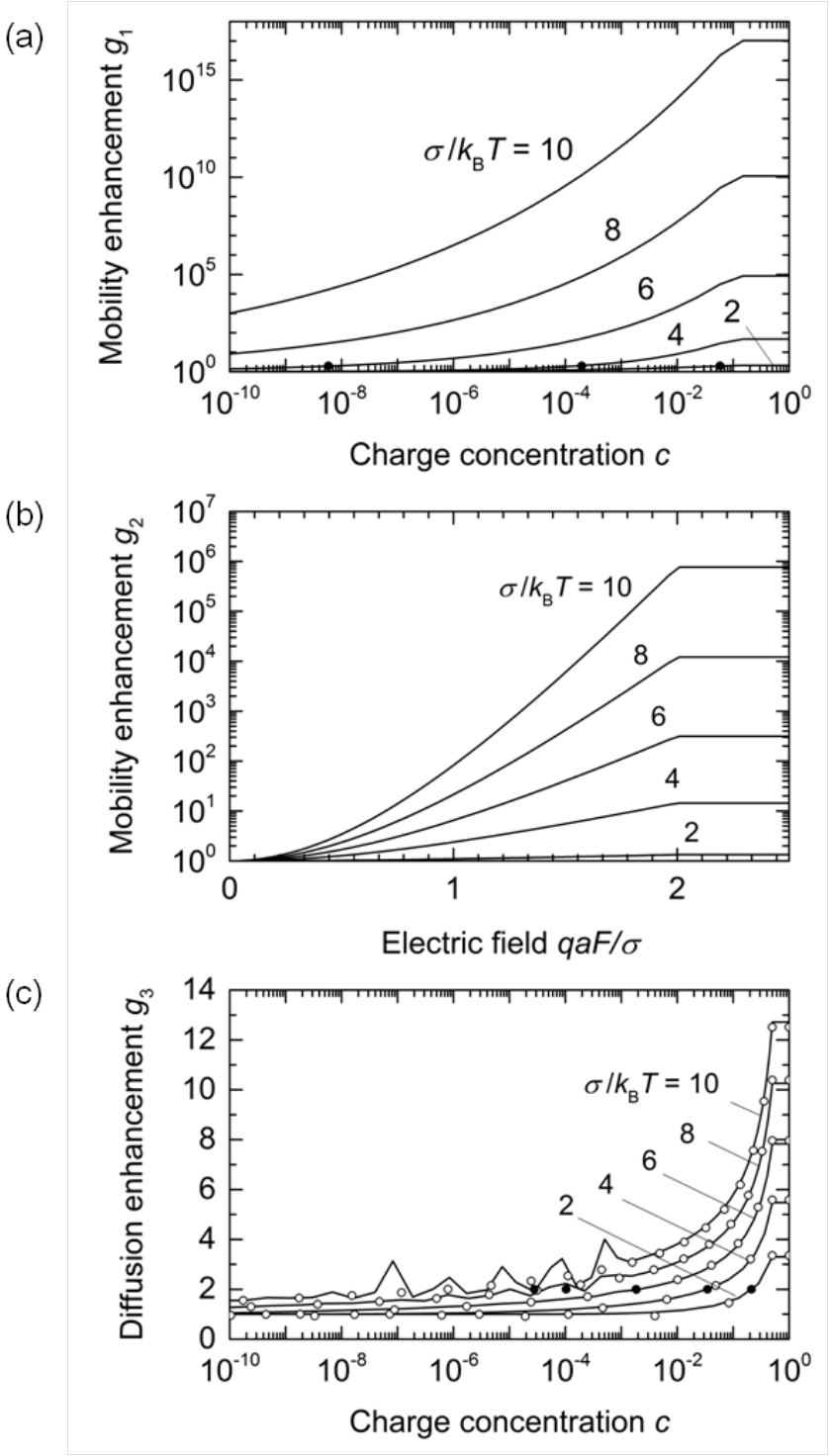

Figure 4-10: Enhancement factors for a Gaussian DOS with dimensionless widths $\hat{\sigma} = \sigma_B T = 2$, 4, 6, 8 and 10: mobility enhancement by (a) the charge carrier concentration and (b) by the electric field, and (c) diffusion enhancement by the charge carrier concentration. The filled circles in (a) and (c) indicate the concentration where the mobility and diffusion coefficient are enhanced by a factor of 2. The open circles in (c) represents values calculated by a robust semianalytical expression in (4.77)-(4.79). Compared to the direct numerical calculation (solid lines) by (4.75)-(4.76), the calculation error is reduced over a wider range of disorder and charge concentration.

given by $\mu_0(T) = \mu(0)c_1\exp(-c_2\hat{\sigma}^2)$ with parametrization constants $c_1 = 1.8 \times 10^9$ and $c_2 = 0.42$. g_1 and g_2 are the drift enhancement factor (i.e. mobility enhancement) by the hole concentration and the electric field:

$$g_1(c,T) = \begin{cases} \exp\left[\frac{1}{2}\left(\hat{\sigma}^2 - \hat{\sigma}\right)(2c)^{\delta}\right] & \text{c} \leqq 0.1 \quad (4.69) \\ g_1(0.1,T) & \text{c} > 0.1, \quad (4.70) \end{cases}$$

and

$$g_2(F,T)$$

$$= \begin{cases} \exp\left[0.44\left(\hat{\sigma}^{3/2} - 2.2\right)\left\{\sqrt{1 + 0.8\left(\frac{qaF}{\sigma}\right)^2} - 1\right\}\right] & F \leqq \frac{2\sigma}{qa} \quad (4.71) \\ g_2\left(\frac{2\sigma}{qa}, T\right) & F > \frac{2\sigma}{qa}, \quad (4.72) \end{cases}$$

where δ is a constant related with the degree of disorder

$$\delta = 2\frac{\ln(\hat{\sigma}^2 - \hat{\sigma}) - \ln(\ln 4)}{\hat{\sigma}^2} \quad (4.73)$$

with $\hat{\sigma} = \sigma/kT$, $c = p/a^3$, a is the lattice constant and E_F is the Fermi energy. In the limit of vanishing hole concentration and electric field, we recover the $\mu \propto \exp(-c\hat{\alpha}^2)$ temperature dependence by Bassler *et al.*

As shown in Figure 4-10(a) and (b), the enhancement by charge concentration and electric field is more pronounced when disorder (represented by σ) is larger, resulting in the difference of enhancement factor (hence mobility) by several orders of magnitude. For a fixed disorder, the mobility enhancement factors monotonously increase with charge concentration and electric field. We note that both enhancement factors converge to unity at low charge concentration and electric field (when $c \to 0$ and $F \to 0$). Therefore, mobility enhancement is negligible when disorder is small, and drift-diffusion current reduces to the Full MIM model (in section 4.1.4.).

The generalized Einstein relation derived from the drift-diffusion equation quantitatively describes the diffusion enhancement:

$$D(p,F,T) = \frac{k_B T}{q}\mu(p,F,T) \times g_3(p,T) \quad (4.74)$$

with a diffusion enhancement factor g_3 which writes

$$g_3(c,T) = \frac{1}{k_\mathrm{B}T}\frac{c}{\left.\frac{\mathrm{d}c'}{\mathrm{d}E_\mathrm{F}}\right|^{c}}$$

$$= \begin{cases} \dfrac{\displaystyle\int_{-\infty}^{\infty} \frac{\exp\left(-\left(\frac{E_r}{\sqrt{2}\hat{\sigma}}\right)^2\right)}{1+\exp\left(-\left(E_r - E_{Fr}(c,T)\right)\right)}\mathrm{d}E_r}{\displaystyle\int_{-\infty}^{\infty} \frac{\exp\left(-\left(\frac{E_r}{\sqrt{2}\hat{\sigma}}\right)^2\right)\exp\left(-\left(E_r - E_{Fr}(c,T)\right)\right)}{\left[1+\exp\left(-\left(E_r - E_{Fr}(c,T)\right)\right)\right]^2}\mathrm{d}E_r} & c \leqq 0.5 \qquad (4.75) \\ g_3(0.5,T) & c > 0.5, \qquad (4.76) \end{cases}$$

where E_r is the dimensionless reduced energy $E_r = E/(k_\mathrm{B}T)$, E_{Fr} is the dimensionless reduced Fermi energy $E_{Fr} = E_F/(k_\mathrm{B}T)$.

As shown in Figure 4-10(c), the diffusion enhancement factor increases with the charge carrier concentration, and shows asymptotic behaviour at low charge carrier concentration. In addition, similar to the mobility enhancement, the diffusion enhancement gets more pronounced when the semiconductor is more disordered. Note, on the other hand, that the diffusion enhancement factor g_3 is less significant than mobility enhancement factor by charge carrier concentration g_1 referring to the filled circles in Figure 4-10(a) and (c) that indicate the carrier concentrations c at which the mobility and diffusion coefficient are enhanced by a factor of 2. Moreover, the mobility enhancement shows a more drastic increase (by several orders) than the diffusion enhancement.

Lastly, we would like to comment on the precision of numerical calculation for diffusion enhancement factor g_3. In (4.75), the integral with infinite upper and lower limits appears on both sides of a fraction. As shown by the solid lines in Figure 4-10(c), the error for this type of numerical calculation is not robust for a wide range of disorder. In particular, the error becomes severe when disorder gets higher. We propose a robust alternative expression for the diffusion enhancement factor adopting the semi-analytical expression for the charge carrier concentration by Paasch [95]:

$g_3(c,T)$

$$= \begin{cases} \left[1 + \dfrac{K(\hat{\sigma})\exp\left\{-K(\hat{\sigma})(E_{Fr}(c,T) - \hat{\sigma}^2)\right\}}{1 + \exp\left\{-K(\hat{\sigma})(E_{Fr}(c,T) - \hat{\sigma}^2)\right\}}\right]^{-1} & 0 < c \leqq \exp\left(-\dfrac{\hat{\sigma}^2}{2}\right) \quad (4.77) \\ \dfrac{\dfrac{1}{2}\mathrm{erfc}\left(\dfrac{E_{Fr}(c,T)}{\sqrt{2}\hat{\sigma}}H(\hat{\sigma})\right)}{\dfrac{H}{\sqrt{2\pi}\hat{\sigma}}\exp\left\{-\left(\dfrac{E_{Fr}(c,T)}{\sqrt{2}\hat{\sigma}}H(\hat{\sigma})\right)^2\right\}} & \exp\left(-\dfrac{\hat{\sigma}^2}{2}\right) < c \leqq 0.5 \quad (4.78) \\ g_3(0.5,T) & c > 0.5, \quad (4.79) \end{cases}$$

where $\mathrm{erfc}(x)$ is a complementary error function and $H(\hat{\sigma})$ and $K(\hat{\sigma})$ are the transition function between degenerate and non-degenerate regime given in (2.13) and (2.14). As shown in Figure 4-10(c), the above analytical expression (open circles) enable a more precise calculation of diffusion enhancement factor for a wider range of disorder and charge carrier concentration than the direct resolution (solid lines) by (4.75)-(4.76).

4.2.2 Calculation method

We solve the drift-diffusion equation (5.47) considering the enhancement of drift and diffusion:

$$j = q\mu(x)p(x)F(x) - qD(x)\frac{\mathrm{d}p(x)}{\mathrm{d}x} \tag{4.80}$$

Now, mobility μ and diffusion coefficient D is regarded as a function of position x.

Then, using the same dimensionless parameters in (4.23) and two additional scaled dimensionless field and concentration parameters $f = F_r/j_r^{1/3}$ and $y = p_r/j_r$, the coupled Poisson's and drift-diffusion equation (4.24) becomes

$$\frac{\mathrm{d}y}{\mathrm{d}f} = \frac{f}{g_3\left[n(y)\right]} - \frac{1}{g_1\left[n(y)\right] \times g_2\left[F(f)\right] \times g_3\left[n(y)\right] \times y}. \tag{4.81}$$

The above equation is solved by numerical calculation to find $f(y)$, from which the current density, potential and carrier concentration across the device can be obtained analytically from following equations:

$$j_r = \left(\int_{f_1}^{f_2} \frac{1}{y(f)}\mathrm{d}f\right)^3 = \left(\int_{f_1}^{f_2} \frac{1}{y(f)}\frac{\mathrm{d}f}{\mathrm{d}y}\mathrm{d}y\right)^3$$

$$= \left(\int_{f_1}^{f_2} \frac{g_1 g_2 g_3}{g_1 g_2 y f(y) - 1} \mathrm{d}f \right)^3, \tag{4.82}$$

$$V_r = V_{d.r} + \int_{y_2}^{y_1} \frac{g_1(y) g_2[f(y)] g_3(y) f(y)}{1 - g_1(y) g_2[f(y)] y f(y)} \mathrm{d}y, \tag{4.83}$$

$$x_r = \int_{y}^{y_1} \frac{g_1(y') g_2[f(y')] g_3(y')}{1^{3/2}[1 - g_1(y') g_2[f(y')] y' f(y')]} \mathrm{d}y', \tag{4.84}$$

where $V_{d.r}$ is the dimensionless diffusion potential given by $V_{d.r} = V_\mathrm{d}/V_T$.

In order to achieve a fast convergence during the numerical calculation of (4.81), we used the iterative solution method by Mensfoort and Coehoorn [167]. Such method has been recently integrated in Atlas Silvaco, a numerical simulator based on the finite-element method. We improved the robustness of the convergence in Atlas at higher disorder σ upto 0.30 eV.

The full MIM model with enhanced drift-diffusion indeed requires a numerical calculation at some point. Nonetheless, the model fully captures the physical phenomena occurring in the disordered organic device with a significantly reduced computational power. For an example, compared to the hours of computation time to reproduce the hopping transport by the Monte Carlo simulation, the model can be executed within a few minutes by an ordinary desktop computer. In the following, we will elaborate how accurate this model is and what could be learn from this semi-analytical model in pursuit of a fully analytical model.

4.2.3 Comparison to the experimental diode current

As shown in Figure 4-11, we obtained an excellent agreement between the experimental and modelled current density-voltage characteristics in both semi-logarithmic and double-logarithmic plot. Table 4.2 summarizes the parameters which gave the best fit to the experimental current voltage characteristics. The parameters used for modelling is either measured or taken from the literature values. Amongst them, following parameters were adjusted $\mu_0(300)$ that indicates mobility at 300 K with zero charge carrier concentration and zero field, σ the width of the Gaussian DOS, injection barrier at the anode $E_\mathrm{bp}^\mathrm{an}$ and diffusion voltage V_d. The permittivity ϵ is measured by impedance spectroscopy. The total DOS N_0 is taken from the molecular density of pentacene [93].

In order to find the modelling parameters with a good fit, we considered the operation mechanism of the rectifying diode illustrated in Figure 4-5. First, $\mu_0(300)$ increases the magnitude of the diode current in all regime. Second, σ has the same

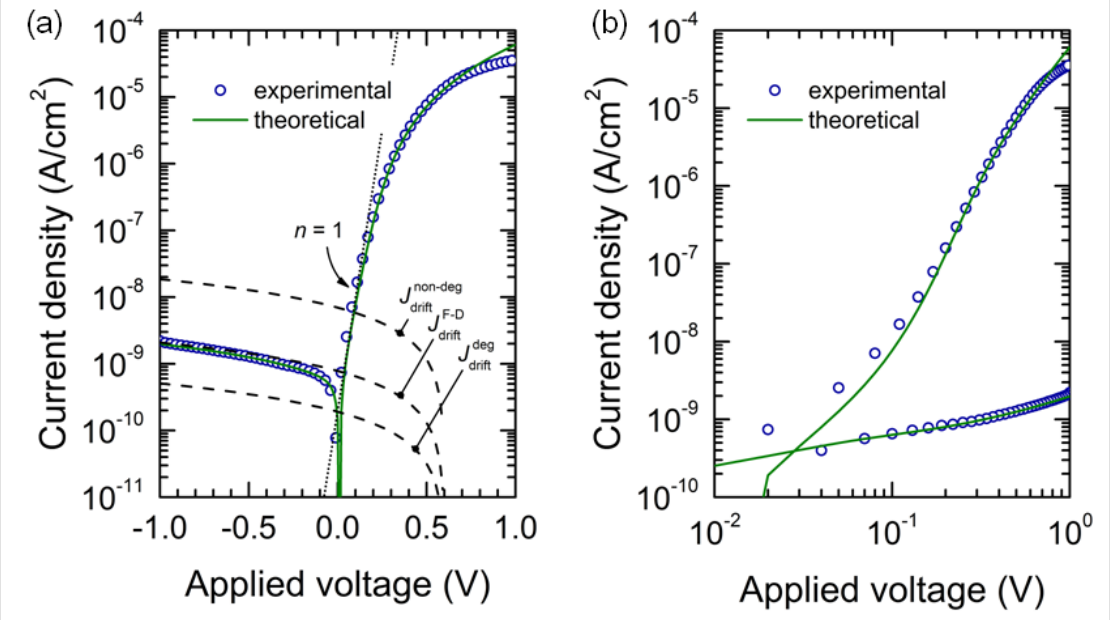

Figure 4-11: Comparison of the current density-voltage characteristics. The symbols represent experimental measurement of the Au/pentacene/Al vertical rectifying diode. The solid line represents the simulation result by the full MIM model with enhanced drift-diffusion. The dashed lines represent the analytical model for reverse bias current with non-degenerate and degenerate approximation and without approximation.

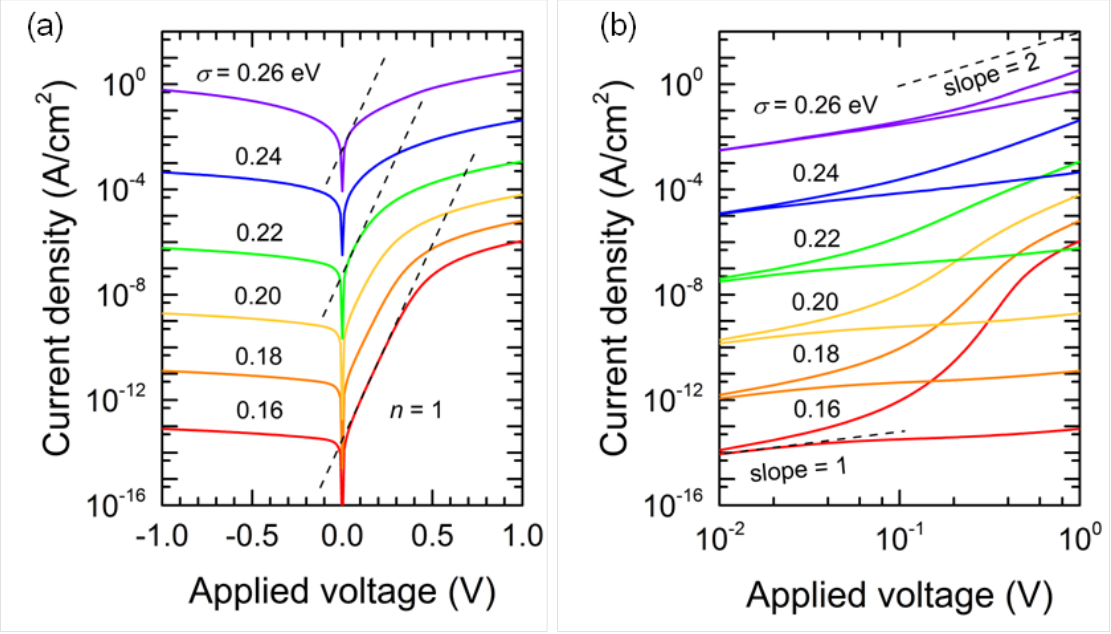

Figure 4-12: Evolution of current density-voltage characteristics upon varying the width of Gaussian DOS. The same parameters in Table 4.2 are used except the width of the Gaussian DOS varied from 0.16, 0.18, 0.20, 0.22 and 0.26 eV.

Table 4.2: Parameters used for modelling which gave the best fit to the experimental current density-voltage characteristics.

Parameters	Values	Units
Temperature, T	300	K
Permittivity, ϵ	$3.9\times\epsilon_0$	$\mathrm{F\cdot cm^{-1}}$
Mobility, μ_{300}	1.27×10^{-7}	$\mathrm{cm^2V^{-1}s^{-1}}$
Total density-of-states (DOS), N_0	3×10^{21}	$\mathrm{cm^{-3}}$
Width of a Gaussian DOS, σ	0.2	eV
Hole injection barrier, $E_{\mathrm{bp.an}}$	0.7	eV
Effective hole injection barrier, $E^{\mathrm{eff}}_{\mathrm{bp.an}}$	0.26	eV
Diffusion potential, V_{d}	0.6	V
Semiconductor thickness, d	500	nm
Device surface area, S	4.3×10^{-4}	$\mathrm{cm^2}$

effect since the injection is facilitated by an increased disorder. In particular, σ increases the forward bias regime current in a greater degree than the reverse bias regime current. It is because charge carriers are injected by forward bias, and the enhancement of mobility and diffusion coefficient by disorder is more significant when the greater number of charge carriers are present. Figure 4-12 illustrates both effect of varying the width of the Gaussian DOS on the current-voltage characteristics. Third, $E_{bp.an}$ affects the magnitude of forward bias current but does not change the reverse bias current. More importantly, it determines the shape of the forward bias current. As discussed in Figure 4-8 and 4-9, a stronger injecting anode results in the loss of exponential current density-voltage characteristics. Based on the definition of effective injection barrier, increasing disorder leads to lowering of injection barrier. Figure 4-12 clearly illustrates 'vanishing' the unity ideality factor. We would like to articulate that what we mean by 'vanishing' is that there is always a part of current-voltage curve that follows exponential function with the slope of q/kT (i.e. $n = 1$) although the range is narrowed down to the very proximity of zero applied voltage, and, in fact, the ideality factor is not 'deviating' from the unity. Thus, what we observe as a non-unity ideality factor is merely due to wrong choice of voltage range for the exponential regression. Lastly, V_{d} determines the rectification ratio and related with the voltage at which the slope of the double-logarithmic plot decreases (i.e. transition from injection limited regime to bulk-limited regime).

We note that the most critical parameter is the width of the Gaussian DOS. The optimized value was $\sigma = 0.2$ eV, which is similar to but slightly smaller than the values measured by the ultra-violet photo-emission spectroscopy which range from $\sigma = 0.25 \sim 0.30$ eV [129, 173–177]. The small difference could result from limited

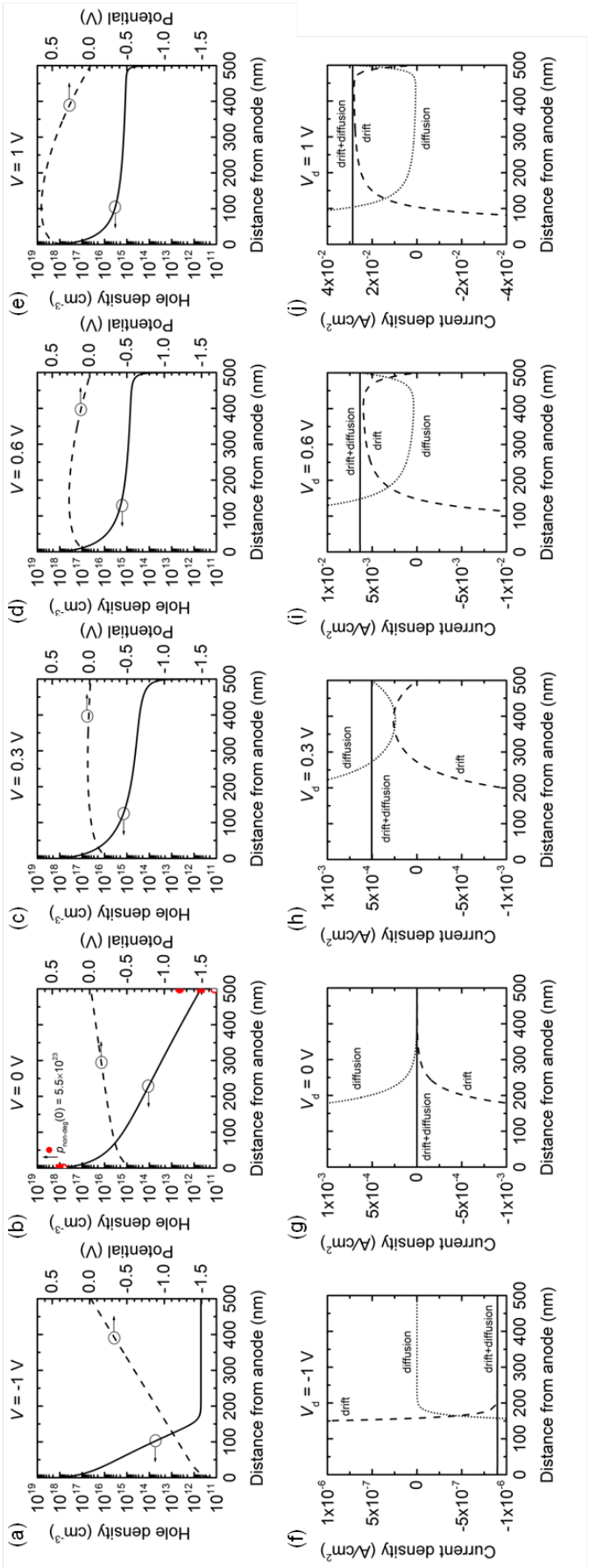

Figure 4-13: The hole concentration and potential profile (upper panels) and the current density and its drift and diffusion components (lower panels) in the device calculated with parameters in 4.2 that gives the best fit to the experimental diode current. Each panel in a row represents different applied voltage: V = -1, 0, 0.3, 0.6 and 1V.

resolution of the measurement technique (broadening of UPS signal by few k_BT) or from different degree of disorder of pentacene thin-film in the literature. On the other hand, we note that the value is larger than $\sigma = 0.14$ eV from NRS-PPV and OC_1C_{10}-PPV based polymer diodes [32], and to the values used for Monte Carlo simulation $\sigma \sim 0.10$ eV [31].

Expectedly, the anode is a strong injecting contact with the hole injection barrier $E_{\mathrm{bp.an}} = 0.7$ eV that corresponds to the effective injection barrier $E^{\mathrm{eff}}_{\mathrm{bp.an}} = 0.26$ eV taking into account the facilitated injection due to disorder. The injection at the anode is strong enough so that the straight band profile of the MIM model is not valid and that bending of voltage profile must be considered as shown in Figure 4-13. In addition, the strong injection makes the semiconductor behave as a degenerate semiconductor. In order to bring more evidence to this argument, we compared the calculated hole concentration at the anode by numerical calculation with Fermi-Dirac distribution function (solid line, $p_{\mathrm{F-D}}$) and by analytical models under Boltzmann (non-degenerate, filled circles, $p_{\mathrm{non-deg}}$) and Heaviside (degenerate, open circles, p_{deg}) approximations in Figure 4-13(b)). At the anode, we clearly see that $p_{\mathrm{deg}} \approx p_{\mathrm{F-D}} \ll p_{\mathrm{non-deg}}$ that support this argument.

Interestingly, despite its role as a blocking contact, the cathode has the injection barrier $E_{\mathrm{bp.an}} = 1.3$ eV (corresponding to $E^{\mathrm{eff}}_{\mathrm{bp.an}} = 0.86$ eV) enough for the Boltzman statistics to fails. At the cathode, we observe $p_{\mathrm{deg}} \sim p_{\mathrm{F-D}} \ll p_{\mathrm{non-deg}}$. Thus, it can be inferred that the Au/pentacene/Al diode operates practically in a degenerate (or quasi-degenerate) regime. In the meantime, we can observe again that the Paasch's model for charge carrier concentration (filled squares, p_{Paasch}) works well over the entire range of carrier concentration: $p_{\mathrm{Paasch}} \approx p_{\mathrm{F-D}}$.

We draw attention to the value of the intrinsic mobility $\mu_{300} = 1.27 \times 10^{-7}$ $\mathrm{cm^2V^{-1}s^{-1}}$ which could be seem too low. However, it is the zero concentration. And this is different to the values extracted by the field effect measurement or by the Mott-Gurney equation regime in the range of $10^{-3} \sim 1$ $\mathrm{cm^2V^{-1}s^{-1}}$, which contains a strong enhancement by the charge carrier concentration and/or the electric field. Considering the enhancement by charge carrier concentration and electric field, mobility gets $\mu = 8.5 \times 10^{-7}\mathrm{cm^2V^{-1}s^{-1}}$ at the cathode and $\mu = 4.5 \times 10^{-3}\mathrm{cm^2V^{-1}s^{-1}}$ at the anode when $V = 1$ V.

Finally, we were able to construct an analytical model for the reverse bias regime. Figure 4-13(f)-(j) show the contribution of the drift and diffusion current to the total diode current at each point in the device for each bias regime. In the reverse bias regime shown (Figure 4-13(f)), the drift current at the cathode successfully represents the total diode current similar to the case of the MIM

model. In fact, when reverse bias is applied the injected holes from anode at thermal equilibrium, which gave rise to the bending, is collected back through the anode. This results in the reduction of bending, and the potential profile could be regarded as a straight line (Figure 4-13(a)). Therefore, following analytical equation is a good model for the reverse bias current j_{rev}:

$$j_{\mathrm{rev}} = -q\mu_{\mathrm{rev}} p_{\mathrm{cat}} \frac{V - V_{\mathrm{d}}}{d} \tag{4.85}$$

where $\mu_{\mathrm{rev}} \approx \mu_0(300) \times g_1(p_{\mathrm{cat}}, T_{300})$ is a constant value consisting only of mobility enhancement by charge carrier concentration, and p_{cat} is the cathode hole concentration calculated with the analytical equation by Paasch. Figure 4-11 shows the quality of a fit to this model. The increasing discrepancy as $V \to 0$ V is due to the growing contribution of diffusion current that cancels the drift current.

Chapter 5

Organic field-effect transistors (OFET)

A transistor is a three terminal semiconductor device used to amplify or switch electronic signals and electrical power. The field-effect transistor (FET) is a type of transistors, in which the electrical conductivity of a channel is modulated by an electric field. The concept of field-effect transistors (FETs) was proposed by Lilienfeld in 1930 [178]. After the description on field effect in organic semiconductors in 1970 [179–181], polythiophene, a class of organic conjugated polymers discovered in the late 1970s, was successfully introduced in OFETs by Koezuka and coworkers in 1986 [10, 11]. The applicability of organic small molecules in FETs was shown more recently although the semiconducting properties had been perceived long before [182, 183].

In principal, the gate electrode is isolated from the semiconductor layer by a gate insulator. The applied voltage at the gate accumulates or repels one type of charge carriers in semiconductor layer, creating a conducting channel. The charge carriers are provided from the source electrode and extracted through the drain electrode. The potential difference between source and drain electrodes contributes

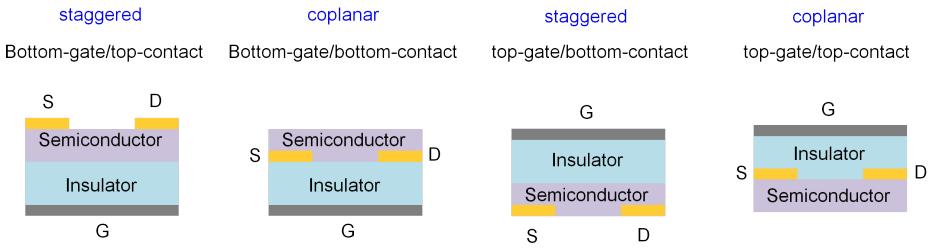

Figure 5-1: Four typical OFET structures characterized by relative positions of the gate electrode (G) and the source (S) and drain (D) electrodes.

to the current along the channel. An OFETs could possess diverse structures according to the sequence of fabrication of its components as shown in Figrue 5-1. In general, a variety of OFET structures can be classified into two main categories according to the position of the source and drain contact relative to the conducting channel [184–186]. An OFET is called coplanar when the channel is in the same plane with the contacts [187,188]. An OFET is called staggered when the channel and the contacts are separated by an organic semiconductor layer. The position of the gate electrode in reference to the semiconductor layer gives two possible variations for each structure.

Amongst many characteristics that OFETs are required to possess for a practical circuit application, a minimum contact resistance, a low-voltage operation and an n-type conduction (electron-transporting) are considered crucial due to their direct influence on high frequency operation, low power consumption, and organic complementary circuit [189]. A significant progress has been made in terms of synthesizing a new organic semiconductor with improved electron/hole transport and injection properties as well as ambient stability [59].A reliable gate dielectric with higher dielectric constant and/or thinner thickness, the easy processing of which is still actively investigated, constitutes a key element for achieving low-voltage operation of the n-type OFETs. The operating voltage is concerned with the thickness d_{i} and relative permittivity (dielectric constant) ϵ_{r} of the gate dielectric because the drain current is proportional to gate dielectric capacitance density $C_{\mathrm{i}} = \epsilon_{\mathrm{r}}\epsilon_0/d_{\mathrm{i}}$ [190]. The state-of-the-art technologies on the gate dielectrics at process temperature below 150°C comprise the use of high permittivity metal oxides [191], nanometer-thick SAMs (2∼3 nm when used alone [192] or around 6 nm with AlO_x [63, 193]), organic-inorganic hybrid multilayer in few nanometer thickness [194] and thin cross-linked polymers [195–198]. However, a full theoretical understanding is still lacking.

In this chapter, we will focus on elucidating the geometrical impact on the drain current and the contact resistance and on providing a compact model suitable for low voltage circuit simulations in consistent with the physical ground emphasized in Chapter 4.

5.1 A staggered OFET

In many experimental studies on comparative analysis of the TC versus BC OFETs [187, 199–201], it has been generally observed that TC OFETs show superior electrical performance compared to the BC OFETs under the same fabrication condi-

tion, particularly in terms of the field-effect mobility μ and the contact resistance R_c.

Several factors have been presented as a plausible explanation for this tendency. First, the semiconductor morphology is presented as a crucial factor especially for OFETs based on molecular semiconductors such as pentacene. In BC geometry, the molecules evaporated on a highly reactive metal surface are lying flat or are randomly oriented, whereas they form well-ordered region on an inert surface of gate dielectric layer, between source/drain contact [199, 202]. This leads to poor electrical transport property at the source/channel interface. On the other hand, there is no such morphological discontinuity in TC OFETs [201]. Another commonly accepted advantage of TC OFETs is related to the metal penetration into the fragile organic film. The metal cluster deposited on top of an organic layer can form a more continuous interface, which could facilitate the charge-carrier injection, in contrast to the BC OFETs where this interface characteristics should be abrupt [185, 203].

Second, a recent theoretical study suggests that there is a purely geometrical benefit of the TC OFETs compared to the BC OFETs [204]. In the study, Kim *et al.* ruled out any process-related or morphological effects on the device properties in their device modelling based on the two-dimensional finite element method by considering the organic semiconductor layer as a continuous medium and all metal/organic interfaces are sharply defined in 2-D models. The presence of a highly resistive transition zone[1] between the channel and the coplanar source/drain contacts was recognized as the origin of the significant contact voltage drop, where the charge carrier concentration at the contact side is limited electro-statistically by the injection barrier between the semiconductor and the metal contact.

In fact, a similar transition zone must exist in TC OFETs. Although, as pointed out by Kim *et al.*, the charge carrier concentration profile remains high along the channel in TC OFETs, the gradient of the profile appears perpendicular to the channel axis in the semiconductor layer under the contacts. This perpendicular transition zone in TC OFETs is indeed analogous to the horizontal transition zone in BC OFETs, in the sense that charge carriers should transport through this low carrier concentration zone in order to be injected into the channel or extracted from the channel, bringing about a similar contact potential drop. Therefore, it is not merely the existence of this transition zone that demerits the BC OFETs over TC OFETs. A deeper understanding on this transition zone is necessary for

[1] Transition in terms of charge carrier concentration from the contact (low) to the channel (high).

further optimization of contact resistance in TC OFETs, especially in regards to the charge injection and transport in the zone.

5.1.1 Current path in a staggered OFET

In OFETs, organic semiconductor is mostly used without intentional doping. Therefore, charge carriers should be injected from the source contact to create a conducting channel. The drain current in OFETs is, then, mediated by the drift and diffusion of charge carriers. which writes for holes:

$$j = j_{\text{drift}} + j_{\text{diff}} = q\mu pF - qD\nabla p. \tag{5.1}$$

Here, for a staggered OFET, the drain current must be considered as a vector due to its two-dimensional(2-D) nature of the device structure. The gradient of potential $F = -\nabla V$ and charge carrier concentration ∇p determines the direction and the magnitude of each element of the current. At given F and ∇p, the magnitude is proportional to the mobility μ, the hole concentration p and the diffusion coefficient D.

The exact source-to-drain current path as well as the contribution of the drift and diffusion current can be visualized when the hole and potential distribution in an organic semiconductor layer, $p(x, y)$ and $V(x, y)$, are determined. For doing so, the coupled drift-diffusion (5.1) and Poisson's equation should be solved in two-dimensional domain by extending the solution method presented in Chapter 4:

$$\nabla F = \frac{qp}{\epsilon}, \tag{5.2}$$

where ϵ is the permittivity of the semiconductor.

Before exact solution, we can predict the 2-D current path in the staggered OFET as shown in Figure 5-2(a). We note that this primitive illustration is established on the fact that the injected charge carriers are locally accumulated near the semiconductor/insulator interface. If the conductivity (and the charge carrier concentration) of the semiconductor layer were uniform, the current path would be quasi 1-D favouring the shortest path between the source and drain contacts. In contrast, when vertical gradient of charge carrier concentration is present, the detouring current path (2-D) could be favoured against the the shortest path due to a lower resistivity near the semiconductor/insulator interface on condition that the additional vertical current path does not cancel out the merit.

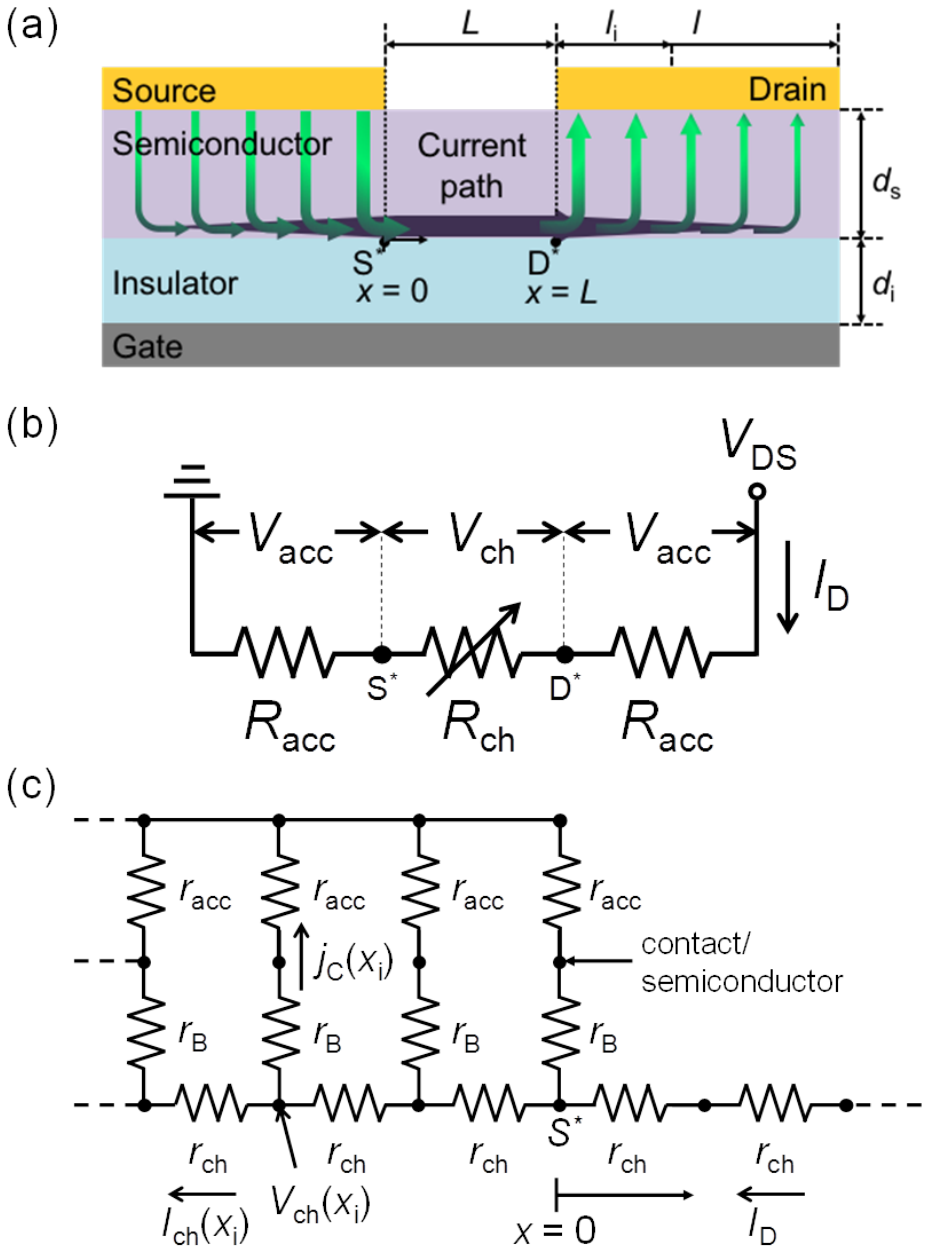

Figure 5-2: (a) Drain current path (thick arrows) in a staggered organic field-effect transistor with bottom-gate top-contact (BGTC) configuration. Injected charge carrier must traverse semiconductor layer (arrows in violet) to reach channel (arrow in red). (b) Conventional equivalent circuit corresponding to the drain current path. The access resistance R_{acc} is assumed independent to the gate voltage. (c) Magnified view of equivalent circuit for current crowding model near source contact. Both the bulk r_B and channel resistivity r_{ch} have gate voltage dependence.

Conducting channel: drift current

In general, the exactly simulated hole and potential distribution supports a classical picture of the source-to-drain current path illustrated in Figure 5-2(a). Figure 5-3(a) and (b) shows the hole and potential distribution in the semiconductor layer of an on-state TC OFET, $V_{\mathrm{GS}} = -20$ V and $V_{\mathrm{DS}} = -2$ V.

The horizontal current $j_x(y)$ is indeed flowing dominantly near the semiconductor/ insulator interface ($y \approx 0$, in the conducting channel). This accounts for the fact that both diffusion and drift current that flow from source to drain ($+x$ direction) are greater near $y \approx 0$. It is clearly shown that the hole concentration near $y \approx 0$ is higher by factor of 1000 compared to $y = d_{\mathrm{s}} \approx 60$ nm (Figure 5-3(a)), and hence the mobility enhancement, leading to $j_{\mathrm{drift}.x}(y = +0) \gg j_{\mathrm{drift}.x}(y = d_{\mathrm{s}} - 0)$ despite nearly invariant electric field $F_x(y)$ (Figure 5-3(b)). We also observe that $\nabla_x p(+0) \gg \nabla_x p(d_{\mathrm{s}} - 0)$, which supports $j_{\mathrm{diff}.x}(y = +0) \gg j_{\mathrm{diff}.x}(y = d_{\mathrm{s}} - 0)$.[2] This confirms that the conducting channel is created near the semiconductor/semiconductor interface, and that the holes must be transported from the contact to the channel and *vice versa* (namely, across the channel or along the y-axis) to completes the current path. In addition, it enables the equivalent circuit modelling in Figure 5-2(b).

An important message is that the total current that flows along the x-axis can be fully represented by the drift current near semiconductor/insulator interface $j_x(y) \approx j_{\mathrm{drift}.x}(y)$ (see Figure 5-3(c)). Therefore, it is legitimate to describe the channel as a conductor with variable conductance:

$$\sigma_{\mathrm{ch}.x} = \frac{j_{\mathrm{drift.x}}}{F_x} = q\mu p \approx \frac{j_{\mathrm{x}}}{F_x}. \tag{5.3}$$

From contact to channel: drift-diffusion current

Now, we turn to the vertical transition zone that connects the conducting channel with the contact. As described previously, the simulated hole distribution varies significantly across the channel $p(y)$ (see Figure 5-3(a)). Therefore, the hole diffusion current across the channel is not negligible, $j_{\mathrm{diff}.y}(x) \neq 0$, in contrast to the current in the conducting channel (compare Figure 5-3(c) and (d)). More precisely, the total current $j_y(x)$ is dominated neither by drift nor diffusion, instead, it originates from a small imbalance between the two. This difference must be taken into account in describing and modelling how the charge transport in this

[2] Be careful with the logarithmic scale.

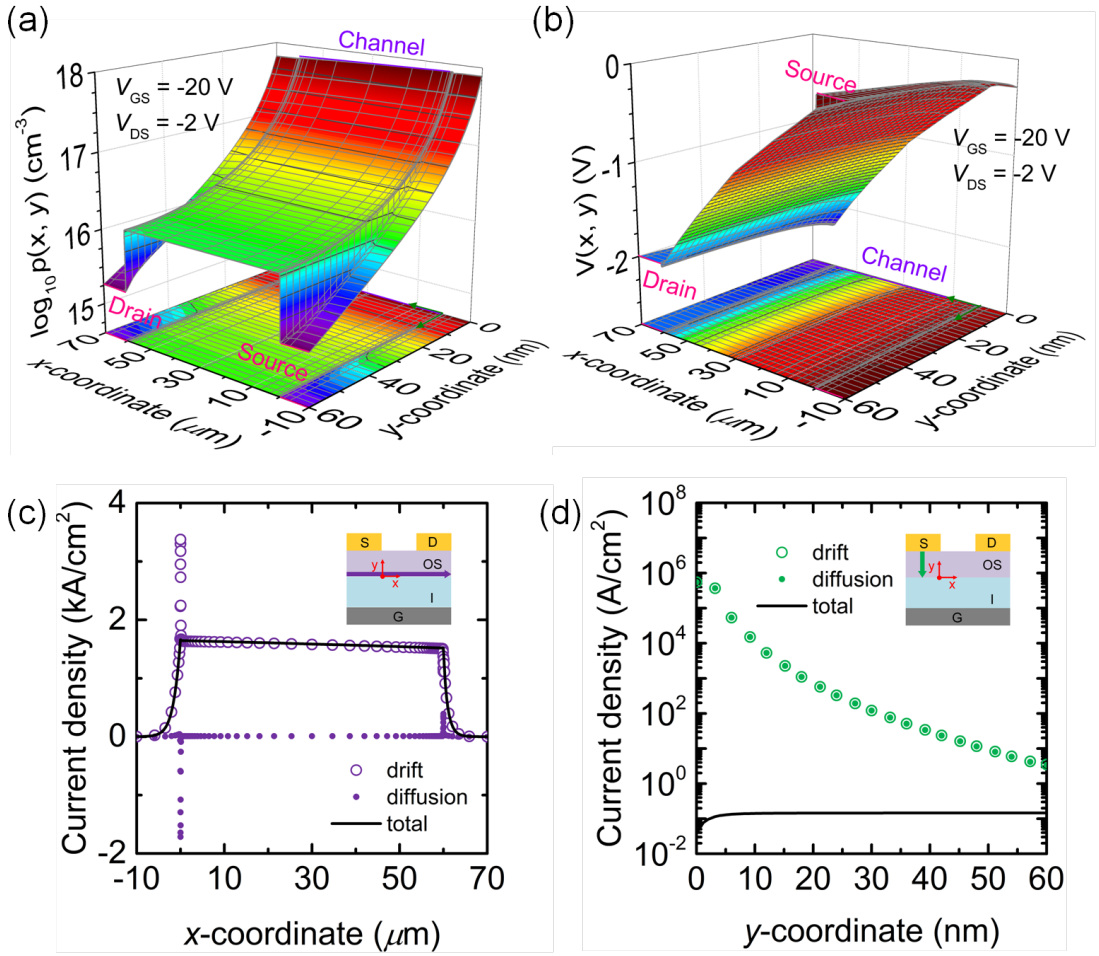

Figure 5-3: Simulated (a) hole concentration and (b) potential distribution in organic semiconductor layer of a staggered OFET under on-state: V_{GS} = -20 V and V_{DS} = -2 V. The channel length is 60 μm, the semiconductor thickness is 60 nm, and the contact length is 10 μm. Simulated drift-diffusion current (c) across the channel at the source (x =-5 μm) and (d) along the channel (y = 0 nm). The total current (solid line) is the sum of the drift (open circles) and diffusion (filled circles) current. The drift current is dominant along the channel (x = 0 to 60 μm), while both drift-diffusion current have comparable magnitude and opposite sign across the channel.

vertical transition zone.

We keep the concept of modelling the current path as a resistive circuit element, pursuing the formation of an equation defining the conductivity. In essence, we are in how the current response to the electric field, where the current is the total current with both drift and diffusion contributions. In this context, we propose a physical quantity $\sigma_{\text{drift.diff}} = j/F$,

$$\sigma_{\text{drift.diff}} \equiv \frac{j}{F} = q\mu p \left[1 - \frac{D}{\mu} \cdot \frac{\nabla p}{pF}\right] = q\mu p \left[1 - \frac{j_{\text{diff}}}{j_{\text{drift}}}\right], \tag{5.4}$$

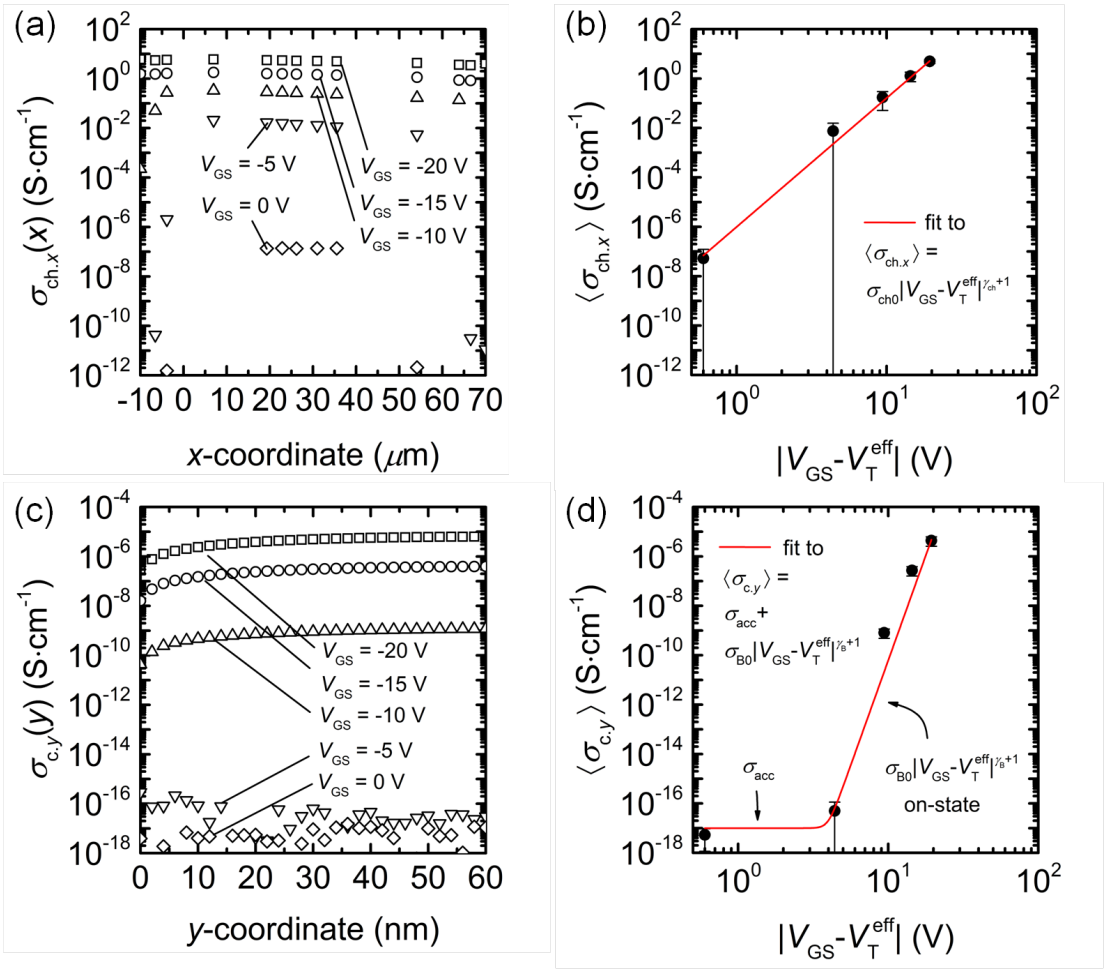

Figure 5-4: (a) Channel conductivity $\sigma_{\mathrm{ch}.x}$ and (b) its average on x-axis $\langle\sigma_{\mathrm{ch}.x}\rangle$ (at $y = 2$ nm), and (c) contact conductivity in the transition zone $\sigma_{\mathrm{c}.y}$ and (d) its average on y-axis $\langle\sigma_{\mathrm{c}.y}\rangle$ (at $x = -5$ μm) calculated at various gate voltage: $V_{\mathrm{GS}} = 0, -5, -10, -15$ and -20 V. Note the power-law dependence of both channel and contact conductivity with respect to the effective gate voltage. In particular, $\langle\sigma_{\mathrm{c}.y}\rangle$ contains an asymptotic element σ_{acc} and a power-law dependent element σ_{B}.

which has the same dimension as the conventional conductivity σ in [S/cm] but contains the effect of diffusion. We note that $\sigma_{\mathrm{drift.diff}} \approx \sigma = q\mu p$ when $j_{\mathrm{diff}} \ll j_{\mathrm{drift}}$ or $j_{\mathrm{diff}} = 0$. Thus, we retrieve $\sigma_{\mathrm{drift.diff}} = \sigma_{\mathrm{ch}.x} = q\mu p$ of (5.3) in the channel.

Then, in the transition zone, we can define the contact conductivity given by $\sigma_{\mathrm{c}.y} = j_y/F_y$,

$$\sigma_{\mathrm{c}.y} \equiv \frac{j_y}{F_y} = q\mu p\left[1 - \frac{D}{\mu}\cdot\frac{\nabla_y p}{pF_y}\right] = q\mu p\left[1 - \frac{j_{\mathrm{diff}.y}}{j_{\mathrm{drift}.y}}\right]. \tag{5.5}$$

In order to check the robustness of the definition, we calculated the channel and contact conductivity at various gate voltages. As shown in Figure 5-4(a),

we note that the channel conductivity stays almost constant along the channel (x-coordinate) when the transistor is under on-state (high V_{GS}). The clear power-law dependence of the channel conductivity shown in Figure 5-4(b) an empirical modelling:

$$\langle \sigma_{\mathrm{ch}.x} \rangle = \sigma_{\mathrm{ch0}} |V_{\mathrm{GS}} - V_{\mathrm{T}}^{\mathrm{eff}}|^{\gamma_{\mathrm{ch}}+1}, \tag{5.6}$$

where $V_{\mathrm{T}}^{\mathrm{eff}} = V_{\mathrm{T}} + V_{\mathrm{DS}}/2$ is the effective threshold voltage. Here, the one (1) in the exponent describes the capacitive modulation of channel charge carrier concentration by the gate voltage and γ_{ch} describes the empirical power-law dependence of mobility on the charge carrier concentration. The latter encompasses the enhancement of mobility by charge carrier concentration in the presence of semiconductor disorder.

In the transition zone, $\sigma_{\mathrm{c}.y}(y)$ decreases moving away from the contact interface $y \to 0$. This is because the insulator/semiconductor interface blocks the charge carriers and the horizontal motion of charge carriers becomes favoured and dominant. Interestingly, the contact conductivity shows a similar power-law dependence on the gate voltage with an asymptote behaviour at low V_{GS} Figure 5-4(d). This lead to an empirical model for the contact conductivity

$$\langle \sigma_{\mathrm{c}.y} \rangle = \sigma_{\mathrm{acc}} + \sigma_{\mathrm{B0}} |V_{\mathrm{GS}} - V_{\mathrm{T}}^{\mathrm{eff}}|^{\gamma_{\mathrm{B}}+1}, \tag{5.7}$$

where σ_{acc} is the access conductivity and $\sigma_{\mathrm{B}} = \sigma_{\mathrm{B0}} |V_{\mathrm{GS}} - V_{\mathrm{T}}^{\mathrm{eff}}|^{\gamma_{\mathrm{B}}+1}$ is the bulk conductivity. Qualitatively speaking, σ_{acc} represents the conductivity due to the intrinsic charge carriers present in the transition zone at thermal equilibrium, which is linked to the injection barrier. And σ_{B} describes the contribution of capacitively induced charge carriers by the gate voltage in enhancing the conductivity.

The current path and two empirical models for channel and contact conductivity will be used as a foundation for a unique equivalent circuit modelling of an OFET to be presented in the following which fully captures the effect of disorder, and concomitant enhancement of mobility and diffusion, on the drain current.

5.1.2 Equivalent circuit model

As briefly described in the beginning of the chapter, the necessity of minimizing the source-and-drain resistance (namely, contact resistance) and evaluating it directly is closely related with the quest for ever decreasing transistor dimensions where the effect of contact becomes more significant. Therefore, the relevant modelling has progressed from the early days of MOS technologies. The most simple equivalent

circuit for a transistor with contact resistance R_C was proposed by Suciu and Johnston [205]. In this equivalent model, the current path between the source and the drain contact is described as a serial connection of a channel resistor and two constant access resistances R_{acc} at the source and the drain Figure 5-2(b). In addition, the channel conductance modulation was solely described as the variation of the capacitively induced channel charge carrier, i.e. con mobility is assumed constant. Subsequent refinements of this primitive model upon adopting it for OFETs are driven by discrepancy between these two assumptions and experimental observations of gate voltage dependence of the mobility and the contact resistance.

The power-law dependence of mobility on gate voltage in amorphous-Silicon (a-Si) and poly-silicon (p-Si) based FETs was observed by Shur [206]. Similar dependence in OFETs was observed in [105, 168, 207]. A recent drain current models for OFETs widely adopts the power-law μ and constant R_C model [208].

On the other hand, no drain current model has sufficiently incorporated the gate voltage dependence of R_C recognized in OFETs [209,210]. We note an initiative works by Chiang, in which gate bias dependence of R_C in a staggered a-Si and p-Si FET was observed and modelled by equivalent circuit approach Figure 5-2(c), namely the current crowding model [211]. In the current crowding model, the contact resistivity is composed of a gate bias dependent and independent elements. We have shown by means of 2-D numerical simulation that this description is valid in OFETs with Gaussian disorder. We will proceed further how this contact resistance model can be adopted for the drain current model for an OFET and consistent parameters extraction method.

5.2 Analytical modelling

We will start by briefly reminding the drain current models in the literatures, and propose an improved model which considers the gate voltage dependence of both mobility and contact resistance. A concise derivation is provided in order to emphasize some points that must not be neglected for achieving a good fit to experimental data. The structure of the staggered OFET is provided in Figure 5-2.

5.2.1 Drain current models in the literatures

Ideal drain current model

The drain current of an ideal p-channel OFET is given by [212]:

$$I_{\mathrm{D}} = -\frac{W}{L}\mu C_{\mathrm{i}}\left\{(V_{\mathrm{GS}} - V_{\mathrm{T}})\,V_{\mathrm{DS}} - \frac{V_{\mathrm{DS}}^2}{2}\right\}, \tag{5.8}$$

where W and L denotes the channel width and length, C_{i} the capacitance density of the gate dielectric, V_{T} the threshold voltage, and V_{GS} and V_{DS} the gate-source and drain-source voltage. The ideal drain current model assumes that R_{C} is nil and μ is a constant independent of applied bias and position. This enables analytical integration of the channel conductance in the channel [212]. Considering the non-negligible effect of V_{DS} on the threshold voltage [213], we write (5.8) alternatively

$$I_{\mathrm{D}} = -\frac{W}{L}\mu C_{\mathrm{i}}\left(V_{\mathrm{GS}} - V_{\mathrm{T}}^{\mathrm{eff}}\right)V_{\mathrm{DS}}, \tag{5.9}$$

where the effective threshold voltage is $V_{\mathrm{T}}^{\mathrm{eff}} = V_{\mathrm{T}} + V_{\mathrm{DS}}/2$. From the constant mobility, it can be inferred that this model would be valid only for highly ordered organic transistors where mobility enhancement is negligible.

Drain current model with constant R_{C} and μ

The drain current equation in presence of a contact resistance can be found in [205,214]. It assumes that the on-state resistance R_{on}, which represents the current path from source to drain (see Figure 5-2(b)), consists of a channel resistance R_{ch} and two access resistances R_{acc} at the source and drain:

$$R_{\mathrm{on}} = 2R_{\mathrm{acc}} + R_{\mathrm{ch}}, \tag{5.10a}$$

$$V_{\mathrm{DS}} = 2V_{\mathrm{acc}} + V_{\mathrm{ch}}, \tag{5.10b}$$

$$I_{\mathrm{D}} = I_{\mathrm{acc}} = I_{\mathrm{ch}}. \tag{5.10c}$$

Here, I_{acc} and I_{ch} denote the current at each resistor. In addition, $2R_{\mathrm{acc}}$ is described as the contact resistance R_{C}.

From (5.10c), I_{D} can be determined when I_{ch} is known. The physical meaning of I_{ch} is the drain current of an ideal transistor without contact resistance that has imaginary source and drain S^* and D^* (see Figure 5-2). Thus, using (5.9) and

(5.10b),

$$I_{\mathrm{ch}} = -\frac{W}{L}\mu C_{\mathrm{i}}\left(V_{\mathrm{GS}} - V_{\mathrm{T}}^{\mathrm{eff}}\right)\left(V_{\mathrm{DS}} - 2V_{\mathrm{acc}}\right). \tag{5.11}$$

Note that, in the first parenthesis, the V_{acc}-term from the imaginary gate-source voltage is exactly cancelled out by the same contained in the effective threshold voltage. It would, however, pertain when the drain current equation is written by neglecting ${V_{\mathrm{DS}}}^2/2$ in (5.8), which Souciou and Johnston [205] and Jain [214] impetuously neglected upon the derivation of R_{ch} and R_{C}. Then, the channel resistance R_{ch} becomes

$$R_{\mathrm{ch}} = \frac{V_{\mathrm{DS}} - 2V_{\mathrm{acc}}}{I_{\mathrm{ch}}} = \frac{L}{W\mu C_{\mathrm{i}}|V_{\mathrm{GS}} - V_{\mathrm{T}}^{\mathrm{eff}}|}. \tag{5.12}$$

By substituting V_{acc} in (5.11) by $R_{\mathrm{acc}}I_{\mathrm{acc}}$ and using (5.10c) and (5.11), we get the drain current model with constant R_{C} and μ,

$$I_{\mathrm{D}} = \frac{\frac{W}{L}\mu C_{\mathrm{i}}|V_{\mathrm{GS}} - V_{\mathrm{T}}^{\mathrm{eff}}|V_{\mathrm{DS}}}{1 + R_{\mathrm{C}}\frac{W}{L}\mu C_{\mathrm{i}}|V_{\mathrm{GS}} - V_{\mathrm{T}}^{\mathrm{eff}}|}, \tag{5.13}$$

which returns to (5.9) when $R_{\mathrm{C}} = 0$. Then, we obtain the on-state resistance R_{on} which is written as

$$R_{\mathrm{on}} = \frac{V_{\mathrm{DS}}}{I_{\mathrm{D}}} = R_{\mathrm{C}} + \frac{L}{W\mu C_{\mathrm{i}}|V_{\mathrm{GS}} - V_{\mathrm{T}}^{\mathrm{eff}}|}. \tag{5.14}$$

or as the width-normalized resistance $R_{\mathrm{on}}W$ for a practical reason to compare devices with different W values

$$R_{\mathrm{on}}W = R_{\mathrm{C}}W + \frac{L}{\mu C_{\mathrm{i}}|V_{\mathrm{GS}} - V_{\mathrm{T}}^{\mathrm{eff}}|}. \tag{5.15}$$

It is clearly shown by (5.15) that the on-state resistance R_{on} is a linear function of the channel length L. This establishes the foundation for the transmission-line method (TLM, a.k.a. transfer length method) used to extract R_{C} and μ from a set of transfer characteristics [210, 215, 216].

Drain current model with constant R_{C} and power-law μ

As will be shown experimentally, it is now clearly established that μ in most FETs is gate voltage dependent [207]. More precisely, μ increases with V_{GS} at low gate voltage. In this regime, the dependence of mobility on V_{GS} is most often

represented by empirical power-law which writes

$$\mu = \kappa |V_{\mathrm{GS}} - V_{\mathrm{T}}^{\mathrm{eff}}|^{\gamma}, \tag{5.16}$$

leading (5.13) and (5.15) to

$$I_{\mathrm{D}} = \frac{\frac{W}{L}\kappa C_{\mathrm{i}} |V_{\mathrm{GS}} - V_{\mathrm{T}}^{\mathrm{eff}}|^{\gamma+1} V_{\mathrm{DS}}}{1 + R_{\mathrm{C}}\frac{W}{L}\kappa C_{\mathrm{i}} |V_{\mathrm{GS}} - V_{\mathrm{T}}^{\mathrm{eff}}|^{\gamma+1}}. \tag{5.17}$$

$$R_{\mathrm{on}}W = R_{\mathrm{C}}W + \frac{L}{\kappa C_{\mathrm{i}} |V_{\mathrm{GS}} - V_{\mathrm{T}}^{\mathrm{eff}}|^{\gamma+1}}, \tag{5.18}$$

It should be pointed out that the rise of μ with V_{GS} is related with the increasing charge carrier density in the channel. The power-law dependent μ on the charge carrier density was formulated firstly based on the multiple trapping-and-releasing (MTR) model [207] and variable range hopping (VRH) model [168] assuming exponential density-of-states (DOS). On both transport models, the exponent of the power-law γ is directly related with the trap characteristic temperature T_c by $\gamma = T_c/T - 1$. More recently, the possibility of extending the power-law dependent mobility to Gaussian DOS was examined based on the VRH model. It was demonstrated that discrete approximations of Gaussian to exponential DOS is possible for a practical operation range of V_{GS} so that the power-law dependent μ would be legitimately represented by a single γ [217]. With a more comprehensive mobility model, we have provided, in the previous section, a fundamental evidence that the channel conductivity shows the power-law dependence.

5.2.2 Origin of power-law R_{C}: current crowding

Now, we will elaborate how the power-law dependent conductivity (a microscopic factor) affects the contact resistance (a measurable quantity) based on the equivalent circuit of the current crowding model [211]. In summary, we propose an analytical model for the gate voltage dependence of the contact resistance as a power-law :

$$R_{\mathrm{C}}W = R_{\mathrm{C}}^{\infty}W + \frac{A}{|V_{\mathrm{GS}} - V_{\mathrm{T}}^{\mathrm{eff}}|^{\gamma+1}}. \tag{5.19}$$

Here, $R_{\mathrm{C}} \to R_{\mathrm{C}}^{\infty}$ when $|V_{\mathrm{GS}} - V_{\mathrm{T}}^{\mathrm{eff}}| \to \infty$. The term $A/|V_{\mathrm{GS}} - V_{\mathrm{T}}^{\mathrm{eff}}|^{\gamma+1}$ indicates the gateable element in the contact resistance $R_{\mathrm{C}}^{G}W$.

In the current crowding model, shown in Figure 5-2(c), the drain current path

from the imaginary source S* (or drain D*) to source S (or drain D) contact is represented by the gateable channel r_{ch} (in Ω/cm) and bulk resistivity r_{B} (in $\Omega\cdot\mathrm{cm}^2$) and non-gateable access resistivity r_{acc} (in $\Omega\cdot\mathrm{cm}^2$)[3]. The r_{B} corresponds to the charge carrier transport in the bulk of semiconductor, whereas r_{acc} corresponds to the voltage drop at the contact-semiconductor junction.

The charge carrier density is nearly constant along the channel (even under the contact) in linear regime Figure 5-3(a). Thus, by using (5.12), the channel resistivity r_{ch} in the region overlapped by the source and drain contact can also be written as

$$r_{\mathrm{ch}} = \frac{R_{\mathrm{ch}}}{L} = \frac{1}{W\kappa_{\mathrm{ch}}C_{\mathrm{i}}|V_{\mathrm{GS}} - V_{\mathrm{T}}^{\mathrm{eff}}|^{\gamma_{\mathrm{ch}}+1}}. \tag{5.20}$$

Next, using the empirical power-law dependence of the contact resistivity observed in Figure 5-4(d), r_{B} could be expressed as shows a similar power-law:

$$r_{\mathrm{B}} = \frac{{d_{\mathrm{s}}}^2}{\kappa_{\mathrm{B}}C_{\mathrm{i}}|V_{\mathrm{GS}} - V_{\mathrm{T}}^{\mathrm{eff}}|^{\gamma_{\mathrm{B}}+1}}. \tag{5.21}$$

Here, d_{s} is the thickness of organic semiconductor layer. κ_{B} and γ_{B} is the constant of proportionality and exponent for the power-law μ in the bulk.

Now, we turn to the equivalent circuit presented in Figure 5-2(c). By the Kirchoff's current law at the node x, we have

$$\frac{\mathrm{d}I_{\mathrm{ch}}(x)}{\mathrm{d}x} = WJ_{\mathrm{C}}(x), \tag{5.22}$$

where $J_{\mathrm{C}}(x)$ is the contact current density flowing through serially connected r_{B} and r_{acc} and $I_{\mathrm{ch}}(x)$ is the channel current density flowing through r_{ch} at position x. Between the node x and source contact, we get

$$J_{\mathrm{C}}(x) = \frac{V_{\mathrm{ch}}(x)}{r_{\mathrm{B}} + r_{\mathrm{acc}}}, \tag{5.23}$$

where $V_{\mathrm{ch}}(x)$ is the electrical potential at x. Similarly, between two nodes x_i and x_{i+1}, we have

$$\frac{\mathrm{d}V_{\mathrm{ch}}(x)}{\mathrm{d}x} = I_{\mathrm{ch}}(x)r_{\mathrm{ch}}. \tag{5.24}$$

Then, from (5.22)-(5.24), we obtain a differential equation which relates $V_{\mathrm{ch}}(x)$

[3]Note that Chiang used a modified the definition for the resistivity. The channel resistivity r_{ch} denotes the channel resistance normalized only by the channel length, $r_{\mathrm{ch}} = R_{\mathrm{ch}}/L = \rho_{\mathrm{ch}}/S_{\mathrm{ch}}$ with ρ_{ch} being the conventional definition for the resistivity and S_{ch} being the channel cross-section area. The bulk resistivity and access resistivity denotes contact resistance normalized only by the contact cross-section area, $r_{\mathrm{c}} = r_{\mathrm{acc}} + r_{\mathrm{B}} = R_{\mathrm{C}}S_{\mathrm{c}} = \rho_{\mathrm{c}}L$

with r_{ch}, r_{B} and r_{acc},

$$\frac{\mathrm{d}^2 V_{\mathrm{ch}}(x)}{\mathrm{d}x^2} = \frac{W r_{\mathrm{ch}}}{r_{\mathrm{B}} + r_{\mathrm{acc}}} V_{\mathrm{ch}}(x). \tag{5.25}$$

The differential equation has two boundary conditions:

$$\left.\frac{\mathrm{d}V_{\mathrm{ch}}(x)}{\mathrm{d}x}\right|_{x=0} = I_0 r_{\mathrm{ch}}, \tag{5.26a}$$

$$\left.\frac{\mathrm{d}V_{\mathrm{ch}}(x)}{\mathrm{d}x}\right|_{x=-l} = 0, \tag{5.26b}$$

where I_0 is the total drain-to-source current and l denotes the contact length. Then, the analytical solution of (5.25) is

$$V_{\mathrm{ch}}(x) = I_0 r_{\mathrm{ch}} l_{\mathrm{i}} \frac{\cosh\left[(x+l)/l_{\mathrm{i}}\right]}{\sinh\left[l/l_{\mathrm{i}}\right]}. \tag{5.27}$$

Here, the transfer length l_{i} is defined as

$$l_{\mathrm{i}} = \sqrt{\frac{r_{\mathrm{B}} + r_{\mathrm{acc}}}{W r_{\mathrm{ch}}}} \tag{5.28}$$

over which most (i.e. $1/e$) of the current transfers to (from) metal into (out of) semiconductor.

Finally, since the potential difference between $x = 0$ and the source contact is $V_{\mathrm{ch}}(x = 0)$, the contact resistance R_{C} is expressed upon assuming symmetric access resistance R_{acc} at the source and drain contacts as

$$R_{\mathrm{C}} = 2R_{\mathrm{acc}} = 2\frac{V_{\mathrm{ch}}(0)}{I_0} = 2 r_{\mathrm{ch}} l_{\mathrm{i}} \coth\left(\frac{l}{l_{\mathrm{i}}}\right). \tag{5.29}$$

As it is written, arranging (5.29) into the gateable and non-gateable elements is not apparent. On the other hand, the separation of two elements is possible by further mathematical approximations. If $l/l_{\mathrm{i}} \gg 1$, $\coth(l/l_{\mathrm{i}}) \sim 1$. Then, by using (5.28), (5.29) becomes,

$$R_{\mathrm{C}} = 2\sqrt{(r_{\mathrm{acc}} + r_{\mathrm{B}})\frac{r_{\mathrm{ch}}}{W}}. \tag{5.30}$$

Then, by using Taylor series $\sqrt{1+x} \approx 1 + x/2$ and substituting r_{ch} and r_{B} by (5.20) and (5.21), this is arranged into

$$R_{\mathrm{C}} W = \frac{r_{\mathrm{acc}}}{d_{\mathrm{s}}} \sqrt{\frac{\kappa_{\mathrm{B}}}{\kappa_{\mathrm{ch}}}} \frac{1}{|V_{\mathrm{GS}} - V_{\mathrm{T}}^{\mathrm{eff}}|^{(\gamma_{\mathrm{ch}} - \gamma_{\mathrm{B}})/2}} + \frac{2 d_{\mathrm{s}}}{\sqrt{\kappa_{\mathrm{ch}} \kappa_{\mathrm{B}}} C_{\mathrm{i}}} \frac{1}{|V_{\mathrm{GS}} - V_{\mathrm{T}}^{\mathrm{eff}}|^{(\gamma_{\mathrm{ch}} + \gamma_{\mathrm{B}} + 2)/2}}. \tag{5.31}$$

On the basis of hopping transport in the Gaussian DOS, mobility does not decrease linearly but shows an asymptotic behaviour as the charge carrier concentration decreases [33]. Thus, when such dependence is described by power-law, the exponent and the constant of proportionality for the power-law μ become smaller as the charge carrier concentration decreases. Therefore, because of lower charge carrier concentration in the bulk compared to the channel, we have $\gamma_{\mathrm{ch}} \geq \gamma_{\mathrm{B}} > 0$ and $\kappa_{\mathrm{ch}} \geq \kappa_{\mathrm{B}} > 0$. This makes the second term in (5.31) decrease more rapidly with the effective gate voltage, which rationalizes the formulation in (5.19). The extreme case, where $\gamma_{\mathrm{ch}} = \gamma_{\mathrm{B}} = \gamma$ and $\kappa_{\mathrm{ch}} = \kappa_{\mathrm{B}} = \kappa$, could be written as:

$$R_{\mathrm{C}}W \approx \frac{r_{\mathrm{acc}}}{d_{\mathrm{s}}} + \frac{2d_{\mathrm{s}}/\kappa C_{\mathrm{i}}}{|V_{\mathrm{GS}} - V_{\mathrm{T}}^{\mathrm{eff}}|^{\gamma+1}}. \tag{5.32}$$

5.2.3 Drain current model with power-law R_{C} and μ

Now, we develop the drain current model with both power-law R_{C} and μ. Substituting μ and R_{C} in (5.13) by (5.16) and (5.19), we obtain the drain current equation

$$I_{\mathrm{D}} = \frac{\frac{W}{L}\kappa C_{\mathrm{i}}|V_{\mathrm{GS}} - V_{\mathrm{T}}^{\mathrm{eff}}|^{\gamma+1}V_{\mathrm{DS}}}{1 + A\kappa C_{\mathrm{i}}/L + R_{\mathrm{C}}^{\infty}\frac{W}{L}\kappa C_{\mathrm{i}}|V_{\mathrm{GS}} - V_{\mathrm{T}}^{\mathrm{eff}}|^{\gamma+1}}. \tag{5.33}$$

This leads to a generalized expression of on-state resistance R_{on} with complete consideration for the power-law dependence of R_{C} and μ. The width normalized on-state resistance $R_{\mathrm{on}}W$ is written as

$$R_{\mathrm{on}}W = R_{\mathrm{C}}^{\infty}W + \frac{A + L/\kappa C_{\mathrm{i}}}{|V_{\mathrm{GS}} - V_{\mathrm{T}}^{\mathrm{eff}}|^{\gamma+1}}. \tag{5.34}$$

Note that (5.34) reduces to (5.15) if there is no such dependence i.e. $A = 0$ and $\gamma = 0$. In the following sections, we will present a consistent parameter extraction method for OFETs with both power-law dependent μ and R_{C} based on the drain current model developed above.

5.2.4 Consistent parameter extraction method

The lack of a drain current model deteriorates the accuracy and physical consistency of a parameter extraction method established on the former. For example, the H-function method extracts the threshold voltage V_{T} and power-law exponent γ neglecting the existence of R_{C} [218], [208]. The H-function involves the integration of I_{D} with respect to V_{GS}, which provides a high immunity to the experimental noise but would not lead to a simple mathematical expression when R_{C}

is considered. Recently, a hybrid of integration and derivative method succeeded to incorporate the constant R_{C} and the power-law dependent μ [219]. However, to the best of our knowledge, no parameter extraction method fully considers the gate voltage dependence of μ and R_{C} while maintaining the high immunity to noise [220]. In this respect, we will propose a parameter extraction method consistent to the drain current model developed in the previous section.

The Ratio method

We start from (5.34) to obtain the first and second derivative of R_{on} with respect to V_{GS}, which are written as

$$\frac{\partial R_{\mathrm{on}}}{\partial V_{\mathrm{GS}}} = -(\gamma+1)\frac{(A+L/\kappa C_{\mathrm{i}})/W}{|V_{\mathrm{GS}}-V_{\mathrm{T}}^{\mathrm{eff}}|^{\gamma+2}} \tag{5.35}$$

and

$$\frac{\partial^2 R_{\mathrm{on}}}{\partial {V_{\mathrm{GS}}}^2} = (\gamma+1)(\gamma+2)\frac{(A+L/\kappa C_{\mathrm{i}})/W}{|V_{\mathrm{GS}}-V_{\mathrm{T}}^{\mathrm{eff}}|^{\gamma+3}}. \tag{5.36}$$

Then, we define the ratio η as the numerical ratio between the first and second derivative of R_{on} with respect to V_{GS}:

$$\eta = -\frac{\partial R_{\mathrm{on}}/\partial V_{\mathrm{GS}}}{\partial^2 R_{\mathrm{on}}/\partial {V_{\mathrm{GS}}}^2} = \frac{V_{\mathrm{GS}}-V_{\mathrm{T}}^{\mathrm{eff}}}{\gamma+2}. \tag{5.37}$$

This is a linear function of V_{GS} along the range of gate voltage where μ and R_{C} depends on the power-law. Then, from the η-versus-V_{GS} plot, the threshold voltage V_{T} and exponent of the power-law dependence γ can be estimated referring respectively to the V_{GS}-axis intercept and slope.

The ratio η method was originally developed for a model with power-law dependent μ and constant R_{C} and tested for inorganic FETs [221]. Here, the feasibility of this method is extended for FETs with the power-law dependent μ and R_{C}. Since the power-law dependence of R_{C} originates from that of μ, this demonstration improves physical completeness of the ratio η method.

Computation of the Ratio η

A simple and compact computation of the ratio η is possible based on Taylor series expansion of R_{on} limited to the second order of V_{GS}. According to the expansion, we have

$$R_{\mathrm{on}_{n\pm1}} \simeq R_{\mathrm{on}_n} \pm \left.\frac{\partial R_{\mathrm{on}}}{\partial V_{\mathrm{GS}}}\right|_n \Delta V_{\mathrm{GS}} + \frac{1}{2}\left.\frac{\partial^2 R_{\mathrm{on}}}{\partial {V_{\mathrm{GS}}}^2}\right|_n \Delta {V_{\mathrm{GS}}}^2, \tag{5.38}$$

where R_{on_n} represents a sequence of on-state resistance obtained discretely from the sequence of drain current I_{D_n} corresponding to the sequence of gate voltage V_{GS_n} that are equally spaced by $\Delta V_{\mathrm{GS}} = V_{\mathrm{GS}_{n+1}} - V_{\mathrm{GS}_n} = V_{\mathrm{GS}_n} - V_{\mathrm{GS}_{n-1}}$. Then, the sequence of ratio η_n can be determined as

$$\eta_n = -\frac{\partial R_{\mathrm{on}}/\partial V_{\mathrm{GS}}|_n}{\partial^2 R_{\mathrm{on}}/\partial {V_{\mathrm{GS}}}^2\big|_n} = \frac{(R_{\mathrm{on}_{n-1}} - R_{\mathrm{on}_{n+1}})\Delta V_{\mathrm{GS}}}{2(R_{\mathrm{on}_{n+1}} - 2R_{\mathrm{on}_n} + R_{\mathrm{on}_{n-1}})}. \tag{5.39}$$

Similarly to conventional metal-insulator-semiconductor FETs, the sub-threshold drain current I_{sub} of OFETs is dominantly manifested by the diffusion of the charge carriers. Thus, at variance with (5.8), I_{sub} is written as

$$I_{\mathrm{sub}} = I_0 \mathrm{exp}\left[-\frac{\ln 10}{S}\left(V_{\mathrm{GS}} - V_{\mathrm{T}}\right)\right], \tag{5.40}$$

where I_0 is the sub-threshold current at V_{T} and S is the sub-threshold slope. Then, R_{on} in sub-threshold regime becomes

$$R_{\mathrm{on}} = \frac{V_{\mathrm{DS}}}{I_{\mathrm{sub}}} = \frac{V_{\mathrm{DS}}}{I_0}\mathrm{exp}\left[\frac{\ln 10}{S}\left(V_{\mathrm{GS}} - V_{\mathrm{T}}\right)\right] \tag{5.41}$$

with its sequence

$$R_{\mathrm{on}_{n\pm1}} = \mathrm{exp}\left[\pm\frac{\ln 10}{S}\Delta V_{\mathrm{GS}}\right] R_{\mathrm{on}_n}. \tag{5.42}$$

Substituting $R_{\mathrm{on}_{n\pm1}}$ in (5.39) by (5.42), we have an asymptotic limit of η below the threshold voltage

$$\eta_n = \frac{\Delta V_{\mathrm{GS}}}{2}\mathrm{coth}\left[\frac{\ln 10 \Delta V_{\mathrm{GS}}}{2S}\right], \tag{5.43}$$

which, as soon as $|\Delta V_{\mathrm{GS}}| > |2S/\ln 10|$, is simplified into

$$\eta_n \simeq \frac{\Delta V_{\mathrm{GS}}}{2}. \tag{5.44}$$

In summary, the ratio η follows a straight line along the range of V_{GS} above threshold voltage and shows asymptotic behaviour near and below threshold voltage.

Other transistor parameters

In order to model I_{D} based on (5.33) from Section 5.2.3, other parameters must be determined such as κ, R_{C}^{∞} and A. First, one method of choice is the TLM which enables a separated extraction of κ by (5.16), R_{C}^{∞} and A by (5.19) from the gate voltage dependent mobility and contact resistance data obtained from multiple

transistors. Second, we emphasize that R_{C}^{∞} and the ensemble of $A + L/\kappa C_{\mathrm{i}}$ can be extracted by (5.34) and used for the subsequent modelling and analysis. This extraction method engages only one transistor. The detailed way of conduct of two methods will be demonstrated in the following section.

5.3 Numerical modelling

The genuine features of the proposed drain current model are power-law dependence of mobility and contact resistance on gate voltage:

$$\mu = \kappa |V_{\mathrm{GS}} - V_{\mathrm{T}}^{\mathrm{eff}}|^{\gamma}, \tag{5.45}$$

and

$$R_{\mathrm{C}} W = R_{\mathrm{C}}^{\infty} W + \frac{A}{|V_{\mathrm{GS}} - V_{\mathrm{T}}^{\mathrm{eff}}|^{-\gamma-1}}, \tag{5.46}$$

where κ is the constant of proportionality for the mobility, γ is the power-law exponent, and $V_{\mathrm{T}}^{\mathrm{eff}} = V_{\mathrm{T}} + V_{\mathrm{DS}}/2$ is the effective threshold-voltage, W is the the channel width, R_{C}^{∞} is the non-gateable contact resistance and A is the constant of proportionality for the contact resistance.

As described earlier, the physical origin was elaborated initially adopting the multiple trapping-and-release model for the charge carrier transport in amorphous silicon semiconductors [207]. However, a relevant study has not been sufficiently conducted for a more adequate theoretical description of charge carrier transport in organic semiconductors established on thermally-assisted hopping transport in Gaussian density-of-states (DOS), i.e. the Gaussian disorder model (GDM) [31].

Under the GDM, the mobility is unambiguously defined by

$$\mu = \sum_{i,j} W_{ij} p_i (1 - p_j) R_{ijx} / pFV \tag{5.47}$$

with the transition rate for hopping W_{ij} from site i to j, probability of occupancy p_i of site i, distance between sites R_{ij}, carrier concentration $p = \langle p_i \rangle / a^3$, electric field F, and system volume V. In spite of its physical exactitude, this *ab inito* method, requiring Monte Carlo simulation, seldom leads to a simple mathematical equation feasible for device and circuit simulation.

Instead, a physical continuous equation was formulated by the product of the temperature dependent intrinsic mobility $\mu_0(T)$, temperature and carrier concentration dependent enhancement factor $g_1(T, c)$, and temperature and electric field

Table 5.1: List of Physical Parameters Used for ATLAS Simulation

Layer	Parameter	Value
Organic semiconductor	Maximum of HOMO	5.6 ∼ 5.9 eV
	Width of Gaussian DOS	0.20 eV
	Total DOS	3×10^{21} cm^{-3}
	Dielectric constant	4
	Hole mobility	3×10^{-3} cm^2/Vs
Gate insulator	Dielectric constant	2.5
Source/drain	Work function	4.9 eV
Gate	Work function	4.3 eV

dependent enhancement factor $g_2\,(T, F)$ [32]:

$$\mu(T, p, F) = \mu_0\,(T) \times g_1\,(p, T) \times g_2\,(F, T)\,, \tag{5.48}$$

which successfully reproduces the charge carrier mobility (5.47). The implementation of (5.48) in a technology computer-aided design (TCAD) software enables a finite-element method (FEM) based 2-D device simulation with a full physical rigorousness. We have presented, in chapter 4, a comparative study in a quasi 1-D rectifying diode showing a good agreement of the mobility model with experimental data.

In this section, we will present a systematic 2-D device simulation of OFETs to delineate on the power-law dependence of the field-effect mobility (5.45) and contact resistance (5.46) on gate voltage and to examine their feasibility. For the analysis of the numerical simulation data, a consistent parameter extraction method is employed.

5.3.1 Injection barrier and contact resistance

We used ATLAS from SILVACO for a systematic numerical simulation of OFETs having 2-D structure based on the FEM. The simulator solves coupled Poisson's, continuity and drift-diffusion equations upon considering Gaussian density-of-states (DOS), Generalized Einstein relation and Pasveer mobility model [32, 145, 222].

Figure 5-5(a) shows the structure of simulated OFETs in a bottom-gate/top-contact configuration. The channel width is $W = 1$ μm, semiconductor layer thickness $d_\mathrm{s} = 60$ nm, insulator layer thickness $d_\mathrm{i} = 600$ nm and contact length $d_\mathrm{l} = 10$ μm. The channel length is varied as $L = 30$, 40, 50, 60 and 80 μm to extract field-effect mobility using the transfer length method (TLM).

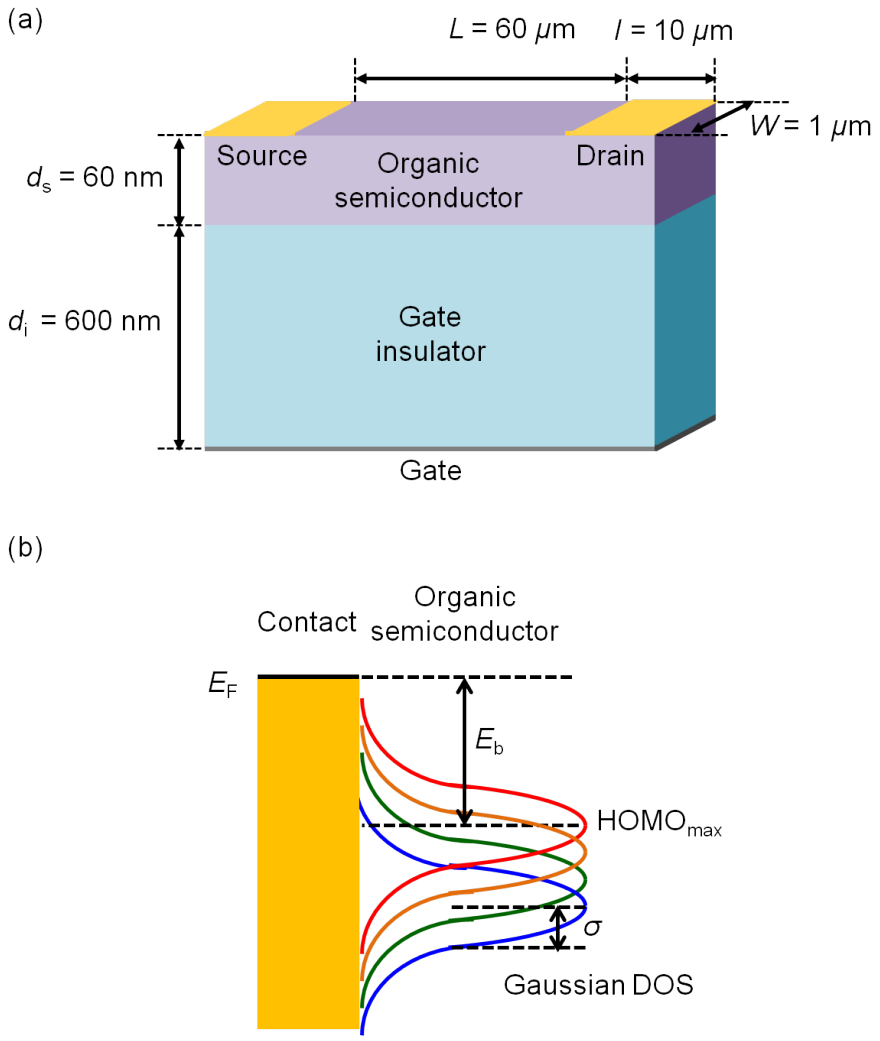

Figure 5-5: (a) OFET device structure in bottom-gate/top-contact configuration. (b) Electronic structures at the contact/organic semiconductor interface. E_{F} denotes the Fermi level, $\mathrm{HOMO}_{\mathrm{max}}$ the maximum of the HOMO, σ the half-width at half-maximum of Gaussian DOS, and E_{b} the injection barrier varied as 0.7, 0.8, 0.9 and 1.0 eV.

Figure 5-5(b) shows the electronic structure at the interface between the contact and organic semiconductor with a Gaussian DOS described by

$$g(E) = \frac{N_0}{\sqrt{2\pi}\sigma} \exp\left[-\frac{(E - \mathrm{HOMO}_{\mathrm{max}})^2}{2\pi\sigma^2}\right], \tag{5.49}$$

where N_0 denotes the total DOS, σ the half-width at half-maximum (a.k.a. the width of Gaussian DOS), $\mathrm{HOMO}_{\mathrm{max}}$ the maximum of the highest-occupied molecular orbital (HOMO). Then, the injection barrier E_{b} is defined as the distance between the $\mathrm{HOMO}_{\mathrm{max}}$ and the Fermi level E_{F} of the contact metal [162]. In order

to analyse the effect of the injection barrier on the contact resistance, E_{b} is varied in from 0.7 to 1.0 eV by changing the position of $\mathrm{HOMO}_{\mathrm{max}}$ while keeping the position of E_{F} constant (see Figure 5-5(b)). Note that the values of E_{b} correspond to around 0.0 to 0.2 eV considering the effect of disorder in lowering E_{b} [162].

Table 5.1 summarizes the physical parameters used for the simulation. The parameters for organic semiconductor are chosen based on experimental measurements of pentacene thin-film: $\sigma = 0.20$ eV from ultra-violet photoemission spectroscopy [129], $N_0 = 3{\times}10^{21}$ cm^{-3} from the density of molecules in thin-film [93], the dielectric constant $\epsilon_{\mathrm{s}} = 4$ from impedance spectroscopy [156]. Hole mobility is denoted by $\mu_0\,(T)$ at 300 K. The dielectric constant of gate insulator, $\epsilon_{\mathrm{i}} = 2.5$, corresponds to poly(methylmethacrylate) polymer gate dielectric material measured from impedance spectroscopy [223]. The work functions of contact and gate electrodes are typical of gold and aluminium.

5.3.2 Robustness of the parameter extraction method

Figure 5-6(a) shows simulated transfer characteristics of OFETs (drain current I_{D} as a function of gate voltage V_{GS}) for several L and E_{b}, where I_{D} decreases with L and E_{b}. The supra-linear transfer characteristics is attributed to the variable hole mobility in (5.48) as well as small contact resistance. For further analysis on the gate voltage dependence of μ and R_{C}, the R_{on}-versus-L plot was drawn upon defining the on-state resistance $R_{\mathrm{on}} = V_{\mathrm{DS}}/I_{\mathrm{D}}$. The linear increase of R_{on} with L for all E_{b} observed in Figure 5-6(b) enables analysis by the TLM based on the proposed contact resistance model:

$$R_{\mathrm{on}}W = R_{\mathrm{C}}^{\infty}W + \frac{A + L/\kappa C_{\mathrm{i}}}{|V_{\mathrm{GS}} - V_{\mathrm{T}}^{\mathrm{eff}}|^{\gamma+1}}. \tag{5.50}$$

where C_{i} is the insulator capacitance per unit area. The field-effect mobility and contact resistance can be extracted from the slope and intercept of the $R_{\mathrm{on}}W$-versus-L plot when the threshold voltage V_{T} is determined.

The ratio η method is a consistent parameter exraction method to extract V_{T} and γ simultaneously from OFETs with power-law mobility and contact resistance, where η is defined by the numerical ratio of the second to the first derivative of R_{on} in the linear regime. The calculated η shows a discretizable linear dependence to V_{GS} above threshold voltage, which gives an evidence to the power-law mobility (see Figure 5-6(c)). Referring to the analytical expression for η (inset equation in Figure 5-6(c)), $V_{\mathrm{T}}^{\mathrm{eff}}$ and γ were estimated from the x-intercept and slope of the η-versus-V_{GS} plot. First, as shown in Figure 5-6(d), the extracted values of $V_{\mathrm{T}}^{\mathrm{eff}}$

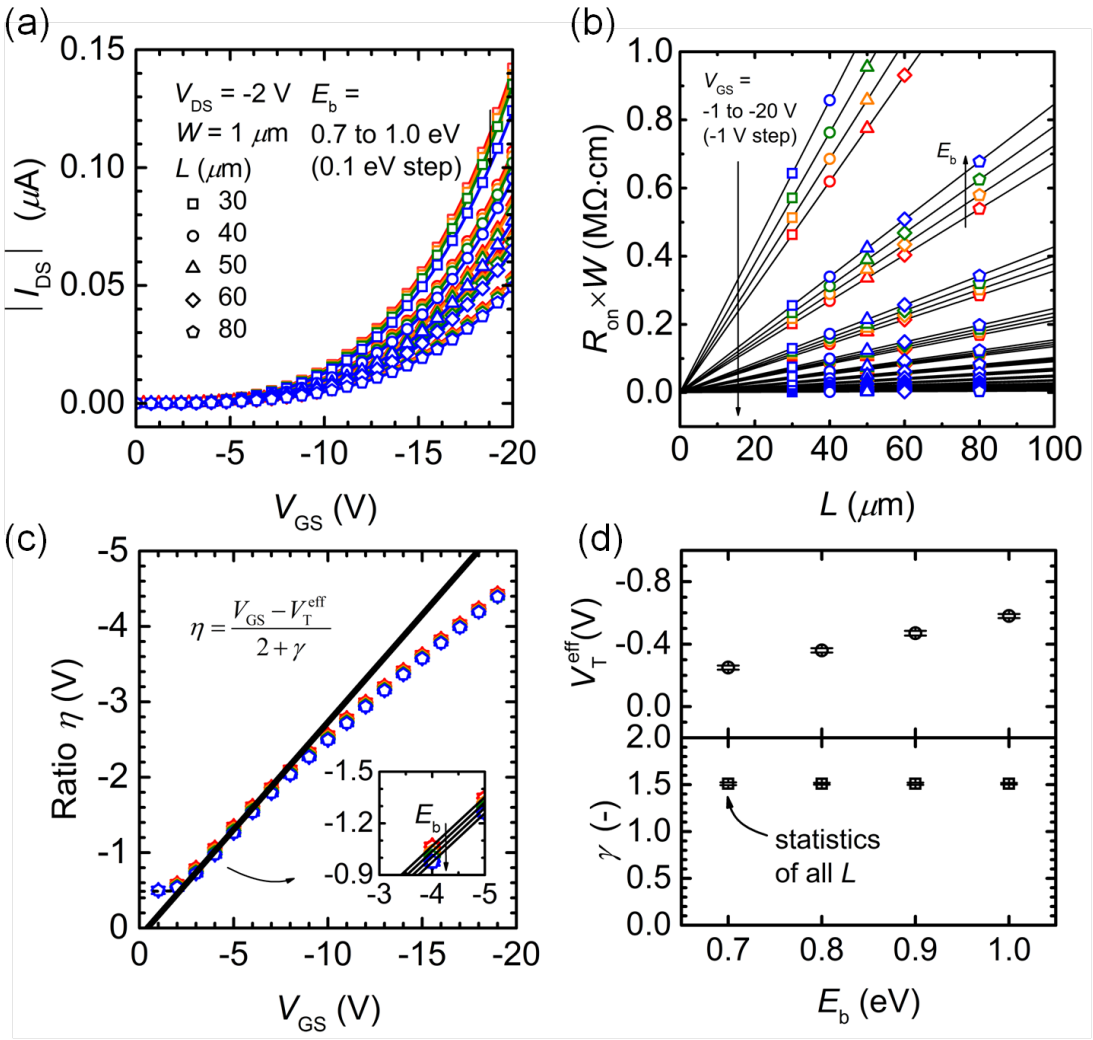

Figure 5-6: (a) Simulated transfer characteristics of OFETs. (b) the $R_{on}W$-versus-L plot. (c) The ratio η-versus-V_{GS} plot for parameter extraction (The inset is a close-up view). In the panels (a-c), each symbol represents a different channel length L and each color represents a different injection barrier E_b. (d) The dependence of the extracted effective threshold voltage V_T^{eff} and power-law exponent γ on E_b and L. Note that V_T^{eff} varies significantly with E_b, whereas γ does not.

and γ do not show the dependence on L. We can infer that the channel length of a transistor has no significant effect on when the transistor turns on and how mobility changes with gate voltage. Second, V_T^{eff} increases with E_b, i.e. V_T^{eff} = -0.25, -0.36, -0.47 and -0.58 V respectively for E_b = 0.7, 0.8, 0.9 and 1.0 eV, whereas γ does not change significantly (γ = 1.51 in average). The former originates from the fact that a larger gate voltage is required to create a conducting channel when the number of holes present in the semiconductor layer at thermal-equilibrium are smaller as a result of a less favorable injection from contact due to a larger injection barrier. The latter implies that how mobility increases with gate voltage is related

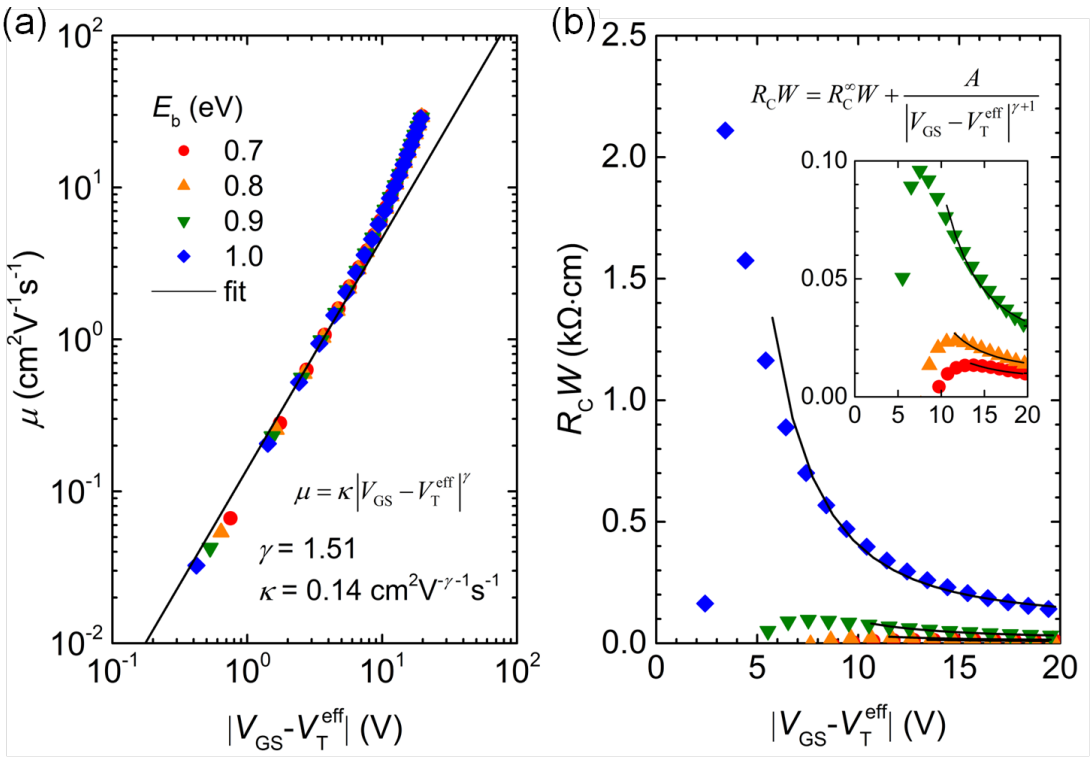

Figure 5-7: Extracted (a) field-effect mobility μ and (b) contact resistance R_C as a function of effective gate voltage $|V_{GS} - V_T^{eff}|$ based on the transfer length method for several injection barriers. Good fits to power-law mobility and contact resistance models are observed (the solid lines and inset equations).

less to the injection barrier but more to the width of Gaussian DOS. A wide range of gate voltage for each discretizable linear dependence could also account for this behavior.

5.3.3 Power-law dependent mobility and contact resistance

Finally, the field-effect mobility and contact resistance were extracted from the slope and intercept of the $R_{on}W$-versus-L plot by using (5.50). Note that, for each electronic structure, different value of V_T^{eff} should be used for the extraction of μ. The principal feature of Figure 5-7 is a good fit of extracted μ and R_C to respective power-law model (inset equations) over a wide range of V_{GS} with all fitting parameters unambiguously extracted.

In depth, first, a perfect overlapping of the extracted field-effect mobility from OFETs with different E_b proves the usefulness of κ and γ for the description of charge carrier transport excluding the effect of the contact resistance as well as the robustness of the extraction method (Figure 5-7(a)). A correlation can be made between the width of Gaussian DOS, $\sigma = 0.20$ eV, and characteristic temperature,

T_C = 753 K, calculated from $\gamma = T_c/T - 1$ assuming the discrete approximation of a Gaussian to exponential DOS [168].

Second, the significant modulation of R_C by V_{GS} can be modelled successfully with a unique power-law exponent ($\gamma = 1.51$) for all E_b despite the great difference in the magnitude of R_C. The effect of E_b on R_C is reflected in the non-gateable contact resistance and constant of proportionality that decrease with E_b: A = 72, 24, 8 and 5 kΩ·cm·$V^{\gamma+1}$ and R_C^{∞} = 95, 19, 10 and 7 Ω·cm for E_b = 0.7, 0.8, 0.9 and 1.0 eV.

This result provides a physical ground to the adoption of the empirical power-law mobility and contact resistance in compact modelling of OFETs and parameters for a quantitative evaluation on the effect of disorder in organic semiconductor on charge carrier transport and injection in OFETs.

5.4 Experimental validation

5.4.1 Transfer and output characteristics

Figure 5-8 shows representative transfer and output characteristics of a pentacene-based p-type OFET with $L = 60$ μm and $W = 1$ mm. For the linear regime transfer characteristics, the OFET is applied with $V_{DS} = -2$ V. If the transfer characteristics were interpreted using the ideal drain current model in Section 5.2.1, then one would infer an effective threshold voltage $V_{T,LEM}^{eff}$ = -24.2 V and field-effect mobility μ_{LEM} = 0.21 $cm^2V^{-1}s^{-1}$ extracted by the linear extrapolation method (LEM) taking C_i = 3.68 nF·cm^{-2}. However, there would be a problem for interpreting the large drain current value in the sub-threshold or around-threshold region. Moreover, the straight line, which also represents the ideal drain current model, shows a limited range of fit.

In fact, this seemingly linear transfer and output characteristics do not provide a conclusive evidence to exclude the existence of gate voltage dependence of μ and R_C which are principal factors giving rise to a non-linearity in the transfer and output characteristics. Therefore, an in-depth analysis is required to verify the existence and gate voltage dependence of μ and R_C.

5.4.2 Ratio η method

The ratio η method is a technique to extract V_T^{eff} and γ that dictate the power-law dependence of μ and R_C to verify the power-law dependence of μ. Figure 5-9 shows η calculated by (5.39) as a function of V_{GS} for different gate voltage spacing

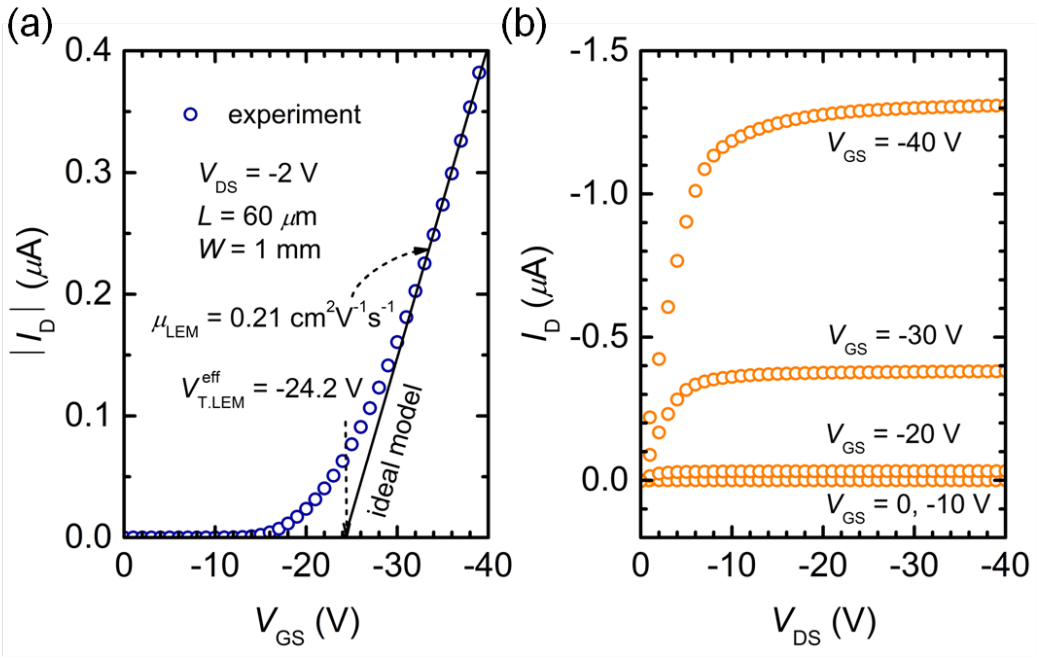

Figure 5-8: Measured (a) transfer and (b) output electrical characteristics of a p-type organic field-effect transistor based on pentacene. The solid line represents the parameter extraction by linear extrapolation method as well as the ideal drain current model.

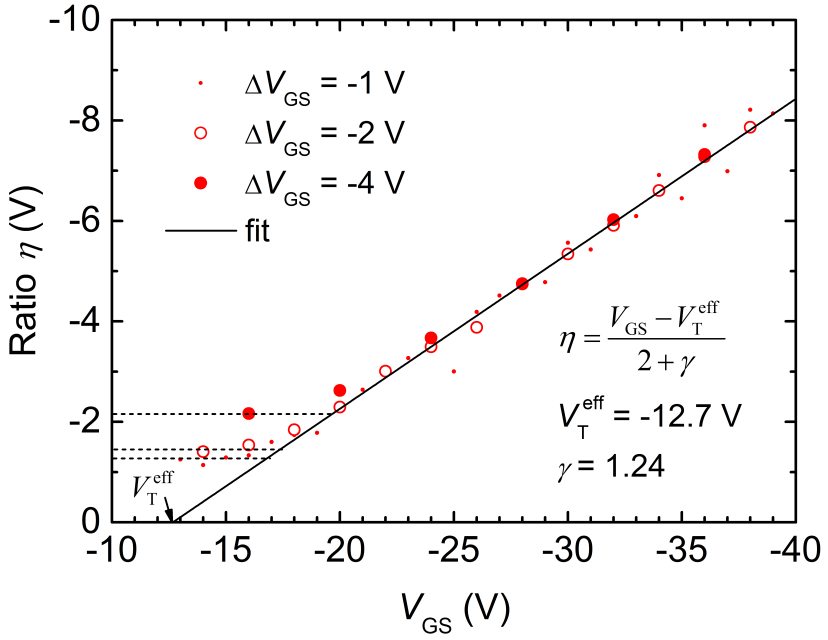

Figure 5-9: Ratio η as a function of V_{GS} calculated for different values of ΔV_{GS} using (5.39) from the transfer characteristics of a pentacene-based OFET with $L = 60$ μm (symbols). The solid line is a fit to (5.37) for the extraction of the effective threshold voltage V_T^{eff} and power-law exponent γ. Dotted lines are a guide to the eye for the asymptotic behaviour calculated by (5.43).

ΔV_{GS} =-1, -2 and -4 V. First, the curves show a linear dependence on V_{GS} for large enough V_{GS}. Although we note a more pronounced noise for a smaller ΔV_{GS}, the extracted values of V_T^{eff} and γ do not exhibit a significant dependence on ΔV_{GS}. This makes the ratio η method free of measurement noise problem unlike other extraction methods that involve differentiation. Furthermore, parameters can be precisely determined from only a few I_D-versus-V_{GS} measurement points spaced apart by ΔV_{GS} amounting to several volts. From the x-intercept and slope of the straight lines, V_T^{eff} and γ are estimated as -12.7 V and 1.24 by (5.37). We note that V_T^{eff} extracted by the ratio η method is around 12 V below $V_{T.LEM}^{eff}$. In addition, a non-zero γ and a good fit of η to (5.37) confirm the power-law dependence of μ on the gate voltage.

Second, the curves show an asymptotic behaviour for V_{GS} near and below V_T^{eff} with different saturation values for each curves. These values match well with the model of (5.43), η = -1.3 V (ΔV_{GS} = -1 V), -1.5 V (-2 V) and -2.2 V (-4 V), where the sub-threshold slope ($S = 2.8$ V/dec) extracted from Figure 5-13(a) is used. We note that the ratio η exhibits a complete asymptotic behaviour at V_T^{eff}. Thus, we can infer that V_T^{eff} indicates the gate voltage at which drain current is dominantly manifested by the diffusion of charge carriers.

5.4.3 Transmission-line method

The TLM allows analysis of both R_C and μ and their gate voltage dependence. Firstly, we draw the $R_{on}W$-versus-L plot and extrapolate the linear regression line to zero L. Then, R_CW is directly read from the y-intercept of the linear regression, while μ is estimated from the slope by excluding the contribution of $C_i|V_{GS} - V_T^{eff}|$ by (5.15). At this point, we emphasize that the value of V_T^{eff} used to extract μ must be obtained from a linear regime the transfer characteristics where (5.15) as well as (5.13) were driven.

As shown in Figure 5-10, $R_{on}W$ increases linearly with L, and the extrapolation of $R_{on}W$ to $L = 0$ indicates a non-zero value. This brings evidence for the existence of R_C, which makes the drain current models with R_C more suitable than the ideal model or a model that uniquely considers the gate voltage dependent mobility. Moreover, in contrast to (5.15) established on the constant R_C model (see Figure 5-2(b)), the gate voltage dependence of R_C is apparent from the change of y-axis intercept. Therefore, R_C must be considered as a variable resistor modulated by the gate voltage (inset of Figure 5-10).

In particular, the power-law dependence on the gate voltage is observed for R_C (see Figure 5-11(b)). This ensures the physical consistency of using the drain

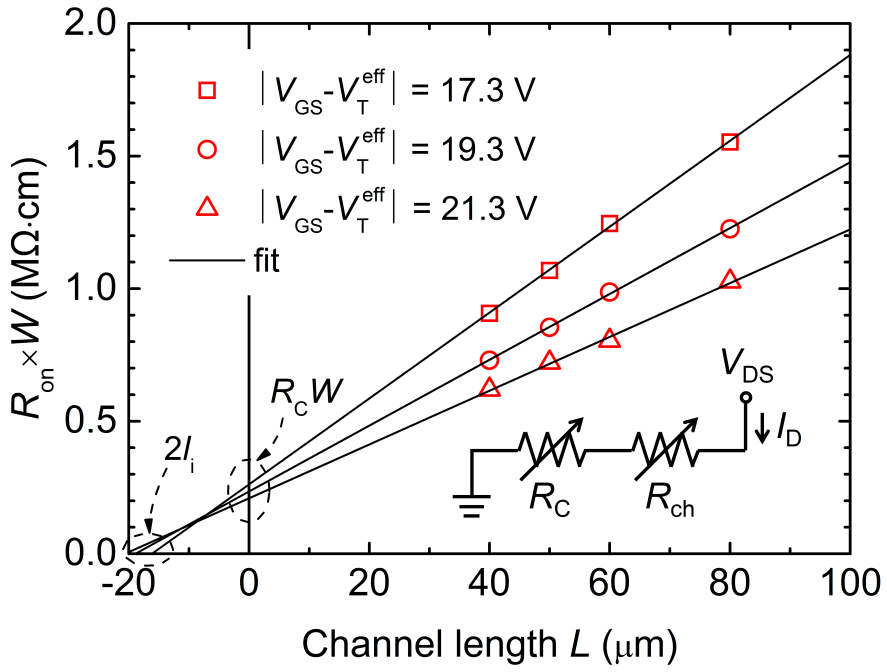

Figure 5-10: $R_{on}W$-versus-L plot for the TLM. The inset is the equivalent circuit for the drain current path that consists of the channel and contact resistors (R_{ch} and R_C). Both resistors are depicted as a variable resistor, which emphasizes the modulation of R_{ch} and R_C by V_{GS}.

current model and on-state resistance equation that encompass the gate voltage dependence of R_C and μ by power-law for the subsequent quantitative analysis and modelling of R_C and μ, and for the extraction of parameters required for the analysis. We note, in addition, that the transfer length l_i estimated from the x-intercept of Figure 5-10 amounts approximately to 10 μm. Since the contact length of the fabricated OFETs is $l = 100$ μm, l/l_i is indeed much greater than 1.

5.4.4 Power-law dependent R_C and μ

Figure 5-11 shows a strong dependence of both μ and $R_C W$ on the effective gate voltage $|V_{GS} - V_T^{eff}|$. In general, μ increases and R_C decreases when $|V_{GS} - V_T^{eff}|$ increases. The former can be properly described by the rise of the Fermi level towards the transport energy in the Gaussian DOS under the hopping transport model [33]. The latter originates from the increase of the mobility and hole concentration in the bulk when $|V_{GS} - V_T^{eff}|$ increases.

Notably, both μ and $R_C W$ exhibit the power-law dependence on the gate voltage. The salient feature of (5.19) is the combination of non-gateable con-

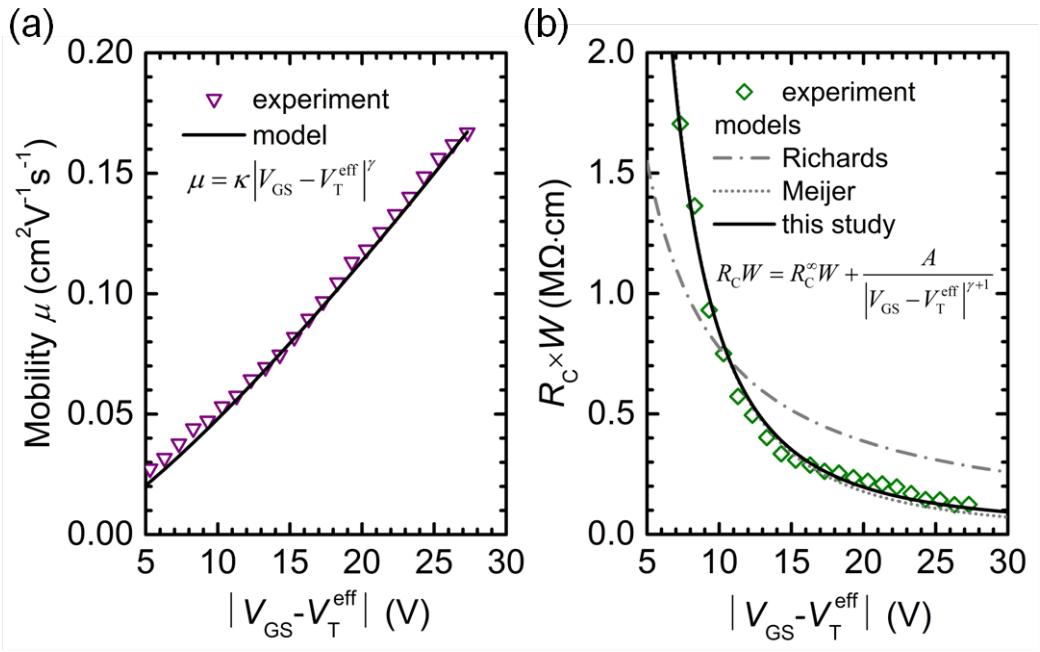

Figure 5-11: (a) Mobility and (b) contact resistance as a function of the effective gate voltage $|V_{GS} - V_T^{eff}|$ extracted by the TLM. The solid lines are a fit to the power-law mobility and contact resistance models (inset equations). Thanks to pre-determined parameters by the ratio method ($V_T^{eff} = -12.7$ V and $\gamma = 1.24$), all the rest (κ, A and $R_C^{\infty}W$) can be determined by linear extrapolation. Dotted and dash-dot lines correspond to the model of Richards and Meijer, which is a specific case of the proposed model where $\gamma = 0$ or $R_C = 0$.

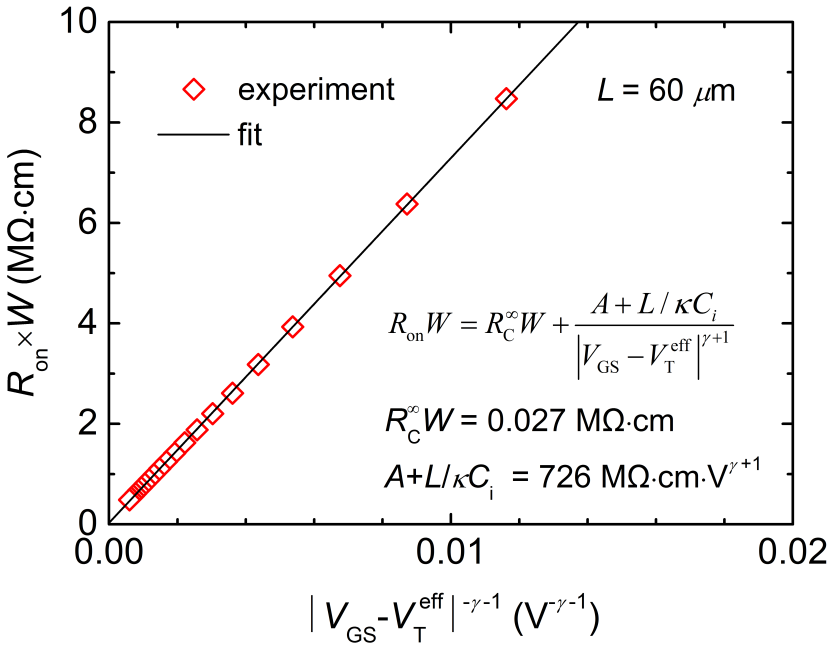

Figure 5-12: Width-normalized on-state resistance extracted from a single OFET ($L = 60$ μm) as a function of $|V_{GS} - V_T^{eff}|^{-\gamma-1}$. The solid line is a fit to the model with power-law R_C and μ that leads to the non-gateable contact resistance R_C^{∞}.

Table 5.2: Comparison of the extracted parameters based on the transmission length method (TLM) and the single transistor method from pentacene OFETs.

Parameters	TLM	Single transistor
Mobility proportionality constant, κ [$\mathrm{cm^2V^{-\gamma-1}s^{-1}}$]	2.8×10^{-3}	-
Width-normalised contact resistance proportionality constant, A [$\mathrm{M\Omega\cdot cm\cdot V^{\gamma+1}}$]	142	-
Width-normalised on-state resistance proportionality constant, $A + L/(\kappa C_\mathrm{i})$ [$\mathrm{M\Omega\cdot cm\cdot V^{\gamma+1}}$]	732	726
Contact resistance asymptote, R_C^∞ [MΩ]	0.023	0.027

tact resistance and gateable contact resistance following power-law the benefit of which can be elaborated more effectively in comparison to previous models (Figure 5-11(b)). First, the proposed model shows significantly improved fit compared to the best least-square fit by the model of Richards [188] that corresponds to a specific case of (5.19) when $\gamma = 0$. This is accounted from the fact the model of Richards considers only the modulation of the bulk carrier concentration by the gate voltage in modelling the bulk resistivity whereas that of the bulk mobility is not counted. Second, the inclusion of non-gateable contact resistance provides a better result compared to the Meijer's model [224] that corresponds to $R_\mathrm{C}^\infty = 0$, especially, in high gate voltage range $|V_\mathrm{GS} - V_\mathrm{T}^\mathrm{eff}| > 15$ V where the contribution of injection at the contact becomes dominant over bulk transport.

Since we are able to extract both γ and $V_\mathrm{T}^\mathrm{eff}$ through the ratio η method, it is possible to extract all other parameters (κ, A and R_C^∞) by linear fitting with no chance of ambiguity: κ from the slope of the μ-versus-$|V_\mathrm{GS}-V_\mathrm{T}^\mathrm{eff}|^\gamma$ plot by (5.16); A and $R_\mathrm{C}^\infty W$ from the slope and y-intercept of the $R_\mathrm{C}W$-versus-$|V_\mathrm{GS} - V_\mathrm{T}^\mathrm{eff}|^{-\gamma-1}$ plot by (5.19). On the contrary, if γ were an unknown fitting parameter, a non-linear numerical fitting would be required to extract γ together with other parameters such as κ, A and R_C^∞, which involves cumbersome computational approach so that estimated fitting parameters would suffer from a certain degree of ambiguity.

We note that R_C^∞ is significantly smaller than R_C (i.e. the sum of non-gateable and gateable contact resistance) even for a large V_GS: 0.023 versus 0.2 MΩ·cm at $V_\mathrm{GS} = 32.7$ V. This indicates that the access resistivity r_acc at the Au/pentacene interface is less responsible for the contact resistance. Instead, R_C mostly originates from the vertical current path across the bulk of pentacene layer within a practical operation range of V_GS, which is co-evidenced by the strong V_GS modulation of R_C

(Section 5.2.2).

5.4.5 Extraction of R_{C}^{∞} from a single OFET

A single transistor can provide sufficient parameters to model I_{D} and to analyse the injection properties at the contact, although one must employ the TLM for a complete analysis on the gate voltage dependence of R_{C} and μ as Natali insisted in [225]. As shown in Figure 5-12, the $R_{\mathrm{on}}W$-versus-$|V_{\mathrm{GS}} - V_{\mathrm{T}}^{\mathrm{eff}}|^{-\gamma-1}$ plot shows an excellent linearity which is coherent to (5.34). Thus, R_{C}^{∞} and $A + L/\kappa C_{\mathrm{i}}$ can be extracted from the intercept and slope. The values determined from a single transistor are remarkably close to the averaged values extracted from the TLM (see Table 5.2). This confirms the robustness of the parameter extraction from a single transistor. Using R_{C}^{∞} and $A + L/\kappa C_{\mathrm{i}}$, drain current can be fully calculated by (5.33).

We emphasize that, based on the constant R_{C} and power-law μ model (5.18), the y-intercept is often mistakenly regarded as the contact resistance legitimate for the entire gate voltage range despite of its several orders of magnitude smaller value than that determined from the TLM [219]. Similarly, κ would be overestimated from the slope by referring to (5.18) rather than (5.35). Distinguishing the non-gateable and gateable contact resistance provides a clear physical meaning to extracted parameters, which enables a rigorous assessment of the contact property of OFETs.

5.4.6 Comparison of experimental data with models

Figure 5-13 compares the experimental data with the ideal (I), constant R_{C} and power-law μ (CR) and power-law R_{C} and μ (PRM) drain current models in terms of the transfer characteristics and relative difference defined as

$$\delta = \frac{I_{\mathrm{D}}^{\mathrm{experiment}} - I_{\mathrm{D}}^{\mathrm{model}}}{I_{\mathrm{D}}^{\mathrm{experiment}}} \times 100. \tag{5.51}$$

The PRM model exhibits an excellent match to the experimental data with a wide range of fit. A more adapted fit ($\delta < 5\%$) is obtained with the parameters extracted from the single transistor (PRM2, see Figure 5-12 for the parameters) than from the TLM (PRM1, see Figure 5-11), which is predictable since the latter is averaged values. On the other hand, the ideal drain current model (5.9) (I, solid line in black) has very limited range of fit ($V_{\mathrm{GS}} < V_{\mathrm{T.LEM}}^{\mathrm{eff}} =$ -23.2 V) not to mention its lack of physical sense. Lastly, we observe that sweeping the value of constant

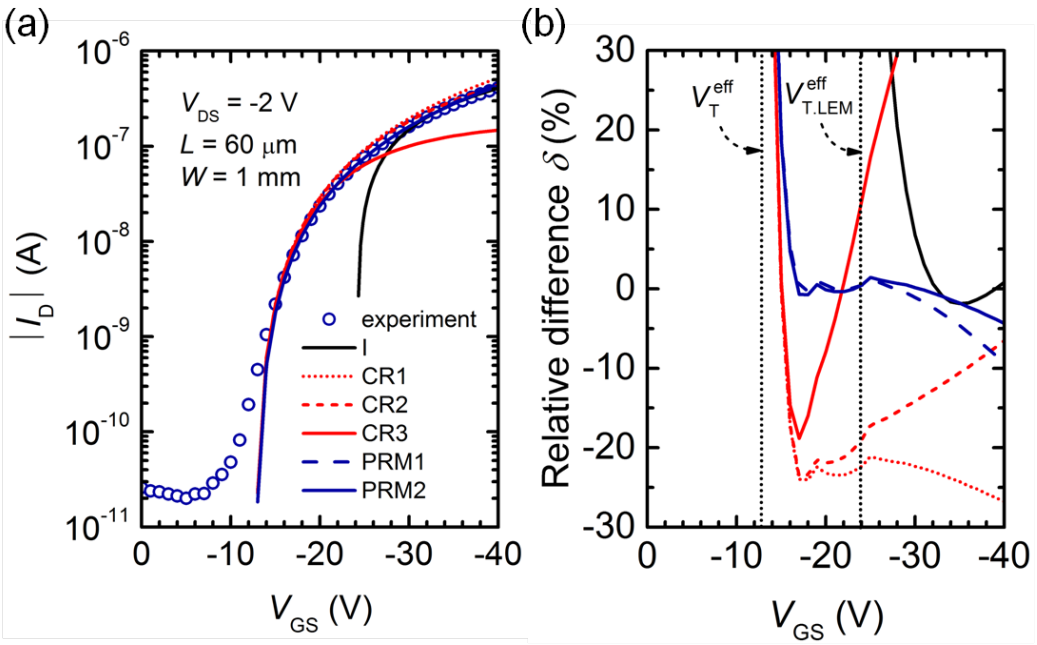

Figure 5-13: Comparison between the experimental data with the ideal (I, solid line in black), constant R_C and power-law μ (CR, lines red) and power-law R_C and μ (PRM, lines in blue) drain current models in terms of (a) transfer characteristics and (b) relative difference.

R_C in (5.17) does not lead to a sufficient fit giving $\delta \sim 20\%$, $R_C W = 0.027$ (CR1), 0.1 (CR2) or 1 MΩ·cm (CR3). In short, a wide range of excellent fit demonstrates convincingly the advantage of considering the power-law dependence of R_C and μ for modelling OFETs.

5.5 Compact modelling

5.5.1 Low voltage n-type OFETs

Based on the proposed above threshold drain current model, we proceed in establishing a physically-based compact model applicable for a circuit simulation. In particular, for its importance in organic complementary circuits, we will examine the robustness of a compact model for modelling a flexible low voltage n-type OFET with high stability under ambient conditions such as humidity, light and oxygen.

Figure 5-14 shows the device structure and the chemical structure of electron transporting organic semiconductor and gate insulator. We used TIPS-tetracyanotriphenodi-oxazine (TIPS-TPDO-4CN) as an n-type semiconductor exhibiting an excellent stability in ambient condition [223, 226]. A reliable gate

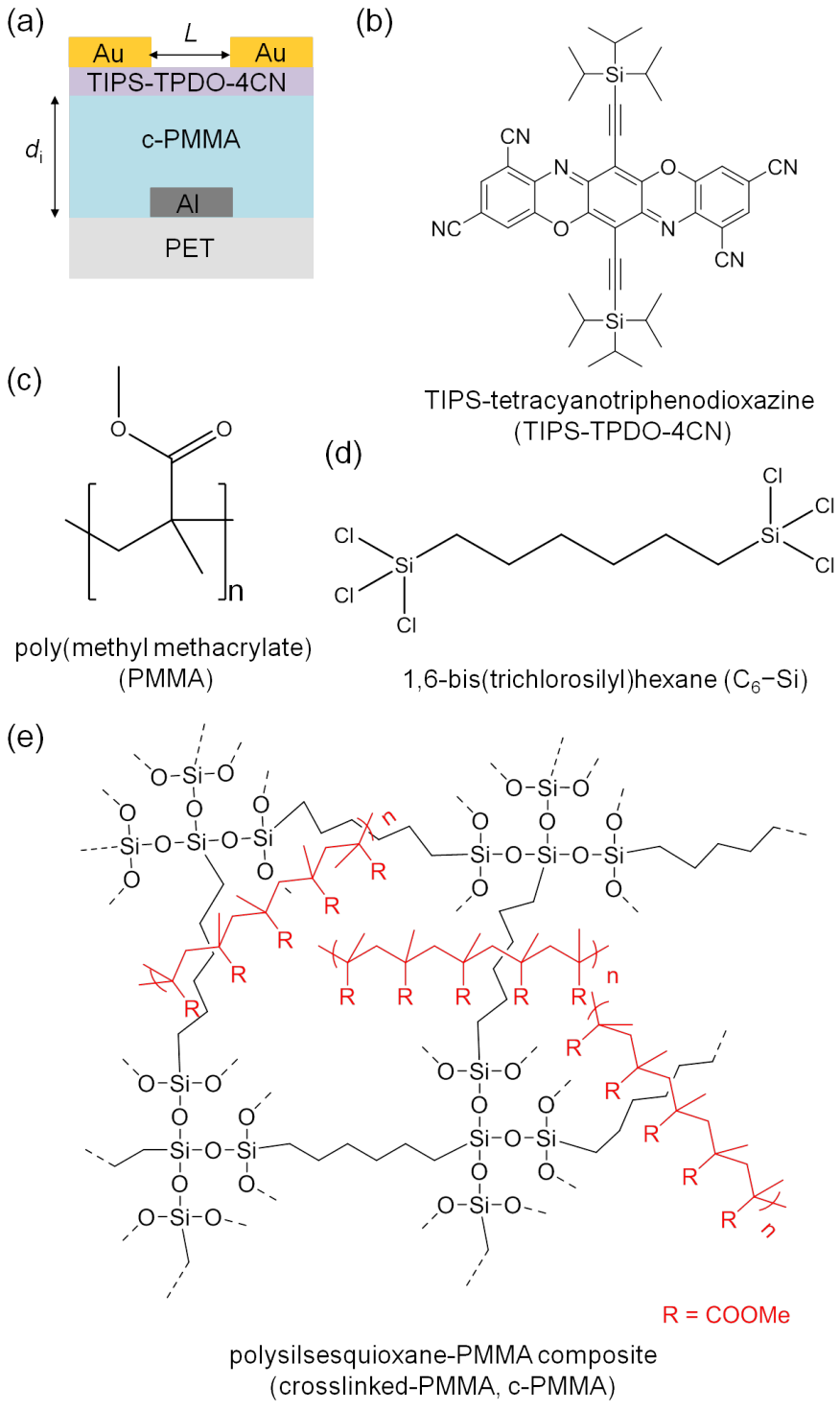

Figure 5-14: (a) Device structure of a low voltage flexible organic field-effect transistor and chemical structures of compounds used in the OFET: (b) TIPS-tetracyanotriphenodioxazine as an *n*-type semiconductor and (c) poly(methyl methacrylate) and (d) 1,6-bis(trichlorosilyl)hexane which form a polymer gate dielectric (e) polysilsesquioxane-PMMA composite. The crosslinking of C_6-Si results in polysilsesquioxane with a three-dimensional structure, which physically confine PMMA reducing the thickness of polymeric gate and increasing the dielectric constant, and hence enabling the low-voltage operation.

dielectric, the easy processing of which is still actively investigated, constitutes a key element for achieving low-voltage operation of OFETs. The operating voltage is concerned with the thickness d_i and relative permittivity (dielectric constant) ϵ_r of the gate dielectric because the drain current is proportional to gate dielectric capacitance density $C_\mathrm{i} = \epsilon_\mathrm{r}\epsilon_0/d_\mathrm{i}$ [190]. The state-of-the-art technologies on the gate dielectrics at process temperature below 150°C comprise the use of high permittivity metal oxides [191], nanometer-thick SAMs (2∼3 nm when used alone [192] or around 6 nm with AlO_x [63, 193]), organic-inorganic hybrid multilayer in few nanometer thickness [194] and thin cross-linked polymers [195–198]. We adopted cross-linked polymer composite as a gate insulator. The polysilsesquioxane-PMMA composite (crosslinked-PMMA or c-PMMA) has a dielectric constant (relative permittivity) of 3.9 at 10 kHz measured by impedance spectroscopy and a thickness of 110 nm, giving capacitance of a 31.4 nF/cm^2.

5.5.2 Improvements on the compact model

Above threshold regime

We express the above-threshold drain current I_above as the product of the linear regime channel conductance g_ch, effective drain voltage V_DSe, and improved saturation asymptotic term $[1 + \lambda(|V_\mathrm{DS}| - \alpha_\mathrm{S}|V_\mathrm{GS} - V_\mathrm{T}|)]$ [227–229]. First, g_ch of a n-type (electron-transporting) OFET is written as

$$g_\mathrm{ch} = \frac{K\mu_\mathrm{FET}(V_\mathrm{GS} - V_\mathrm{T}^\mathrm{eff})}{1 - R_\mathrm{C}K\mu_\mathrm{FET}(V_\mathrm{GS} - V_\mathrm{T}{}^\mathrm{eff})} \tag{5.52}$$

considering, for the first time, the gate bias dependent contact resistance R_C as well as mobility μ_FET by power-law:

$$\mu_\mathrm{FET} = \kappa|V_\mathrm{GS} - V_\mathrm{T}^\mathrm{eff}|^\gamma \tag{5.53}$$

$$R_\mathrm{C} = R_\mathrm{C}^\infty + \frac{A/W}{|V_\mathrm{GS} - V_\mathrm{T}^\mathrm{eff}|^{\gamma+1}}. \tag{5.54}$$

In (5.52), $K = (W/L)C_\mathrm{i}$ and $V_\mathrm{T}^\mathrm{eff} = V_\mathrm{T} + V_\mathrm{DSe}/2$ where W denotes the channel width, L the channel length, C_i the insulator capacitance per unit area, and $V_\mathrm{T}^\mathrm{eff}$ denotes the effective threshold-voltage and V_T the threshold voltage. In (5.53), κ and γ are the constant of proportionality and exponent of the power-law mobility. In (5.54), R_C^∞ is the non-gateable contact resistance and A is a parameter that describes how contact resistance varies with gate bias related to the bulk mobility,

insulator capacitance per unit area, and semiconductor thickness.

Second, the transition from linear-to-saturation regime accounts for the use of V_{DSe} in (5.52)-(5.54):

$$V_{\mathrm{DSe}} = V_{\mathrm{DS}} \left[1 + \left(\frac{V_{\mathrm{DS}}}{V_{\mathrm{sat}}} \right)^{m} \right]^{-1/m}, \tag{5.55}$$

which, as V_{DS} increases, follows V_{DS} when $V_{\mathrm{DS}} \ll V_{\mathrm{sat}}$ and saturates to V_{sat} when $V_{\mathrm{DS}} \gg V_{\mathrm{sat}}$. It is note worthy that $V_{\mathrm{DSe}} \to 0$ when $V_{\mathrm{GS}} \to V_{\mathrm{T}}$.

Finally, by incorporating a saturation modulation parameter $V_{\mathrm{sat}} = \alpha_{\mathrm{S}}(V_{\mathrm{GS}} - V_{\mathrm{T}})$, we obtain a completely new above-threshold drain current equation I_{above} with power-law mobility and contact resistance:

$$I_{\mathrm{above}} = \frac{V_{\mathrm{DS}} \left[1 + \lambda(|V_{\mathrm{DS}}| - \alpha_{\mathrm{S}}|V_{\mathrm{GS}} - V_{\mathrm{T}}|) \right]}{\left[R_{\mathrm{C}}^{\infty} + \dfrac{A/W + 1/(K\kappa)}{\left|V_{\mathrm{GS}} - V_{\mathrm{T}}^{\mathrm{eff}}\right|^{\gamma+1}} \right] \left[1 + \left| \dfrac{V_{\mathrm{DS}}}{\alpha_{\mathrm{S}}(V_{\mathrm{GS}} - V_{\mathrm{T}})} \right|^{m} \right]^{1/m}}. \tag{5.56}$$

Here, we can separately evaluate the contribution of the contact property and the bulk transport on contact resistance by referring to R_{C}^{∞} and A and γ. In addition, the degree disorder and its effect on mobility enhancement can be quantified by γ and κ. The former can be used to estimate the approximated width of the Gaussian DOS T_0.

Sub-threshold regime

As previously shown by the asymptotic behaviour of the ratio η near and sub-threshold voltage, the sub-threshold drain current in this regime could be modelled as an exponential function of gate voltage:

$$I_{\mathrm{sub}} = I_0 \exp \left[\frac{\ln 10}{S} |V_{\mathrm{GS}} - V_{\mathrm{T}}| \right]. \tag{5.57}$$

Here, I_0 is the current at $V_{\mathrm{GS}} = V_{\mathrm{T}}$, where, by definition, I_{sub} must show an apparent exponential increase, and S is the sub-threshold swing. The equation expressed with V_{T}, which can be precisely estimated by the ratio method, enables to demonstrate the coherence and the validity of the extracted threshold voltage. Note that, due to its diffusion mediated conduction mechanism, the drain current in this regime is independent to the drain voltage as long as $V_{\mathrm{DS}} > kT/q$ [37]. This model is, thus, applicable to most unintentionally doped molecular semiconductors that are characterized by low thermal carrier density on the order of -10^{14} cm^3 [156].

Nonetheless, we would like to emphasize that, in the framework of the Gaussian disorder and diffusion enhancement by charge carrier concentration, any factors that modify the charge carrier concentration at this around-thermal equilibrium condition could contribute to the drain voltage dependence of the sub-threshold current. In this case, we can extend the model by taking the values of I_{D} at V_{T} for different V_{DS} and using them as a variable I_0.

Complete Model for All Regimes

Finally, a physically-based compact model for OFETs is proposed which encompasses all operation regimes. As depicted in Figure 5-15(a), models for each regime have a distinctive range of validity. A conventional method used for silicon TFTs is to take $[(1/I_{\mathrm{above}}) + (1/I_{\mathrm{sub}})]^{-1}$ to combine the equations [104]. However, it is found that this method is generally not applicable to OFETs, especially when the below-to-above transition zone is spread over a wide voltage range (i.e. transfer characteristics with a larger sub-threshold swing). Although an alternative approach introduced in [230] overcome this limitation by making use of a transition function for effective gate voltage, it is not compatible with our model with an independently defined I_{sub} and I_{above}. Therefore, we propose a hyperbolic tangent transition function as the suitable method for OFETs with a tunability of the position and the degree of transition. Another advantage is the mathematical continuity at the transition point of both the hyperbolic tangent function and its first derivative.

$$I_{\mathrm{total}} = I_{\mathrm{above}} \times \frac{1}{2}\left[1 - \tanh\left[-\frac{V_{\mathrm{GS}} - V_{\mathrm{B}}}{V_{\mathrm{B}} - V_{\mathrm{T}}}\right]\right] + I_{\mathrm{sub}} \times \frac{1}{2}\left[1 + \tanh\left[-\frac{V_{\mathrm{GS}} - V_{\mathrm{B}}}{V_{\mathrm{B}} - V_{\mathrm{T}}}\right]\right] + I_{\mathrm{off}} \quad (5.58)$$

with only one additional parameter, namely the transition voltage V_{B}. In essence, V_{B} defines the center of the transition. Mathematically speaking, the above and sub-threshold current contribute to the total current by the same factor $(1/2)$ at this voltage. Therefore, a practical choice of V_{B}. is done by referring to the voltage at which the vertical distance between I_{sub} and I_{above} is the minimum.

Importantly, in contrast to our initial attempt [229], where we used a purely numerical fitting parameter B for the description of the degree of transition, we were able to provide the physical meaning of B in a continuous effort to minimize the fitting parameter without a physical meaning or explanation. Inspired by its mathematical role of describing the degree (or the range) of transition, we propose

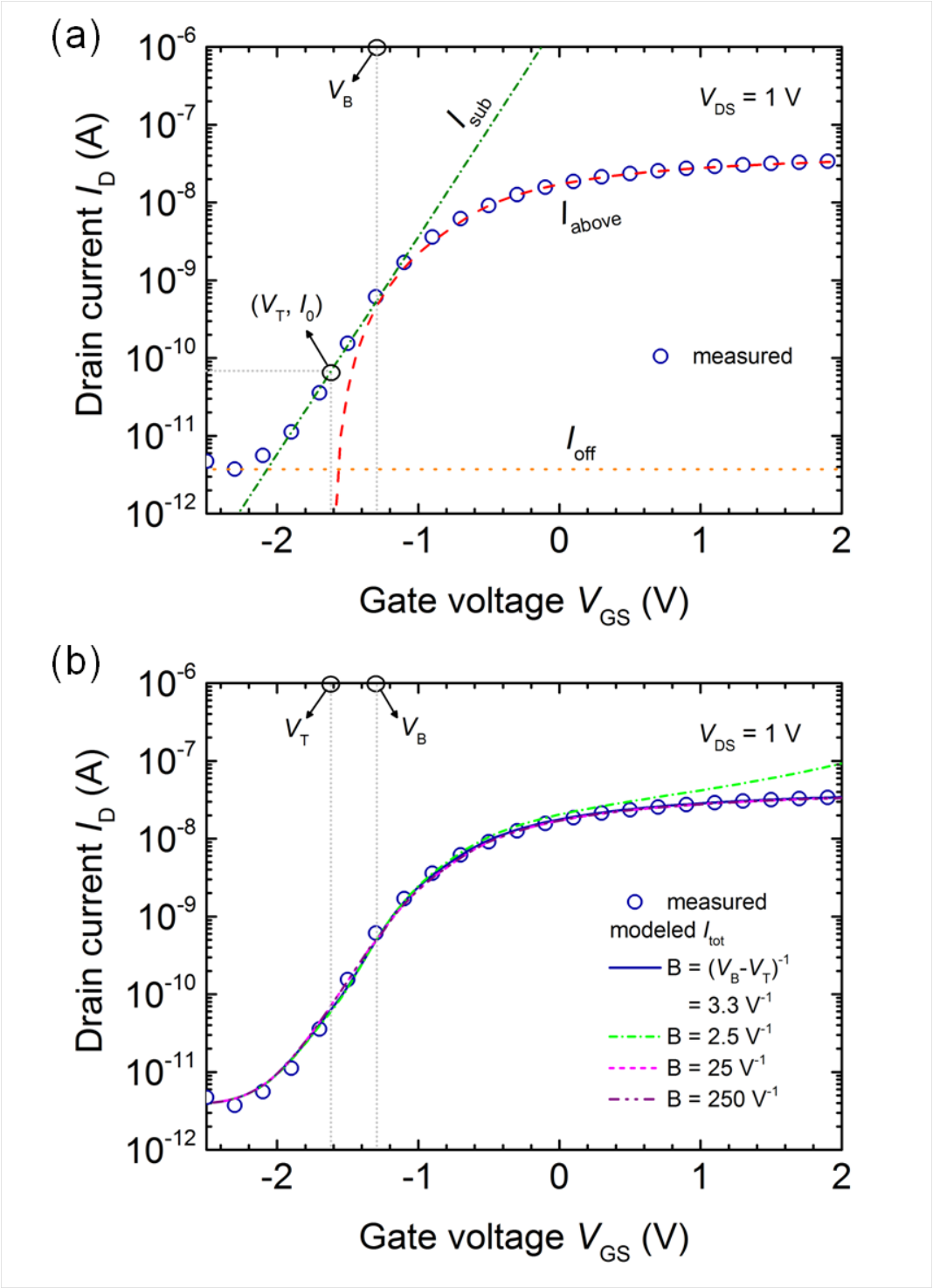

Figure 5-15: (a) A measured linear-regime transfer characteristics and the elements of the drain current compact model: above-threshold current I_{above}, sub-threshold current I_{sub} and off current I_{off}. V_{T} is the threshold voltage. V_{B} is the voltage at which the difference between I_{sub} and I_{above} is the minimum. (b) The effect of the transition parameter B on the compact model. When V_{T} and V_{B} are a precisely determined, the model has a large tolerance on B, and it can be defined as $B = (V_{\text{B}} - V_{\text{T}})^{-1}$.

that the numerical fitting parameter can b replaced by the horizontal distance between the transition and threshold voltage, $B = (V_{\mathrm{B}} - V_{\mathrm{T}})^{-1}$. It can be inferred, by its definition, that B is dependent to the operation voltage. As shown in Figure 5-15(b), a smooth fitting is achieved by this unambiguously definition of transition parameter B.

We would like to emphasize that the large margin of B shown by the good quality of fit for $B > (V_{\mathrm{B}} - V_{\mathrm{T}})^{-1}$ upto (but not limited to) 250 V^{-1} owes to the precisely determined threshold voltage. A larger B means the transition occurs along a narrower range of voltage, and, when the distant between the above and sub-threshold current is large due to imprecisely estimated threshold voltage, B would take in general a smaller value to ensure a smooth transition over a wider range of voltage.

5.5.3 Final compact modelling result

Figure 5-16 shows the final comparison of the new compact model with the experimental data. The proposed model precisely reproduces measured current-voltage characteristics over off, sub-threshold, linear, and saturation regimes with a single set of the extracted parameters listed in Table 5.3.

Comparing the key extracted parameters from TIPS-TPDO-4CN OFETs with pentacene OFETs from the previous section summarized in Table 5.4, we can gain a fundamental insight on the material and device properties. The first difference is the mobility. It can be inferred from the mobility proportionality constant that TIPS-TPDO-4CN is a better charge carrier transporting material than pentacene ($\kappa = 2.6{\times}10^{-2}$ versus $2.8{\times}10^{-3}$ $\mathrm{cm^2V^{-\gamma-1}s^{-1}}$). A plausible origin is higher order in the TIPS-TPDO-4CN thin film evidence by a smaller power-law exponent ($\gamma = 0.47$ versus 1.24). As a consequence, high gate voltage bulk resistance R_{C}^{B} is lower in the TIPS-TPDO-4CN transistor than the pentacene transistor. Interestingly, in contrast to the pentacene device, the injection at the contact gives greater contribution to the the high gate voltage contact resistance than the bulk transport in the transition zone ($R_{\mathrm{C}} : R_{\mathrm{C}}^{\infty} = 22{:}21$ versus 2:0.3 in $\mathrm{M\Omega}$). Given the good mobility and molecular order, a more adaptive tailoring of the semiconductor energy structure would be a reasonable strategy for further improvement of the material.

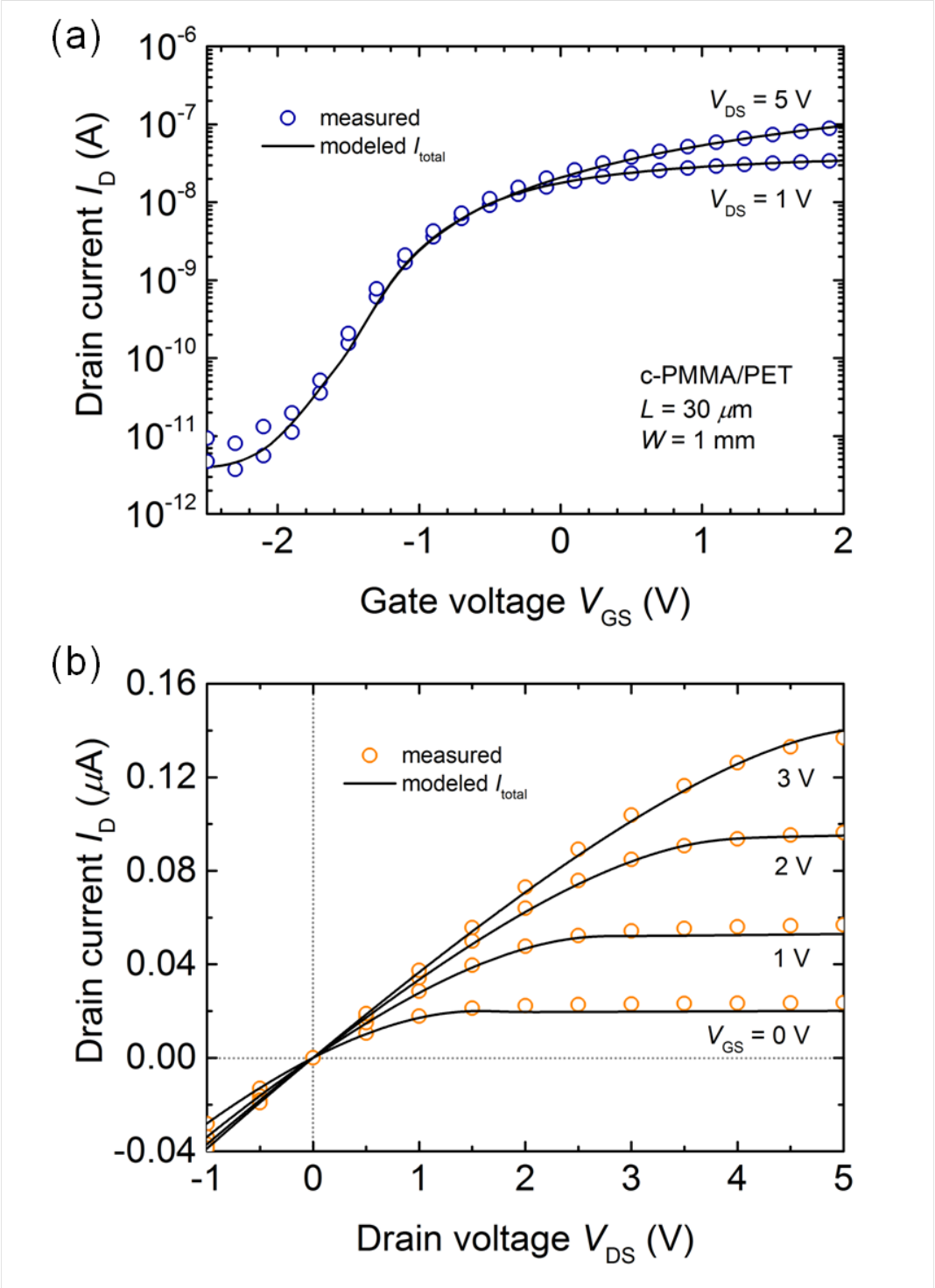

Figure 5-16: Final comparison of the compact model with the measured (a) transfer characteristics and (b) output characteristics of a flexible low voltage n-type OFET.

Table 5.3: Extracted Parameters from the Modelled TIPS-TPDO-4CN OFETs

Parameters	Values	Units
Threshold voltage, V_{T}	-1.6	[V]
Power-law exponent, γ	0.47	[-]
Contact resistance asymptote, R_{C}^{∞}	21	[MΩ]
Approximate width of DOS, T_{c}	439	[K]
Mobility proportionality constant, κ	2.6×10^{-2}	$[\mathrm{cm^2V^{-\gamma-1}s^{-1}}]$
Contact resistance proportionality constant, A/W	8.1	$[\mathrm{M\Omega\cdot V^{\gamma+1}}]$
On-state resistance proportionality constant, $A/W + 1/(K\kappa)$	44	$[\mathrm{M\Omega\cdot V^{\gamma+1}}]$
Saturation modulation parameter, α_{s}	1.1	[-]
Linear-to-saturation transition parameter, m	19	[-]
Saturation coefficient, λ	0.017	$[\mathrm{V^{-1}}]$
Subthreshold swing, S	0.36	[V/dec]
Threshold current, I_0	68	[pA]
Off current, I_{off}	3.7	[pA]
Transition voltage, V_{B}	-3.3	[V]

Table 5.4: Comparison between pentacene versus TIPS-TPDO-4CN transistors by key parameters

Parameters	TIPS-TPDO-4CN OFETs	Pentacene OFETs
Power-law exponent, γ [-]	0.47	1.24
Mobility proportionality constant, κ $[\mathrm{cm^2V^{-\gamma-1}s^{-1}}]$	2.6×10^{-2}	2.8×10^{-3}
High gate voltage† mobility, μ $[\mathrm{cm^2V^{-1}s^{-1}}]$	4.9×10^{-2}	1.1×10^{-2}
High gate voltage† contact resistance, R_{C} $[\mathrm{M\Omega\cdot V^{\gamma+1}}]$	22	2.0
Contact resistance asymptote, R_{C}^{∞} [MΩ]	21	0.3
High gate voltage† bulk resistance, R_{C}^{B} [MΩ]	1.0	1.7

†V_{GS} = 2 V for TIPS-TPDO-4CN OFETs and V_{GS} = -32.7 V for pentacene OFETs

Chapter 6

Conclusion and perspectives

In this thesis, we presented a physically-based compact modelling of organic electronic devices. Two main electronic devices, a rectifying diode and a transistor, were studied by multiple modelling methods as well as experimental validation. This chapter summarizes the major results and provides perspectives for further works.

A single layer organic rectifying diode in vertical stack of Au/pentacene/Al was fabricated. By means of impedance spectroscopy and current-voltage measurement, we clarified that the capacitive behaviour [156] of the diode is restricted in the reverse bias regime. When forward bias is applied, the capacitive behaviour gets lost due to regional accumulation of charge carriers injected from the anode. We found that the strength of the injecting contact dictated by the injection barrier determines upto what voltage the capacitive behaviour pertains, and according to this criteria two distinct cases were classified: strong injection and week injection. A new definition of the effective injection barrier $E_{\mathrm{b}}^{\mathrm{eff}}$ was presented to analytically describes how Gaussian disorder (described by the width of DOS, σ) contributes in lowering injection barrier [162]. When $E_{\mathrm{b}}^{\mathrm{eff}}$ is lower than about 0.3 eV (for $\sigma =$ 0.15 eV, we showed that the diode readily abandon the capacitive behaviour at thermal equilibrium. We showed that when injection and/or disorder becomes dominant, key approximations of the MIM model, such as the straight potential profiles and constant mobility and diffusion coefficient, are no longer valid, and, concomitantly, the exponential $I - V$ characteristics disappears. Lastly, the modelling results of the Au/pentacene/Al diode revealed that the width of Gaussian DOS for pentacene thin-film is $\sigma = 0.20$ eV, which is high enough so that for a commonly used metal for injecting contact, such as Au, the semiconductor acts as a degenerate semiconductor.

We have focused on a staggered OFET, which exhibits superior performance

compared to a coplanar OFET. From 2-D numerical simulation, we identified that the bulk transport in the transition zone (overlapping region of gate-source/drain contact) and injection barrier at the contact give rise to the contact resistance, and demonstrated that the power-law gate voltage dependence of both channel and contact conductivity originates from the charge carrier concentration (i.e. the gate voltage) dependence of the mobility in disordered organic semiconductor transistors. In addition, we found that the contact conductivity consists of an asymptotic access conductivity and a bulk conductivity with power-law gate voltage dependence. Then, by adopting the equivalent circuit of the current crowding model, we proved that the power-law conductivity leads to the power-law contact resistance. Based on this result, we formulated the above-threshold drain current model with power-law mobility and contact resistance, and proposed a consistent parameter extraction method. By using the model and extraction method, we analysed quantitatively a p-type pentacene-based OFET and n-type TIPS-TPDO-4CN-based OFET. It was shown that, comparing the mobility proportionality constant, TIPS-TPDO-4CN was a better charge carrier transporting material than pentacene ($\kappa = 2.6\times10^{-2}$ versus 2.8×10^{-3} $\mathrm{cm^2V^{-\gamma-1}s^{-1}}$) thanks to higher order in the TIPS-TPDO-4CN thin film evidence by a smaller power-law exponent ($\gamma = 0.47$ versus 1.24.). In addition, two contrasting situations are observed, where the contact resistance is dominated by the bulk resistance (transport in the transition zone) in pentacene devices whereas it is contact resistance asymptote in TIPS-TPDO-4CN devices.

For rectifying diodes, we anticipate establishing a fully analytic model for the forward bias diode current for the case of strong injection (degenerate case) could be achieved through an empirical approach. We have clearly demonstrated that the forward bias diode current could be represented by the diffusion current at the cathode. Thus, if we could find an approximate bend profile near the cathode considering how initial band banding is modified due to additional injected charges by applied voltage, we can, being able to convert it to the charge carrier concentration profile by Poisson's equation, obtain the charge carrier concentration gradient and hence diffusion current. (Note that an attempt to approximate the potential profile to the straight line will fail since it will produce the zero charge carrier concentration and the concentration profile cannot be determined.)

In the meantime, a comparative study would be desirable to check the robustness of the Gaussian disorder framework. More specifically, different organic semiconductor materials or semiconductor process techniques could be envisaged such as single crystal organic solids grown from solution or vacuum sublimation [231],

organic semiconductor thin-films by various printing and blading techniques [232] etc., which will provide a wider experimental spectrum of energy structures and degrees of disorder. The physical ground for this motivation highlighted by Baranovskii is the capability of the Gaussian disorder model for describing both Arrhenius and non-Arrhenius type temperature dependence of the charge carrier mobility [33].

For OFETs, we infer that an analytical correlation between the width of a Gaussian DOS and power-law exponent γ can be achieved. Note that we showed that γ is correlated to the slope of an approximated discrete exponential function of a Gaussian DOS by $\gamma = T_c/T = 1$. We note that the semi-logarithmic slope of the Gaussian DOS is given by $-E^2/(2\sigma^2)$, and, equating this with the slope of the approximated function given by $-1/T_c$, we have an analytical relationship between σ and T_c, $\sigma = \sqrt{kT_cE}$, with an unknown variable E being the energy at which the approximation is made. The physical meaning of E is the energy to which charge carriers are filled and can be represented by the Fermi level E_{F}. Thus, if we could formulate an other equation relating the average charge carrier concentration in the channel with the Fermi level of the semiconductor, $p = f(E_{\mathrm{F}}, \sigma)$, where p is will be evidently related with σ and can be estimated by dimensionally normalisation of the capacitively induced charge $Q = C_{\mathrm{i}}|V_{\mathrm{GS}} - V_{\mathrm{T}}^{\mathrm{eff}}|$, we might be able to determine σ from γ.

In addition, a standardization effort with the compact model council (CMC) should be taken seriously. This will put the developed model onto the world stage if it is adopted. For this, first, translation of the analytical model into Verilog A formulation is required. Since the compact model was developed encompassing all physical phenomena captured in the previous compact model, we anticipate a higher change of success.

Lastly, theoretical analysis on the anisotropic charge carrier transport, which has been observed experimentally in [233], should be conducted in a systematic manner. The incorporation of anisotropic mobility has not been incorporated in the numerical simulator of Silvaco. We note that the analytical model proposed in (5.31) is suitable for adopting the anisotropy. In a staggered OFET, considering only one of two orthogonal elements of mobility vector would be sufficient for describing the charge carrier transport in the transition zone and the channel. could be represented respectively by κ_{B}- γ_{B} and κ_{ch}- γ_{ch}. In doing so, preliminary results on 2-D consideration of diffusion enhancement should be considered [234].

Appendix A

Résumé Long en Français

En dépit d'une amélioration remarquable de la performance des composants électroniques organiques, il y a encore un manque de compréhension théorique rigoureux sur le fonctionnement du composant. Cette thèse est consacrée à la création de modèles pratiques pour composants électroniques organiques à base physique complète afin de rendre possible la prédiction et l'évaluation du fonctionnement du composant.

Un modèle compact à base physique d'un élément de circuit est une équation mathématique qui permet une dèscription précise, rigoureuse et simple du fonctionnement du dispositif et est généralement évalué selon ces trois critères. Premièrement, il faut être précis afin que le résultat des simulateurs soit utile pour les concepteurs de circuits. Deuxièmement, il faut être rigoureux pour capturer des phénomènes physiques se produisant dans le composant. Troisièmement, il faut être suffisamment simple pour être incorporé dans des simulateurs de circuits. Les trois elements sont interdependants. Par exemple, un modèle simplifié à l'excès en l'absence de physique rigoureuse cause la précision insuffisante ou les parametres sans signification physique. En revanche, un modèle n'ayant aucune approximation ne possède pas toujours une forme simple malgré la précision suffisant et les parametres avec signification physique provenant de la physique rigoureuse.

Dans ce contexte, les caractéristiques distinctives de l'injection et du transport des porteurs de charge dans les semi-conducteurs organiques sont incorporées dans les modèles qui améliorent la précision sans compromettre la simplicité mathématique. En particulier, la densité d'états Gaussienne est considéré où tous les états sont localisés et sa distribution suit la fonction Gaussienne. Il est pris en compte que l'injection et le transport des porteurs de charge manifestent via le sautillage (*hopping* en français) dans les états Gaussiens. La reduction de barrier d'injection ainsi que la dépendance en temperature, concentration des porteurs de

charge et le champ èlèctrique de la mobilité des porteurs de charge sont inclus dans les modèles.

L'effet concomitant sur les caractéristiques courant-tension des diodes et des transistors organiques prototypiques sont étudiés. Par rapport au modèle d'une diode de rectification, le concept d'appauvrissement total dans les semi-conducteurs organiques involontairement dopés est présenté et sa limite par rapport à l'injection de charge est décrite. Le développement théorique pour la distribution de charge et potentiel et les caractéristiques de courant-tension sont élaborés dans les conditions d'injection faible et forte.

Par rapport au modèle d'un transistor à l'effet de champ, des preuves théoriques et expérimentales sont fournies pour soutenir la déscription de la dépendance en tension grille-source de la mobilité de l'effet de champ et de la résistance de contact par la loi de puissance. La dépendance en tension grille-source de la mobilité de l'effet de champ, qui résulte de la mobilité des porteurs de charge ayant la dépendance en concentration des porteurs de charge, est identifiè comme l'origine de celle de la résistivité de contact en utilisant la conception de l'effet de foule de courant (*current crowding effect* en français). De tels phénomènes sont nouvellement introduits dans le modèle de courant de drain.

En plus, les méthodes d'extraction des paramètres cohérents aux modèles sont présentées qui permettent la détermination univoque des paramètres du composant utilisés pour prévoir le fonctionnement du composant et évaluer la performance du composant et les propriétés de couches minces et interfaces organiques.

Les approches englobent le dévelopement analytique des équations physiques, la simulation numérique à deux dimensions basé sur la méthode des éléments finis et la validation expérimentale.

Les modèles compacts originaux et entièrement analytiques et des méthodes d'extraction de paramètres fournissent une compréhension fondamentale sur la façon dont le désordre énergétique dans une couche mince de semi-conducteur organique, décrit par la densité d'états Gaussienne, affecte les caractéristiques courant-tension observables des composants.

Appendix B

Publications

Journal articles

(1) Sungyeop Jung, Yvan Bonnassieux and Gilles Horowitz, "A Physically-Based Compact Model for Low-Voltage Organic Field-Effect Transistors," **(in preparation)**

(2) Sungyeop Jung, Andrew Plews, Ahmed Nejim, Yvan Bonnassieux and Gilles Horowitz, "Gaussian Disorder and Gate Voltage Power-Law Dependence of Mobility and Contact Resistance in Organic Field-Effect Transistors," **(in preperation)**

(3) Sungyeop Jung, Jong Woo Jin, Vincent Mosser, Yvan Bonnassieux and Gilles Horowitz, "A New Model and Extraction Method for Organic Field-Effect Transistors with Power-Law Contact Resistance and Mobiltiy," **(in preperation)**

(4) Jong Woo Jin, Sungyeop Jung, Yvan Bonnassieux, Gilles Horowitz Alexandra Stamateri, Christos Kapnopoulos, Argiris Laskarakis and Stergios Logothetidis, "Universal Compact Model for Organic Solar Cell," IEEE Transactions on Electron Devices (2016)

(5) Sungyeop Jung, Mohammed Al-Bariqi, Guillaume Gruntz, Thamer Al-Hathal, Yohann Nicolas, Thierry Toupance, Yvan Bonnassieux and Gilles Horowitz, "A TIPS-TPDO-tetraCN-based n-type organic field-effect transistors with cross-linked PMMA polymer gate dielectric," Applied Materials and Interfaces 8 (23), 14701-14708 (2016).

(6) Sungyeop Jung, Chang-Hyun Kim, Yvan Bonnassieux and Gilles Horowitz, "In-

jection barrier at metal/organic semiconductor junction with a Gaussian density-of-states," Journal of Physics D: Applied Physics 48, 395103 (2015).

(7) Sungyeop Jung, Chang-Hyun Kim, Yvan Bonnassieux and Gilles Horowitz, "Fundamental insights into the threshold characteristics of organic field-effect transistors," Journal of Physics D: Applied Physics 48, 035106 (2015).

(8) Francois Baert, Clement Cabanetos, Antoine Leliege, Eva Kirchner, Olivier Segut, Olivier Aleveque, Magali Allain, Gijun Seo, Sungyeop Jung, Bernard Geffroy, Denis Tondelier, Jean Roncali, Philippe Leriche, "A bridged low band gap A-D-A quaterthiophene as efficient donor for organic solar cells," Journal of Materials Chemistry C 3, 309 (2015).

Conference presentations

(1) Sungyeop Jung, Jong Woo Jin, Yvan Bonnassieux and Gilles Horowitz, "Gate bias dependence of mobility in organic field-effect transistors with Gaussian density-of-states," International Conference on Organic Electronics (ICOE), Bratislava, Slovakia, June 13-15 (2016). **Oral**

(2) Sungyeop Jung, Jong Woo Jin, Vincent Mosser, Yvan Bonnassieux and Gilles Horowitz, "Modeling organic field effect-transistors with power-law dependent mobility and contact resistance," International Thin-Film Transistor Conference (ITC), Hsinchu, Taiwan, February 25-26 (2016). **Poster**

(3) Sungyeop Jung, Vincent Mosser, Yvan Bonnassieux and Gilles Horowitz, "Self-consistent parameter extraction method for organic-field effect transistors with power-law dependent mobility," Materials Research Society Fall Meeting (MRS), Boston, USA, November 29-December 4 (2015). **Poster**

(4) Chang-Hyun Kim, Sungyeop Jung, Yvan Bonnassieux, John E. Anthony, Ioannis Kymissis, Myung-Han Yoon, and Gilles Horowitz, "Analytically correlated charge transport and injection in solution-processed organic field-effect transistors," European Conference on Molecular Electronics (ECME), Strasbourg, France, September 1-5 (2015). **Oral**

(5) Sungyeop Jung, Mohammed Al-Bariqi, Guillaume Gruntz, Yohann Nicolas, Lionel Hirsch, Thierry Toupance, Yvan Bonnassieux and Gilles Horowitz, "N-type organic field-effect transistors with high performance and low operation voltage," International Conference on Organic Electronics (ICOE), Erlangen, Germany, June 15-17 (2015). **Oral**

(6) Sungyeop Jung, Yvan Bonnassieux and Gilles Horowitz, "Fundamental difference in the electrical characteristics of organic rectifying diodes under non-degenerate and degenerate regime related with a Gaussian density-of-states," European Materials Research Society Spring Meeting (E-MRS), Lille, France, May 11-15 (2015). **Oral**

(7) Sungyeop Jung, Chang-Hyun Kim, Yvan Bonnassieux and Gilles Horowitz, "Defining the injection barrier at metal/organic semiconductor interface with a Gaussian density-of-states," International Thin-Film Transistor Conference (ITC), Rennes, France, February 26-27 (2015). **Oral**

(8) Mohammed Albariqi, Thamer Alhathal, Sungyeop Jung, Yvan Bonnassieux and Gaël Zucchi, "Ultra-thin gate dielectric for organic field-effect transistors," International Thin-Film Transistor Conference (ITC), Rennes, France, February 26-27 (2015). **Poster**

(9) Sungyeop Jung, Chang-Hyun Kim, Yvan Bonnassieux and Gilles Horowitz, "The effect of width of Gaussian density-of-states function on electrical characteristics of organic rectifying diodes," International Conference on Organic Electronics (ICOE), Modena, Italy, June 11-13 (2014). **Oral**

(10) Sungyeop Jung, Chang-Hyun Kim, Yvan Bonnassieux and Gilles Horowitz, "Physical modeling of the threshold in organic field-effect transistors," International Thin-Film Transistor Conference (ITC), Delft, Netherlands, January 23-24 (2014). **Poster**

(11) Sungyeop Jung, Chang-Hyun Kim, Jongyoon Park, Denins Tondelier, Bernard Geffroy, Yvan Bonnassieux and Gilles Horowitz, "Modeling the threshold voltage and sub-threshold current of organic field-effect transistors," Matériaux et Nanostructures Pi-Conjugués (MNPC), Annecy, France, October 07-11 (2013). **Oral**

(12) Jongyoon Park, Chang-Hyun Kim, Sungyeop Jung, Denis Tondelier, Bernard Geffroy, Yvan Bonnassieux and Gilles Horowitz, "Theoretical and experimental analysis of the contact resistance in organic field-effect transistors," Matériaux et Nanostructures Pi-Conjugués (MNPC), Annecy, France October 07-11 (2013). **Poster**

Appendix C

Activities

Research visits

(1) Columbia University, New York, USA, June-August 2016
Hosting advisor: Prof. Ioannis Kymissis

(2) Cambridge University, Cambridge, UK, December 2015
Hosting advisor: Prof. Arokia Nathan

(3) Silvaco Europe Ltd., St Ives, UK, November-December 2015
Hosting advisor: Dr. Ahmed Nejim and Dr. Andrew Plews

Training

(1) Ateliers du Groupements de Recherche Électronique Organique (GDR 3368) 2015
(Workshop of Organic Electronics Research Society 2015)
March 26, 2015, Paris, France

Teaching

(1) Tutoring lecture at École polytechnique, PHY559 Circuits Intégrés Numériques & Analogiques (Digital & Analog Integrated Circuits), Spring 2015-Present

Journal peer-reviewing

(1) IEEE Electon Device Letters, Since 2016

(2) ACS Advanced Materials Interfaces, Since 2016

(3) Sensors and Actuators B: Chemical, Since 2016

Appendix D

Experimental Details

Organic rectifying diode

The glass or PET substrates were cleaned successively with acetone, isopropanol and, finally, by a UV-ozone post-treatment. Au anode (30 nm) was thermally evaporated through a specific shadow mask on Al (5 nm) adhesion layer. Pentacene (500 nm) was thermally evaporated through a specific shadow mask at 0.1 nm/sec. Finally, Al cathode (100 nm) was thermally evaporated through a specific shadow mask. All evaporation processes were done under 1.9×10^{-7} mbar and fixed substrate temperature of 25°C. Samples are taken out from evaporation chamber installed in the nitrogen glove box for changing masks. From the beginning of the fabrication process upto the end of electrical measurement, samples stayed in the glove box being isolated from exposure to oxygen and humidity. Keithley 4200 and HP 4192A LF impedance analyzer installed in the glove box were used for dc and ac electrical characterization.

OFETs: PMMA gate dielectric

The glass or PET substrates were cleaned successively with acetone, isopropanol and, finally, by a UV-ozone post-treatment. Then, the PET substrate was attached on a supporting glass substrate. Subsequent fabrication processes and characterizations of OFETs were carried out in a glove box under nitrogen atmosphere. The Al (gate electrode, 100 nm), pentacene or TIPS-TPDO-tetraCN (organic semiconductor, 60 nm) and Au (contact electrodes, 30 nm) were thermally evaporated through a specific shadow mask. All evaporation processes were done

under 1.9×10^{-7} mbar and fixed substrate temperature of 25°C. The evaporation rate of pentacene or TIPS-TPDO-tetraCN was maintained at 0.01 nm/sec in average. Between the evaporation processes of Al and organic semiconductor, the polymer gate dielectrics were spin-coated.

For PMMA gate dielectric, the PMMA solution (200 mg of PMMA dissolved in 3 ml of toluene for 24 hours) was spin-coated at 3000RPM/5s/60s (Rotation Per Minutes/acceleration time to reach the target RPM/spin-coating time).

OFETs: cross-linked PMMA gate dielectric

All process is identical to OFETs with PMMA gate dielectric except for the spin-coating process for the cross-linked PMMA gate dielectric. For cross-linked PMMA gate dielectric (c-PMMA), 10 μl of C_6-Si was introduced to the PMMA solution (25 mg of PMMA dissolved for 40 min at 80°C in 1 ml of n-Butyl acetate and cooled down to 50°C) 2 min before spin-coating at 5000RPM/5s/60s. After annealing at 100°C for 60 min, PMMA and c-PMMA gate dielectrics have thickness of 510±10 and 100±16 nm (measured using a Dektak 150 surface profiler, Veeco).

Note that, in the work of Noh *et al.* on a cross-linked PMMA [197], the solution consisting of the base polymer and cross-linking agent was prepared under nitrogen environment and then spin-coated and post-annealed in air for a spontaneous cross-linking due to ambient moisture. In this study, the whole spin-coating process was conducted in a glove box, which is similar to the study of Yang *et al.* [235].

All transfer and output characteristics of the n-type OFETs were measured with Keithley 4200 in the dark under nitrogen atmosphere directly after device fabrication without exposure to air except for the air stability test. In particular, bending tests were performed with a custom-built apparatus which consists of a hemicylindrical objects with different radii. The transfer characteristics were measured while the devices were being bent. For the air stability test, transistors were stored and measured in the dark under ambient atmosphere without encapsulation. The results for bending and ambient stability can be found in [223].

Bibliography

[1] W. H. Brown and T. Poon, *Introduction to Organic Chemistry*, 2nd ed. Wiley, 2004.

[2] *The Nobel Prize in Chemistry: Conductive polymers*, 2000 (accessed May 6, 2016). [Online]. Available: http://nobelprize.org

[3] G. Inzelt, *Conducting Polymers: A New Era in Electrochemistry. Monographs in Electrochemistry*, 2nd ed. Springer, 2008.

[4] H. Naarmann, *Ullmann's Encyclopedia of Industrial Chemistry.* Wiley-VCH, 2002.

[5] G. A. Chamberlain, "Organic Solar Cells: A Review," *Solar Cells*, vol. 8, no. 1, pp. 47–83, 1983.

[6] H. Hoppe and N. S. Sariciftci, "Organic Solar Cells: An Overview," *J. Mater. Res.*, vol. 19, no. 07, pp. 1924–1945, 2011.

[7] C. W. Tang and S. A. VanSlyke, "Organic Electroluminescent Devices," *Appl. Phys. Lett.*, vol. 51, no. 12, pp. 913–915, 1987.

[8] F. Gutmann and L. E. Lyons, *Organic Semiconductors.* Wiley, 1967.

[9] H. Kallmann and M. Silver, *Symposium on Electrical Conductivity in Organic Solids.* Wiley Interscience, 1961.

[10] A. Tsumura, H. Koezuka, and T. Ando, "Macromolecular Electronic Device: Field-Effect Transistor With a Polythiophene Thin Film," *Appl. Phys. Lett.*, vol. 49, no. 18, pp. 1210–1212, 1986.

[11] ——, "Polythiophene Field-Effect Transistor: Its Characteristics and Operation Mechanism," *Synth. Met.*, vol. 25, no. 1, pp. 11–23, 1988.

[12] M. Singh, H. M. Haverinen, P. Dhagat, and G. E. Jabbour, "Inkjet Printing-Process and Its Applications," *Adv. Mater.*, vol. 22, no. 6, pp. 673–685, 2010.

[13] M. Caironi and Y.-Y. Noh, Eds., *Large Area and Flexible Electronics*, 1st ed. John Wiley Sons, 2015.

[14] S. Electronics, *Galaxy S6 Edge*, 2015 (accessed May 6, 2016). [Online]. Available: http://www.samsung.com/us/explore/galaxy-s-6-features-and-specs/

[15] L. Electronics, *OLED CINEMA 3D SMART TV*, 2016 (accessed May 6, 2016). [Online]. Available: http://www.lg.com/uk/tvs/lg-55EA980W

[16] S. Reineke, F. Lindner, G. Schwartz, N. Seidler, K. Walzer, B. Lüssem, and K. Leo, "White Organic Light-Emitting Diodes with Fluorescent Tube Efficiency," *Nature*, vol. 459, no. 7244, pp. 234–238, 2009.

[17] B. W. D'Andrade and S. R. Forrest, "White Organic Light-Emitting Devices for Solid-State Lighting," *Adv. Mater.*, vol. 16, no. 18, pp. 1585–1595, 2004.

[18] OsramOLED, *ORBEOS*, 2016 (accessed May 6, 2016). [Online]. Available: http://www.osram-oled.com/oled/en/products/orbeos-sdw-058/index.jsp

[19] InfinityPV, *Organic Solar Foil*, 2016 (accessed May 6, 2016). [Online]. Available: https://www.infinitypv.com

[20] PolyIC, *A Polymer Flexible RFID Tag*, 2006 (accessed May 6, 2016). [Online]. Available: http://www.polyic.com/company.html

[21] Y. Nakajima, Y. Fujisaki, T. Takei, H. Sato, M. Nakata, M. Suzuki, H. Fukagawa, G. Motomura, T. Shimizu, Y. Isogai, K. Sugitani, T. Katoh, S. Tokito, T. Yamamoto, and H. Fujikake, "Low-Temperature Fabrication of 5-in. QVGA Flexible AMOLED Display Driven by OTFTs Using Olefin Polymer as the Gate Insulator," *J. Soc. Inf. Display*, vol. 19, no. 12, pp. 861–6, 2011.

[22] S. Steudel, K. Myny, S. Schols, P. Vicca, S. Smout, A. Tripathi, B. van der Putten, J.-L. van der Steen, M. van Neer, F. Schütze, O. R. Hild, E. van Veenendaal, P. van Lieshout, M. van Mil, J. Genoe, G. Gelinck, and P. Heremans, "Design and Realization of a Flexible QQVGA AMOLED Display with Organic TFTs," *Org. Electron.*, vol. 13, no. 9, pp. 1729–1735, 2012.

[23] Plasticlogics, *Display Platform with Gate and Source Drivers*, 2016 (accessed May 6, 2016). [Online]. Available: http://www.plasticlogic.com

[24] T. Someya, T. Sekitani, S. Iba, Y. Kato, H. Kawaguchi, and T. Sakurai, "A Large-Area, Flexible Pressure Sensor Matrix with Organic Field-Effect Transistors for Artificial Skin Applications," *PNAS*, vol. 101, no. 27, pp. 9966–9970, 2004.

[25] T. Someya, Y. Kato, S. Iba, Y. Noguchi, T. Sekitani, H. Kawaguchi, and T. Sakurai, "Integration of Organic FETs With Organic Photodiodes for a Large Area, Flexible, and Lightweight Sheet Image Scanners," *IEEE Transactions on Electron Devices*, vol. 52, no. 11, pp. 2502–2511, 2005.

[26] I. Nausieda, K. Ryu, I. Kymissis, A. I. Akinwande, V. Bulović, and C. G. Sodini, "An Organic Active-Matrix Imager," *IEEE Trans. Electron Devices*, vol. 55, pp. 527–532, 2008.

[27] Y.-J. Hsu, Z. Jia, and I. Kymissis, "A Locally Amplified Strain Sensor Based on a Piezoelectric Polymer and Organic Field-Effect Transistors," *IEEE Trans. Electron Devices*, vol. 58, pp. 910–917, 2011.

[28] K. Svennersten, K. C. Larsson, and M. Berggren, "Organic Bioelectronics in Nanomedicine," *Biochim. Biophys. Acta-Gen. Subj.*, vol. 1810, pp. 267–285, 2011.

[29] O. R. M. and G. G. Malliaras, "Organic Electronics at the Interface with Biology," *MRS Bull.*, vol. 35, p. 449âĂŞ456, 2010.

[30] P. Lin and F. Yan, "Organic Thin-Film Transistors for Chemical and Biological Sensing," *Adv. Mater.*, vol. 24, no. 1, pp. 34–51, 2011.

[31] H. Bässler, "Charge Transport in Disordered Organic Photoconductors a Monte Carlo Simulation Study," *Phys. Status Solidi B*, vol. 175, no. 1, pp. 15–56, 1993.

[32] W. Pasveer, J. Cottaar, C. C. Tanase, R. Coehoorn, P. Bobbert, P. W. M. Blom, D. de Leeuw, and M. Michels, "Unified Description of Charge-Carrier Mobilities in Disordered Semiconducting Polymers," *Phys. Rev. Lett.*, vol. 94, no. 20, p. 206601, 2005.

[33] S. D. Baranovskii, "Theoretical Description of Charge Transport in Disordered Organic Semiconductors," *Phys. Status Solidi B*, vol. 251, no. 3, pp. 487–525, 2014.

[34] G. Gildenblat, Ed., *Compact Modeling: Principles, Techniques and Applications*, 1st ed. Springer, 2010.

[35] *AIM-Spice*, 2014 (accessed May 6, 2016). [Online]. Available: http://www.aimspice.com

[36] S. M. Sze and K. K. Ng, *Physics of Semiconductor Devices*, 3rd ed. New York: Wiley, 2007.

[37] J.-P. Colinge and C. A. Colinge, *Physics of Semiconductor Devices*. Boston, MA: Kluwer, 2002.

[38] R. S. Muller and T. I. Kamins, *Device Electronics for Integrated Circuits*, 3rd ed. New York: Wiley, 2003.

[39] I. McCulloch, M. Heeney, C. Bailey, K. Genevicius, I. MacDonald, M. Shkunov, D. Sparrowe, S. Tierney, R. Wagner, W. Zhang, M. L. Chabinyc, R. J. Kline, M. D. McGehee, and M. F. Toney, "Liquid-Crystalline Semiconducting Polymers with High Charge-Carrier Mobility," *Nat Mater*, vol. 5, no. 4, pp. 328–333, 2006.

[40] H. Sirringhaus, T. Kawase, R. H. Friend, T. Shimoda, M. Inbasekaran, W. Wu, and E. P. Woo, "High-Resolution Inkjet Printing of All-Polymer Transistor Circuits," *Science*, vol. 290, no. 5499, pp. 2123–2126, 2000.

[41] D. J. Gundlach, J. E. Royer, S. K. Park, S. Subramanian, O. D. Jurchescu, B. H. Hamadani, A. J. Moad, R. J. Kline, L. C. Teague, O. Kirillov, C. A. Richter, J. G. Kushmerick, L. J. Richter, S. R. Parkin, T. N. Jackson, and J. E. Anthony, "Contact-Induced Crystallinity for High-Performance Soluble Acene-Based Transistors and Circuits," *Nat. Mater.*, vol. 7, no. 3, pp. 216–221, 2008.

[42] J. E. Anthony, "The Larger Acenes: Versatile Organic Semiconductors," *Angew. Chem.*, vol. 47, no. 3, pp. 452–483, 2008.

[43] K.-J. Baeg, "Polymer Dielectrics and Orthogonal Solvent Effects for High-Performance Inkjet-Printed Top-Gated P-Channel Polymer Field-Effect Transistors," *ETRI J*, vol. 33, no. 6, pp. 887–896, 2011.

[44] A. M. Gaikwad, Y. Khan, A. E. Ostfeld, S. Pandya, S. Abraham, and A. C. Arias, "Identifying Orthogonal Solvents for Solution Processed Organic Transistors," *Org. Electron.*, vol. 30, pp. 18–29, 2016.

[45] G. Horowitz, F. Kouki, P. Spearman, and D. Fichou, "Evidence for n-Type Conduction in a Perylene Tetracarboxylic Diimide Derivative," *Adv. Mater.*, vol. 8, no. 3, pp. 242–245, 1996.

[46] D. Bode, C. Rolin, S. Schols, M. Debucquoy, S. Steudel, G. H. Gelinck, J. Genoe, and P. Heremans, "Noise-Margin Analysis for Organic Thin-Film Complementary Technology," *IEEE Trans. Electron Devices*, vol. 57, no. 1, pp. 201–208, 2009.

[47] T. N. Ng, D. E. Schwartz, L. L. Lavery, G. L. Whiting, B. Russo, B. Krusor, J. Veres, P. Bröms, L. Herlogsson, N. Alam, O. Hagel, J. Nilsson, and C. Karlsson, "Scalable Printed Electronics: an Organic Decoder Addressing Ferroelectric Non-Volatile memory," *Sci. Rep.*, vol. 2, pp. 1–7, 2012.

[48] G. Guillaud, M. Al Sadoun, M. Maitrot, and J. Simon, "Field-Effect Transistors Based on Intrinsic Molecular Semiconductors," *Chem. Phys. Lett.*, vol. 167, no. 6, pp. 503–506, 1990.

[49] C. W. Tang, "Two-Layer Organic Photovoltaic Cell," *Appl. Phys. Lett.*, vol. 48, no. 2, pp. 183–4, 1986.

[50] C. W. Tang and S. A. VanSlyke, "Organic Electroluminescent Diodes," *Appl. Phys. Lett.*, vol. 51, no. 12, pp. 913–915, 1987.

[51] N. C. Greenham, S. C. Moratti, D. Bradley, and R. H. Friend, "Efficient Light-Emitting Diodes Based on Polymers with High Electron Affinities," *Nature*, vol. 365, no. 6447, pp. 628–630, 1993.

[52] M. Hiramoto, H. Fujiwara, and M. Yokoyama, "p-i-n Like Behavior in Three-Layered Organic Solar Cells Having a Co-Deposited Interlayer of Pigments," *J. Appl. Phys.*, vol. 72, no. 8, pp. 3781–3787, 1992.

[53] M. Strukelj, F. Papadimitrakopoulos, T. M. Miller, and L. J. Rothberg, "Design and Application of Electron-Transporting Organic Materials," *Science*, vol. 267, no. 5206, pp. 1969–1972, 1995.

[54] L.-L. Chua, J. Zaumseil, J.-F. Chang, E. C. W. Ou, P. K. H. Ho, H. Sirringhaus, and R. H. Friend, "General Observation of n-Type Field-Effect Behaviour in Organic Semiconductors," *Nature*, vol. 434, no. 7030, pp. 194–199, 2005.

[55] A. Facchetti, "Semiconductors for Organic Transistors," *Materials Today*, vol. 10, no. 3, pp. 28–37, 2007.

[56] H. Yan, Z. Chen, Y. Zheng, C. Newman, J. R. Quinn, F. Dotz, M. Kastler, and A. Facchetti, "A High-Mobility Electron-Transporting Polymer for Printed Transistors," *Nature*, vol. 457, no. 7230, pp. 679–686, 2009.

[57] J. E. Anthony, A. Facchetti, M. Heeney, S. R. Marder, and X. Zhan, "n-Type Organic Semiconductors in Organic Electronics," *Adv. Mater.*, vol. 22, no. 34, pp. 3876–3892, 2010.

[58] H. Klauk, "Organic Thin-Film Transistors," *Chem. Soc. Rev.*, vol. 39, no. 7, pp. 2643–2666, 2010.

[59] Y. Zhao, Y. Guo, and Y. Liu, "25th Anniversary Article: Recent Advances in n-Type and Ambipolar Organic Field-Effect Transistors," *Adv. Mater.*, vol. 25, no. 38, pp. 5372–5391, 2013.

[60] B. A. Jones, A. Facchetti, M. R. Wasielewski, and T. J. Marks, "Tuning Orbital Energetics in Arylene Diimide Semiconductors. Materials Design for Ambient Stability of n-Type Charge Transport," *J. Am. Chem. Soc.*, vol. 129, no. 49, pp. 15 259–15 278, 2007.

[61] J. H. Oh, S.-L. Suraru, W.-Y. Lee, M. Könemann, H. W. Höffken, C. Röger, R. Schmidt, Y. Chung, W.-C. Chen, F. Würthner, and Z. Bao, "High-Performance Air-Stable n-Type Organic Transistors Based on Core-Chlorinated Naphthalene Tetracarboxylic Diimides," *Adv. Funct. Mater.*, vol. 20, no. 13, pp. 2148–2156, Jun. 2010.

[62] J. Soeda, T. Uemura, Y. Mizuno, A. Nakao, Y. Nakazawa, A. Facchetti, and J. Takeya, "High Electron Mobility in Air for N,N-1H,1H-Perfluorobutyldicyanoperylene Carboxydi-imide Solution-Crystallized Thin-Film Transistors on Hydrophobic Surfaces," *Adv. Mater.*, vol. 23, no. 32, pp. 3681–3685, 2011.

[63] Y. Chung, E. Verploegen, A. Vailionis, Y. Sun, Y. Nishi, B. Murmann, and Z. Bao, "Controlling Electric Dipoles in Nanodielectrics and Its Applications for Enabling Air-Stable n-Channel Organic Transistors," *Nano Lett.*, vol. 11, no. 3, pp. 1161–1165, 2011.

[64] S. P. Senanayak, V. K. Sangwan, J. J. McMorrow, K. Everaerts, Z. Chen, A. Facchetti, M. C. Hersam, T. J. Marks, and K. S. Narayan, "Self-Assembled Nanodielectrics for High-Speed, Low-Voltage Solution-Processed Polymer Logic Circuits," *Adv. Electron. Mater.*, vol. 1, no. 12, p. 1500226, 2015.

[65] C.-a. Di, J. Li, G. Yu, Y. Xiao, Y. Guo, Y. Liu, X. Qian, and D. Zhu, "Trifluoromethyltriphenodioxazine: Air-Stable and High-Performance n-Type Semiconductor," *Organic Letters*, vol. 10, no. 14, pp. 3025–3028, 2008.

[66] Y. Nicolas, F. Castet, M. Devynck, P. Tardy, L. Hirsch, C. Labrugère, H. Allouchi, and T. Toupance, "TIPS-triphenodioxazine versus TIPS-pentacene: Enhanced Electron Mobility for n-Type Organic Field-Effect Transistors," *Org. Electron.*, vol. 13, no. 8, pp. 1392–1400, 2012.

[67] T. Sekitani, U. Zschieschang, H. Klauk, and T. Someya, "Flexible Organic Transistors and Circuits with Extreme Bending Stability," *Nat. Mater.*, vol. 9, pp. 1–8, 2010.

[68] G. H. Gelinck, H. E. A. Huitema, E. van Veenendaal, E. Cantatore, L. Schrijnemakers, J. B. P. H. van der Putten, T. C. T. Geuns, M. Beenhakkers, J. B. Giesbers, B.-H. Huisman, E. J. Meijer, E. M. Benito, F. J. Touwslager, A. W. Marsman, B. J. E. van Rens, and D. M. de Leeuw, "Flexible Active-Matrix Displays and Shift Registers Based on Solution-Processed Organic Transistors," *Nat. Mater.*, vol. 3, no. 2, pp. 106–110, 2004.

[69] D. K. Hwang, C. Fuentes-Hernandez, J. B. Kim, W. J. Potscavage Jr, and B. Kippelen, "Flexible and Stable Solution-Processed Organic Field-Effect Transistors," *Org. Electron.*, vol. 12, no. 7, pp. 1108–1113, 2011.

[70] Y. Fujisaki, "Current Status of Nonvolatile Semiconductor Memory Technology," *Jpn. J. Appl. Phys.*, vol. 49, no. 10, pp. 100 001–14, 2010.

[71] W. Warta, R. Stehle, and N. Karl, "Ultrapure, High Mobility Organic Photoconductors," *Appl. Phys. A*, vol. 36, no. 3, pp. 163–170, 1985.

[72] R. A. Laudise, C. Kloc, P. G. Simpkins, and T. Siegrist, "Physical Vapor Growth of Organic Semiconductors," *J. Cryst. Growth*, vol. 187, no. 3–4, pp. 449–454, 1998.

[73] V. Podzorov, S. E. Sysoev, E. Loginova, V. M. Pudalov, and M. E. Gershenson, "Single-Crystal Organic Field Effect Transistors with the Hole Mobility ~ 8 cm^2/Vs," *App. Phys. Let.*, vol. 83, no. 17, pp. 3504–4, 2003.

[74] N. Zaitseva, L. Carman, A. Glenn, J. Newby, M. Faust, S. Hamel, N. Cherepy, and S. Payne, "Application of Solution Techniques for Rapid Growth of Organic Crystals," *J. Cryst. Growth*, vol. 314, no. 1, pp. 163–170, 2011.

[75] G. Horowitz, "Organic Field-Effect Transistors," *Adv. Mater.*, vol. 10, no. 5, pp. 365–377, 1998.

[76] C. Nacci, F. Ample, D. Bleger, S. Hecht, C. Joachim, and L. Grill, "Conductance of a Single Flexible Molecular Wire Composed of Alternating Donor and Acceptor Units," *Nat. Commun.*, vol. 6, p. 7397, 2015.

[77] L. Grill, M. Dyer, L. Lafferentz, M. Persson, M. V. Peters, and S. Hecht, "Nano-Architectures by Covalent Assembly of Molecular Building Blocks," *Nat. Nanotechnol.*, vol. 2, no. 11, pp. 687–691, 2007.

[78] C. Nacci, A. Viertel, S. Hecht, and L. Grill, "Covalent Assembly and Characterization of Nonsymmetrical Single-Molecule Nodes," *Angew. Chem.*, vol. 128, no. 44, pp. 13 928–13 932, 2016.

[79] A. Einstein, "Über einen die Erzeugung und Verwandlung des Lichtes betreffenden heuristischen Gesichtspunkt," *Ann. Phys.*, vol. 322, no. 6, pp. 132–148, 1905.

[80] E. U. Condon, "Note on the External Photoelectric Effect of Semi-Conductors," *Phys. Rev.*, vol. 54, no. 12, p. 1089, 1938.

[81] L. Apker, E. Taft, and J. Dickey, "Photoelectric Emission and Contact Potentials of Semiconductors," *Phys. Rev.*, vol. 74, no. 10, p. 1462, 1948.

[82] P. W. Anderson, "Absence of Diffusion in Certain Random Lattices," *Phys. Rev.*, vol. 109, no. 5, pp. 1492–1505, 1958.

[83] N. F. Mott, "Electrons in Disordered Structures," *Adv. Phys.*, vol. 16, no. 61, pp. 49–144, 1967.

[84] M. H. Cohen, H. Fritzsche, and S. R. Ovshinsky, "Simple Band Model for Amorphous Semiconducting Alloys," *Phys. Rev. Lett.*, vol. 22, no. 20, p. 1065, 1969.

[85] R. A. Street, *Hydrogenated Amorphous Silicon*. Cambridge: Cambridge University Press, 2005.

[86] C. W. Peterson, J. H. Dinan, and T. E. Fischer, "Photoemission from Amorphous Silicon," *Phys. Rev. Lett.*, vol. 25, no. 13, p. 861, 1970.

[87] N. Mott, "The Mobility Edge since 1967," *J. Phys. C: Solid State Phys.*, vol. 20, no. 21, p. 3075, 1987.

[88] K. Tanaka and S.-i. Nakayama, "Where is the Mobility Edge in Amorphous Semiconductors," *J. Optoelectron. Adv. M.*, vol. 2, pp. 5–11, 2000.

[89] H. Bässler, *Hopping and Related Phenomena: Advances in Disordered Semiconductors*. Singapore: World Scientific, 1990, vol. 2.

[90] W. D. Gill, "Drift Mobilities in Amorphous Charge-Transfer Complexes of Trinitrofluorenone and Poly-n-vinylcarbazole," *J. Appl. Phys.*, vol. 43, no. 12, pp. 5033–9, 1972.

[91] M. Abkowitz, "Behavior of the Drift Mobility in the Glass Transition Region of Some Hole-Transporting Amorphous Organic Films," *J. Appl. Phys.*, vol. 52, no. 5, pp. 3453–6, 1981.

[92] S. J. Santos Lemus and J. Hirsch, "Charge Carrier Transport in Poly(phenylene vinylene) Films," *Philos. Mag. B*, vol. 53, p. 25, 1986.

[93] D. V. Lang, X. Chi, T. Siegrist, A. M. Sergent, and A. P. Ramirez, "Amorphouslike Density of Gap States in Single-Crystal Pentacene," *Phys. Rev. Lett.*, vol. 93, no. 8, p. 086802, 2004.

[94] N. Tessler and Y. Roichman, "Amorphous Organic Molecule/Polymer Diodes and Transistors—Comparison between Predictions Based on Gaussian or Exponential Density of States," *Org. Electron.*, vol. 6, no. 5–6, pp. 200–210, 2005.

[95] G. Paasch and S. Scheinert, "Charge Carrier Density of Organics with Gaussian Density of States: Analytical Approximation for the Gauss–Fermi integral," *J. Appl. Phys.*, vol. 107, no. 10, p. 104501, 2010.

[96] J. D. Livingston, *Electronic Properties of Engineering Materials*. New York: Wiley, 1999.

[97] W. Warta, R. Stehle, and N. Karl, "Ultrapure, High Mobility Organic Photoconductors," *Appl. Phys. A*, 1985.

[98] H. Bässler and A. Köhler, "Charge Transport in Organic Semiconductors," in *Unimolecular and Supramolecular Electronics I.* Berlin, Heidelberg: Springer Berlin Heidelberg, 2011, pp. 1–65.

[99] C. Liu, T. Minari, X. Lu, A. Kumatani, K. Takimiya, and K. Tsukagoshi, "Solution-Processable Organic Single Crystals with Bandlike Transport in Field-Effect Transistors," *Adv. Mater.*, vol. 23, no. 4, pp. 523–526, 2010.

[100] N. A. Minder, S. Ono, Z. Chen, A. Facchetti, and A. F. Morpurgo, "Band-Like Electron Transport in Organic Transistors and Implication of the Molecular Structure for Performance Optimization," *Adv. Mater.*, vol. 24, no. 4, pp. 503–508, 2011.

[101] T. Sakanoue and H. Sirringhaus, "Band-Like Temperature Dependence of Mobility in a Solution-Processed Organic Semiconductor," *Nat. Mater.*, vol. 9, no. 9, pp. 736–740, 2010.

[102] O. Ostroverkhova, D. G. Cooke, S. Shcherbyna, R. F. Egerton, F. A. Hegmann, R. R. Tykwinski, and J. E. Anthony, "Bandlike Transport in Pentacene and Functionalized Pentacene Thin Films Revealed by Subpicosecond Transient Photoconductivity Measurements," *Phys. Rev. B*, vol. 71, no. 3, pp. 035 204–6, 2005.

[103] M. Shur, M. Hack, and J. G. Shaw, "A New Analytic Model for Amorphous Silicon Thin-Film Transistors," *J. Appl. Phys.*, vol. 66, no. 7, pp. 3371–11, 1989.

[104] M. S. Shur, M. D. Jacunski, H. C. Slade, and M. Hack, "Analytical Models for Amorphous-Silicon and Polysilicon Thin-Film Transistors for High-Definition-Display Technology," *J. Soc. Inf. Display*, vol. 3, no. 4, pp. 223–236, 1995.

[105] G. Horowitz, R. Hajlaoui, and P. Delannoy, "Temperature Dependence of the Field-Effect Mobility of Sexithiophene. Determination of the Density of Traps," *J. Phys. III France*, vol. 5, no. 4, pp. 355–371, Apr. 1995.

[106] A. Miller and E. Abrahams, "Impurity Conduction at Low Concentrations," *Phys. Rev.*, vol. 120, no. 3, pp. 745–755, 1960.

[107] Y. N. Gartstein and E. M. Conwell, "High-Field Hopping Mobility in Molecular Systems with Spatially Correlated Energetic Disorder," *Chem. Phys. Lett.*, vol. 245, pp. 351–358, 1995.

[108] H. Bässler, G. Schönherr, M. Abkowitz, and D. M. Pai, "Hopping Transport in Prototypical Organic Glasses," *Phys. Rev. B*, vol. 26, pp. 3105–3113, 1982.

[109] P. M. Borsenberger, "Hole Transport in Tri-p-tolylamine-Doped Bisphenol-A-polycarbonate," *J. Appl. Phys.*, vol. 68, no. 12, pp. 6263–12, 1990.

[110] P. M. Borsenberger, L. Pautmeier, and H. Bässler, "Charge Transport in Disordered Molecular Solids," *J. Chem. Phys.*, vol. 94, no. 8, pp. 5447–9, 1991.

[111] G. Horowitz, *Semiconducting Polymers*. Weinheim: Wiley-VCH, 2000.

[112] S. Baranovski, *Charge Transport in Disordered Solids with Applications in Electronics*. Chichester: John Wiley Sons, 2006.

[113] S. D. Baranovskii, I. P. Zvyagin, H. Cordes, S. Yamasaki, and P. Thomas, "Percolation Approach to Hopping Transport in Organic Disordered Solids," *Phys. Status Solidi B*, vol. 230, no. 1, pp. 281–288, 2002.

[114] C. C. Tanase, E. J. Meijer, P. W. M. Blom, and D. M. de Leeuw, "Unification of the Hole Transport in Polymeric Field-Effect Transistors and Light-Emitting Diodes," *Phys. Rev. Lett.*, vol. 91, no. 21, p. 216601, 2003.

[115] W. J. Schottky, "Theoretical Models of Barriers," *Z. Phys.*, vol. 113, no. 516, pp. 367–371, 1939.

[116] N. F. Mott, "The Theory of Crystal Rectifiers," *Proc. Roy. Soc. Ser. A*, vol. 171, no. 27, p. 38, 1939.

[117] H. Schweikert, *Verh. Phys. Ges.*, vol. 99, no. 3, 1939.

[118] A. Kahn, N. Koch, and W. Gao, "Electronic Structure and Electrical Properties of Interfaces Between Metals and π-Conjugated Molecular Films," *J. Polym. Sci. B Polym. Phys.*, vol. 41, no. 21, pp. 2529–2548, 2003.

[119] H. Ishii and K. Seki, "Energy Level Alignment at Organic/Metal Interfaces Studied by UV Photoemission: Breakdown of Traditional Assumption of a Common Vacuum Level at the Interface," *IEEE Trans. Electron Devices*, vol. 44, no. 8, pp. 1295–1301, 1997.

[120] H. Fukagawa, S. Kera, T. Kataoka, S. Hosoumi, Y. Watanabe, K. Kudo, and N. Ueno, "The Role of the Ionization Potential in Vacuum-Level Alignment at Organic Semiconductor Interfaces," *Adv. Mater.*, vol. 19, no. 5, pp. 665–668, 2007.

[121] M. Knupfer and H. Peisert, "Electronic Properties of Interfaces Between Model Organic Semiconductors and Metals," *phys. stat. sol. (a)*, vol. 201, no. 6, pp. 1055–1074, 2004.

[122] N. Koch and A. Vollmer, "Electrode-Molecular Semiconductor Contacts: Work-Function-Dependent Hole Injection Barriers versus Fermi-Level Pinning," *App. Phys. Let.*, vol. 89, no. 16, p. 162107, 2006.

[123] M. Oehzelt, N. Koch, and G. Heimel, "Organic Semiconductor Density of States Controls the Energy Level Alignment at Electrode Interfaces," *Nat. Comm.*, vol. 5, pp. 1–8, 2014.

[124] J. Ivanco, F. P. Netzer, and M. G. Ramsey, "On Validity of the Schottky-Mott Rule in Organic Semiconductors: Sexithiophene on Various Substrates," *J. Appl. Phys.*, vol. 101, no. 10, p. 103712, 2007.

[125] J. Bardeen, "Surface States and Rectification at a Metal Semi-Conductor Contact," *Phys. Rev.*, vol. 71, pp. 717–727, 1947.

[126] W. Monch, "On the Physics of Metal-Semiconductor Interfaces," *Rep. Prog. Phys.*, vol. 53, no. 3, p. 221, 1990.

[127] R. T. Tung, "Recent Advances in Schottky Barrier Concepts," *Mater. Sci. Eng., R*, vol. 35, no. 1, pp. 1–138, 2001.

[128] L. Ley, Y. Smets, C. I. Pakes, and J. Ristein, "Calculating the Universal Energy-Level Alignment of Organic Molecules on Metal Oxides," *Adv. Funct. Mater.*, vol. 23, no. 7, pp. 794–805, 2012.

[129] F. Amy, C. Chan, and A. Kahn, "Polarization at the Gold/Pentacene Interface," *Org. Electron.*, vol. 6, no. 2, pp. 85–91, Apr. 2005.

[130] H. Yoshida, "Measuring the Electron Affinity of Organic Solids: An Indispensable New Tool for Organic Electronics," *Anal. Bioanal. Chem.*, vol. 406, no. 9-10, pp. 2231–2237, 2014.

[131] S. D. Baranovskii, O. Rubel, and P. Thomas, "Theoretical Description of Hopping Transport in Disordered Materials," *Thin Solid Films*, vol. 487, no. 1, pp. 2–7, 2005.

[132] S. D. Baranovskii, T. Faber, F. Hensel, and P. Thomas, "The Applicability of the Transport-Energy Concept to Various Disordered Materials," *J. Phys.: Condens. Matter*, vol. 9, no. 13, pp. 2699–2706, 1997.

[133] J. Hwang, A. Wan, and A. Kahn, "Energetics of Metal–Organic Interfaces: New Experiments and Assessment of the Field," *Mater. Sci. Eng., R*, vol. 64, no. 1-2, pp. 1–31, 2009.

[134] J. R. Macdonald, "Impedance Spectroscopy," *Annals of Biomedical Engineering*, vol. 20, no. 3, pp. 289–305, 1992.

[135] J. Drechsel, M. Pfeiffer, X. Zhou, A. Nollau, and K. Leo, "Organic Mip-diodes by p-Doping of Amorphous Wide-gap Semiconductors: CV and Impedance Spectroscopy," *Synth. Met.*, vol. 127, no. 1–3, pp. 201–205, 2002.

[136] G. Garcia-Belmonte, P. P. Boix, J. Bisquert, M. Sessolo, and H. J. Bolink, "Simultaneous Determination of Carrier Lifetime and Electron Density-of-States in P3HT:PCBM Organic Solar Cells under Illumination by Impedance Spectroscopy," *Sol. Energ. Mat. Sol. Cells*, vol. 94, no. 2, pp. 366–375, 2010.

[137] M. Glatthaar, N. Mingirulli, B. Zimmermann, T. Ziegler, R. Kern, M. Niggemann, A. Hinsch, and A. Gombert, "Impedance Spectroscopy on Organic Bulk-Heterojunction Solar Cells," *Phys. Status Solidi A*, vol. 202, no. 11, pp. R125–R127, 2005.

[138] G. Garcia-Belmonte, A. Munar, E. M. Barea, J. Bisquert, I. Ugarte, and R. Pacios, "Charge Carrier Mobility and Lifetime of Organic Bulk Heterojunctions Analyzed by Impedance Spectroscopy," *Org. Electron.*, vol. 9, no. 5, pp. 847–851, 2008.

[139] T. Okachi, T. Nagase, T. Kobayashi, and H. Naito, "Determination of Charge-Carrier Mobility in Organic Light-Emitting Diodes by Impedance Spectroscopy in Presence of Localized States," *Jpn. J. Appl. Phys.*, vol. 47, no. 12R, p. 8965, 2008.

[140] BioLogic, *EC-LAB*, 2015 (accessed May 6, 2014). [Online]. Available: http://www.bio-logic.info/potentiostat/eclab.html

[141] V. S. Reddy, S. Das, S. K. Ray, and A. Dhar, "Studies on Conduction Mechanisms of Pentacene Based Diodes Using Impedance Spectroscopy," *J. Phys. D: Appl. Phys.*, vol. 40, no. 24, p. 7687, 2007.

[142] C.-C. Chen, B.-C. Huang, M.-S. Lin, Y.-J. Lu, T.-Y. Cho, C.-H. Chang, K.-C. Tien, S.-H. Liu, T.-H. Ke, and C.-C. Wu, "Impedance Spectroscopy and Equivalent Circuits of Conductively Doped Organic Hole-Transport Materials," *Org. Electron.*, vol. 11, no. 12, pp. 1901–1908, 2010.

[143] PTC, *Mathcad Prime 3.0*, 2016 (accessed May 6, 2016). [Online]. Available: http://www.ptc.com/engineering-math-software/mathcadl

[144] MathWorks, *Matlab 2010a*, 2010 (accessed May 6, 2016). [Online]. Available: https://fr.mathworks.com/products/matlab/

[145] *SILVACO 2016 Atlas User's Manual*. Santa Clara, CA: SILVACO International, 2016.

[146] M. S.-C. Research and I. S. E. M.-R. Program, *Design Oriented ModellINg for flexible electrOnics (DOMINO)*, 2014-2016 (accessed November 11, 2015). [Online]. Available: http://cordis.europa.eu/project/rcn/194386_en.html

[147] R. Feynman, *The Character of Physical Law*, 1st ed. New York: Modern Library, 1965.

[148] S. Steudel, K. Myny, V. Arkhipov, C. Deibel, S. De Vusser, J. Genoe, and P. Heremans, "50 MHz Rectifier Based On an Organic Diode," *Nat. Mater.*, vol. 4, no. 8, pp. 597–600, 2005.

[149] C.-m. Kang, J. Wade, S. Yun, J. Lim, H. Cho, J. Roh, H. Lee, S. Nam, D. D. C. Bradley, J.-S. Kim, and C. Lee, "1 GHz Pentacene Diode Rectifiers Enabled by Controlled Film Deposition on SAM-Treated Au Anodes," *Adv. Electron. Mater.*, vol. 2, no. 2, pp. 1 500 282–7, 2015.

[150] A. Haldi, A. Sharma, W. J. Potscavage, and B. Kippelen, "Equivalent Circuit Model for Organic Single-Layer Diodes," *J. Appl. Phys.*, vol. 104, no. 6, p. 064503, 2008.

[151] D. M. Taylor and H. L. Gomes, "Electrical Characterization of the Rectifying Contact Between Aluminium and Electrodeposited Poly(3-methylthiophene)," *J. Phys. D: Appl. Phys.*, vol. 28, no. 12, pp. 2554–2568, 1995.

[152] P. Stallinga, H. L. Gomes, M. Murgia, and K. Müllen, "Interface State Mapping in a Schottky Barrier of the Organic Semiconductor Terrylene," *Org. Electron.*, 2002.

[153] R. S. Muller and T. I. Kamins, *Device Electronics for Integrated Circuits*, 3rd ed. New York: Wiley, 2003.

[154] T. Kirchartz, W. Gong, S. A. Hawks, T. Agostinelli, R. C. I. MacKenzie, Y. Yang, and J. Nelson, "Sensitivity of the Mott–Schottky Analysis in Organic Solar Cells," *J. Phys. Chem. C*, vol. 116, no. 14, pp. 7672–7680, 2012.

[155] D. Braga, M. Campione, A. Borghesi, and G. Horowitz, "Organic Metal-Semiconductor Field-Effect Transistor (OMESFET) Fabricated on a Rubrene Single Crystal," *Adv. Mater.*, vol. 22, no. 3, pp. 424–428, 2010.

[156] C. H. Kim, O. Yaghmazadeh, D. Tondelier, Y. B. Jeong, Y. Bonnassieux, and G. Horowitz, "Capacitive Behavior of Pentacene-Based Diodes: Quasistatic Dielectric Constant and Dielectric Strength," *J. Appl. Phys.*, vol. 109, no. 8, p. 083710, 2011.

[157] W. Gao and A. Kahn, "Electrical Doping: the Impact on Interfaces of π-Conjugated Molecular Films," *J. Phys.: Condens. Matter*, vol. 15, no. 38, pp. S2757–S2770, 2003.

[158] M. Pfeiffer, K. Leo, X. Zhou, J. S. Huang, M. Hofmann, A. Werner, and J. Blochwitz-Nimoth, "Doped Organic Semiconductors: Physics and Application in Light Emitting Diodes," *Org. Electron.*, vol. 4, no. 2-3, pp. 89–103, 2003.

[159] O. D. Jurchescu, J. Baas, and T. T. M. Palstra, "Electronic Transport Properties of Pentacene Single Crystals Upon Exposure to Air," *Appl. Phys. Lett.*, vol. 87, no. 5, pp. 052 102–4, 2005.

[160] P. H. Nguyen, S. Scheinert, S. Berleb, and W. Brütting, "The Influence of Deep Traps on Transient Current–Voltage Characteristics of Organic Light-Emitting Diodes," *Org. Electron.*, 2001.

[161] P. de Bruyn, A. H. P. van Rest, G. A. H. Wetzelaer, D. M. de Leeuw, and P. W. M. Blom, "Diffusion-Limited Current in Organic Metal-Insulator-Metal Diodes," *Phys. Rev. Lett.*, vol. 111, no. 18, p. 186801, 2013.

[162] S. Jung, C. H. Kim, Y. Bonnassieux, and G. Horowitz, "Injection Barrier at Metal/Organic Semiconductor Junctions with a Gaussian Density-of-States," *J. Phys. D: Appl. Phys.*, vol. 48, no. 39, pp. 1–10, 2015.

[163] J. S. Bonham and D. H. Jarvis, "Theory of Space-Charge-Limited Current with One Blocking Electrode," *Aust. J. Chem.*, vol. 31, no. 10, pp. 2103–2115, 1978.

[164] M. J. Kearney and R. J. Martin, "Airy Asymptotics: the Logarithmic Derivative and Its Reciprocal," *J. Phys. A: Math. Theor.*, vol. 42, no. 42, p. 425201, 2009.

[165] N. F. Mott and R. W. Gurney, *Electronic Processes in Ionic Crystals*, 2nd ed. Oxford: Clarendon Press, 1940.

[166] Y. Roichman and N. Tessler, "Generalized Einstein Relation for Disordered Semiconductors—Implications for Device Performance," *Appl. Phys. Lett.*, vol. 80, no. 11, p. 1948, 2002.

[167] S. L. M. van Mensfoort and R. Coehoorn, "Effect of Gaussian Disorder on the Voltage Dependence of the Current Density in Sandwich-Type Devices Based on Organic Semiconductors," *Phys. Rev. B*, vol. 78, no. 8, pp. 085 207–16, 2008.

[168] M. Vissenberg and M. Matters, "Theory of the Field-Effect Mobility in Amorphous Organic Transistors," *Phys. Rev. B*, 1998.

[169] C. C. Tanase, P. W. M. Blom, and D. de Leeuw, "Origin of the Enhanced Space-Charge-Limited Current in Poly(p-phenylene vinylene)," *Phys. Rev. B*, vol. 70, no. 19, p. 193202, 2004.

[170] Y. Roichman, Y. Preezant, and N. Tessler, "Analysis and Modeling of Organic Devices," *Phys. Status Solidi A*, vol. 201, no. 6, pp. 1246–1262, 2004.

[171] R. Coehoorn, W. Pasveer, P. Bobbert, and M. Michels, "Charge-Carrier Concentration Dependence of the Hopping Mobility in Organic Materials with Gaussian Disorder," *Phys. Rev. B*, vol. 72, no. 15, p. 155206, 2005.

[172] S. L. M. van Mensfoort, S. I. E. Vulto, R. A. J. Janssen, and R. Coehoorn, "Hole Transport in Polyfluorene-Based Sandwich-Type Devices: Quantitative Analysis of the Role of Energetic Disorder," *Phys. Rev. B*, vol. 78, no. 8, pp. 085 208–10, 2008.

[173] S. Kang, Y. Yi, C. Kim, K. H. Yoo, A. Moewes, M. Cho, J. Denlinger, C. Whang, and G. Chang, "Chemical Reaction at the Interface between Pentacene and HfO2," *Phys. Rev. B*, vol. 72, no. 20, p. 205328, 2005.

[174] W. Han, H. Yoshida, N. Ueno, and S. Kera, "Electron Affinity of Pentacene Thin Film Studied by Radiation-Damage Free Inverse Photoemission Spectroscopy," *Appl. Phys. Lett.*, vol. 103, no. 12, pp. 123 303–6, 2013.

[175] Y. M. Lee, J. W. Kim, H. Min, T. G. Lee, and Y. Park, "Growth Morphology and Energy Level Alignment of Pentacene Films on SiO2 Surface Treated with Self-Assembled Monolayer," *Current Applied Physics*, vol. 11, no. 5, pp. 1168–1172, 2011.

[176] W. Zhao, Y. Qi, T. Sajoto, S. Barlow, S. R. Marder, and A. Kahn, "Remote Doping of a Pentacene Transistor: Control of Charge Transfer by Molecular-Level Engineering," *Appl. Phys. Lett.*, vol. 97, no. 12, pp. 123 305–4, 2010.

[177] G. Horowitz, "Validity of the Concept of Band Edge in Organic Semiconductors," *J. Appl. Phys.*, vol. 118, no. 11, pp. 115 502–6, 2015.

[178] J. E. Lilienfeld, "Method and apparatus for controlling electric currents," 1930, uS Patent 1 745 175. [Online]. Available: https://www.google.com/patents/US1745175

[179] D. F. Barbe and C. R. Westgate, "Surface State Parameters of Metal-Free Phthalocyanine Single Crystals," *Journal of Physics and Chemistry of Solids*, vol. 31, no. 12, pp. 2679–2687, 1970.

[180] M. L. Petrova and R. L. D., "Field-eeffect in organic semiconductors," *Fiz. Tverd. Tela (Sov. Phys.-Solid State)*, vol. 12, p. 961, 1970.

[181] F. Ebisawa, T. Kurokawa, and S. Nara, "Electrical Properties of Polyacetylene/polysiloxane Interface," *J. Appl. Phys.*, vol. 54, no. 6, pp. 3255–6, 1983.

[182] D. D. Eley, "Phthalocyanines as Semiconductors," *Nature*, vol. 162, no. 4125, pp. 819–819, 1948.

[183] D. D. Eley, G. D. Parfitt, M. J. Perry, and D. H. Taysum, "The Semiconductivity of Organic Substances. Part 1," *Trans. Faraday Soc.*, vol. 49, pp. 79–86, 1953.

[184] C. R. Newman, C. D. Frisbie, D. A. da Silva Filho, J.-L. Brédas, P. C. Ewbank, and K. R. Mann, "Introduction to Organic Thin Film Transistors and Design of n-Channel Organic Semiconductors," *Chem. Mater.*, vol. 16, no. 23, pp. 4436–4451, 2004.

[185] D. Braga and G. Horowitz, "High-Performance Organic Field-Effect Transistors," *Adv. Mater.*, vol. 21, no. 14-15, pp. 1473–1486, Apr. 2009.

[186] S. A. DiBenedetto, A. Facchetti, M. A. Ratner, and T. J. Marks, "Molecular Self-Assembled Monolayers and Multilayers for Organic and Unconventional Inorganic Thin-Film Transistor Applications," *Adv. Mater.*, vol. 21, no. 14-15, pp. 1407–1433, 2009.

[187] R. A. Street and A. Salleo, "Contact Effects in Polymer Transistors," *App. Phys. Let.*, vol. 81, no. 15, p. 2887, 2002.

[188] T. J. Richards and H. Sirringhaus, "Analysis of the Contact Resistance in Staggered, Top-Gate Organic Field-Effect Transistors," *J. Appl. Phys.*, vol. 102, no. 9, pp. 094 510–6, 2007.

[189] H. Klauk, "Organic Thin-Film Transistors," *Chem. Soc. Rev.*, vol. 39, no. 7, p. 2643, 2010.

[190] G. Horowitz and P. Delannoy, "An Analytical Model for Organic-Based Thin-Film Transistors," *J. Appl. Phys.*, vol. 70, no. 1, pp. 469–475, 1991.

[191] W.-Y. Lin, R. Müller, K. Myny, S. Steudel, J. Genoe, and P. Heremans, "Room-Temperature Solution-Processed High-k Gate Dielectrics for Large Area Electronics Applications," *Org. Electron.*, vol. 12, no. 6, pp. 955–960, Jun. 2011.

[192] D. Vuillaume, C. Boulas, J. Collet, J. V. Davidovits, and F. Rondelez, "Organic Insulating Films of Nanometer Thicknesses," *Appl. Phys. Lett.*, vol. 69, no. 11, pp. 1646–1648, 1996.

[193] H. Klauk, U. Zschieschang, J. Pflaum, and M. Halik, "Ultralow-Power Organic Complementary Circuits," *Nature*, vol. 445, no. 7129, pp. 745–748, 2007.

[194] Y.-G. Ha, J. D. Emery, M. J. Bedzyk, H. Usta, A. Facchetti, and T. J. Marks, "Solution-Deposited Organic–Inorganic Hybrid Multilayer Gate Dielectrics. Design, Synthesis, Microstructures, and Electrical Properties with Thin-Film Transistors," *J. Am. Chem. Soc.*, vol. 133, no. 26, pp. 10 239–10 250, 2011.

[195] M.-H. Yoon, H. Yan, A. Facchetti, and T. J. Marks, "Low-Voltage Organic Field-Effect Transistors and Inverters Enabled by Ultrathin Cross-Linked Polymers as Gate Dielectrics," *J. Am. Chem. Soc.*, vol. 127, no. 29, pp. 10 388–10 395, 2005.

[196] C. Kim, Z. Wang, H.-J. Choi, Y.-G. Ha, A. Facchetti, and T. J. Marks, "Printable Cross-Linked Polymer Blend Dielectrics. Design Strategies, Synthesis, Microstructures, and Electrical Properties, with Organic Field-Effect Transistors as Testbeds," *J. Am. Chem. Soc.*, vol. 130, no. 21, pp. 6867–6878, 2008.

[197] Y.-Y. Noh and H. Sirringhaus, "Ultra-Thin Polymer Gate Dielectrics for Top-Gate Polymer Field-Effect Transistors," *Org. Electron.*, vol. 10, no. 1, pp. 174–180, 2009.

[198] F. Loffredo, I. A. Grimaldi, R. Miscioscia, G. Nenna, F. Villani, C. Minarini, M. Petrosino, A. Rubino, H. Usta, and A. Facchetti, "Photosensing Properties of Pentacene OFETs Based on a Novel PMMA Copolymer Gate Dielectric," *J. Display Technol.*, vol. 11, no. 6, pp. 533–540, 2015.

[199] I. Kymissis, C. D. Dimitrakopoulos, and S. Purushothaman, "High-performance bottom electrode organic thin-film transistors," *IEEE Transactions on Electron Devices*, vol. 48, no. 6, pp. 1060–1064, 2001.

[200] Y. Xu, T. Minari, K. Tsukagoshi, J. A. Chroboczek, and G. Ghibaudo, "Direct Evaluation of Low-Field Mobility and Access Resistance in Pentacene Field-Effect Transistors," *J. Appl. Phys.*, vol. 107, no. 11, pp. 114 507–8, 2010.

[201] K. P. Puntambekar, P. V. Pesavento, and C. D. Frisbie, "Surface Potential Profiling and Contact Resistance Measurements on Operating Pentacene Thin-Film Transistors by Kelvin Probe Force Microscopy," *App. Phys. Let.*, vol. 83, no. 26, pp. 5539–4, 2003.

[202] C. Bock, D. V. Pham, U. Kunze, D. Käfer, G. Witte, and C. Wöll, "Improved Morphology and Charge Carrier Injection in Pentacene Field-Effect Transistors with Thiol-Treated Electrodes," *J. Appl. Phys.*, vol. 100, no. 11, pp. 114 517–8, 2006.

[203] P. V. Pesavento, R. J. Chesterfield, C. R. Newman, and C. D. Frisbie, "Gated Four-Probe Measurements on Pentacene Thin-Film Transistors: Contact Resistance as a Function of Gate Voltage and Temperature," *J. Appl. Phys.*, vol. 96, no. 12, pp. 7312–14, 2004.

[204] C. H. Kim, Y. Bonnassieux, and G. Horowitz, "Fundamental Benefits of the Staggered Geometry for Organic Field-Effect Transistors," *IEEE Electron Device Lett.*, vol. 32, no. 9, pp. 1302–1304, 2011.

[205] P. Suciu and R. L. Johnston, "Experimental Derivation of the Source and Drain Resistance of MOS Transistors," *IEEE Trans. Electron Devices*, 1980.

[206] M. S. Shur, H. C. Slade, M. D. Jacunski, A. A. Owusu, and T. Ytterdal, "SPICE Models for Amorphous Silicon and Polysilicon Thin Film Transistors," *J. Electrochem. Sco.*, vol. 144, pp. 2833–2839, 1997.

[207] G. Horowitz, M. E. Hajlaoui, and R. Hajlaoui, "Temperature and Gate Voltage Dependence of Hole Mobility in Polycrystalline Oligothiophene Thin Film Transistors," *J. Appl. Phys.*, vol. 87, no. 9, pp. 4456–4463, 2000.

[208] M. Estrada, A. Cerdeira, J. Puigdollers, L. Reséndiz, J. Pallares, L. F. Marsal, C. Voz, and B. Iñiguez, "Accurate Modeling and Parameter Extraction Method for Organic TFTs," *Solid-State Electron.*, vol. 49, no. 6, pp. 1009–1016, Jun. 2005.

[209] H. Klauk, G. Schmid, W. Radlik, W. Weber, L. Zhou, C. D. Sheraw, J. A. Nichols, and T. N. Jackson, "Contact Resistance in Organic Thin Film Transistors," *Solid-State Electron.*, vol. 47, no. 2, pp. 297–301, 2003.

[210] G. B. Blanchet, C. R. Fincher, M. Lefenfeld, and J. A. Rogers, "Contact Resistance in Organic Thin Film Transistors," *Appl. Phys. Lett.*, vol. 84, no. 2, pp. 296–3, 2004.

[211] C.-s. Chiang, S. Martin, J. Kanicki, Y. Ugai, T. Yukawa, and S. Takeuchi, "Top-Gate Staggered Amorphous Silicon Thin-Film Transistors: Series Resistance and Nitride Thickness Effects," *Jpn. J. Appl. Phys.*, vol. 37, pp. 5914–5920, 1998.

[212] G. Horowitz, X. Peng, and D. Fichou, "The Oligothiophene-Based Field-Effect Transistor: How It Works and How to Improve It," *J. Appl. Phys.*, vol. 67, no. 1, p. 528, 1990.

[213] S. Jung, C. H. Kim, Y. Bonnassieux, and G. Horowitz, "Fundamental Insights into the Threshold Characteristics of Organic Field-Effect Transistors," *J. Phys. D: Appl. Phys.*, vol. 48, no. 3, p. 035106, 2015.

[214] S. Jain, "Measurement of Threshold Voltage and Channel Length of Submicron MOSFETs," *IEE Proceedings I (Solid-State and Electron Devices)*, vol. 135, no. 6, pp. 162–164, 1988.

[215] S. Luan and G. W. Neudeck, "An Experimental Study of the Source/Drain Parasitic Resistance Effects in Amorphous Silicon Thin Film Transistors," *J. Appl. Phys.*, vol. 72, no. 2, pp. 766–8, 1992.

[216] D. Boudinet, G. Le Blevennec, C. Serbutoviez, J.-M. Verilhac, H. Yan, and G. Horowitz, "Contact Resistance and Threshold Voltage Extraction in n-Channel Organic Thin Film Transistors on Plastic Substrates," *J. Appl. Phys.*, vol. 105, no. 8, pp. 084 510–9, 2009.

[217] C. C. Tanase, P. W. M. Blom, D. M. de Leeuw, and E. J. Meijer, "Charge Carrier Density Dependence of the Hole Mobility in Poly(p-phenylene vinylene)," *Phys. Status Solidi A*, vol. 201, no. 6, pp. 1236–1245, 2004.

[218] A. Cerdeira, M. Estrada, R. Garcìa, and A. Ortiz-Conde, "New Procedure for the Extraction of Basic a-Si:H TFT Model Parameters in the Linear and Saturation Regions," *Solid-State Electron.*, vol. 45, pp. 1077–1080, 2001.

[219] J. W. Jin, M. Oudwan, D. Daineka, and O. Moustapha, "Parameter Extraction Method for Universal Amorphous Silicon Thin-Film Transistors Simulation Program with Integrated Circuit Emphasis Model," *IET Circuits Devices Syst.*, 2012.

[220] A. Ortiz-Conde, F. J. Garcìa-Sánchez, J. Muci, A. T. Barrios, J. J. Liou, and C.-S. Ho, "Revisiting MOSFET Threshold Voltage Extraction Methods," *Microelectron. Reliab.*, vol. 53, no. 1, pp. 90–104, 2013.

[221] V. Mosser, D. Seron, and Y. Haddab, "Threshold Voltage Extraction Method in Field-Effect Devices with Power-Law Dependence of Mobility on Carrier Density," in *Proc. IEEE Int. Conf. Microelectron. Test Struct. (ICMTS) 2015*, Tempe, AZ, USA, Mar. 23–26, 2015.

[222] S. van Mensfoort and R. Coehoorn, "Effect of Gaussian Disorder on the Voltage Dependence of the Current Density in Sandwich-Type Devices Based on Organic Semiconductors," *Phys. Rev. B*, vol. 78, no. 8, p. 085207, 2008.

[223] S. Jung, A. Mohammed, G. Guillaume, A.-H. Thamer, P. Alba, G.-C. Enric, N. Yohann, T. Thierry, Y. Bonnassieux, and G. Horowitz, "A TIPS-TPDO-tetraCN Based n-Type Organic Field-Effect Transistor with a Cross-linked PMMA Polymer Gate Dielectric," *Appl. Mater. Inter.*, vol. 8, no. 23, pp. 14 701–14 708, 2016.

[224] E. J. Meijer, G. H. Gelinck, E. van Veenendaal, B. H. Huisman, D. M. de Leeuw, and T. M. Klapwijk, "Scaling Behavior and Parasitic Series Resistance in Disordered Organic Field-Effect Transistors," *Appl. Phys. Lett.*, vol. 82, no. 25, pp. 4576–3, 2003.

[225] D. Natali, L. Fumagalli, and M. Sampietro, "Modeling of Organic Thin Film Transistors: Effect of Contact Resistances," *J. Appl. Phys.*, vol. 101, no. 1, pp. 014 501–13, 2007.

[226] G. Gruntz, H. Lee, L. Hirsch, F. Castet, T. Toupance, A. L. Briseno, and Y. Nicolas, "Nitrile Substitution Effect on Triphenodioxazine-Based Materials for Liquid-Processed Air-Stable n-Type Organic Field Effect Transistors," *Adv. Electron. Mater.*, p. 1500072, Apr. 2015.

[227] K. Lee, M. Shur, T. A. Fjeldly, and T. Ytterdal, "Semiconductor device modeling for VLSI," Prentice-Hall, Inc., Upper Saddle River, NJ, USA, 1993.

[228] B. Iñiguez, R. Picos, D. Veksler, A. Koudymov, M. S. Shur, T. Ytterdal, and W. Jackson, "Universal Compact Model for Long- and Short-Channel Thin-Film Transistors," *Solid-State Electron.*, vol. 52, no. 3, pp. 400–405, 2008.

[229] C. H. Kim, A. Castro-Carranza, M. Estrada, A. Cerdeira, Y. Bonnassieux, G. Horowitz, and B. Iñiguez, "A Compact Model for Organic Field-Effect Transistors With Improved Output Asymptotic Behaviors," *IEEE Trans. Electron Devices*, vol. 60, no. 3, pp. 1136–1141, 2013.

[230] O. Marinov, M. J. Deen, U. Zschieschang, and H. Klauk, "Organic Thin-Film Transistors: Part I-Compact DC Modeling," *IEEE Trans. Electron Devices*, vol. 56, no. 12, pp. 2952–2961, 2009.

[231] R. W. I. de Boer, M. E. Gershenson, A. F. Morpurgo, and V. Podzorov, "Organic single-crystal field-effect transistors," *physica status solidi (a)*, vol. 201, no. 6, pp. 1302–1331, 2004.

[232] Y. Diao, L. Shaw, Z. Bao, and S. C. B. Mannsfeld, "Morphology control strategies for solution-processed organic semiconductor thin films," *Energy Environ. Sci.*, vol. 7, pp. 2145–2159, 2014.

[233] R. L. Headrick, S. Wo, F. Sansoz, and J. E. Anthony, "Anisotropic Mobility in Large Grain Size Solution Processed Organic Semiconductor Thin Films," *Appl. Phys. Lett.*, vol. 92, no. 6, 2008.

[234] L. Li, N. Lu, M. Liu, and H. Bässler, "General Einstein Relation Model in Disordered Organic Semiconductors Under Quasiequilibrium," *Phys. Rev. B*, vol. 90, no. 21, p. 214107, 2014.

[235] Y. S. Yang, I. K. You, J. B. Koo, S. S. Lee, S. C. Lim, and S. Y. Kang, "Characteristics of Via-Hole Interconnections Fabricated by Using an Inkjet Printing Method," *J. Korean Phys. Soc.*, vol. 57, pp. 1699–1701, 2010.

université PARIS-SACLAY
ÉCOLE DOCTORALE
INTERFACES
Approches Interdisciplinaires : Fondements, Applications et Innovation

Titre : Modèllisation Compacte à Base Physique des Composants Électroniques Organiuqes

Mots clés : Électronique organique, diodes, transistors à effet de champ, physique des composants électroniques, modélisation analytique, densité d'états Gaussienne

Résumé : En dépit d'une amélioration remarquable de la performance des composants électroniques organiques, il y a encore un manque de compréhension théorique rigoureuse sur le fonctionnement du composant. Cette thèse est consacrée à la création de modèles pratiques pour composants électroniques organiques à base physique complète. Un modèle compact à base physique d'un élément de circuit est une équation mathématique qui permet une déscription précise, simple et rigoureuse du fonctionnement du dispositif. Dans ce contexte, les caractéristiques distinctives de l'injection et du transport des porteurs de charge dans les semi-conducteurs organiques sont incorporées dans les modèles qui améliorent la précision sans compromettre la simplicité mathématique. L'effet concomitant sur les caractéristiques courant-tension des diodes et des transistors organiques prototypiques sont étudiés. Les méthodes d'extraction des paramètres cohérents aux modèles sont présentées qui permettent la détermination univoque des paramètres du composant utilisés pour prévoir le fonctionnement du composant et évaluer la performance du composant et les propriétés des couches minces et interfaces organiques. Les approches englobent le développement analytique des équations physiques, la simulation numérique à deux dimensions basée sur la méthode des éléments finis et la validation expérimentale. Les modèles compacts originaux et entièrement analytiques et des méthodes d'extraction de paramètres fournissent une compréhension fondamentale sur la façon dont le désordre énergétique dans une couche mince de semiconducteur organique, décrit par la densité d'états Gaussienne, affecte les caractéristiques courant-tension observables des composants.

Title : Physically-Based Compact Modelling of Organic Electronic Devices

Keywords : Organic electronics, diodes, field-effect transistors, device physics, analytical modeling, Gaussian density-of-states

Abstract : In spite of a remarkable improvement in the performance of organic electronic devices, there is still a lack of rigorous theoretical understanding on the device operation. This thesis is dedicated to establishing practical models of organic electronic devices with a full physical basis. A physically-based compact model of a circuit element is a mathematical equation that enables an accurate, simple and rigorous description of the device operation. In this context, distinctive features of charge carrier injection and transport in organic semiconductors are incorporated in the models that improves the accuracy without compromising the mathematical simplicity. The concomitant effect on the current-voltage characteristics of prototypical organic diodes and transistors are studied. Parameter extraction methods consistent to the models are presented which enable unambiguous determination of device parameters used to predict device operation and evaluate device performance and properties of organic thin-films and interfaces. The approaches encompass analytical development of physical equations, two-dimensional numerical simulation based on finite-volume method and experimental validation. The original and fully analytical compact models and parameter extraction methods provide fundamental understanding on how energetic disorder in an organic semiconductor thin-film, described by the Gaussian density of states, affects the observable current-voltage characteristics of the devices.

Université Paris-Saclay
Espace Technologique / Immeuble Discovery
Route de l'Orme aux Merisiers RD 128 / 91190 Saint-Aubin, France